

UNIVERSITI MALAYA

ORIGINAL LITERARY WORK DECLARATION

Name of Candidate: *Kow Kien Woh* (I.C./Passport No:

Registration/ Matric. No.: *KHA090059*

Name of Degree: *Doctor of Philosophy*

Title of Project/Paper/Research Report/Dissertation/Thesis (“this work”):

Synthesis and characterizations of bamboo leaf based carbon-opacified silica aerogel (COSA)

Field of Study: *Advanced Materials*

I do solemnly and sincerely declare that:

- (1) I am the sole author/ writer of this work;
- (2) This Work is original;
- (3) Any use of any work in which copyright exists was done by way of fair dealing and for permitted purposes and any excerpt or extract from, or reference to or reproduction of any copyright work has been disclosed expressly and sufficiently and the title of the Work and its authorship have been acknowledged in this work;
- (4) I do not have any actual knowledge nor do I ought reasonably to know that the making of this work constitutes an infringement of any copyright work;
- (5) I hereby assign all and every rights in the copyright to this Work to the University of Malaya (“UM”), who henceforth shall be owner of the copyright in this Work and that any reproduction or use in any form or by any means whatsoever is prohibited without the written consent of UM having been first had and obtained;
- (6) I am fully aware that if in the course of making this Work I have infringed any copyright whether I intentionally or otherwise, I may be subject to legal action or any other action as may be determined by UM.

Candidate’s signature:

Date:

Subscribed and solemnly declared before,

Witness’s signature :

Date:

Name :

Designation

ABSTRACT

Silica aerogel with extremely low thermal conductivity has great potential to be used as thermal insulating material. Its application is currently restricted by the expensive raw materials such as tetramethyl-orthosilicate (TMOS) and tetraethyl-orthosilicate (TEOS). In addition, pure silica aerogel has low absorption of infrared radiation at 3 – 8 μm and led to increase in thermal conductivity at high temperature. Carbon is commonly used as an opacifier in silica aerogel to absorb the radiation and therefore suppress thermal conductivity of aerogel. However, separated source of carbon is required for the opacification of aerogel. Biomass such as bamboo leaves and cogon grass contain both silica and carbon. They can provide both sources to synthesize carbon-opacified silica aerogel (COSA). The use of biomass in the synthesis of COSA not only can reduce the cost of expensive raw materials, but also to minimize agriculture waste. Hence, this work is aimed to synthesize COSA by using biomass as a single source of raw material. Effects of gelation pH, carbon loading, silica concentration and temperatures on the thermal conductivity of COSA were investigated and optimized by using statistical model. Its thermal insulative performance was compared with the silica aerogel synthesized via conventional method including TEOS and carbon black. The study revealed that thermal conductivity of silica aerogel opacified with activated carbon is comparable to those opacified with carbon black. The result showed that optimal carbon loading which minimized the thermal conductivity present at different temperatures. Such optimal loading increased as temperature applied to the opacified aerogel increased. Tie lines that optimized thermal conductivity at different temperatures were obtained for various combinations of carbon loading and silica concentration. Thermogravimetry (TGA) results of the aerogels also indicate that opacified aerogel is thermally stable up to 495 °C and therefore suitable to be used at high temperature.

ABSTRAK

Aerogel silika dengan kekonduksian haba yang amat rendah mempunyai potensi untuk digunakan sebagai bahan penebat haba. Aplikasinya kini adalah terhad oleh bahan mentah yang mahal seperti tetramethyl-orthosilicate (TMOS) dan tetramethyl-orthosilicate (TEOS). Satu lagi kelemahan aerogel silika tulen adalah penyerapan radiasi pada panjang gelombang (3-8 μm) yang rendah. Karbon biasanya digunakan sebagai agen opasifikasi aerogel silika untuk menyerap radiasi tersebut dan mengurangkan kekonduksian haba aerogel pada suhu tinggi. Sumber karbon opasifikasi aerogel perlu disediakan secara berasingan. Daun buluh dan lalang mengandungi jumlah silika amorfus dan karbon yang tinggi. Biojisim tersebut boleh digunakan menyediakan kedua-dua sumber silika dan karbon yang diperlukan untuk mensintesis aerogel silika yang diopasifikasi karbon (COSA). Kegunaan daun buluh dalam sintesis COSA boleh mengurangkan kos bahan mentah yang mahal dan mengurangkan sisa pertanian. Kerja ini bertujuan untuk mensintesis COSA dengan menggunakan biojisim sebagai sumber bahan tunggal. Kesan pH, kadar karbon, kepekatan silika dan suhu kepada kekonduksian haba telah disiasat dan dioptimumkan dengan model statistik. Keberkesanannya juga dibandingkan dengan aerogel silika lain yang dihasilkan daripada TEOS and karbon hitam. Keputusan menunjukkan kekonduksian haba aerogel silika yang diopasifikasi oleh karbon aktif adalah berbanding dengan yang diopasifikasi dengan karbon hitam. Keputusan juga menunjukkan terdapat kadar optimal karbon yang meminimalkan kekonduksian haba pada suhu berlainan dan kadar tersebut bertambah apabila suhu menaik. Garis-kait telah diterbitkan bagi pelbagai gabungan kadar karbon dan kepekatan silika bertujuan meminimalkan kekonduksian haba aerogel. Analisis thermo-gravimetri (TGA) menunjukkan aerogel teropasifikasi adalah stabil sampai 495 °C dan sesuai digunakan pada suhu tinggi.

ACKNOWLEDGEMENTS

I am indebted to my supervisor Dr. Rozita Yusoff who has never stop from motivating, encouraging and giving support as well as sincere guidance to me in this research work. My special gratitude is also extended to my co-supervisor Ir. Prof. Dr. Abdul Aziz Abdul Raman for his efforts throughout the years as good and supportive supervisor. I am also thankful to them for the painstaking task of reviewing this thesis.

The unflagging support given by my colleagues, especially Joseph Ho and Chan Chung Hung are gratefully acknowledged. I would also like to thank other post graduate students in the department for their companionship over the last few years. I have also been fortunate to receive the supports from our helpful department staffs, Pn. Norhaya and En. Jalaluddin, for not only allowed me to carry out experimental work but also assisted me in setting up experimental apparatus. Special thanks to BERNAS (*Padiberas Nasional*) Berhad in sponsoring rice husks to the department throughout the project.

Finally, I am very grateful to my family for their endless support, love and encouragement during completion of this research work. Any further comments and suggestions for improvement of the thesis would be gratefully received.

TABLE OF CONTENTS

	Page
Original literary work declaration	i
Abstract	ii
Abstrak	iii
Acknowledgements	iv
Table of contents	v
List of tables	ix
List of figures	xi
Notations	xvi
Symbols	xviii
Chapter 1 Introductions	
1.1 Background	1
1.2 Problem statement	3
1.3 Objectives	4
1.4 Framework of thesis	5
Chapter 2 Literature review	
2.1 Silica aerogel	
2.1.1 <i>Properties and uses of silica aerogel</i>	6
2.1.2 <i>Syntheses of silica aerogel</i>	7
2.2 Bio-silica	
2.2.1 <i>Forms of silica</i>	20
2.2.2 <i>Amorphous silica from biomasses</i>	21

	Page
2.3 Thermal transfer in silica aerogel	
2.3.1 <i>Convection</i>	25
2.3.2 <i>Conduction</i>	26
2.3.3 <i>Radiation</i>	29
2.4 Carbon as opacifiers	
2.4.1 <i>Activated carbon as opacifier</i>	32
2.5 Summary	34
Chapter 3 Research methodology	
3.1 Flow of research	36
3.2 Materials and apparatus	
3.2.1 <i>Materials</i>	37
3.2.2 <i>Apparatus</i>	38
3.3 Extraction and characterizations of bio-silica	
3.3.1 <i>Extraction of silica</i>	39
3.3.2 <i>Characterizations of bio-silica</i>	43
3.4 Synthesis and characterization of silica aerogel from bamboo leaf silica (BLS)	
3.4.1 <i>Preparation of water glass</i>	43
3.4.2 <i>Syntheses of silica aerogel</i>	46
3.4.3 <i>Characterizations of silica aerogel</i>	51
3.5 Synthesis and characterizations of activated carbon from bamboo leaf	
3.5.1 <i>Carbonization and activation of carbon</i>	53

	Page
3.6 Optimization of thermal conductivity via carbon opacification	
3.6.1 <i>Synthesis and characterizations of carbon opacified aerogel</i>	55
3.6.2 <i>Optimizations of thermal conductivity</i>	56
Chapter 4 Synthesis of bamboo leaf aerogel	
4.1 Extraction and characterizations of bio-silica	
4.1.1 <i>Ash content after combustion</i>	58
4.1.1.1 <i>Combustion in electric furnace</i>	58
4.1.1.2 <i>Thermo-gravimetric analysis (TGA)</i>	60
4.1.2 <i>Silica content by EDX</i>	65
4.1.3 <i>CHNS - carbon content and organic matters</i>	70
4.1.4 <i>XRD and amorphicity</i>	71
4.1.5 <i>Determination of kinetic parameters</i>	76
4.1.6 <i>Summary</i>	81
4.2 Preparation of water glass as precursor	
4.2.1 <i>Optimization of silica yield (ξ) in water glass</i>	82
4.2.2 <i>Characterizations of water glass</i>	88
4.2.3 <i>Summary</i>	89
4.3 Synthesis of silica aerogel	
4.3.1 <i>Hydrogels</i>	
4.3.1.1 <i>Opacity of hydrogels</i>	90
4.3.1.2 <i>Particle sizes of hydrosols</i>	94
4.3.1.3 <i>Removal of salts from hydrogels</i>	95

	Page
4.3.2 Aerogels	
4.3.2.1 Visual observation	96
4.3.2.2 Density, porosity, shrinkage and amorphicity	97
4.3.2.3 Microstructure and fractal dimensions	101
4.3.2.4 Adsorption properties	103
4.3.2.5 Chemical groups on surface	110
4.3.2.6 Thermal conductivity	111
4.3.2.7 Thermal stability	115
4.3.2.8 Summary	116
Chapter 5 Opacification of bamboo leaf aerogel	
5.1 Synthesis and characterizations of activated carbon	
5.1.1 Carbonization	117
5.1.2 Properties of activated carbon	125
5.1.3 Summary	129
5.2 Opacification of silica aerogel with activated carbon	
5.2.1 Effect of temperature	129
5.2.2 Effect of carbon loading	132
5.2.3 Effect of silica concentration in water glass	135
5.2.4 Modeling and optimization	140
5.2.5 Comparisons with other aerogels	153
5.2.6 Summary	158

	Page
Chapter 6 Conclusions and recommendations	
6.1 Conclusions	159
6.2 Novelty and contributions	162
6.3 Recommendations for future work	163
References	164
List of publications	176
Appendix – Originality report generated by turnitin software	177

LIST OF TABLES

		Page
Table 2.1	Molecular structures of TMOS and TEOS	8
Table 2.2	Properties of silica aerogels obtained via APD using various silylation agents	19
Table 2.3	Common polymorphs of crystalline silica	20
Table 3.1	List of materials	37
Table 3.2	List of apparatus	38 - 39
Table 3.3	Selected processing parameters that may affect the silica yield (ξ) in water glass	44
Table 4.1	Statistical analyses of ash content based on t-statistics at 95% level of confidence	59
Table 4.2	ANOVA & <i>t</i> -statistics analyses of ash content from TGA at 95% level of confidence	64
Table 4.3	Purity of silica and silica content in raw biomass estimated based on EDX [†]	67
Table 4.4	Summary of ANOVA on potassium leaching based on coded parameters	69
Table 4.5	Elemental analysis of CHNS [†]	70
Table 4.6	Effect of processing parameters on the silica yield in water glass [†]	83
Table 4.7	Time of gelation	90
Table 4.8	α -parameter of samples	91
Table 4.9	Fractals structural parameters determined by SAXS	102
Table 4.10	Comparison of specific surface area obtained via various methods	108
Table 4.11	Thermal conductivities calculated based on Eq. 4.8 – 4.12 compared with total conductivity measured in Figure 4.29.	112
Table 5.1	Summary of ANOVA on carbonization of bamboo leaf based on coded parameters	119

Table 5.2	Effect of activation temperature and time to the carbon burnt-off	121
Table 5.3	Effect of activation temperature and time to the density of activated carbon	121
Table 5.4	Adsorption characteristics of activated carbon	126
Table 5.5	Fractal characteristics of activated carbon fitted at 95% level of confidence	127
Table 5.6	Total thermal conductivity data fitted into second order model [Equation (5.15)]	140
Table 5.7	Total thermal conductivity data fitted into third order model [Equation (5.20)]	146

LIST OF FIGURES

	Page
Figure 2.1	Effects of pH to the gelation of silica sol (Iler, 1979) 11
Figure 2.2	Supercritical drying using methanol (Dorcheh and Abbasi, 2008b) 15
Figure 2.3	Supercritical drying using carbon dioxide (Dorcheh and Abbasi, 2008b) 16
Figure 2.4	Effect of silylation on silica network in silica gel (Dorcheh and Abbasi, 2008b) 17
Figure 2.5	Spectroscopic behavior of pure silica aerogel (Stangl et al., 1995) 30
Figure 2.6	Specific extinction coefficients of silica aerogel with and without carbon opacification (Lu et al., 1995) 31
Figure 2.7	Effect of carbon doping to the thermal conductivity of silica aerogel at 20°C (Lee et al., 1995) 31
Figure 2.8	Composition of the thermal conductivity of silica aerogels: gas, solid, and radiation transport depending on the density of the material (Hüsing and Schubert, 2000) 35
Figure 3.1	Stages to optimize thermal conductivity of carbon opacified silica aerogel 36
Figure 3.2	Process flow of the preparation of water glass from bamboo leaf 44
Figure 3.3	Synthesis scheme of silica aerogels from bamboo leaf water glass 45
Figure 3.4	Supercritical CO ₂ Drying rig (<i>Thar SFE 5000F2 system</i>) 47
Figure 3.5	Schematic diagram of <i>Thar SFE 5000F2 system</i> 48
Figure 3.6	Opacification of silica aerogel with activated carbon 55
Figure 4.1	Photographs taken for (a) dried and (b) combusted bamboo leaves, (c) dried and (d) combusted cogon grass, (e) dried and (f) combusted rice husks, and FESEM images of combusted (g) bamboo leaves, (h) cogon grass and (i) rice husks 58

		Page
Figure 4.2	DTG - Differential Thermo-gravimetry analysis at $10\text{ }^{\circ}\text{C min}^{-1}$ (<i>left</i>) and corresponding thermograms (<i>right</i>) for (a) bamboo leaves, (b) cogon grass, (c) rice husk and (d) rice straw	60
Figure 4.3	Fractional conversion of bamboo leaves (BB) and cogon grass (IC) at (a) 5, (b) 10 and (c) $20\text{ }^{\circ}\text{C min}^{-1}$	62- 63
Figure 4.4	EDX results of ashes of unleached (a) Bamboo leaves and (b) cogon grass	65
Figure 4.5	EDX results of ashes of leached (a) Bamboo leaves and (b) cogon grass	66
Figure 4.6	Weight fraction (%) of potassium leached from biomass (a) bamboo leaves, (b) cogon grass, (c) rice husks and (d) rice straw	68
Figure 4.7	XRD results of unleached (a) bamboo leaves, (b) cogon grass, (c) rice husk and (d) rice straw combusted in air at 650°C	71
Figure 4.8	XRD results of cogon grass combusted at various temperatures	73
Figure 4.9	XRD results of acid leached (a) bamboo leaf, (b) cogon grass, (c) rice husk and (d) rice straw combusted in nitrogen at 650°C	74
Figure 4.10	Differential thermogravimetry (DTG) of (a) bamboo leaf, (b) cogon grass	75
Figure 4.11	Thermograms of (a) bamboo leaf and (b) cogon grass	76
Figure 4.12	TGA iso-conversional data of (a) bamboo leaf and (b) cogon grass at three heating rates ($\beta = 5, 10$ and $20\text{ }^{\circ}\text{C.min}^{-1}$) fitted using the <i>Flynn-Wall-Ozawa</i> model.	77
Figure 4.13	DSC result of (a) bamboo leaf and (b) cogon grass combusted in air	79
Figure 4.14	Effects of the processing parameters on the silica yield in water glass	82 - 83
Figure 4.15	Optimization of the processing conditions with minimum (i) <i>t-T</i> , (ii) <i>t-A</i> and (iii) <i>T-A</i>	85
Figure 4.16	Silicates form may be formed in water glass	86

	Page
Figure 4.17 EDX spectrum of water glass that synthesized from the bamboo leaf silica	88
Figure 4.18 Colour of hydrogel formed. Top view (<i>up</i>) and side view (<i>down</i>)	89
Figure 4.19 Average particle sizes of hydrosols	93
Figure 4.20 Degree of salts removal in hydrogels as a function of soaking period	95
Figure 4.21 Photographs of (a) Hydrogel (before drying), (b) aerogel (after drying), (c) aerogel taken without camera flash and (d) aerogel taken with camera flash	96
Figure 4.22 Comparison of density, porosity and shrinkage of aerogels	97
Figure 4.23 XRD diffractograms of aerogels	99
Figure 4.24 SAXS scattering plot of aerogels	100-101
Figure 4.25 BET specific surface area and nanoparticle size of aerogels	103
Figure 4.26 Pore volume and average pores size of aerogels	103
Figure 4.27 Adsorption-Desorption isotherm of aerogels. Insets show the pore size distribution calculated based on BJH (adsorption) and DFT method	104-106
Figure 4.28 <i>FT-IR</i> spectra of aerogels	107
Figure 4.29 Thermal conductivity of aerogels and the correlation with fractal dimension	111
Figure 4.30 Thermal stability of aerogels determined by TGA	114
Figure 5.1 Photographs of bamboo leaves carbonized at various temperatures and time	117
Figure 5.2 Photograph (<i>close up view</i>) of bamboo leaves carbonized at axial points of CCD	118
Figure 5.3 Response surface of experimental region and the corresponding contour plot for the carbonization of bamboo leaf	120

	Page
Figure 5.4	Response surface of carbon burnt off and the corresponding contour plot for the activation of bio-char 122
Figure 5.5	Response surface of density and the corresponding contour plot for the activation of bio-char 123
Figure 5.6	EDX spectrum of activated carbon 125
Figure 5.7	EDX spectra of (a) activated carbon compared with (b) carbon black N330 125
Figure 5.8	Infrared absorption of activated carbon and carbon black N330 126
Figure 5.9	Linear dependence of total thermal conductivity to T^3 at various carbon loading (0-25 wt%). (a) 3.22 wt%, (b) 4.25 wt% and (c) 10 wt% of silica concentration in water glass. Regressed equations are shown following the sequence of increasing carbon loading from top to bottom 129-130
Figure 5.10	Effect of carbon loading to total thermal conductivity at various temperatures (30 – 300 °C). (a) 3.22 wt%, (b) 4.25 wt% and (c) 10 wt% of silica concentration in water glass 132-133
Figure 5.11	Effect of silica concentration in water glass to total thermal conductivity of opacified aerogel (25 wt% carbon) at various temperatures (30 – 300 °C) 134
Figure 5.12	(a) Estimated effect of aerogel density to the total thermal conductivity and (b) Minima of λ_T at various temperatures. Total thermal conductivity was estimated using equation (5.3) with $C=1$, $\varphi=1.5$, average $e = 40 \text{ m}^2 \text{ kg}^{-1}$, $\rho_s = 2.2 \text{ g cm}^{-3}$, $n=1$, average $S_{\text{BET}} = 400 \text{ m}^2 \text{ g}^{-1}$ and $p=1 \text{ bar}$ 135
Figure 5.13	Response surface of total thermal conductivity fitted with second order model at (a) 30 °C, (b) 100 °C, (c) 200 °C and (d) 300 °C. 141-142
Figure 5.14	Optimal tie lines to minimize total thermal conductivity of opacified aerogel at various temperatures based on equation (5.18) 144
Figure 5.15	Optimal tie lines to minimize total thermal conductivity of opacified aerogel with various silica concentrations based on equation (5.18) 144

	Page
Figure 5.16 Response surface of total thermal conductivity fitted with third order model at (a) 30 °C, (b) 100 °C, (c) 200 °C and (d) 300 °C.	147-148
Figure 5.17 Optimal tie lines to minimize total thermal conductivity of opacified aerogel at various temperatures based on equation (5.23)	149
Figure 5.18 Optimal tie lines to minimize total thermal conductivity of opacified aerogel with various silica concentrations based on equation (5.23)	150
Figure 5.19 Optimal tie lines to minimize total thermal conductivity of opacified aerogel at a given temperature obtained from solutions of equations (5.23) and (5.25)	152
Figure 5.20 Comparison of thermal conductivity of bamboo leaf aerogels opacified activated carbon and carbon black. Both types of aerogel are synthesized with 4.25 wt% of silica concentration and 1 – 25 wt% of carbon loading. (I) and (II) are rotated views to illustrate the comparison clearly.	153
Figure 5.21 Comparison of thermal conductivity of aerogels bamboo leaf aerogels with TEOS aerogels. Both types of aerogel are synthesized with 4.25 wt% of silica concentration and opacified with 0 – 25 wt% of activated carbon. (I) and (II) are rotated views to illustrate the comparison clearly.	155
Figure 5.22 Bulk density of bamboo leaf aerogels compared with TEOS aerogels. All aerogels were synthesized with 4.25 wt% silica concentration and opacified with 1 – 25 wt% of activated carbon.	156

NOTATIONS

Abbreviations

ABPR	Automated Back Pressure Regulator
APD	Ambient pressure drying
BB	Bamboo leaf
BET	Brunauer–Emmett–Teller
BJH	Barrett-Joyner-Halenda
CCD	Central composite design
COSA	Carbon-opacified silica aerogel
CVD	Chemical vapor deposition
DFT	Density Functional Theory
DLCA	Diffusion-Limited-Clusters-Aggregation
DSC	Differential scanning calorimeter
DTG	Differential Thermo-gravimetric Analysis
EDX	Energy Dispersive X-Ray
EtMeIm ⁺ Tf 2N ⁻	1-ethyl-3-methylimidazolium bis amide
FT-IR	Fourier transform infrared spectroscopy
HMDS	Hexamethyl-disiloxane
HMDZ	Hexamethyl-disilazane
IC	Cogon grass
ICP-AES	Inductively Coupled Plasma–Atomic Emission Spectroscopy
LHV	Lower heating value
MOR	Modulus of rupture
MTES	Methyl-triethoxysilane

MTMS	Methyl-trimethoxysilane
PEDS	Polyethoxydisiloxane
RF	Resorcinol – formaldehyde
SAXS	Small angle X-ray scattering
SCFD	Supercritical fluid drying
TEOS	Tetraethyl-orthosilicate
TGA	Thermogravimetric analysis
TMCS	Trimethyl-chlorosilane
TMES	Trimethyl-ethoxysilane
TMOS	Tetramethyl-orthosilicate
XRD	X-ray diffractometer

Symbols

W_{ash}	ash content
W_t	instantaneous weight percentage of biomass residue in TGA
W_f	final weight percentage of ash remained in TGA
β	heating rate of TGA
E_a	activation energy
M_{SiO_2}	molar mass of silica
W_{Si}	weight percentage of silicon in ash
W_{ch}	weight percentage of the biomass residue that remained after acid leaching
V_{NaOH}	NaOH volume reacted with silica in dissolution
ϕ	purity of silica determined by EDX
m_{BS}	mass of bio-silica used in the NaOH dissolution
M_{Si}	molar mass of silicon
ρ_{ae}	bulk density of aerogel
ρ_s	true density of aerogel
V_{ae}	volume of aerogel
V_{hyd}	volume of hydrogel
$I(q)$	scattering intensity of SAXS
D_s	surface fractal dimension
Γ	gamma function
ζ	characteristics length of a fractal structure

S/V	surface per unit volume ratio
K_p	Porod's law constant
S_{SAXS}	specific surface area determined by SAXS
X_{char}	percentage bio-char produced per gram of biomass carbonized
W_0	initial weight of biomass used in carbonization
W_R	weight of residue remained after carbonization
C_{burnt}	carbon burnt off in carbonization
W_{char}	weight of bio-char used in activation
W_{ac}	weight of activated carbon produced after activation
Θ_C	carbon loading in opacification
m_{ac}	mass of activated carbon used in opacification
m_{silica}	mass of silica used in opacification
m_{wg}	mass of water glass
Θ_{Si}	silica concentration in water glass
d_p	particle diameter
Q^n	local number of bridging oxygen between silicon atoms
D_f	apparent mass fractal dimension
λ_g	gaseous thermal conductivity
λ_r	radiative thermal conductivity
λ_s	solid thermal conductivity
λ_T	total thermal conductivity

S_{BET}	BET specific surface area
e	specific <i>Rosseland</i> mean extinction coefficients
$\hat{\lambda}_s$	true solid thermal conductivity
τ_i	regressed coefficients of parameters for second order model
γ_i	regressed coefficients of parameters for third order model
V_m	molar volume
d_g	diameter gas molecules
μ_g	dynamic viscosity of gas
ρ_g	density of gas
\hat{a}	radius of the pore
\bar{A}	frequency factor
\tilde{C}	pre-factor that depends on the interconnectivity of particles in aerogels
\tilde{e}	sample thickness to determine Rayleigh number
\tilde{P}	capillary pressure
Π	porosity
\bar{R}	universal gas constant
φ	constant depends on the interconnectivity of solid particles
$\hat{\alpha}$	size parameter of light scattering
$\tilde{\beta}$	thermal expansion coefficient of gas
σ	Stefan – Boltzman constant
k_B	Boltzman constant
l_m	mean free path of gas molecules,

A	agitation speed
a	primary particle size determined by SAXS
C	concentration of NaOH in water glass
D	mass fractal dimension
g	gravitational acceleration
$g(\alpha)$	integral conversion function
K	permeability coefficient
m_0	initial mass of biomass used in furnace combustion
m_{ash}	mass of ash collected after furnace combustion
n	refractive index of aerogel
p	pressure
q	scattering vector of SAXS
r	radius of curvature
R	volume-to-mass ratio in water glass
Ra	Rayleigh number
S	solubility of particle with radius r
S_0	solubility of silica with flat surface
T	absolute temperature
X	fractional conversion in TGA
α	degree of conversion
γ_{SL}	specific energy of solid-liquid interface
γ_{SV}	specific energy of solid-vapor interface
ΔT	temperature difference
ξ	silica yield in NaOH dissolution

CHAPTER 1

INTRODUCTION

1.1 Background

Silica aerogel is well known as the lightest solid that consists of amorphous 3-dimensional silica network with > 96% of its volume is filled with air. Aerogel was first invented by Steven Kistler in 1930s by using supercritical fluid drying (SCFD) of silica gel (Kistler, 1931, Kistler, 1932). This technique had successfully dried silica gel without collapsing its internal network. The result was a porous material (80-99.8% porosity) with extremely low density. Other unique properties of silica aerogel are including high specific surface area, low thermal conductivity, ultra-low dielectric constant and low refractive index. These special properties made aerogel a suitable material to be used in thermal insulation, acoustic barriers, supercapacitors, catalytic support, adsorption and studies of high energy physics (Dorcheh and Abbasi, 2008a).

Among the applications of silica aerogel, its thermal insulating property has received much attention from researchers. Thermal conductivity of silica aerogel is lower than still air and equivalent to the thermal insulation *R*-value of polyurethane foam used in refrigerators. Its *R*-value can be further enhanced when aerogel is used under partial vacuum (~0.1 atm), thus giving a much more energy efficient insulating material (Dorcheh and Abbasi, 2008a).

Heat transfer in silica aerogel occurred in three modes; i.e. solid conductivity through silica network, gaseous conductivity through open pores, and radiation. Since silica network consist of many “dead ends”, solid thermal conduction occurs through various tortuous paths and thus not effective in transferring heat. Gaseous conductivity can be suppressed if the mean free path of air is lengthened to exceed the pore size in aerogel. This can be achieved easily by applying modest vacuum pressure because silica

aerogel consists mainly of mesopores (2-50 nm). For radiative transport in silica aerogel, it is mainly caused by its low absorption coefficients for wavelengths in 3-8 μm , i.e. in the region of infrared. Under vacuum condition, the heat transfer in silica aerogel is attributed to solid and radiative components; each contributed about half of the heat passes. At elevated temperature ($>200^\circ\text{C}$), the radiative transport in silica aerogel becomes the dominant mode of heat transfer. Therefore, the radiative transport must be suppressed if silica aerogel is used for insulation purposes at high temperature. Researchers had attempted to opacify silica aerogel with carbon because carbon has good absorption in infrared region. Thermal conductivity of carbon-opacified silica aerogel (COSA) under room condition is ranged from 0.013 to 0.018 $\text{W}\cdot\text{m}^{-1}\cdot\text{K}^{-1}$ (Dorcheh and Abbasi, 2008a).

Carbon opacification was carried out mainly by dispersing stable carbon into pure silica aerogel. In such cases, external carbon sources are required. Both amorphous silica and carbon can be obtained from bamboo leaf and cogon grass upon pyrolysis. Thus they have great potential to be cheap raw materials for the production of COSA. Bamboo leaf is the agricultural waste commonly arises from paper production. It is normally burnt in open landfills in which airborne pollutants are the direct consequence of this open burning. Cogon grass (*Imperata cylindrica*) is considered as one of the worst invasive weeds which had infested more than 500 million hectares of land worldwide (Lowe S, 2004, MacDonald, 2007) because it is pyrogenic, rhizomatous perennial, hardly decompose, unpalatable and allelopathic. There is very limited reported work on the silica content in cogon grass. Some literature speculated cogon grass is rich in silica, hence can be considered as another potential candidate to produce high purity bio-silica. However, no information or data had been reported to support such statement. Rice husk, which contains averagely 20 wt% of silica, was previously used to synthesize pure silica aerogel without any opacification (Li and Wang, 2008,

Tang and Wang, 2005). To the best of author's knowledge, rice husk is the only biomass attempted to synthesize silica aerogel. Hence, rice husk was used as a comparison biomass throughout this study.

1.2 Problem statement

Conventionally, silica aerogel is mostly produced by using expensive precursors such as tetramethyl orthosilicate (TMOS) and tetraethyl orthosilicate (TEOS). Both of these materials are hazardous, especially TMOS can cause blindness (Dorcheh and Abbasi, 2008a). By using biomass such as bamboo leaf and cogon grass, it not only eliminates these problems but also helps to convert agriculture waste to value added product. However, attempt on synthesizing COSA using bamboo leaf and cogon grass had not been reported so far. Hence, in this work, it is expected that silica and carbon content in bamboo leaf and cogon grass can be utilized as a new alternative source to produce COSA. Parameters in the extraction of silica and carbon, gelation, and opacification are expected to influence the characteristics of aerogel produced. Such parameters will be studied to optimize the performance of COSA produced as a thermal insulating material.

1.3 Objectives

This work is aimed to:

- (i) investigate the suitability of bio-silica extracted from bamboo leaf and cogon grass to synthesize silica aerogel;
- (ii) synthesize and characterize silica aerogel using silica extracted from bamboo leaf;
- (iii) opacify and characterize the silica aerogel that opacified with activated carbon (COSA);
- (iv) develop correlations on the processing parameters that optimize performance of COSA as thermal insulating material; and
- (v) compare the thermal insulation performance of COSA with aerogels synthesized using TEOS and carbon black.

1.3 Framework of thesis

The thesis contains six chapters and the content of each chapter are outlined as follows:

- Chapter 1** introduces the background and objectives of this research.
- Chapter 2** presents the synthesis and opacification process of silica aerogel. Sources and potential of selected biomass in synthesizing aerogel are discussed. Theory on various modes of heat transfer is also introduced in this chapter.
- Chapter 3** describes the research methodology for the synthesis, opacification and optimization of bamboo leaf aerogel.
- Chapter 4** discuss on the extraction of silica from biomass and synthesis of aerogel from the extracted silica. Optimization of silica dissolution to form water glass is also detailed in this chapter.
- Chapter 5** focuses on the opacification of silica aerogel obtained. Various statistical models are developed to optimize the performance of opacified aerogel.
- Chapter 6** concludes all the findings in this work and recommends relevant future direction of this research. The chapter also highlights the novelty contributed by this study

CHAPTER 2

LITERATURE REVIEW

2.1 Silica aerogel

2.1.1 *Properties and uses of silica aerogel*

Aerogel is referred as airy solid where 80-99% of its volume is filled with air. This gives rise to its extremely low density, which reaching a minimum density of 0.003 g.cm^{-3} (Dorcheh and Abbasi, 2008b). Among many types of aerogel, silica aerogel has the unusual properties including high specific surface area, $500 - 1200 \text{ m}^2.\text{g}^{-1}$ (Fricke and Emmerling, 1992a), low thermal conductivity, $0.005 \text{ W.m}^{-1}.\text{K}^{-1}$ (Jensen et al., 2004, Schultz et al., 2005), ultra-low dielectric constant, ($k = 1.0 - 2.0$) and low refractive index (1.005) (Fricke and Emmerling, 1992b, Fricke, 1988).

The extraordinary characteristics of silica aerogel make it suitable to be used in many engineering applications. For instance, super-capacitor can be made from silica aerogel due to its ultra-low dielectric constant (Du et al., 2009, Mohanan and Brock, 2004). In nuclear studies, the low refractive index of silica aerogel had been used to detect Cherenkov's radiation (Brajnik et al., 1994, Brajnik et al., 1995, Fricke and Emmerling, 1998, Carlson et al., 1995). Silica aerogel is also used in chemical industries as absorbent to remove toxic compounds from wastes (Liu et al., 2009, Hrubesh et al., 2001, Standeker et al., 2007, Rao et al., 2007b). Other engineering applications include acoustics barrier (Wang et al., 2010), catalyst (Cutrufello et al., 2011, Pajonk, 1991) and catalytic support (Dominguez et al., 2010, Dominguez et al., 2008, Tai et al., 2009, Dias et al., 2006).

Among the applications of silica aerogel, its thermal insulating property has received much attention from researchers. Thermal conductivity of silica aerogel is lower than still air, i.e. ranged from $0.017 - 0.02 \text{ W.m}^{-1}.\text{K}^{-1}$ at room condition (Fricke et

al., 1987, Hummer et al., 1992, Hummer et al., 1993, Wei et al., 2009a, Wei et al., 2011). When aerogel is used under partial vacuum (~0.1atm), its R-value can be increased to R20 per inch (Hrubesh and Pekala, 1994). Glazing was built by using the translucent properties of silica aerogel coupled with its low thermal conductivity (Reim et al., 2002, Reim et al., 2005).

2.1.2 *Synthesis of silica aerogel*

The properties of silica aerogel can be altered easily by many parameters involved in the synthesis. Hence, it is crucial to understand the process to synthesize aerogel with desired characteristics. Synthesis of silica aerogel can be generally divided into four stages:

(a) Sol preparation

Suspension of solid colloidal particles ranged in 1-1000 nm is termed as sol. In a sol-gel process, particles in sol are polymerized to form 3-dimensional rigid gel network. The most common type of sol used in synthesis of silica aerogel is silicon alkoxides such as silicon tetra-methoxide (more known as tetramethyl orthosilicate, TMOS) and silica tetra-ethoxide (more known as tetraethyl orthosilicate, TEOS). Table 2.1 shows molecular structures of TMOS and TEOS.

Despite their toxicity, TMOS and TEOS are being commonly used to synthesize silica aerogel due to their purity and ease to hydrolyze in water (Brinker and Scherer, 1990). The partial hydrolysis of such alkoxides in water produces intermediate sol, which condense and polymerize to form gel. Equation (2.1) shows the formation of sol from the hydrolysis of alkoxides:

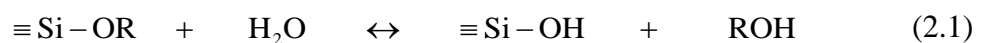
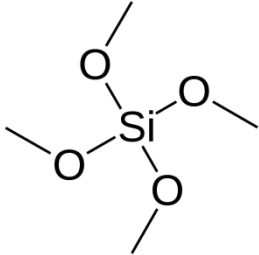
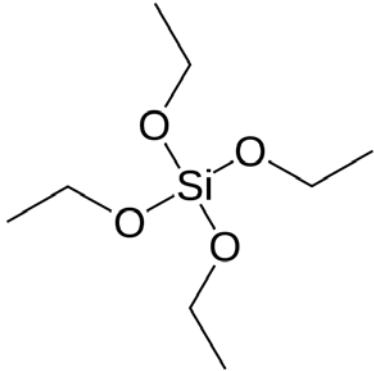


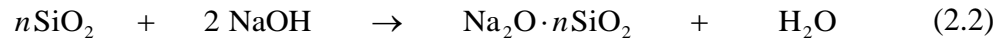
Table 2.1: Molecular structures of TMOS and TEOS

Silicon alkoxides	Molecular formula	Structural formula
Tetramethyl orthosilicate (TMOS)	$\text{Si}(\text{OCH}_3)_4$	
Tetraethyl orthosilicate (TEOS)	$\text{Si}(\text{OC}_2\text{H}_5)_4$	

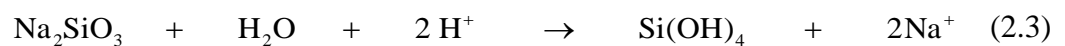
where R is either methyl group (TMOS) or ethyl group (TEOS). Attempts to synthesize silica aerogels with other precursors such as polyethoxydisiloxane (PEDS) (Chao et al., 2009, Rigacci et al., 1998, Wagh et al., 1999), methyltrimethoxysilane (MTMS) (Anderson et al., 2010, Hayase et al., 2011, Bhagat et al., 2007c, Nadargi and Rao, 2009, Rao and Haranath, 1999), and methyltriethoxysilane (MTES) (Aravind and Soraru, 2011, Nadargi and Rao, 2009) were also reported. According to the results, silica aerogels that produced with PEDS generally has narrower and more uniform pore size distribution as well as lower thermal conductivity as compared with those made of TEOS (Wagh et al., 1999). Whereas, super hydrophobic silica aerogels are usually obtained from precursors like MTMS and MTES.

Alternatively, sodium silicate solution, which usually known as water glass can be served as precursor for the sol. The use of water glass is less hazardous, economical and more environmental friendly as compared with alkoxides, because water glass is

non-toxic and cheap. Graded in term of molar ratio $\text{Na}_2\text{O}:\text{SiO}_2$, water glass is manufactured by dissolving sources of amorphous silica into sodium hydroxide solution as shown in reaction [equation \(2.2\)](#):



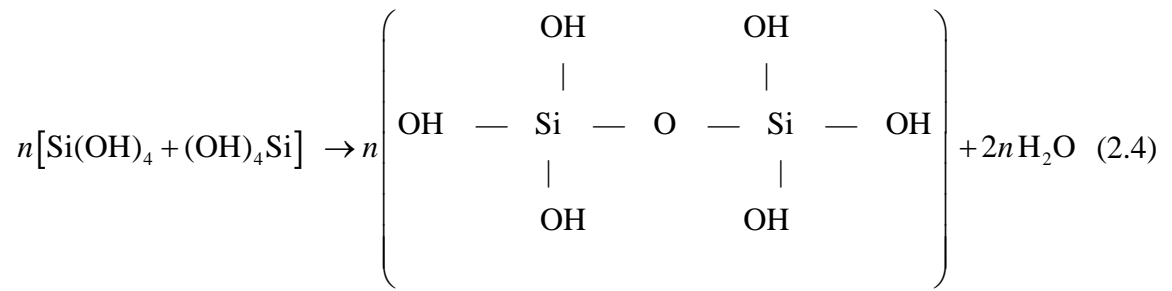
When sodium silicate reacts with acidic solution as in [equation \(2.3\)](#), monomers of silicic acid are formed:



However, the molar ratios of $\text{Na}_2\text{O}:\text{SiO}_2$ reported in previous studies are greatly varied from 1:0.43 (Shi et al., 2010) to 1:3.4 (Hwang et al., 2008, Rao et al., 2001). It is remains unclear how this molar ratio will affect the thermal conductivity of silica aerogel synthesized. High molar ratio may lead to over hydrolysis, but low molar ratio may also cause difficulty in gelation. The author of this work suspects that it is not the molar ratio that contributes to the gelation but rather the concentration of SiO_2 in the water glass solution. Low concentration of SiO_2 as the consequence of several dilution may cause the oligomers formed sparsely in the liquor and are not able to develop into 3-dimensional network. The study on the effect of SiO_2 concentration to the gelation is thus one of the objectives in this work.

(b) Gelation

Monomers of silicic acid gelled as the consequence of the condensation sol which followed by polymerization. [Equation \(2.4\)](#) shows the polymerization of silicic acid formed by sodium silicate:



According to Iler (Iler, 1979), the polymerization can be divided into three stages as follows:

- (i) Polymerization of monomer to form particles;
- (ii) Growth of particles
- (iii) Linking particles into chain, followed by networks formed extended throughout the liquid medium which thickening to gel

Unlike polymerization in organic polymers, silicic acid monomers first polymerize into discrete particles. These particles are aggregated, instead of branched and cross-linked as in organic polymers; then formed rings and networks creating larger 3-dimensional aggregates. As these aggregates condense to compact state and grow sufficiently large across the liquid medium, gel point is reached and monolith gel is formed.

Figure 2.1 shows the effects of pH in silica water system. Polymerization of silicic acid is highly affected by pH of the solution (Iler, 1979, Brinker and Scherer, 1990). Rapid aggregation occurs in the range of pH 4 – 7.5. At pH more than 7.5, the gel time increased with the pH, owing to high dissolution of silicic acid to form ionic species including HSiO_3^- and $\text{Si}(\text{OH})_5^-$ (Iler, 1979). These ionic species are mutually repulsive and aggregation is hard to occur at this range of pH. Salts can be added to overcome this as charges carried by salts can reduce the surface charges of the electric double layers.

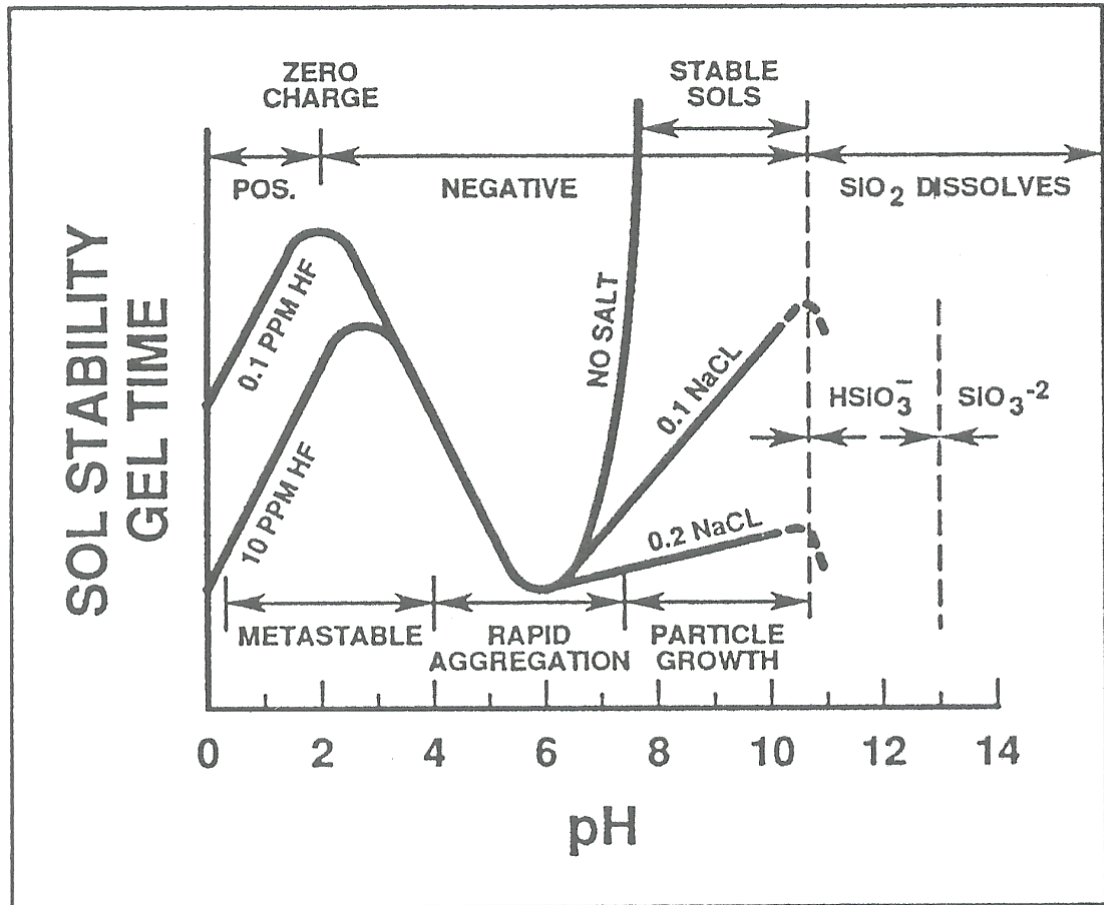


Figure 2.1: Effects of pH to the gelation of silica sol (Iler, 1979)

(c) Aging of gel

The growth of aggregate does not cease in parallel with the gel point. Aggregation of monomers within the liquid medium can still proceed to strengthen the skeleton of gel formed. This is due to the fact that strong backbone of gel is desired to reduce shrinkage of gel during drying. The process of this growth is known as aging of gel.

Ostwald ripening process is involved during aging. The solubility of silica is very much related to the particle size as shown in Ostwald-Freundlich equation:

$$S = S_0 \exp\left(\frac{2\gamma_{SL} V_m}{R T r}\right) \quad (2.5)$$

where

- S : solubility of particle with radius r
- S_0 : solubility of silica with flat surface
- γ_{SL} : liquid-solid interfacial energy, 50-100 ergs.cm^{-2} for amorphous silica (Iler, 1979)
- V_m : molar volume (27.2 cm^3 for amorphous silica) (Iler, 1979)
- \bar{R} : universal gas constant ($8.3 \times 10^7 \text{ ergs.mol}^{-1} \cdot \text{K}^{-1}$)
- T : absolute temperature (K)
- r : radius of curvature (cm)

From [equation \(2.5\)](#), small particles tend to dissolve more into the liquid medium. As the neck (where two larger particles are in contact) has negative curvature ($r < 0$), the dissolved particles will re-precipitate at the neck and toughening the structure. Despite aging helps to strengthen the gel, it is reported that prolong aging caused coarsening of structure (Haereid et al., 1995a) and also increase in density of gel owing to severe shrinkage (Rao et al., 2004).

Modulus of rupture (MOR) and shear modulus (G) of gel are generally used as proxy to the degree of aging. They indicate the strength of gel along the aging period. Factors such as aging temperature and aging time had already been investigated extensively (Haereid et al., 1995a, Rangarajan and Lira, 1991, Rao et al., 2004, Reichenauer, 2004, Bangi et al., 2008b, He et al., 2009, Strom et al., 2007, Hdach et al., 1990). Generally, the results show that the optimum aging period is about 3 hours (Bangi et al., 2008b, Haereid et al., 1995a, Strom et al., 2007). For aging temperature, it has a range resulted in optimum MOR and shear modulus of aerogel. The maximum MOR and shear modulus attained at various temperatures do not vary much but the

aging time required to reach such maximum can be greatly reduced at higher temperature (Haereid et al., 1995a, Reichenauer, 2004).

Silica based organic solvents are sometimes added during aging to strengthen the gel. Solvents such as TEOS/ethanol (Hwang et al., 2007, He et al., 2009, Haereid et al., 1995b, Einarsrud and Nilsen, 1998a, Einarsrud and Nilsen, 1998b), hexamethyl-disilazane (HMDZ) (Bhagat et al., 2007b) and trimethylchlorosilane (TMCS) (Wei et al., 2007, Bhagat et al., 2008, Shlyakhtina and Oh, 2008) are used in aging not only to add new monomers but also to promote crosslinking to silica network in wet gel. The aerogel produced with these solvents are hydrophobic due to the addition of alkyl groups on the surface of the gel.

As an alternative, ionic liquid with zero vapor pressure was used in aging. It would be an advantage to age silica gel in ionic liquid where no vaporization can occur within the gel network, which led to shrinkage and cracks. Dai (Dai et al., 2000) had aged silica hydrogel in ionic liquid 1-ethyl-3-methylimidazolium bis amide ($\text{EtMeIm}^+ \text{Tf} 2\text{N}^-$) and the results is encouraging as no shrinkage were observed in aerogel obtained. In spite of that, there is no follow-up study been reported. This is most probably due to economic infeasibility of using high cost ionic liquid.

(d) Drying of gel

Drying of wet gel is most critical step in the synthesis of aerogel. Enormous capillary pressure is induced by nano-pores within the gel during drying process. Its magnitude may reach 100 - 200 MPa (Brinker and Scherer, 1990, Scherer and Smith, 1995), and collapse of gel is an inevitable consequence of drying the gel rapidly under room pressure. The dry collapsed gel is known as xerogel, which has very high density as compared with aerogel.

During drying, the liquid on the outer surface of gel is evaporated and the inner pores together with its solid wall are exposed to liquid and vapor. The three solid-liquid, solid-vapor and liquid-vapor interfaces produced capillary pressure on the wall of pore, i.e. the solid skeleton of the gel. By assuming pores within the gel are in cylindrical shape, the capillary pressure can be estimated using [equation \(2.6\)](#):

$$\tilde{P} = -\frac{2(\gamma_{SV} - \gamma_{SL})}{\hat{a}} \quad (2.6)$$

where

- \tilde{P} : Capillary pressure (J.m⁻³)
- γ_{SV} : Specific energy of solid-vapor interface (J.m⁻³)
- γ_{SL} : Specific energy of solid-liquid interface (J.m⁻³)
- \hat{a} : Radius of the pore (m)

The inverse relation between \tilde{P} and \hat{a} explains the reason the capillary pressure increases drastically as pore size within the gel approaches nanometer range. In addition, the non-uniformity in pore size worsens the scenario. Should the pore size is uniform throughout the gel, or at least distributed narrowly, capillary pressure will be balanced in every direction, thus only very little shrinkage will occur in drying.

In the early of 1930s, Kistler (Kistler, 1931, Kistler, 1932) had dried the gel successfully using supercritical fluid technique. It is well known when a fluid enters supercritical state, the liquid-vapor boundary becomes indistinguishable and forms a homogenous fluid. Consequently, the liquid within the pores is converted into supercritical fluid without collapsing the gel network. The supercritical fluid is then being brought into gas phase by lowering the pressure gradually at temperature higher than its critical temperature to ensure no condensation occurs. Aerogel is produced as the gas within the pores is replaced with air under room conditions. Kistler's original attempt used alcohol as solvent in supercritical drying instead of water, which present in

the pores of hydrogel. Ultra high critical point of water makes the supercritical drying process economically infeasible. Alcohol such as ethanol with lower critical point is used, as it is totally miscible in water to replace pore water in gel. Alcolgel is formed as the result of this solvent exchange process. [Figure 2.2](#) illustrates the supercritical fluid drying process with methanol:

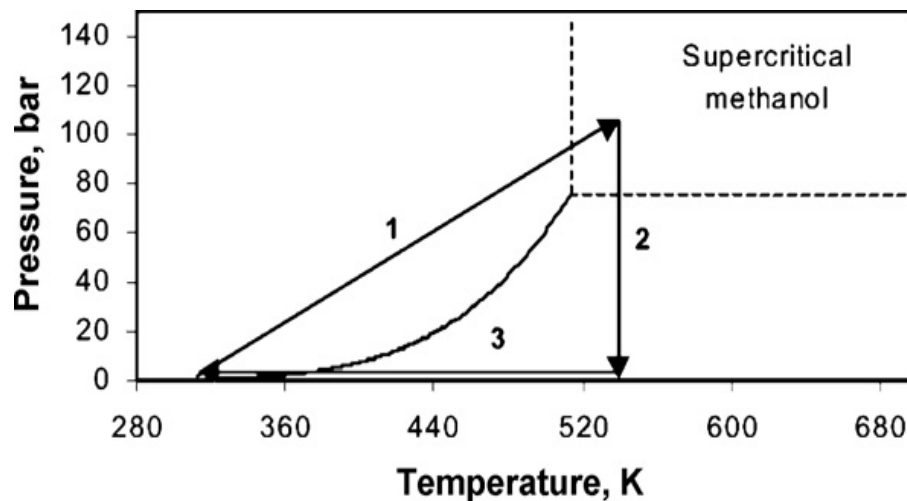


Figure 2.2: Supercritical drying using methanol (Dorcheh and Abbasi, 2008b)

Supercritical drying of aerogel in alcohol had received much attention but none had been brought into industrial production. Beside high temperature and high pressure involve, flammability of alcohol under such condition posed a great challenge to the safety of the process. This causes the response of this technique was then slowly receded. It was not until late 1980s the attention of such technique been reignited, when alcohol been replaced with carbon dioxide in supercritical fluid drying of aerogel (Phalippou et al., 1995, Tewari et al., 1985, Fricke and Emmerling, 1992a). Replacing alcohol with carbon dioxide makes the process possible to operate safely (as carbon dioxide is inert) under lower temperature (due to lower critical point of carbon dioxide). [Figure 2.3](#) shows the stages involve in the supercritical drying of aerogel using carbon dioxide. The success of CO₂ supercritical drying causes a drastic growth of research in aerogels. In this process, due to poor solubility of water in liquid carbon dioxide, water in pores is first solvent exchanged with alcohol to form alcolgel. Alcohol in pores is then

exchanged with liquid carbon dioxide before subject to drying. The major drawback of this method is the solvent

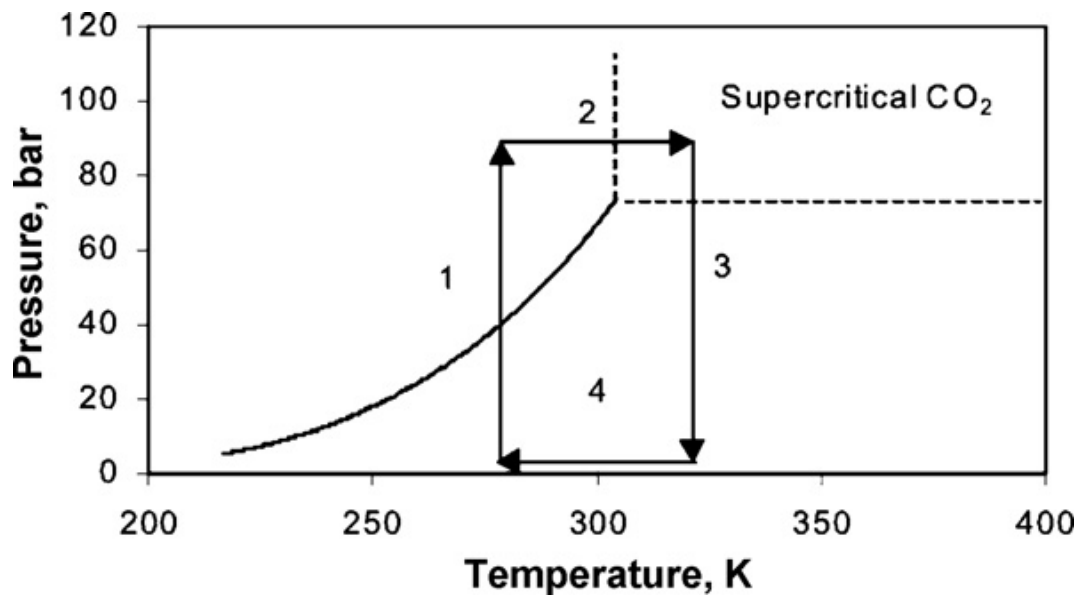


Figure 2.3: Supercritical drying using carbon dioxide (Dorcheh and Abbasi, 2008b)

exchange process is rather time consuming, where the process is diffusion control. Many researchers had tried to overcome the problem but none has come out with an ideal solution that can compromise between processing time and quality of aerogel produced. Some of those methods attempted are as follows:

- (a) Increased diffusion coefficient by heat treatment (Novak and Knez, 1997, Rogacki and Wawrzyniak, 1995)
- (b) Dried the alcogel under supercritical conditions without CO₂ – alcohol solvent exchange (Vanbommel and Dehaan, 1995, Sui et al., 2004)
- (c) Direct synthesis and drying of hydrogel in supercritical CO₂ (Gross et al., 1998, Scherer et al., 2002, Gauthier et al., 2004)

It is found that conditions during supercritical drying including temperature (as long as higher than critical temperature), extraction time, depressurizing temperature, and depressurizing rate has no effect on the density and porosity of silica aerogel formed (Tamon et al., 1998). However, the surface characteristics of aerogel produced is dependent on the solvent used in supercritical drying, i.e. hydrophobic with alcohols but hydrophilic with carbon dioxide (Tajiri et al., 1995).

While the works of improving supercritical drying are still going on, new drying method under ambient pressure had begun to attract more attention among researchers and also investor. The key idea of ambient pressure drying (APD) is to reduce interfacial energy by turning the surface of gel skeleton into hydrophobic. It can be accomplished by silylating the gel with alkoxisilanes compounds such as TEOS, TMCS (trimehtlychlorosilane), HDMS (hexamethyldisiloxane), HDMZ (hexamethyldisilazane), MTMS (methyltrimethoxysilane) MTES (methyltriethoxysilane) and TMES (trimethylethoxysilane). The effect of silylation is shown in [Figure 2.4](#):



Figure 2.4: Effect of silylation on silica network in silica gel (Dorcheh and Abbasi, 2008b)

As the hydroxyl groups on the surface are replaced with alkyl group, water in hydrogel is being displaced from the gel. The gel obtained is then soaked in other hydrophobic solvents such as hexane and heptane and is dried in oven under ambient pressure. [Table 2.2](#) shows the summarized properties of aerogel obtained via silylation corresponding to agents commonly used. Generally, silylated aerogels suffers wider degree of shrinkage as compared with supercritical fluid drying, depending on the silylating condition.

Table 2.2: Properties of silica aerogels obtained via APD using various silylation agents

Silylation agents	Sources	Properties of aerogels					
		Density (g.cm ⁻³)	Porosity (%)	Shrinkage (%)	Specific surface area (m ² .g ⁻¹)	Thermal conductivity (W.m.K ⁻¹)	Optical transmission
TEOS	(Haereid et al., 1996, Scherer et al., 1996, In-Sub et al., 2008, Nayak and Bera, 2009a)	0.21-0.67	80	1.5	273-1050	0.029	Transparent / Semitransparent
TMCS	(Mahadik et al., 2012, Liu et al., 2008, Kim et al., 2009, Gurav et al., 2009b, Sarawade et al., 2010, Wang et al., 2009, Bangi et al., 2008b)	0.06-0.4	78-97	10-51	347-917	0.05-0.32	Transparent / Semitransparent
HMDZ	(Sarawade et al., 2010, Nazriati et al., 2011, Rao and Rao, 2010, Gurav et al., 2009a, Rao et al., 2007a, Rao et al., 2005b, Gurav et al., 2008)	0.06-0.18	89-97	1-51	450-1360	0.07-0.19	Transparent / Semitransparent
HMDS	(Rao and Rao, 2010, Rao and Rao, 2009, Gurav et al., 2008, Lin et al., 2011)	0.04-0.5	72-98	3-85	450-863	0.05-1.02	Transparent / Semitransparent
MTMS	(Gurav et al., 2008, Wu et al., 2011, Kanamori, 2011, Anderson et al., 2010, Nadargi et al., 2009, Hegde and Rao, 2007, Rao et al., 2003b)	0.04-0.27	85-98	4.62-65	528-1005	0.03-1.01	Transparent / Semitransparent
MTES	(Nadargi and Rao, 2009, Aravind and Soraru, 2011, Cui et al., 2011)	0.05-0.09	94-98	16-22	416-850	0.05-0.06	Transparent / Semitransparent
TMES	(Gurav et al., 2008, Rao et al., 2003a, Hegde et al., 2007, Standeker et al., 2007, Standeker et al., 2009)	0.06-0.35	81-98	8-82	732-812	0.062-1.02	Semitransparent

2.2 Bio-silica

It is known that some biomass like rice husk contains considerable amount of silica, which can be used to synthesize silica aerogel (Nayak and Bera, 2009a, Hou, 2003, Li and Wang, 2008, Li et al., 2007, Tang and Wang, 2005). Silica in the form of silicic acid in soil is normally absorbed by plants as a result of water consumption (Motomura et al., 2002). It was then distributed in stems and leaf of the plant in the form of amorphous silica. The family of plants like *Equisetaceae* (horsetail), *Cyperaceae* (sedges) and *Poaceae* (true grasses) are especially well known of its uptake of silicic acid (Motomura et al., 2006). Hence in this work, two biomasses i.e. bamboo leaf (*bambusa heterostachya*) and cogon grass (*imperata cylindrica*), were used as sources to produce aerogel. For the best of author's knowledge, similar attempt has never been reported by other sources prior to this work. Bio-silica is also obtained from rice husk for the purpose of comparison.

2.2.1 Forms of silica

Silica is most abundant compounds that found in the earth crust. It can exist in either crystalline or amorphous form. Table 2.3 shows some of the polymorphs of crystalline silica.

Table 2.3: Common polymorphs of crystalline silica

Polymorphs	Crystal symmetry	Condition of conversion from quartz	
		Temperature (°C)	Pressure (kbar)
Tridymite	Orthorhombic, hexagonal	867	Ambient
Cristobalite	Tetragonal, cubic	1470	Ambient
Keatite	Tetragonal	400	0.8-1.3
Stishovite	Tetragonal	1200	160
Coesite	Monoclinic	700	35

It is known that amorphous silica is more reactive than its crystalline form (Foletto et al., 2006, Natarajan et al., 1998), owing to its porous structure (high specific surface area). With crystalline silica (e.g. sand), it is only possible to produce sodium silicate (water glass) by reacting it with sodium carbonate at its melting point, i.e. in the range of 1100 – 1200 °C. Alternatively, sodium silicate can also be easily obtained by dissolving reactive amorphous silica in sodium hydroxide (refer to [equation 2.2](#)) at much lower temperature and faster rate. Since sodium silicate is the major precursor to synthesize silica hydrogel in this work, it is aimed to obtain amorphous silica from biomasses rather than its crystalline form.

2.2.2 Amorphous silica from biomasses

Silica in this work was extracted from bamboo leaf and cogon grass due to the following reasons:

(a) Bamboo leaf (*Bambusa heterostachya*)

Bamboo is one of the most diverse groups of plant in grass family that belongs to the subfamily of *Bambusoidae*. Paper pulp processing is the main motivation to cultivate bamboo in many countries including Brazil, China and India, which led to a worldwide bamboo production of 20 million tonnes per year (Dwivedi et al., 2006, Vatsala, 2003). Despite its great contribution to economy, it also generates humongous amount of wastes. Bamboo leaf is commonly being stripped off from the plants in pulp processing. It is then disposed, due to its little commercial value, mainly by open burning in landfills. This in turn induced air pollution when the suspended air borne ashes entered the community in vicinity. In Brazil for instance, processing of 500 kilotonnes per year of bamboo had annually generated about 190 kilotonnes of waste, accounted approximately 28% of bamboo mass used (Villar-Cocina et al., 2011).

Several previous researches had been conducted to investigate silica content in bamboo leaf. Typical silica content reported so far is ranged from as little as 12.7 wt% to as high as 41 wt% (Motomura et al., 2002, Lux et al., 2003). The observed wide variation of silica content is attributed to the variations in bamboo species and also silicic acid uptake patterns under different climates and geographical influences. It is also confirmed silica in bamboo leaf is amorphous.

Extraction of silica had been reported and these are mainly focused on incorporating the silica obtained into pozzolanic materials to produce cements (Dwivedi et al., 2006, Villar-Cocina et al., 2011, Hosseini et al., 2011) and silicon carbide (Mohapatra et al., 2011). Most of these studies extracted silica by decomposing organic matters in bamboo leaf via thermal treatment. Nevertheless, Kamiya (Kamiya et al., 2000) had also successfully obtained silica from bamboo leaf by chemical oxidation. Temperature is most important parameter in thermal treatment because high temperature may convert amorphous silica into crystalline form as stated previously in **Table 2.3**. Crystallization of amorphous silica obtained from rice husk had been reported previously where cristobalite were detected at 700°C-750°C (Della et al., 2002, Thy et al., 2006) and tridymite at 750°C – 1100°C (Thy et al., 2006, Zhang et al., 2010), by heating rice husk in muffle furnace. In order to avoid crystallization of silica during thermal treatment of bamboo leaf, it is crucial to maintain the temperature below 700°C. Even crystallization can be completely eliminated; the silica ashes obtained from thermal treatment is not pure. The purity of silica in the ash obtained is typically ranged from 76% - 80.4% (Dwivedi et al., 2006, Villar-Cocina et al., 2011, Hosseini et al., 2011). This is due to the fact that some bamboo leaf contain high amount minerals such as potassium oxides and iron oxides, which cannot be vapourized at that operating temperature. Presence of potassium oxides had worsen the scenario, where it causes the formation of fixed carbons that just cannot be removed regardless how long the heating

was carried out. Rapid heating can cause the potassium to melt before all carbon can be oxidized, the molten potassium were then coated on the surface of carbons. Krishnarao (Krishnarao et al., 2001) had proved that fixed carbons in rice husk ash can be removed by leaching the rice husk with acid solution. The addition of acid solution also removed minerals from rice husk.

In Malaysia, more than 50 species of bamboo have been discovered covering c.a. 420000 hectares of land across Peninsular and West Malaysia (Mohmod, 1999). Among those, only 13 species are utilized commercially (Mohmod, 1999). Bamboo of species *bambusa heterastachya* , also known as *buluh galah*, was selected in this work as it is most common type of bamboo found in Malaysia. Also, the data on the silica content of this species is still unknown.

(b) Cogon grass (*Imperata cylindrica*)

Cogon grass, commonly known as blady grass, spear grass or *lalang* , is considered one of the worst weed globally (Holzmueller and Jose, 2011, Lowe S, 2004). According to MacDonald (MacDonald, 2007), cogon grass had infested approximately 500 million hectares of land worldwide. This poses serious ecological threats to the countries in Southeast Asia, Australia and Africa. Cogon grass is categorized as weed for the following reasons:

- (a) *Perennial* : Cogon grass invaded surrounding plants where its rhizome penetrates deep and wide in soil. The penetrated rhizomes can then grow in the vicinity by intercepting nutrients to surrounding plants;
- (b) *Allelopathic* : The rhizomes also released some chemicals that retard and inhibit growth of other plants;

- (c) *Unpalatable* : The crop was initially brought into America as forage but later found out that it has low nutritive value. Its sharp and rough edges added difficulty for livestock to graze the grass. As a result, cogon grass can grow uncontrolled without consumed by other livestock;
- (d) *Pyrogenic* : Leaf of cogon grass are very flammable which always cause forest fire. It can burns in open area with temperature much higher than other plants, thus eliminating surrounding plants from competition. The act of burning will not harm itself as its extensive rhizomes can regrow in short period.

Currently, cogon grass has no practical application and commercial values. According to Dozier (Dozier, 1998) and Shilling (Shilling, 1993), cogon grass is rich in silica. This makes it possible to be used as the source of silica for aerogel production. Presently, data on the silica content in cogon grass has not been reported.

(c) **Rice husk** (*Oryza sativa*)

Rice husk and rice straw are usually disposed as waste. They contain to approximately 20 wt% of silica (Liou and Wu, 2010, Tsai et al., 2007, Park et al., 2003). High purity amorphous silica from rice husk was mainly obtained via pyrolysis and subsequently by NaOH leaching (Kalapathy et al., 2000, Kalapathy et al., 2002, Yalcin and Sevinc, 2001, Zhang et al., 2010). Since the extraction of amorphous silica from rice husk and straw is a well-established technique, amorphous silica from these two biomasses will be used as comparison with those obtained from bamboo leaf and cogon grass in this study.

2.3 Thermal transfer in silica aerogel

One of the aims of this work is to synthesize aerogel from biomasses and use as thermal insulation material. It is then crucial to understand the routes of thermal transfer in silica aerogels, so that to suppress the thermal conductivity in best possible ways. Three conventional thermal transfers, namely conduction, convection and radiation, in silica aerogel will be discussed. This not only helps to explain the ultralow thermal conductivity of silica aerogel but also highlighting the conditions where thermal resistivity of silica aerogel diminished; indicating its decreased effectiveness as thermal insulant.

2.3.1 Convection

Among the three possible routes, convective transfer has the least contribution to the total thermal conductivity of silica aerogel. Convective transfer usually involves a fluid flow in the scale that is comparable with the scale of sample. As the size of particles and pores in silica aerogel are in the range of nanometer, convective flow hardly occur within such medium. In fact, it is reported that free convection of gas in porous medium with pore size smaller than 1 mm is negligible (Lee et al., 2002, Hrubesh and Pekala, 1994). In a more theoretical way, the tendency of free convection to conduction of gas can be estimated by Rayleigh number:

$$Ra = \frac{g \tilde{\beta} K \tilde{e} \Delta T \rho_g}{\mu_g \lambda_g} \quad (2.7)$$

where

Ra : Rayleigh number (dimensionless)

g : Gravitational acceleration in m.s^{-2}

- $\tilde{\beta}$: Thermal expansion coefficient of gas, 3.43 K^{-1} for air at 20°C
- K : Permeability coefficient (dimensionless)
- \tilde{e} : Sample thickness, 1 mm
- ΔT : Temperature difference, 10 K
- ρ_g : Density of gas, 1.2 kg. m^{-3} for air
- μ_g : Dynamic viscosity of gas, $1.86 \times 10^{-5} \text{ kg.m}^{-1}.\text{s}^{-1}$ for air
- λ_g : Thermal conductivity of gas, $0.024 \text{ W.m}^{-1}.\text{K}^{-1}$ for air

For porous medium, the K value can be estimated by Carman- Kozeny equation:

$$K = \frac{\Pi d_p^2}{173(1-\Pi)^2} \quad (2.8)$$

where

- Π : Porosity (dimensionless), averagely 0.8 for silica aerogel
- d_p : Particle diameter in nm, i.e., averagely 50 nm for silica aerogel

The resulted Rayleigh number is much smaller than unity, thus, heat transfer of gas in aerogel favors conduction than convection.

2.3.2 Conduction

Conduction of heat in aerogel occurs through both solid network and also gas that filled the pores. In aerogel, the solid network formed by aggregates of silica particles creates long and torturous path for conduction with many dead ends. Heat conduction through these dead ends is highly ineffective, hence causing the solid network to have very low thermal conductivity. According to Zeng *et al.* (Zeng et al., 1995a), the intrinsic solid conductivity of silica is only $1.34 \text{ W.m}^{-1}.\text{K}^{-1}$. However, the porous structure of aerogel altered its solid conductivity making aerogel to have solid conductivity less than $0.1 \text{ W.m}^{-1}.\text{K}^{-1}$ (Wei et al., 2009a). The solid conductivity of

aerogel is related to the structure of solid network formed, which in turn dependent on the conditions during gel synthesis. Density of aerogel is usually a proxy of its solid conductivity. Generally, denser aerogels have higher solid conductivity. Equation (2.9) (Zeng et al., 1995a, Lu et al., 1995), shows the solid conductivity of monolithic aerogels scaled with density:

$$\lambda_s = \tilde{C} \rho_{ae}^\varphi \quad (2.9)$$

where

- λ_s : solid conductivity of aerogel
- \tilde{C} : pre-factor that depends on interconnectivity of particles in aerogel
- ρ_{ae} : density of aerogel
- φ : constant which is depended on the interconnectivity of solid particles, usually 1.5 for silica aerogel

The parameters in sol-gel processing play an important role in determining the density of aerogel produced. Thus, by manipulating these parameters, solid conductivity of aerogel can be controlled. Such parameters include concentration of silica precursors used, pH of catalyst and aging of gel. As these parameters are varied, the rate of dissolution and re-precipitation silica particles will change, altering the density of aerogel formed. Generally, density of aerogel increased with concentration of precursors (Moner-Girona et al., 2003a, Moner-Girona et al., 2002, Moner-Girona et al., 2003b, Ehrburgerdolle et al., 1995), pH of catalyst (Deng et al., 2000, Mezza et al., 1999, Wu et al., 2000, Alaoui et al., 1998, Rao et al., 2005a), and aging time (Rao et al., 2004, Smitha et al., 2006).

Comparing with conduction of solid network, gas conduction in aerogel can be suppressed much easily. The efficiency of gas conduction is dependent on the mean free path of gas molecules. If the mean free path of gas molecules is large, molecules

travelled longer distance to conduct heat. The mean free path of gas molecules are related to the pressure as:

$$l_m = \frac{k_B T}{\sqrt{2} \pi d_g^2 P} \quad (2.10)$$

where

l_m : mean free path of gas molecules,

k_B : Boltzman constant, $1.38 \times 10^{-23} \text{ J.K}^{-1}$

T : absolute temperature in K

d_g : diameter gas molecules, typically $3.53 \times 10^{-10} \text{ m}$ for air

P : pressure in Pa

Thus, the mean free path of air molecules at 25 °C and 1 atmospheric pressure is estimated to be 75 nm. The mean free path is comparatively large to pores size of aerogel. As pore size in aerogel is averagely 50 nm, air molecules are very unlikely to collide with each other to transfer energy and therefore the conduction of gas in pore is partially suppressed. Kuhn *et al.* reported that the gas thermal conductivity in silica aerogel under ambient condition is only about $0.01 \text{ W.m}^{-1}.\text{K}^{-1}$ (Kuhn et al., 1995), i.e. only half of the conductivity in free air. Further lowering the pressure to one-hundredth of atmospheric pressure will cause the mean free path to increase by 100 folds. As a results, the gas thermal conductivity becomes negligibly small. According to Lee *et al.* (Lee et al., 1995, Smith et al., 1998), the total thermal conductivity of silica aerogel was suppressed to $0.007 \text{ W.m}^{-1}.\text{K}^{-1}$ at one-hundredth of atmospheric pressure attributed to the decrease in gas conductivity. However, further reduction in thermal conductivity was not significant at pressure lower than that.

2.3.3 Radiation

Figure 2.5 shows the transmission spectrum in silica aerogel. It can be seen there exist an optical window, 2000 – 2500 cm⁻¹ (corresponding to wavelength of 4 – 5 μm) and above 4000 cm⁻¹ (corresponding to wavelength below 2.5 μm), where silica aerogel is transparent to those radiation. These wavelengths fall in the infrared region of electromagnetic radiation. At ambient temperature, 25°C for instance, the radiative heat transfer in the infrared region is relatively small, thus, can be assumed negligible. At augmented temperature (>200°C), however, the radiation spectrum shifted towards infrared region. This making thermal conductivity of aerogel increased drastically at high temperature. For an optically thick silica aerogel, the radiative thermal conductivity is diffusive and can be expressed as follows:

$$\lambda_r = \frac{16}{3} \left(\frac{\sigma n^2 T^3}{\rho_{ae} e} \right) \quad (2.11)$$

where

λ_r : radiative thermal conductivity in W.m⁻¹.K⁻¹

σ : Stefan – Boltzman constant, 5.67 × 10⁻⁸ W.m⁻²

T : absolute temperature in K

n : refractive index of aerogel, dimensionless

ρ_{ae} : density of aerogel in kg.m⁻³

e : specific coefficient of extinction in m².kg⁻¹, as a function of temperature

From equation (2.11), though by increasing density of silica aerogel may reduce the radiative conductivity, it also may resulted in an increase in solid conductivity. In order to suppress the thermal conductivity of silica aerogel at elevated temperature without having effect on its solid conductivity, the specific extinction coefficient can be increased by doping the silica aerogel with materials which are opaque to infrared

radiation. Carbon black is one of the best candidates for this purpose. Many researchers had tried to integrate carbon black into silica aerogel to lower its radiative transfer.

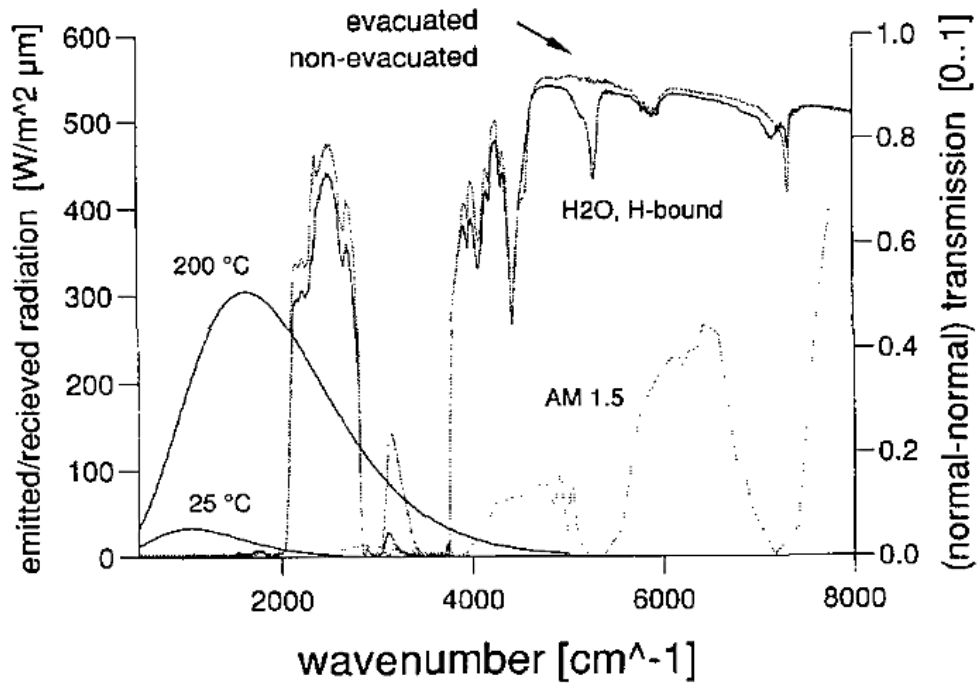


Figure 2.5: Spectroscopic behavior of pure silica aerogel (Stangl et al., 1995)

Among them, Lu *et al.* (Lu et al., 1995) had proved that the incorporation of carbon in silica aerogel caused the opacified gel to absorb infrared radiation of 3 – 8 μm (refer to Figure 2.6). Hermann *et al.* (Herrmann et al., 1995) reported that thermal conductivity of opacified silica aerogel from room temperature to 200°C was only increased by 30% (from 0.018 to 0.024 $\text{W}\cdot\text{m}^{-1}\cdot\text{K}^{-1}$) as compared to 300% for silica aerogel with no opacifying agent. Zeng *et al.* (Zeng et al., 1995a) developed model of carbon content to minimize heat transfer in silica aerogel concluded that thermal conductivity (at optimal loading) increased from 5.9 to only 11.3 $\text{mW}\cdot\text{m}^{-1}\cdot\text{K}^{-1}$, compared with clear aerogel from 8.8 to 143 $\text{mW}\cdot\text{m}^{-1}\cdot\text{K}^{-1}$, when temperature increased from 300 - 600K, Lee *et al.* (Lee et al., 1995) doped carbon into silica aerogel via chemical vapor infiltration (CVI) method, coupled with gas evacuation, had successfully reduced thermal conductivity to 6 $\text{mW}\cdot\text{m}^{-1}\cdot\text{K}^{-1}$ as shown in Figure 2.7.

One of the major problem with carbon opacification is that the solid conductivity of carbon black is relatively high, i.e. $4.18 \text{ W}\cdot\text{m}^{-1}\cdot\text{K}^{-1}$ (Zeng et al., 1995a). This is almost four times higher than this intrinsic solid conductivity of silica, making solid conductivity of opacified aerogel increased drastically. The addition of carbon will increase the density of aerogel which further increase the solid conductivity of opacified gel. Cracks may also be induced in silica aerogel as a result of addition of carbon.

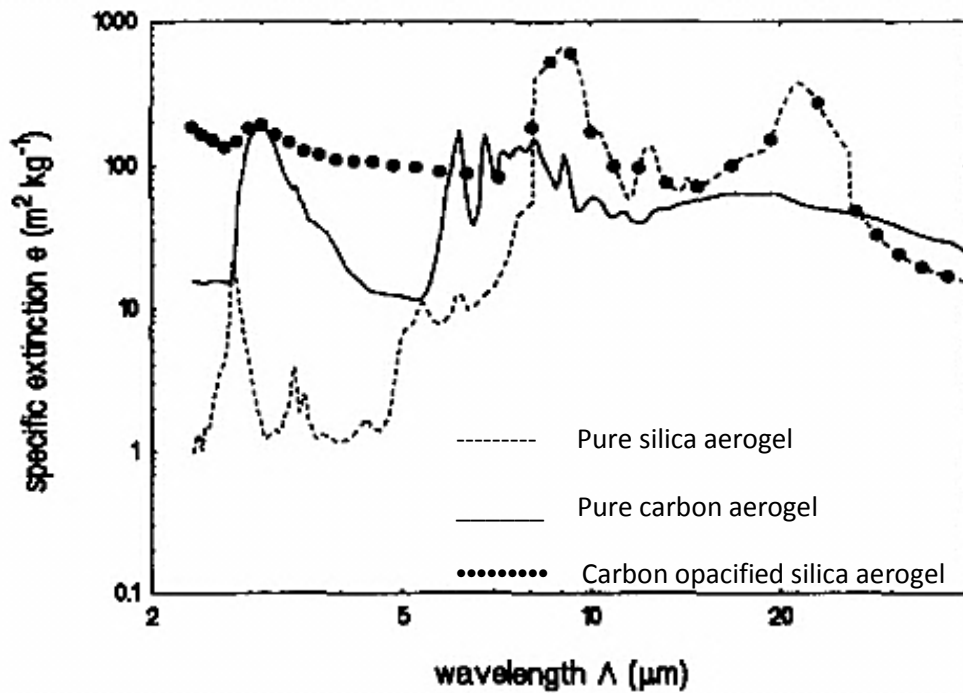


Figure 2.6: Specific extinction coefficients of silica aerogel with and without carbon opacification (Lu et al., 1995)

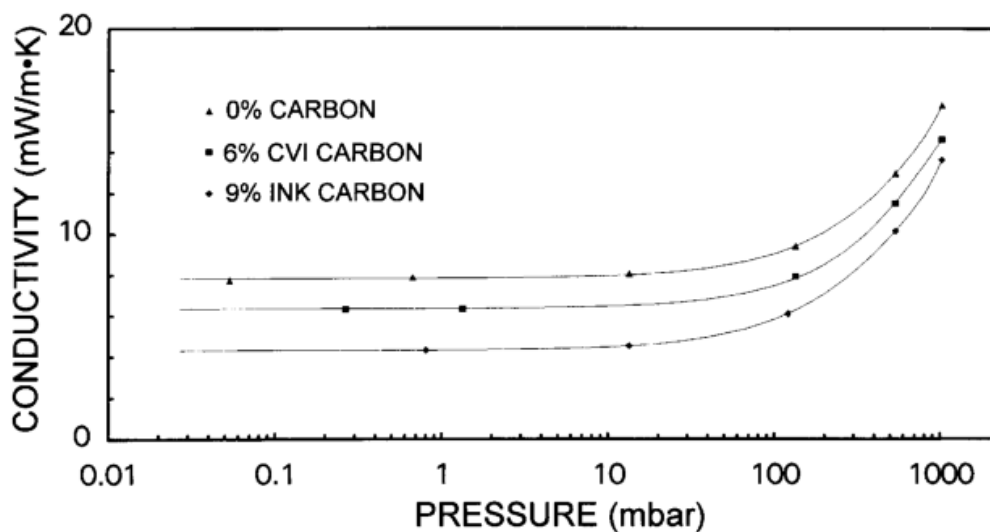


Figure 2.7: Effect of carbon doping to the thermal conductivity of silica aerogel at 20°C (Lee et al., 1995)

Others had also attempted to opacify silica aerogel with mineral powders such as titanium oxides and ceramics (Wang et al., 1995, Kuhn et al., 1995). Thermal conductivity lower than carbon doped silica aerogel was obtained. However, the result also indicates that thermal conductivity mineral doped aerogel is very sensitive towards absorption of water in air (Wang et al., 1995).

2.4 Carbon as opacifiers

As mentioned earlier in section 2.3.4, the search for low density opacifiers will help to find the best trade-off between conduction and radiation. Carbon used in opacification had so far focused only on carbon black due to its low cost. This form of carbon particle is usually dense and quite heat conductive, causing the solid conductivity of opacified aerogel to increase. What if carbon black is replaced with other forms of carbon? Hence, the possibility to use other forms of carbon as opacifier will be explored in this work.

2.4.1 *Activated carbon as opacifier*

Carbon can exist in many forms, some are crystalline, like diamond and graphite, and other can be amorphous, such as carbon black and soot. Activated carbon is another form of amorphous carbon which can be obtained from organic sources. It is commonly produced by heating bio-char in oxidative environment to create mesoporous structure, and thus termed “activated”. This porous structure gives activated carbon very large specific surface area, usually larger than $3000 \text{ m}^2 \cdot \text{g}^{-1}$ (Dias et al., 2007). Large surface area coupled with massive mesopores makes it suitable to be used as catalyst and absorption materials (Ioannidou and Zabaniotou, 2007).

Activation of carbon is usually carried out in two ways, i.e. physical activation and chemical activation. Physical activation is carried out by heating carbon

with oxidative gases such as steam and carbon dioxide under very high temperature (700 °C – 1100 °C) (Dias et al., 2007). Activated carbon obtained in this way can normally achieve a surface area of more than 1500 m².g⁻¹. Alternatively, activation also can be carried at lower temperature (400 °C) by impregnating char with chemicals such as zinc chloride, sodium hydroxide, potassium hydroxide or phosphoric acid. Though chemical activation has the advantage of lower activation temperature and time, it is inevitably contaminated by those chemicals and additional washing step is needed.

Activated carbon may replace carbon black as opacifier in silica aerogel. There are several obvious advantages to use activated carbon silica aerogel. First, it is extremely light weight where the density of activated carbon can be as low as 0.75 kg.m⁻³ (Plantard et al., 2010). This can reduce the overall density of opacified aerogel and thus to limit the solid conductivity within a reasonable range. Second, the porous structure activated carbon may exhibit very different solid conductivity as compared to carbon black. So far only very limited data reported on the conductivity of activated carbon. According to Kuwagaki (Kuwagaki et al., 2003) the conductivity of activated carbon is in the range of 0.17 – 0.28 W.m⁻¹.K⁻¹. This is in agreement with the values predicted by Jones (Jones, 1998), ranging from 0.15 – 0.27 W.m⁻¹.K⁻¹. These limited data suggested that the thermal conductivity of activated carbon, due to its porous structure, is at least an order of magnitude smaller than carbon black. Third, the thermal stability of activated carbon at high temperature is expected to be higher than carbon black, and this can retard the deterioration of carbon aerogel for high temperature applications.

Despite these advantages, the absorption of radiation by activated carbon remains uncertain. The optical window of silica aerogel is between 3 – 8 μm, activated carbon as opacifier should be able to absorb this specific range of infrared radiation. The author cannot find any data on the spectral properties of activated carbon. Thus, it

is one of the objectives in this work to determine the effect of opacifying aerogel with activated carbon to its thermal conductivity. Some encouraging results were reported where resorcinol – formaldehyde (RF) carbon aerogel (Lu et al., 1995), with density and porosity comparable with activated carbon, absorbed near infrared radiation. Lazar *et al.* (Lazar et al., 2005) investigated infrared absorption of amorphous carbon thin films via chemical vapor deposition (CVD) method and found that thin films absorbed part of the radiation in 2.5 – 13.8 μm . It is then expected that activated carbon, which is also amorphous in nature, to have same absorption in near infrared region.

In this study, activated carbon produced from bamboo leaf was used to opacify silica aerogel. As amorphous silica is obtained by combusting carbon in this biomass, making use of the carbon as opacifier may not only improve the thermal resistance of aerogel but also reduce CO_2 release to the environment in the processing.

2.5 Summary

Synthesis of silica aerogel using alkoxides such TMOS and TEOS is costly and hazardous. By using bamboo leaf to synthesize silica aerogel, it not only eliminates these problems but also helps to convert the agriculture waste to value added product. The relation between the three modes of heat transfer in silica aerogel is intricate. As the convection is negligible and gas conduction can be greatly reduced under partial vacuum, the overall thermal conductivity is mainly contributed by solid conduction and radiation. At high temperature ($>200\text{ }^\circ\text{C}$), the influence of radiative transfer starts to outweigh conduction and become major mode of heat transfer. Though the relation is complex, they are all related to the density of aerogel produced, as shown in [Figure 2.8](#). On one hand, lower radiative conductivity can be achieved by increasing the density of aerogel as expected from [equation \(2.11\)](#). On the other hand, increase in density causes the solid conductivity increase exponentially as in [equation \(2.9\)](#). A minimum point

exists to compromise between these two in the curve of combined thermal conductivity (refer to in [Figure 2.8](#)). If one can find an opacifier with both low density and solid conductivity, the problem may then be overcome. Hence, this work is aimed to reduce the thermal conductivity of silica aerogel by opacifying it with activated carbon. Such attempt if successful can make full use of the biomass without much carbon release to the environment, and may improve the thermal insulation performance of silica aerogel.

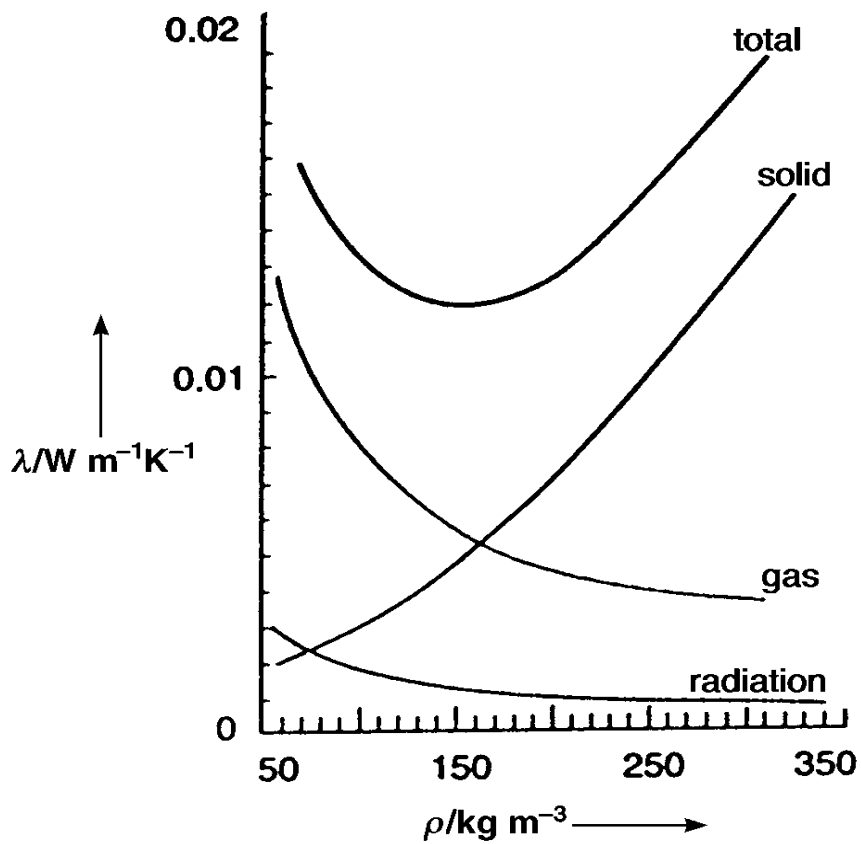


Figure 2.8: Composition of the thermal conductivity of silica aerogels: gas, solid, and radiation transport depending on the density of the material (Hüsing and Schubert, 2000)

CHAPTER 3

RESEARCH METHODOLOGY

3.1 Flow of research

This work was carried out following the sequence shown in [Figure 3.1](#). The extraction and determination of silica content in bamboo leaves and cogon grass were carried out first. Bio-silica obtained were then been characterized for their elemental composition and amorphicity. In second step, the purified bio-silica was used in sol-gel processing of hydrogel. The hydrogel was then supercritically dried to obtain silica aerogel. Properties such as density, porosity, specific surface area, and thermal conductivity of aerogel were determined and compared with conventional aerogel. In the third stage, biomass were carbonized and activated to synthesize activated carbon. Similarly, activated carbon obtained was characterized in term of thermal density, conductivity and infrared absorption. Finally, activated carbon obtained in the third stage was doped into silica aerogel as opacifier. The thermal conductivity of opacified aerogel was then minimized by optimizing the activated carbon content and parameters in sol-gel processing.

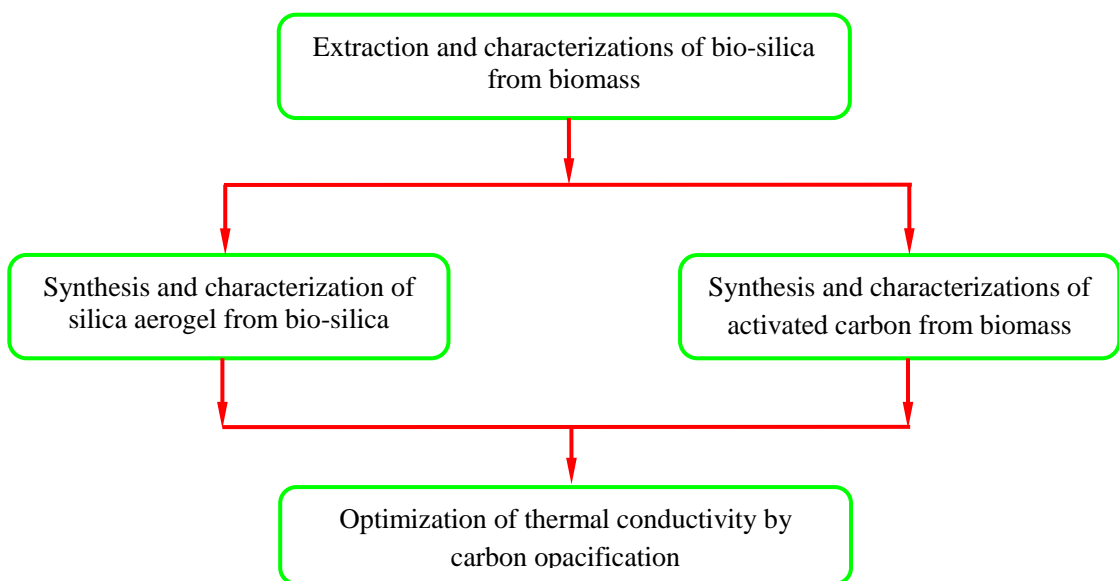


Figure 3.1 Stages to optimize thermal conductivity of carbon opacified silica aerogel

3.2 Materials and apparatus

3.2.1 Materials

The list of materials and chemicals used are summarized in [Table 3.1](#).

Table 3.1
List of materials

Materials	Sources	Descriptions
Bamboo leaves	Forest Research Institute Malaysia (<i>FRIM</i>) and University of Malaya	Species of <i>Bambusa heterostachya</i> . The average length of samples is 20 cm from tip to node
Cogon grass	University of Malaya	Species of <i>Imperata cylindrica</i> . The average length of samples is 70 cm from tip to node
Rice husks and straws	Padiberas Nasional (<i>BERNAS</i>) Berhad rice mill, Malaysia.	Species of <i>Oryza sativa</i> .
Ethanol	<i>R&M</i> chemicals	Reagent grade, 99.8%.
Tetraethyl-orthosilicate (TEOS)	<i>Sigma-Aldrich</i>	Reagent grade, 98%.
Liquid carbon dioxide	<i>Linde Industrial Gas</i>	99.97% with dip siphon (35 kg cylinder)
Nitrogen gas	<i>Linde Industrial Gas</i>	95% (35 kg cylinder)
1,1,1,3,3,3-Hexamethyl disilazane (HMDZ)	<i>Merck chemicals</i>	Synthesis grade
<i>n</i> -hexane	<i>Merck chemicals</i>	EMSURE® ACS grade w
Acidic cation-exchange resin	<i>Sigma-Aldrich</i>	IR-120H resin
Sodium hydroxide solution (NaOH)	<i>R&M</i> chemicals	6 mol L ⁻¹

3.2.2 Apparatus

The list of apparatus used is summarized in Table 3.2.

Table 3.2
List of apparatus

Apparatus	Model	Descriptions
Muffle furnace	<i>Lindberg Blue M</i>	Maximum temperature of 1200 °C. With Yokogawa UP550 temperature controller and nitrogen supply
Ultrasound homogenizer	<i>UP 400S Hielscher</i>	Maximum power output of 400 W with corresponding intensity of 85 Wcm ⁻²
Supercritical CO ₂ drying rig	<i>Thar SFE 5000F2</i>	5 liters capacity. Maximum pressure 350 bar with Automated Back Pressure Regulator (APBR)
ICP-AES	<i>Perkin Elmer Optima 7000 DV</i>	With both radial and axial view
TGA	<i>TA Instrument Q500</i>	Measuring range from ambient temperature to 1000 °C
CHNS analyzer	<i>Perkin Elmer 2400 Series II CHNS/O</i>	Combustion temperature of 900 °C
EDX	<i>INCA Energy 40, XL 40</i>	Coupled with FESEM (FEI Quanta 200F)
XRD	<i>PANalytical Empyrean</i>	2θ ranged from 10-90 degrees (step size 0.026 degree, $K_{\alpha 1} = 1.5406$ Å, Cu anode)
Physisorption unit	<i>Micromeritics ASAP 2020</i>	Pore size: 0.35 to 500 nm Nitrogen gas was used as adsorptive gas throughout measurements

Table 3.2 (cont.)
List of apparatus

Apparatus	Model	Descriptions
FT-IR	<i>Perkin Elmer Spectrum 400</i>	Mid-infrared region ($450 \text{ cm}^{-1} - 4000 \text{ cm}^{-1}$) with attenuated total reflectance (ATR)
Thermal conductivity analyzer	<i>Hot Disk, TPS 2500 S</i>	Measurement range: 0.005 to $1800 \text{ W m}^{-1} \text{ K}^{-1}$ Temperature: Ambient to $750 \text{ }^\circ\text{C}$ (with furnace)
DSC	<i>Mettler Toledo DSC 1</i>	Max. temperature: $700 \text{ }^\circ\text{C}$ Max. sampling rate: 50 Hz
SAXS	<i>PANalytical Empyrean</i>	2θ from 0 - 5 degrees (step size 0.01 degree, $K_{al} = 1.5406 \text{ \AA}$)
Particle size analyzer	<i>Malvern Zetasizer Nano ZS</i>	Measurement range: $0.3 \text{ nm} - 10.0 \text{ microns}$
Envelope density analyzer	<i>Micromeritics GeoPyc 1360</i>	Reproducibility: $\pm 1.1\%$
Gas pycnometer	<i>Micromeritics AccuPyc II 1340</i>	Reproducibility: $\pm 0.01\%$ Thermally equilibrated samples using helium in the 15 to $35 \text{ }^\circ\text{C}$ range

3.3 Extraction and characterizations of bio-silica

3.3.1 Extraction of silica

(a) Pre-treatment

Bamboo leaves, cogon grass, rice husk and rice straw were washed with deionised water and dried in oven at $90 \text{ }^\circ\text{C}$ for 24 hours. All dried biomass were cut into smaller pieces (approximately 8 cm) for the ease of leaching and combustion. Rice husk and rice straw were also tested for the purpose of comparison. As mentioned earlier by

Krishnarao (Krishnarao et al., 2001), the purity of silica obtained from rice husks was lowered by minerals such as potassium in biomass. Thus for all biomass, comparison tests were carried out to investigate the purity of silica, with and without leaching using hydrochloric acid. During the acid leaching, two parameters, namely duration of leaching and concentration of hydrochloric acid were varied. A 2^2 factorial experimental design was used to study the effect of these parameters on the amount of potassium leached. The leached samples were filtered and the filtrates were analyzed with ICP-AES (Inductively Coupled Plasma – Atomic Emission Spectroscopy, *Model: Perkin Elmer Optima 7000 DV*) to determine the amount of potassium leached. All samples were diluted with deionized water prior to analysis to suit the calibrated range of ICP-AES.

(b) **Thermal decomposition of organic compounds**

The elemental compositions of the major elements in raw biomass such as carbon, hydrogen, nitrogen and sulfur were determined by CHNS analyzer (*Model: Perkin Elmer 2400 Series II CHNS/O*). Biomass was ball milled and sieved prior to combustion in CHNS analyzer. The lower heating value (LHV) of bamboo leaf and cogon grass was determined using differential scanning calorimeter (DSC, *Model: Mettler Toledo DSC 1*) from 25 °C to 500 °C at 5 °C min⁻¹ in air. The LHV was then calculated by integrating the DSC data for the corresponding temperature ranges.

Both leached and unleached biomass was combusted in an electric muffle furnace (*Model: Lindberg Blue M*, with *Yokogawa UP550 temperature controller*) at 650°C for four hours. Samples were combusted in air and heating rate of 10 °C min⁻¹ in the presence of air. Samples were loaded into porcelain crucibles during heating to prevent contamination due to high temperature. Ashes collected after combustion was

weighed, ball milled and sieved prior to characterizations. Ash content, which mainly composed of silica, was calculated as follows:

$$\text{Ash content, } W_{\text{ash}} (\text{wt}\%) = \frac{m_{\text{ash}}}{m_0} \quad (3.1)$$

where

m_{ash} = mass of ash collected after combustion

m_0 = initial mass of biomass used in combustion

In order to confirm sufficient time taken for the combustion to ensure decomposition of all organic compound, biomass were also combusted using TGA (Thermogravimetric analysis, *Model: TA Instrument Q500*). Samples were heated from 30°C to 650°C via three heating rates of 5, 10 and 20 °C min⁻¹, followed by isothermal heating at 650°C for 3 hours. The samples were then heated up to 1000°C. Ash content obtained from TGA was then compared with the ash content obtained via electric muffle furnace. The fractional conversion of organic matters in biomass (i.e. excluded ashes) was calculated based on the [equation \(3.2\)](#):

$$\text{Fractional conversion, } X = \frac{100 - W_t}{100 - W_f} \quad (3.2)$$

where W_t = instantaneous weight percentage of biomass residue during combustion

W_f = final weight percentage of ash remained after combustion

(c) **Determination of kinetics parameters in thermal decomposition**

Combustion of biomass was analyzed using TGA. Samples were heated from 30 °C to 650 °C at 5, 10 and 20 °C min⁻¹ followed by isothermal heating at 650 °C for 3 hours. The activation energy and frequency factor of combustion were obtained by fitting the non-isothermal iso-conversional kinetics data to the Flynn-Wall-Ozawa

model with the degree of conversion, α , in the range of $0.39 < \alpha < 0.64$. α can be calculated using equation (3.3) as follows:

$$\alpha = \frac{1 - W_t}{1 - W_f} \quad (3.3)$$

The Flynn-Wall-Ozawa model was chosen for the fitting because it is suitable for biomass such as cogon grass that contains mainly cellulose (Fisher et al., 2002). To determine the activation energy and frequency factor of the first decomposition, non-isothermal iso-conversional TGA data at three different rates were fitted with the Flynn-Wall-Ozawa model as shown in equation (3.4):

$$\ln \beta = \ln \left(\frac{\bar{A} E_a}{\bar{R} g(\alpha)} \right) - 5.331 - 1.052 \left(\frac{E_a}{\bar{R} T} \right) \quad (3.4)$$

where β = heating rate in $^{\circ}\text{C min}^{-1}$,

\bar{A} = frequency factor in min^{-1} ,

E_a = activation energy in J mol^{-1} ,

\bar{R} = universal constant $8.314 \text{ J mol}^{-1} \text{ K}^{-1}$,

T = absolute temperature in K,

α = degree of conversion,

$g(\alpha)$ = integral conversion function. Both activation energy and

frequency can be obtained from the plot of $\ln \beta$ against the reciprocal of T . By assuming the decomposition is a phase-boundary controlled reaction with a contracting area, the integral conversion function can be approximated using equation (3.5) (Jankovic, 2008) as follows:

$$g(\alpha) = 1 - (1 - \alpha)^{\frac{1}{2}} \quad (3.5)$$

3.3.2 Characterizations of bio-silica

Purity of bio-silica obtained from combustion was determined by EDX (Energy Dispersive X-Ray, *Model: INCA Energy 400*) analysis. As the elemental composition of silicon in the ash was determined by EDX, the silica content in biomass can be calculated using equation (3.6). By assuming all the silicon is in the form of SiO_2 , the silica content can be estimated as follows:

$$\text{Silica content (wt\%)} = \frac{M_{\text{SiO}_2}}{M_{\text{Si}}} \times W_{\text{Si}} \times W_{\text{ash}} \times W_{\text{lch}} \quad (3.6)$$

where M_{SiO_2} = molar mass of silica, i.e., $60.084 \text{ g mol}^{-1}$;

M_{Si} = molar mass of silicon, i.e., $28.086 \text{ g mol}^{-1}$;

W_{Si} = weight percentage of silicon in ash, which is determined using EDX; W_{ash} is the weight percentage of ash after combustion;

W_{lch} = weight percentage of the biomass residue that remained after acid leaching.

In order to confirm that the silica obtained is amorphous, bio-silica were tested with XRD (X-ray diffractometer, *Model: PANalytical Empyrean*). The XRD with 2θ ranged from 10-90 degrees (step size 0.026 degree, $K_{\alpha 1} = 1.5406 \text{ \AA}$, Cu anode) was used to check for the formation of any crystalline structure.

3.4 Synthesis and characterization of silica aerogel from bamboo leaf silica (BLS)

3.4.1 Preparation of water glass

Water glass (sodium silicate solution) was prepared by dissolving the bamboo leaf silica into sodium hydroxide solution (2 mol L^{-1}) without heating. It was then filtered and the filtrate obtained is sodium silicate solution. The silica yield in the water

glass formed was determined using ICP-AES; the silica yield (ξ) is defined as in equation (3.7):

$$\text{Yield, } \xi = \frac{\Theta_{\text{Si}} V_{\text{NaOH}}}{\phi m_{\text{BS}}} \left(\frac{M_{\text{SiO}_2}}{M_{\text{Si}}} \right) \quad (3.7)$$

where Θ_{Si} = silica concentration in water glass, which is determined using ICP and measured in g L^{-1} ;

V_{NaOH} = NaOH volume reacted with bio-silica, measured in L;

ϕ = purity of bio-silica, which is determined using EDX and measured in wt%;

m_{BS} = mass of bio-silica used in the reaction, measured in g;

M_{SiO_2} = molar mass of silica i.e., $60.084 \text{ g mol}^{-1}$ and; M_{Si} is molar mass of silicon i.e., $28.086 \text{ g mol}^{-1}$.

In order to identify the processing parameters that affected the silica yield in water glass, the reactions of bio-silica with NaOH were repeated by varying the parameters in the range stated in Table 3.3. Then, the processing condition was optimized to achieve high silica yield in water glass. The water glass with optimized silica yield (ξ) was characterized to obtain its elemental composition, density and pH. The overall process involved in the preparation of water glass are summarized in Figure 3.2.

Table 3.3
Selected processing parameters with the range

Parameter	Range
Time, t (h)	24 - 72
Temperature, T ($^{\circ}\text{C}$)	30 - 60
NaOH concentration, C (mol L^{-1})	2 - 6
$m_{\text{BS}}/V_{\text{NaOH}}$ ratio, R (g L^{-1})	12 - 60
Agitation speed, A (rpm)	0 - 200

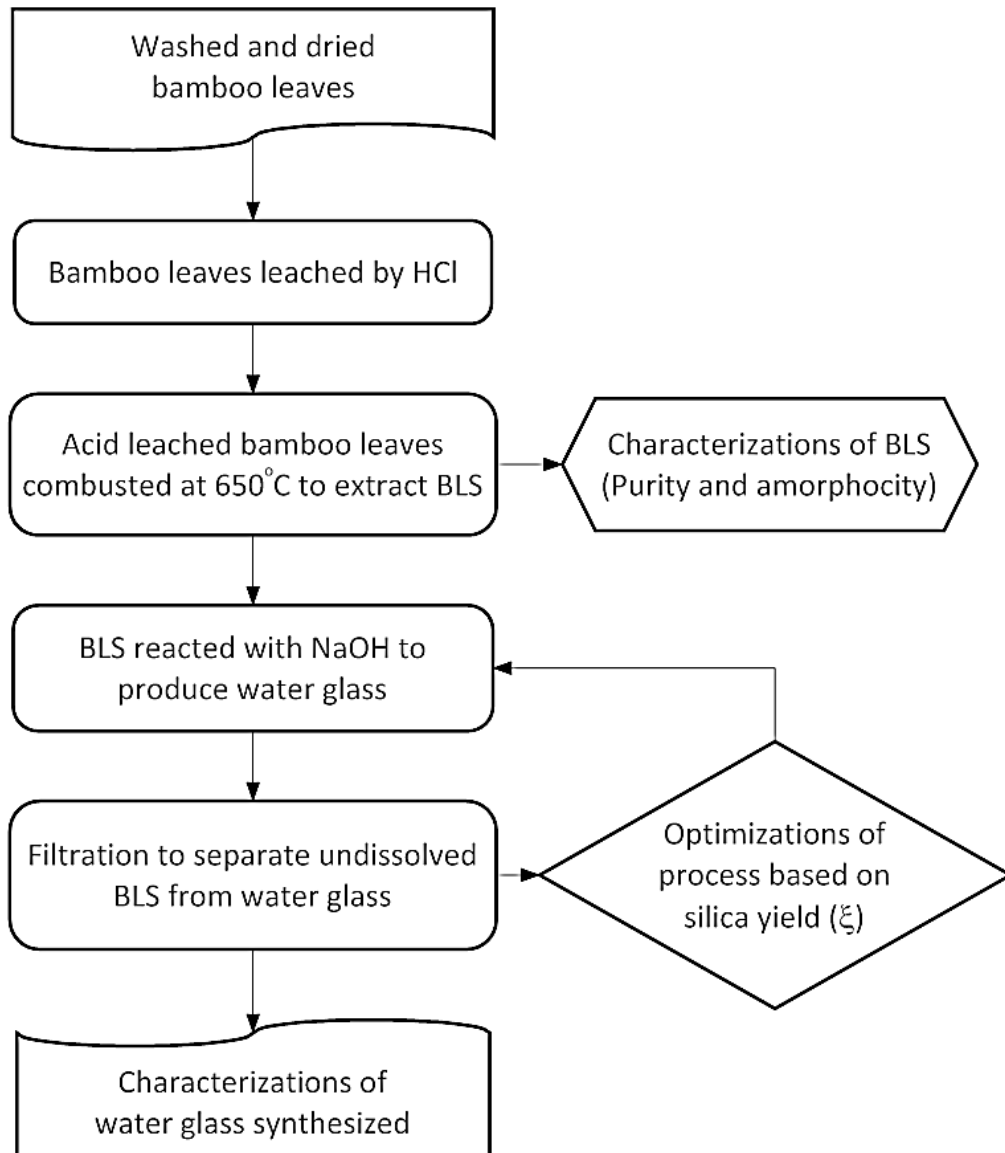


Figure 3.2 Process flow of the preparation of water glass from bamboo leaf

3.4.2 Syntheses of silica aerogel

Figure 3.3 shows synthesis scheme of silica aerogels from bamboo leaf water glass with ultralow silica concentration (3.5 wt%).

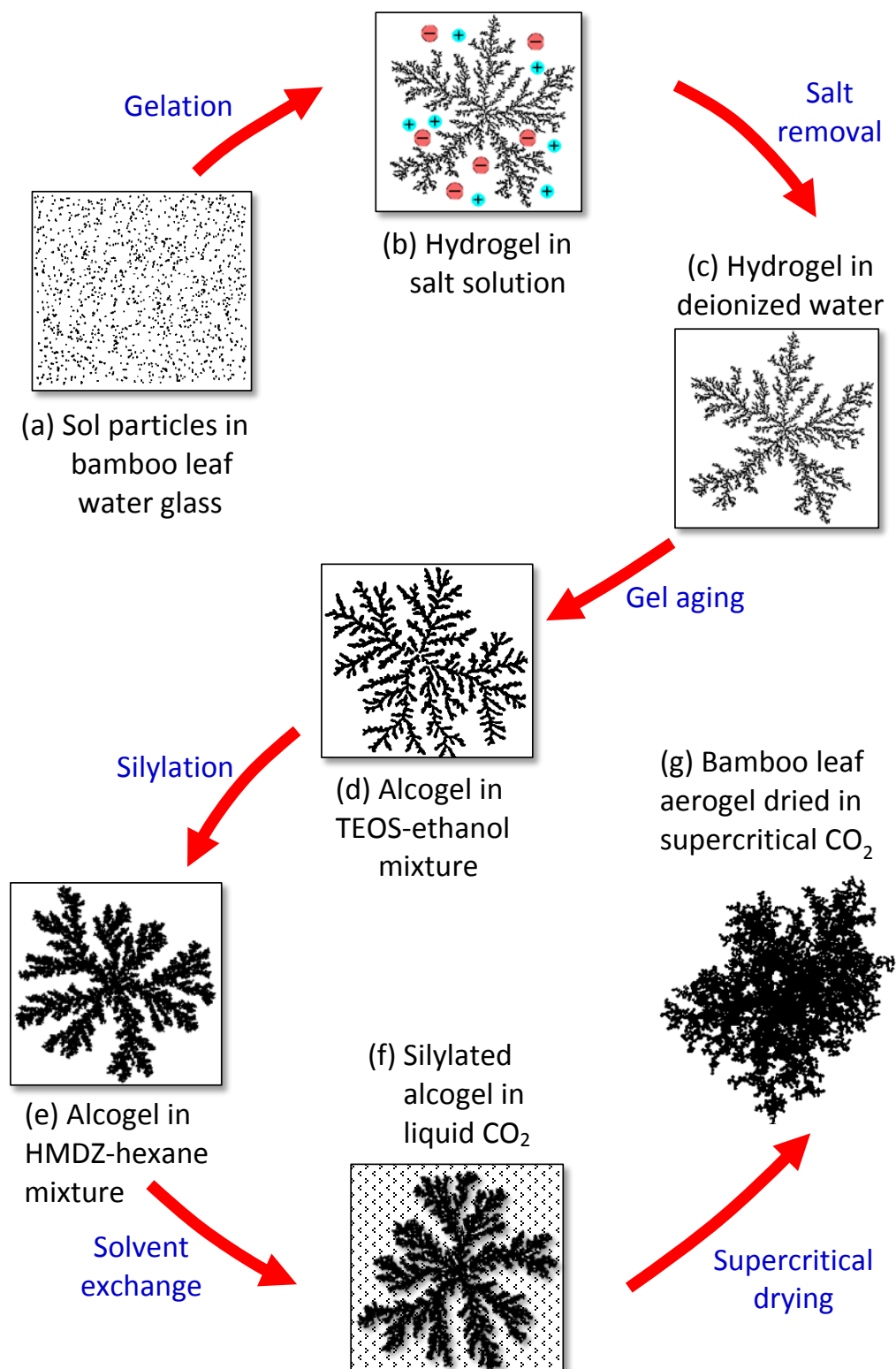


Figure 3.3 Synthesis scheme of silica aerogels from bamboo leaf water glass

The synthesis of aerogels began with the dilution of water glass obtained in [section 3.4.1](#). In order to synthesize low density aerogel, water glass with ultralow silica concentration was prepared by diluting the water glass from $R = 60 \text{ g L}^{-1}$ (5.25 wt% silica) to 40 g L^{-1} (3.5 wt% silica). Such R value was chosen based on the preliminary studies which showed that R smaller than 36 g L^{-1} gave hydrogels that collapsed easily in solvent exchange. In order to study the effect of gelation pH, water glass (3.5 wt% silica) was gelled in the following conditions:

- (i) *ion exchange column* (sample ID: BLG 3.5E) – water glass was flow into Amberlite resin column (length ≈ 60 cm, inner diameter 10.7 mm). The resulted silicic acid with (pH 4.5) was let to gel at ambient condition;
- (ii) *precipitated silica* (sample ID: BLG 3.5B) – HCl was added drop-by-drop to water glass (HCl : water glass = 1:2 v/v) until precipitate formed at pH ≈ 9.5 ;
- (iii) *water glass-into acid* (sample ID: BLG 3.5N) – excessive acid (2 ml) was added into water glass (6 ml) in a single step. The resulted silicic acid had pH 4.5. The pH was then adjusted again to ~ 7 by adding 0.025 ml of NaOH. The pH of the resulted was 4.5 and was then adjusted to pH 7. The mixture formed was let to gel at ambient condition.

The salts in the hydrogel were then removed by soaking in deionized water. Deionized water was replaced for every 4 hours. The degree of salt removal was determined as sodium percentage remained in dried gel using EDX analysis. The salt-free gel was then aged in ethanol. It was observed in the preliminary study that the gel shrunk severely in absolute ethanol. Therefore, hydrogel was aged in TEOS-ethanol

mixture (15 vol% TEOS) for 24 hours (Rao et al., 2011, Einarsrud and Nilsen, 1998a) to reduce shrinkage during aging. The alcogel formed was then silylated with HMDZ-hexane mixture (15 vol% HMDZ) for 12 hours (Rao et al., 2004). Silylated gels is normally dried under ambient pressure because silica concentration in precursors is high (8 – 25 wt%) (In-Sub et al., 2008, Chandradass et al., 2008, Bhagat et al., 2006, Bangi et al., 2010, Sarawade et al., 2012, Rao et al., 2001, Rao et al., 2004, Bangi et al., 2008a, Bhagat et al., 2007a, Sarawade et al., 2010, Nayak and Bera, 2009b, Wei et al., 2009b). However, water glass used in this study has ultralow silica content (3.5 wt%), and the preliminary studies had shown aerogel collapsed under ambient drying. Thus, the silylated alcogel was dried in supercritical carbon dioxide to prevent aerogel from collapsing. Supercritical drying was performed using supercritical drying unit (*Thar*, SFE 5000F2) as shown in [Figure 3.4 and 3.5](#).

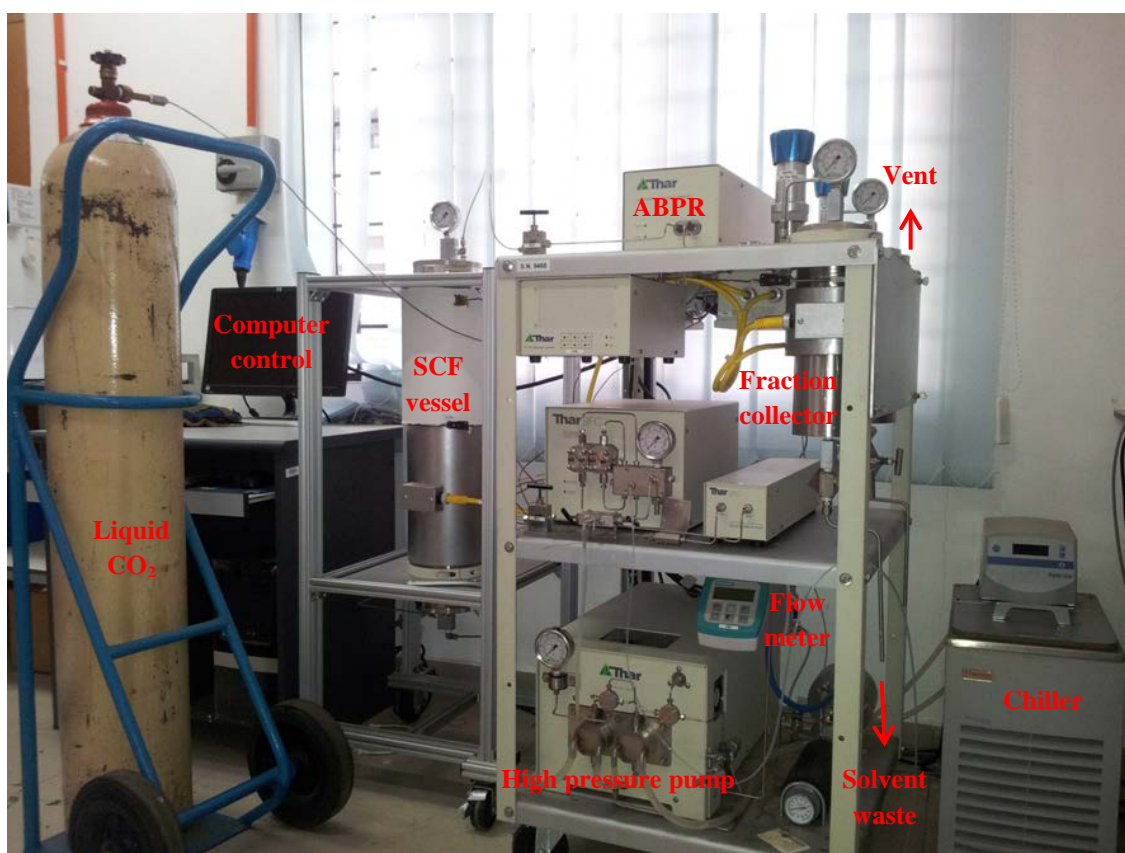


Figure 3.4 Supercritical CO₂ Drying rig (*Thar SFE 5000F2* system)

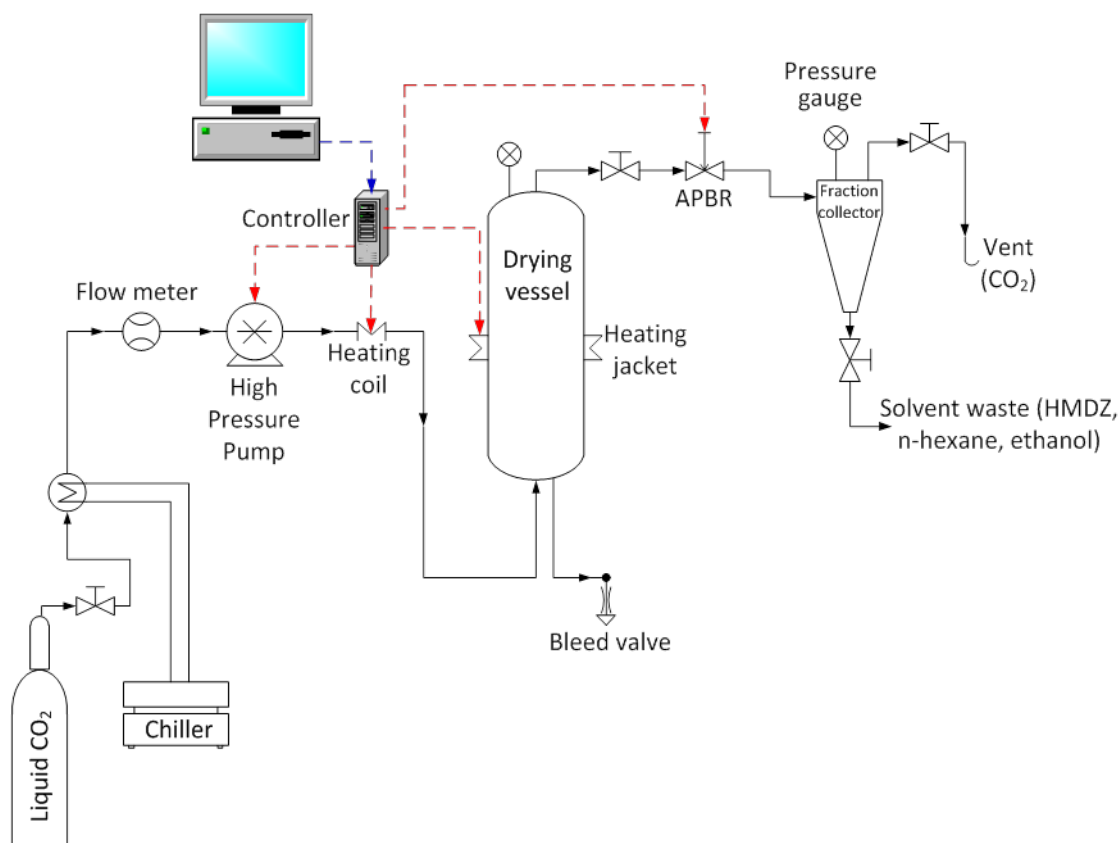


Figure 3.5 Schematic diagram of *Thar SFE 5000F2* system

In the drying process, alcogel samples were first loaded into the extraction vessel. The vessel was then closed and the air inside the vessel was flushed out with CO₂ gas. Before entering the vessel, liquid CO₂ was first cooled down to 2 °C. The flow rate was monitored by the computer system. Liquid CO₂ was then pumped into vessel to the desire pressure (100 bar) where CO₂ remained in liquid state. Once the pressure set point was reached, the Automated Back Pressure Regulator (ABPR) was used to control the pressure within the vessel by releasing CO₂ to the collector. ABPR was then closed and the system was left for 24 hours for the solvent exchange of alcogel to take place. The temperature must be maintained below its critical temperature to prevent the liquid CO₂ turns into supercritical state.

After 24 hours, the vessel was heated above the critical temperature where liquid CO₂ in the pores can now be vapourized without damaging the aerogel. The pressure and temperature were maintained above the critical point by flushing out the excess

CO₂ from the vessel at 25 g.min⁻¹ (100 bar, 45°C) for 4 hours. After the drying completed, the vessel was depressurized at 2 bar min⁻¹ to ambient pressure; while maintaining the temperature above 40°C. Finally, vessel was cooled down to room temperature and aerogel was unloaded from the vessel.

For comparison purpose, TEOS aerogels with two different silica concentrations were synthesized as follow:

- (i) TEOS aerogel with ultralow silica concentration (3.5 wt%, sample ID: TEOS 3.5) – TEOS was hydrolyzed with dilute HCl and DI water at pH 4.5. The pH was then adjusted to ~7 by adding NaOH. Hydrogel formed was further processed as in [Figure 3.3](#).

- (ii) TEOS aerogel with high silica concentration (15 wt%, sample ID: TEOS 15) – TEOS was hydrolyzed with dilute HCl and DI water at pH 4.5. The pH was then adjusted to ~7 by adding NaOH. Hydrogel formed was aged in ethanol for 24 hours without adding TEOS and then supercritically dried without silylation. Conventionally, silica aerogel are synthesized with high concentration of TEOS (>10 wt%) without silylation (Rao et al., 2001, Chandradass et al., 2008, Wei et al., 2009b, In-Sub et al., 2008). Thus, TEOS 15 is used to highlight the difference between aerogels with high and ultralow silica concentration. In addition, TEOS 15 with high silica concentration can be dried supercritically without silylation. It can then be used as control experiment to study the effect of silylation.

TEOS was chosen as comparison because it is the most common alkoxide precursor to synthesize aerogel. In addition, it is less hazardous as compared to TMOS.

3.4.3 Characterizations of silica aerogel

Time for gelation was estimated as time when precursor's mixtures did not fall and remained rigid, when its container was slanted at 90 degrees. The particle size distribution of silica sol near gel point was determined using dynamic light scattering (*Model: Malvern Zetasizer Nano ZS*). The salt content in hydrogel for various soaked periods was determined indirectly as the sodium element remained in gel by using EDX. XRD was also used to detect any formation of crystals. The porosity of aerogels was calculated based on bulk density (ρ_{ae}) and true density (ρ_s) as in [equation \(3.8\)](#):

$$\text{Porosity, } \Pi = 1 - \frac{\rho_{ae}}{\rho_s} \quad (3.8)$$

where the bulk density (ρ_{ae}) and true density (ρ_s) of silica aerogels were determined using the density analyzer (*Model: Micromeritics GeoPyc 1360*) and the gas pycnometer (*Model: Micromeritics AccuPyc II 1340*). Volume of aerogel (V_{ae}) and the volume of hydrogel (V_{hyd}) was measured to estimate the shrinkage of aerogel using [equation \(3.9\)](#):

$$\text{Shrinkage (\%)} = \left(1 - \frac{V_{ae}}{V_{hyd}} \right) \times 100\% \quad (3.9)$$

The fractal structure was studied using data of SAXS (Small angle X-ray scattering, *PANalytical Empyrean*) with 2θ from 0-5 degrees (step size 0.01 degree, $K_{\alpha 1} = 1.5406$ Å). In order to interpret the SAXS data, its scattering intensity was $I(q)$ plotted as a function of scattering vector $q = (4\pi/\lambda)\sin(\theta/2)$ of SAXS, where λ is the wavelength of X-ray and θ is the scattering angle. It is well known that porous medium obeys the power law $I(q) \propto q^{-\alpha}$, where α can be determined as the slope of $\lg I$ against $\lg q$. In the linear regime, the surface fractal dimension (D_s) can be calculated using the following equation (Donatti et al., 2001a, Donatti et al., 2001b):

$$D_s = 6 - \alpha \quad (3.10)$$

where α_2 is the slope in the linear region and D_s is typically $2 \leq D_s \leq 3$. For particles with smooth surface, $D_s = 2$. Scattering intensity relations will then reduce to $I(q) \propto q^{-4}$, which is the well-known Porod's law. For monodispersed aerogel, real mass fractal dimension (D) is approximated to the apparent mass dimension (D_f), which can be determined as the slope (α_1) at low- q regime ($q < 0.015 \text{ \AA}^{-1}$) (Martin, 1986). In case the aerogel is highly polydispersed, the scattering data at the same regime is fitted into the following model (Freltoft et al., 1986, Vacher et al., 1988, Vollet et al., 2006, Teixeira, 1988) to obtain the real mass fractal dimension (D):

$$I(q) = A \zeta^3 \Gamma(D-1) \frac{\sin[(D-1)\arctan(q\zeta)]}{q\zeta(D-1)(1+q^2\zeta^2)^{\frac{(D-1)}{2}}} \quad (3.11)$$

where $A = \text{constant}$,

$\Gamma(D-1) = \text{gamma function of } D-1$, and

$\zeta = \text{characteristics length of a fractal structure}$.

The fractal structure diminishes at a length scale larger than ζ and becomes homogeneous. In addition, the surface per unit volume (S/V) ratio in nm^{-1} was determined using equation (3.12) as follows:

$$S/V = \pi \Pi (1 - \Pi) \left(\frac{K_p}{Q} \right) \quad (3.12)$$

where $K_p = \text{the Porod's law constant}$:

$$K_p = \lim_{q \rightarrow \infty} I(q) q^4 \quad (3.13)$$

and $Q =$ the invariant of the system:

$$Q = \int_0^{\infty} q^2 I(q) dq \quad (3.14)$$

Using the S/V ratio obtained, the corresponding specific surface area (S_{SAXS}) in $m^2 g^{-1}$ can then be calculated as:

$$S_{SAXS} = \left(\frac{1000}{\rho_{ae}} \right) \left(\frac{S}{V} \right) \quad (3.15)$$

where ρ_{ae} = bulk density of aerogel in $g.cm^{-3}$.

Adsorption characteristics including adsorption-desorption isotherm, BET specific surface area, total pore volume, BJH and DFT pore size distributions, and nanoparticle size of aerogels were characterized by physisorption unit (*Model: Micromeritics ASAP 2020*) in nitrogen atmosphere. The chemical functional groups on aerogel surface were studied using Fourier transform infrared spectroscopy (FT-IR, *Model: Perkin Elmer Spectrum 400*) which was equipped with attenuated total reflectance (ATR). Thermal conductivity of aerogels was measured by thermal analyzer (*Model: Hot Disk, TPS 2500S*) which uses transient hot disk method. The stability of aerogels at elevated temperature (30 – 550°C) was studied by TGA in air via heating rate of 5 °C min⁻¹.

3.5 Synthesis and characterizations of activated carbon from bamboo leaf

3.5.1 Carbonization and activation of carbon

Two steps chemical activation was applied in this study, where bamboo leaf was first carbonized and then activated chemically. Two steps activation is more effective in producing high quality activated carbon (Ioannidou and Zabaniotou, 2007). Bamboo leaf was first leached with hydrochloric acid (2 mol L⁻¹) to remove its minerals content.

It was then carbonized in muffle furnace (*Model: Lindberg Blue M*) to obtain bio-char. In order to retain maximum amount of carbon in bio-char, effects of carbonization temperature and time were investigated. Temperature range of 300 °C – 450 °C and time range of 25 min – 45 min were chosen for the study. The samples were loaded only when the furnace reached the targeted temperature and the temperature was maintained constant throughout the carbonization period. Samples were carbonized in nitrogen inert atmosphere. The percentage bio-char produced per gram of biomass carbonized (X_{char}) is determined using equation (3.16) as follows:

$$X_{\text{char}} = \frac{W_R}{W_0} \times 100\% \quad (3.16)$$

where W_0 = initial weight of biomass used in carbonization, and
 W_R = weight of residue remained after carbonization. It is aimed to optimize the temperature and time of carbonization to retain maximum amount of bio-char.

For the removal of silica from bio-char, bio-char was mixed with NaOH (2 mol L⁻¹) solution. NaOH was chosen because it can leach out silica from bio-char and at the same time bio-char was pretreated for chemical activation. The NaOH impregnated bio-char was activated in air at various temperatures and time. Based on previous research done on other biomass (Ioannidou and Zabaniotou, 2007, Dias et al., 2007), effects of activation temperatures and time on the carbon burnt off of activated carbon was investigated by varying temperature from 450 °C – 550 °C and time from 30 min – 90 min. The carbon burnt off (C_{burnt}) in carbonization or activation is calculated as:

$$C_{\text{burnt}} = \left(\frac{W_{\text{char}} - W_{\text{ac}}}{W_{\text{char}}} \right) \times 100\% \quad (3.17)$$

where W_{char} = weight of bio-char used in activation, and

W_{ac} = weight of activated carbon produced.

The bulk density of activated carbon produced was determined using density analyzer. As stated previously in [section 2.3.3](#), the addition of carbon black into aerogel causes the solid conductivity to increase. Thus, the solid conductivity of carbon in the composite may be reduced if porous carbon with low density is used. Hence, it is also aimed to minimize the density of activated carbon produced by varying the activation temperature and time. The activated carbons produced were washed thoroughly with deionized water to remove salts and residue of NaOH. The carbon burnt off and bulk density of activated carbon synthesized was determined to obtain the best combination of temperature and time to activate the bamboo leaf.

3.6 Optimization of thermal conductivity via carbon opacification

3.6.1 *Synthesis and characterizations of carbon opacified aerogel*

Activated carbon produced in [section 3.5](#) was doped into aerogel to opacify silica aerogel. The doping of activated carbon was carried out into precursor (sodium silicate) prior to gelation. In order to avoid agglomeration of activated carbon in aerogel, it was first ultrasonicated (*Model: UP 400S Hielscher*, maximum power output of 400 W) with water glass prior to adjustment of pH with acid. Hydrogels formed were aged in mother liquor for 24 hours and then washed with deionized water for every 8 hours of time interval. Solvent exchange was then carried out by soaking the salt free hydrogel in ethanol and the fresh ethanol was exchanged for every 8 hours. Solvent exchange was further carried out by replacing ethanol with HMDZ and n-hexane prior to supercritical drying as described in [section 3.4.2](#). The thermal conductivity of opacified aerogels was determined to optimize the performance of aerogel. The opacification process of bamboo lead aerogel is summarized in [Figure 3.6](#).

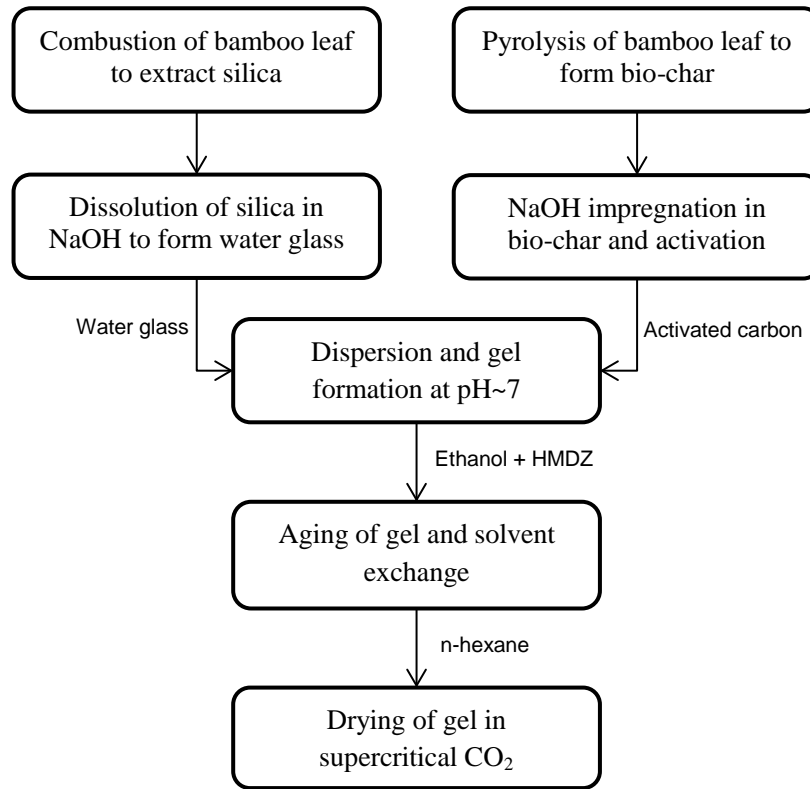


Figure 3.6 Opacification of silica aerogel with activated carbon

3.6.2 Optimizations of thermal conductivity

Effect of several parameters had been studied to optimize thermal conductivity of carbon opacified silica aerogel. These parameters are carbon loading, concentration of silica in water glass, and temperature where thermal conductivities were measured. The thermal conductivity of opacified aerogels with various carbon loading and silica concentration were measured at temperatures ranged from 30 °C to 300 °C in furnace. The carbon loading is the mass percentage of activated carbon (m_{ac}) to silica (m_{silica}), as shown in [equation \(3.18\)](#).

$$\text{Carbon loading, } \Theta_c = \frac{m_{ac}}{m_{silica}} \times 100\% \quad (3.18)$$

The carbon loading ranged from 0% to 25% were used in the experiment because the homogeneity of carbon in water glass can hardly be achieved before

gelation under higher loading. Furthermore, an optimal carbon loading exist as a result of the increase in solid conductivity under high carbon loading. Such optimal carbon loading was modeled in between 8% to 30% for temperature ranged from 30 °C to 300 °C (Zeng et al., 1995).

The silica concentration in water glass was varied from 3.22 wt% to 10 wt% where the silica concentration is determined as:

$$\text{Silica concentration, } \Theta_{\text{Si}} = \frac{m_{\text{silica}}}{m_{\text{wg}}} \times 100\% \quad (3.19)$$

where m_{silica} = mass of silica in water glass in g, and

m_{wg} = mass of water glass in g.

Viscous slurry of silica in sodium hydroxide solution is formed when the silica concentration exceeded 10 wt% and the dissolution of silica to form water glass become harder. Thus a maximum 10 wt% of silica concentration is used in this work. Optimal combination of carbon loading and silica concentration to minimize thermal conductivity of aerogel at each temperature level was determined. Statistical correlations and tie-lines for such optimal combinations were developed.

For comparison purposes, aerogels were opacified with carbon black with the same carbon loading range. TEOS aerogels with same carbon loading and silica concentration range were also prepared.

RESULTS AND DISCUSSION

CHAPTER 4 SYNTHESIS OF BAMBOO LEAF AEROGEL

Results obtained are reported based on the two major sections, i.e., (i) synthesis of bamboo leaf aerogel and (ii) opacification of bamboo leaf aerogel (COSA). In this chapter, the extraction of amorphous silica and the synthesis of silica aerogel will be discussed.

4.1 Extraction and characterization of bio-silica

Silica content of various biomasses were determined and compared. The purity and amorphicity of silica obtained using EDX and XRD with regards to potassium content were discussed. Finally, statistical analysis was carried out on the removal of potassium in biomasses by acid leaching.

4.1.1 Ash content after combustion

4.1.1.1 *Combustion in electric furnace*

Figure 4.1 shows the photographs taken for bamboo leaves and cogon grass before and after the combustion. As can be seen in **Figure 4.1(b and g)**, the ashes of bamboo leaves remained intact in shape as prior to combustion (*refer* to **Figure 4.1(a)**). This shows that the bamboo leaves contain high amount of silica that are uniformly distributed along the leaves. In contrast, ashes of cogon grass are obviously the residue from its parallel veins. Hence, the silica in cogon grass is mainly distributed in its parallel veins. Unlike bamboo leaves, ashes of cogon grass contain many black particles which was suspected to be fixed carbon. Fixed carbon is carbon that cannot be removed by simple thermal decomposition. Rice husks as comparison had shown little formation of black particles.

Among the four biomasses, bamboo leaf and cogon grass have the highest and

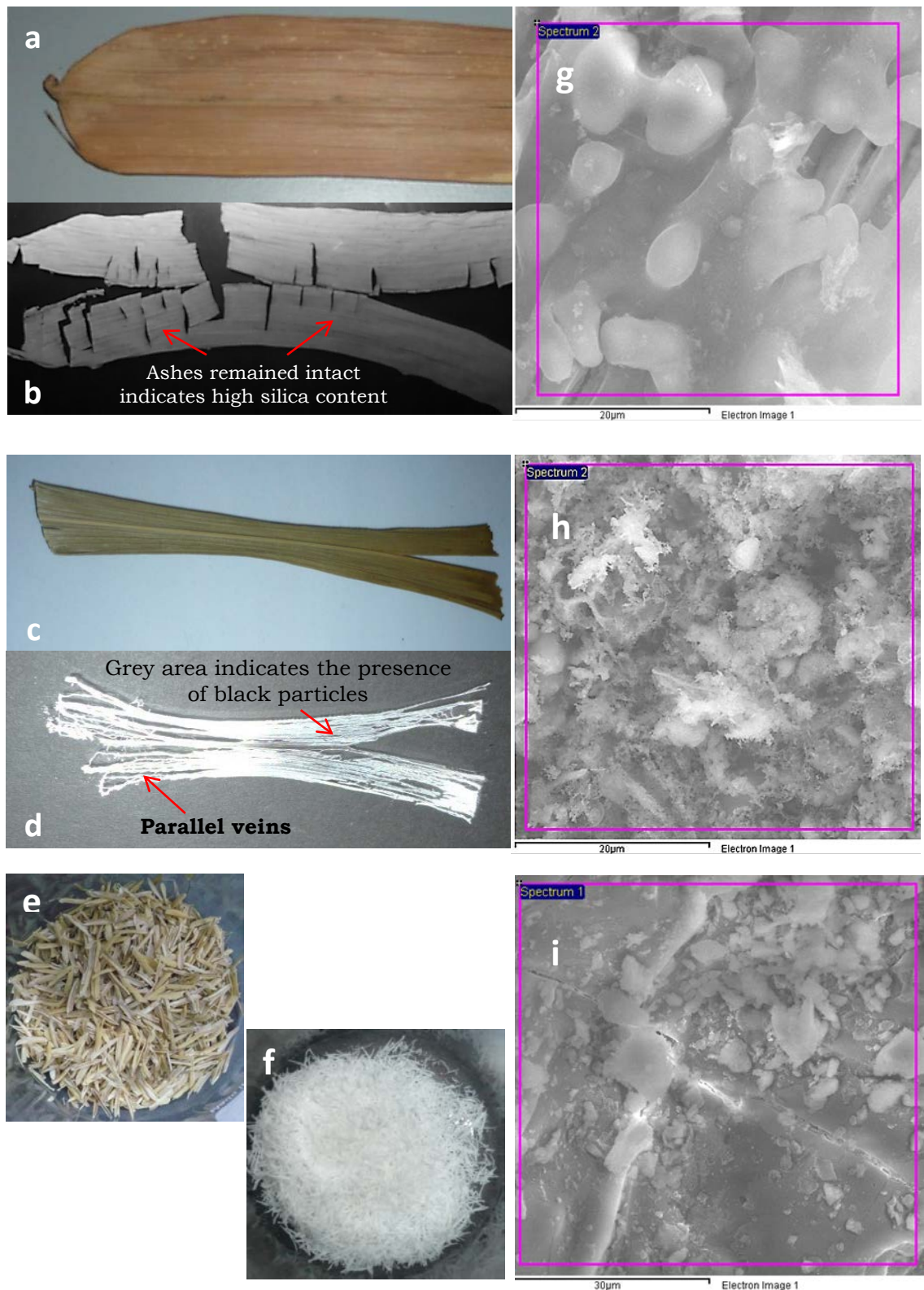


Figure 4.1 Photographs of (a) dried bamboo leaves (b) combusted bamboo leaves, (c) dried cogon grass (d) combusted cogon grass, (e) dried rice husks (f) combusted rice husks. FESEM images of (g) combusted bamboo leaves, (h) combusted cogon grass and (i) combusted rice husks

Table 4.1Statistical analyses of ash content based on *t*-statistics at 95% level of confidence

Biomass	Ash content[†] (wt%)	Standard deviation (%)	Confidence interval (wt%)
Bamboo leaves	29.7	1.7	29.3 - 30.2
Cogon grass	9.1	9.6	7.5 - 10.8
Rice husks	14.5	3.0	14.1 - 14.9
Rice straw	12.7	3.1	11.9 - 13.4

[†] Average of more than four batches of biomass collected from different places and time

the lowest ash content respectively (refer to **Table 4.1**). Since ashes mainly contain silica, this suggests that bamboo leaves contained almost double the silica of rice husks, despite rice husks had been long recognized as biomass that contains very high silica content. The ash content of cogon grass is not very consistent as shown by its standard deviation in **Table 4.1**. This may be due to the non-uniform distribution of silica in cogon grass as shown in **Figure 4.1(d and h)**. This is supported by observations where mid-rib and veins of cogon grass remained as ashes after combustion. As long as cogon grass (>70 cm) was cut into smaller pieces (approximately 8 cm), the part closer to the node (bigger mid-rib and parallel veins) may contains more silica than the tip (smaller mid-rib and parallel veins). Hence, combustion of cogon grass with higher portion close to the node may be varied as compared to those with higher portion of that close to the tip.

4.1.1.2 Thermo-gravimetric analysis (TGA)

Figure 4.2 (left) shows the Differential Thermo-gravimetric Analysis (DTG) of four biomass combusted at 10 °C min⁻¹. Moisture content was removed at the initial stage of heating within the range of 30 °C – 100 °C. The decomposition of cogon grass,

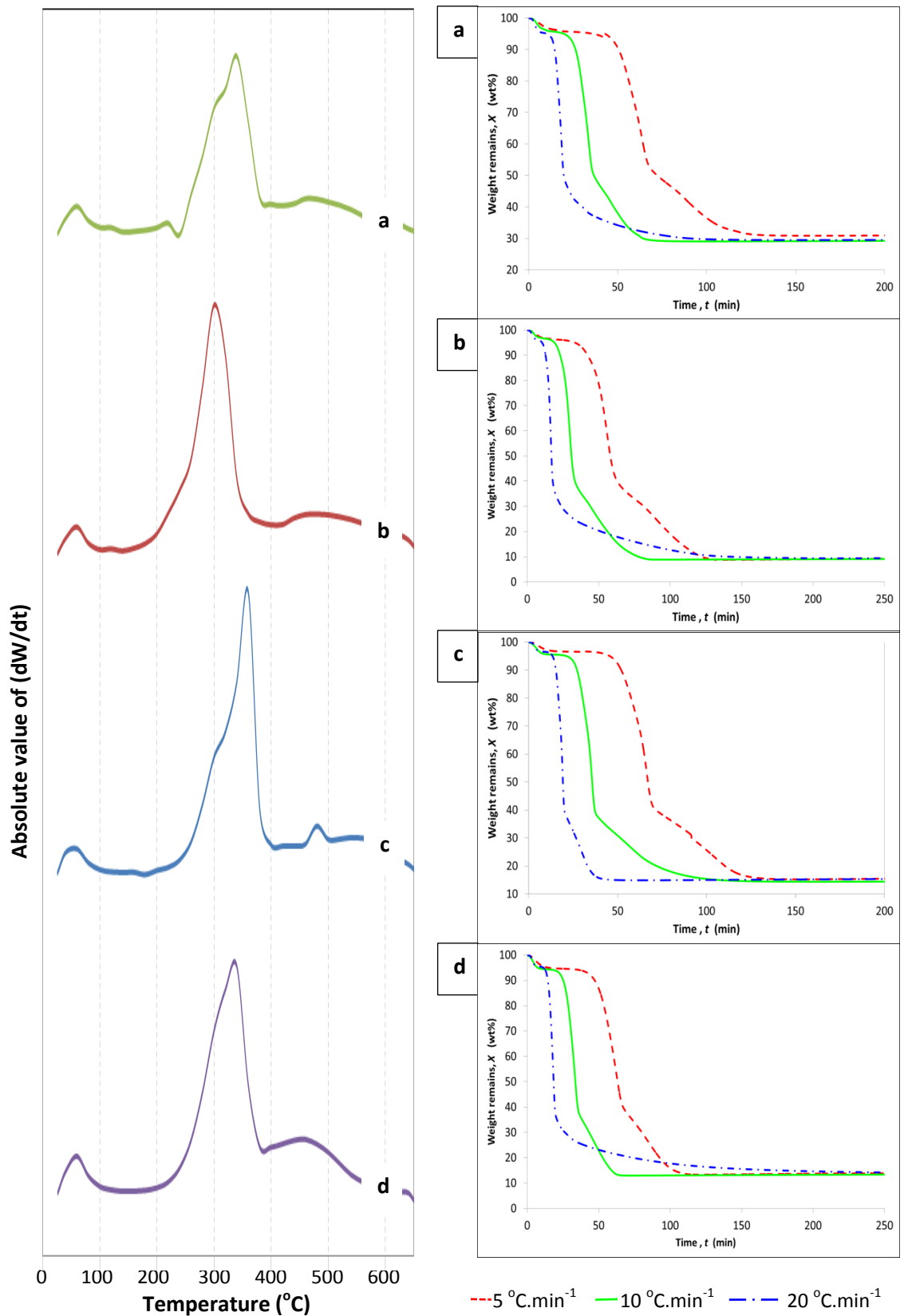


Figure 4.2 DTG - Differential Thermo-gravimetry analysis at $10\text{ }^{\circ}\text{C min}^{-1}$ (left) and corresponding thermograms (right) for (a) bamboo leaves, (b) cogon grass, (c) rice husk and (d) rice straw

started at slightly lower temperature, i.e. around 150 °C. Whereas for bamboo leaf, rice husk and rice straw; pyrolysis only began at approximately 200 °C. This first stage of reaction was the decomposition of major volatile organic compounds (cellulose and hemicellulose) to bio-char, which is corresponding to the high and broad peaks across 200 °C to 400 °C. Decomposition proceeded gradually until the second stage, where bio-char further decomposed to produce ash. The reaction in second stage was sluggish and the corresponding weight loss is relatively small as compared to the earlier stage. Above 700 °C, there is no significant change in the weight loss. If carbon is still detected in the ash after prolong heating, this shows that the carbon cannot be removed by simple thermal decomposition and it is usually termed as fixed carbon. Thermograms (*right*) in **Figure 4.2** display thermal decomposition of biomass as a function of time at three different heating rates (5, 10 and 20 °C min⁻¹). Except for rice husk, it is observed that slope of plots (the reaction rate) for all other biomass that combusted at 20 °C.min⁻¹ became smaller than those at 5 °C min⁻¹ and 10 °C min⁻¹. Therefore, it took longer time to reach final ash content than those combusted at 10 °C min⁻¹. This might be due to the incomplete decomposition of many complex organic matters and intermediates in the biomass under high heating rate, which suppressed the rate of subsequent reactions in the later stage.

The fractional conversion of organic matters within bamboo leaves and cogon grass were plotted against time in **Figure 4.3**. This can be used to determine time needed to complete the pyrolysis at various heating rates. It is evidenced from **Figure 4.3** that decomposition of cogon grass began at shorter time and therefore at lower temperature as compared to bamboo leaves. The times taken for both bamboo leaves and cogon grass reactions to complete at 5, 10 and 20 °C min⁻¹ are approximately 120,

80 and 200 minutes, respectively. Hence, combustion done at a rate $10\text{ }^{\circ}\text{C min}^{-1}$ is a more appropriate in terms of time and energy saving.

Table 4.2 shows the average ash content at three different heating rates. These values are generally consistent with the results obtained in **Table 4.1**. As comparison, the standard deviations of ash contents are all smaller than those obtained by combustion with electric furnace. Such difference is attributed to the ball milling applied to biomass prior to TGA analysis. The non-uniformity of silica in milled biomass is greatly reduced as compared to those combusted with furnace. ANOVA was carried to investigate the effect of the three heating rates to the ash content. The *p*-values calculated suggest that the final ash content of all biomass is invariant under the three heating rates.

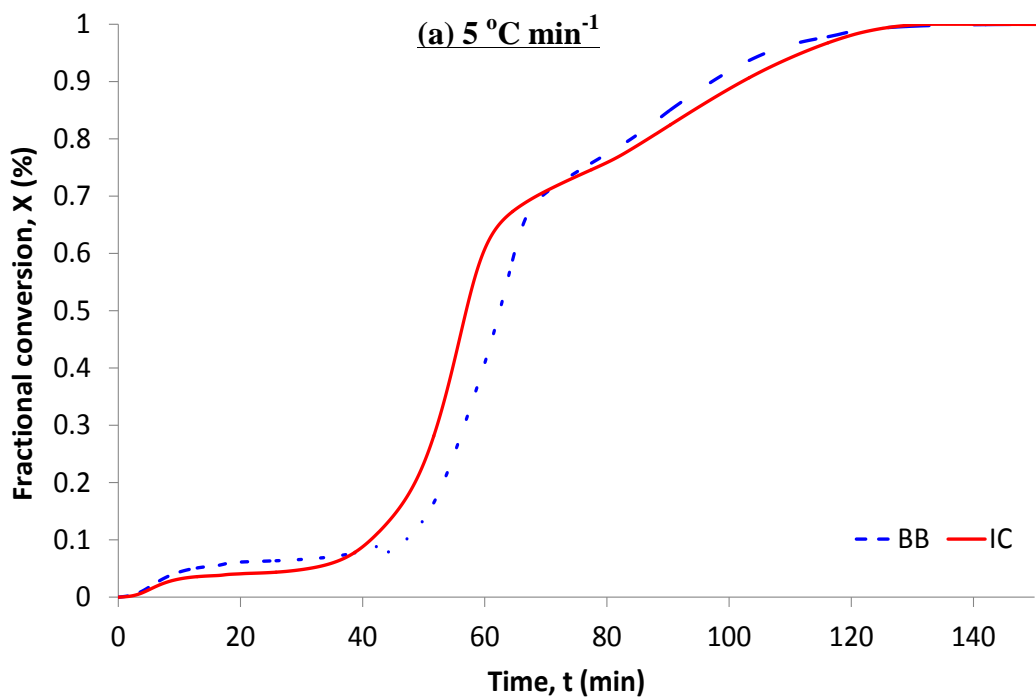


Figure 4.3 Fractional conversion of bamboo leaves (BB) and cogon grass (IC) at 5, 10 and $20\text{ }^{\circ}\text{C min}^{-1}$

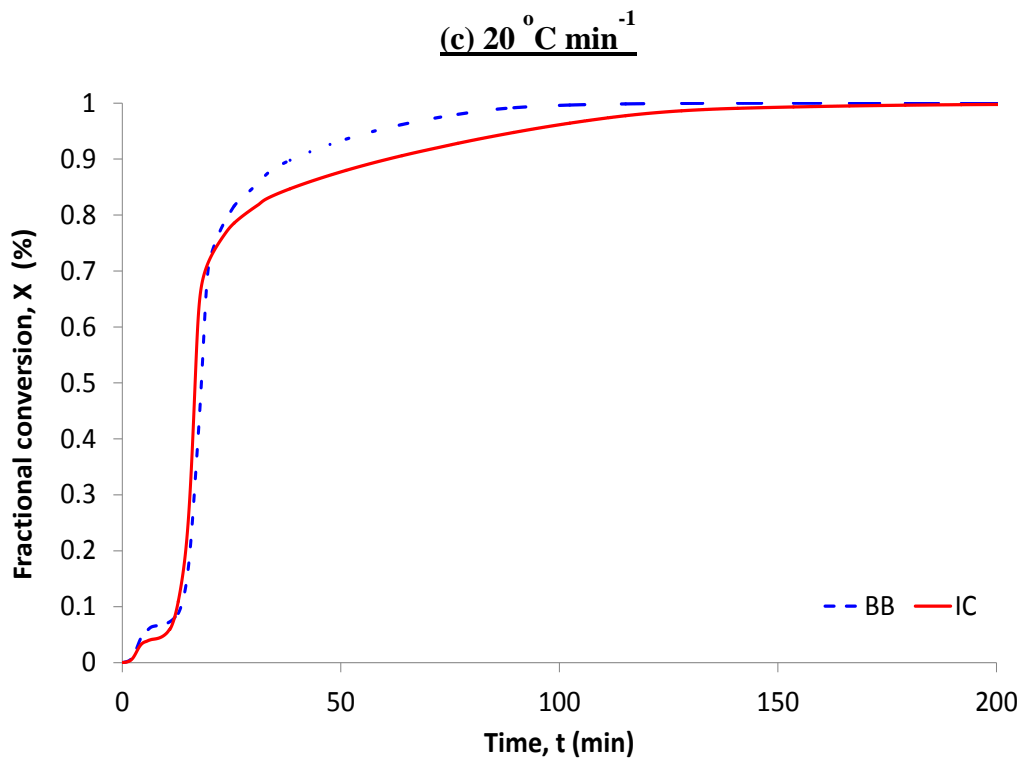
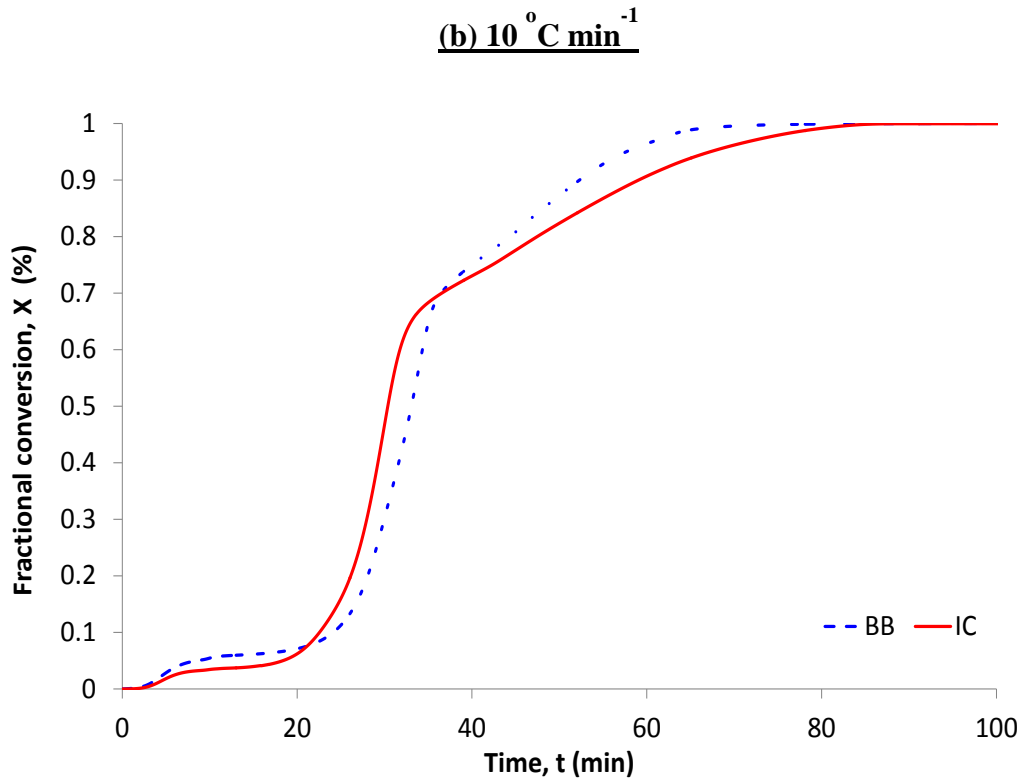


Figure 4.3 (cont.) Fractional conversion of bamboo leaves (BB) and cogon grass (IC) at (a) 5, (b) 10 and (c) 20 $^{\circ}\text{C min}^{-1}$

Table 4.2
ANOVA & *t*-statistics analyses of ash content from TGA at 95% level of confidence

Biomass	Ash content [†] (wt%)	Standard deviation [†] (%)	<i>p</i> -value ^{††}	Confidence interval of ash content (wt%)
Bamboo leaf	29.8	2.58	0.59	28.4 - 31.2
Cogon grass	8.9	2.10	0.14	8.6 - 9.3
Rice husk	14.8	2.39	0.86	14.2 - 15.5
Rice straw	13.3	2.18	0.55	12.8 - 13.9

[†] Average and standard deviation based on ash obtained at three heating rates 5, 10 and 20 °C min⁻¹

^{††} *p*-value obtained by from ANOVA of three heating rates 5, 10 and 20 °C min⁻¹. *p*-value > 0.05 indicates heating rates has no significant effect on the ash content

4.1.2 Silica content by EDX

EDX results of ash content for both leached samples are shown in **Figure 4.4**. The ashes mainly contain silicon and oxygen (in the form of silica) and carbon. It is verified that ash of unleached cogon grass (**Figure 4.4(b)**) contains higher amount of potassium (18.7 wt%) than other biomass. Ashes of leached samples in **Figure 4.5** do not contain potassium and this implied complete removal of potassium via acid leaching prior to combustion.

Silica content in biomass was calculated using **equation (3.3)** and tabulated in **Table 4.3**. Among the biomasses, bamboo leaf has the highest silica content (20.3 wt%). This is lower than 41 wt% reported by Motomura *et al.* (Motomura *et al.*, 2002), which was obtained from *sasa veitchii* bamboo. Its silica content is about double of rice husk, which agreed with the expectations deduced from its ash content. Conversely, cogon grass has very low silica content, i.e. 2.9 wt%. The silica content of unleached cogon grass is much lower than what expected from its corresponding ash content (**Table 4.2**). The very low purity of silica obtained from the ash (31.4 wt%) is caused by

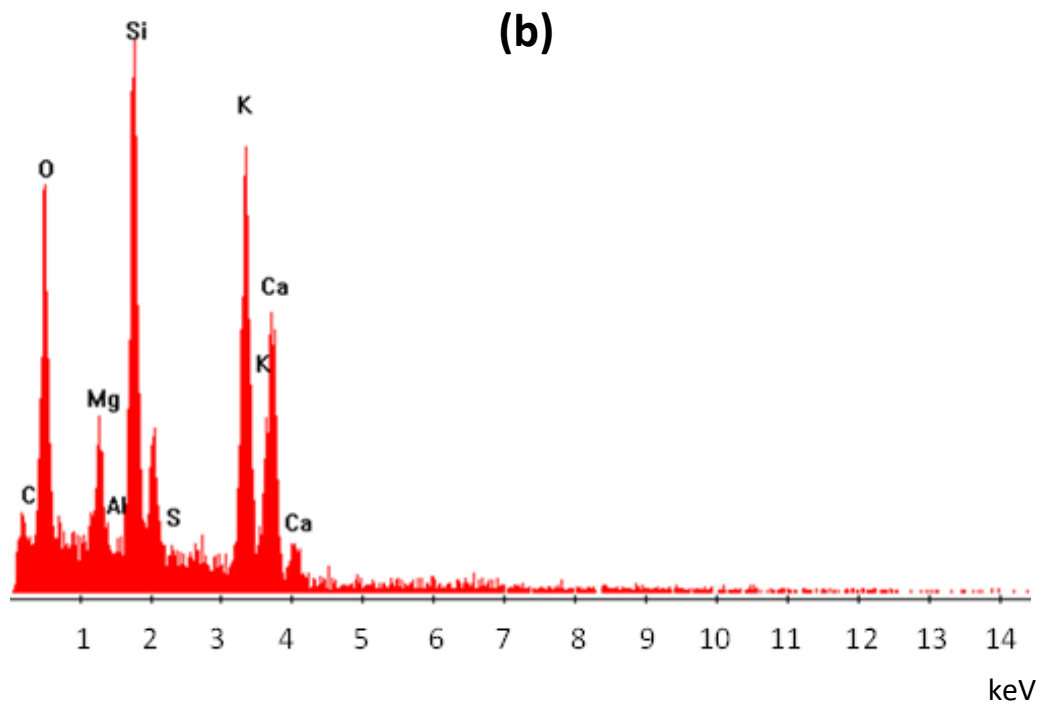
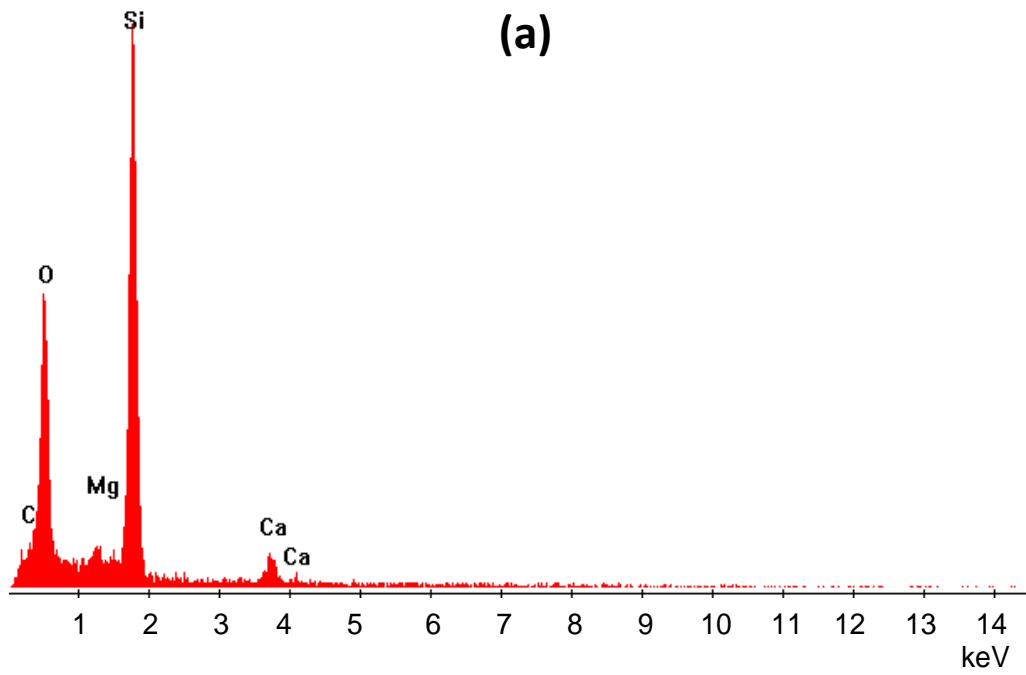


Figure 4.4 EDX results of ashes of unbleached (a) Bamboo leaves and (b) cogon grass [Intensity of EDX in count per second]

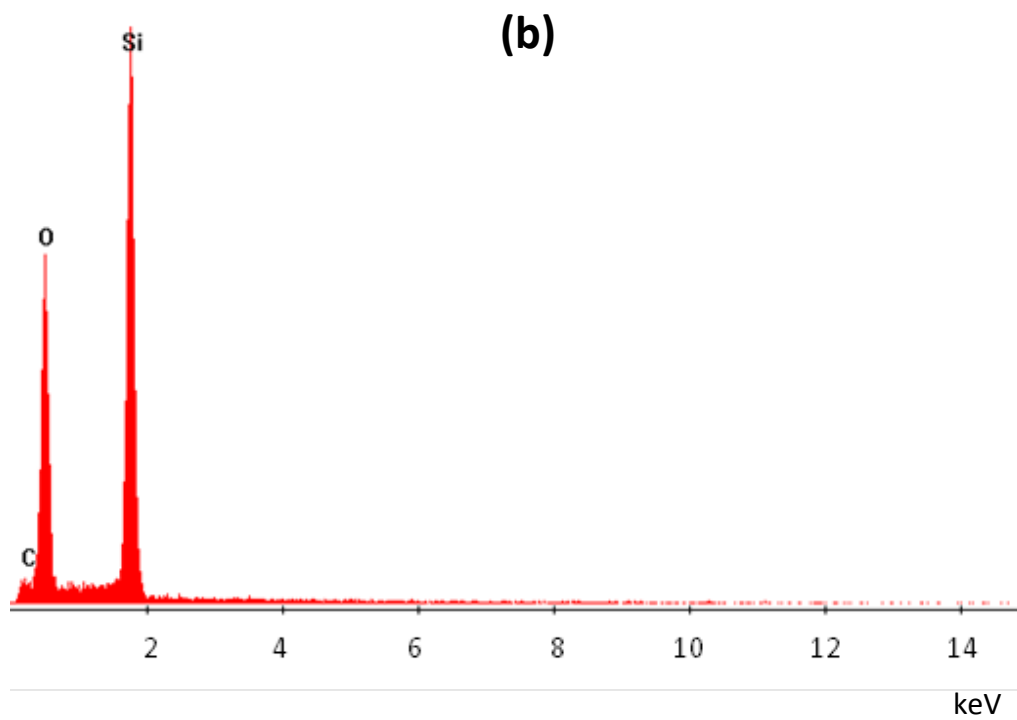
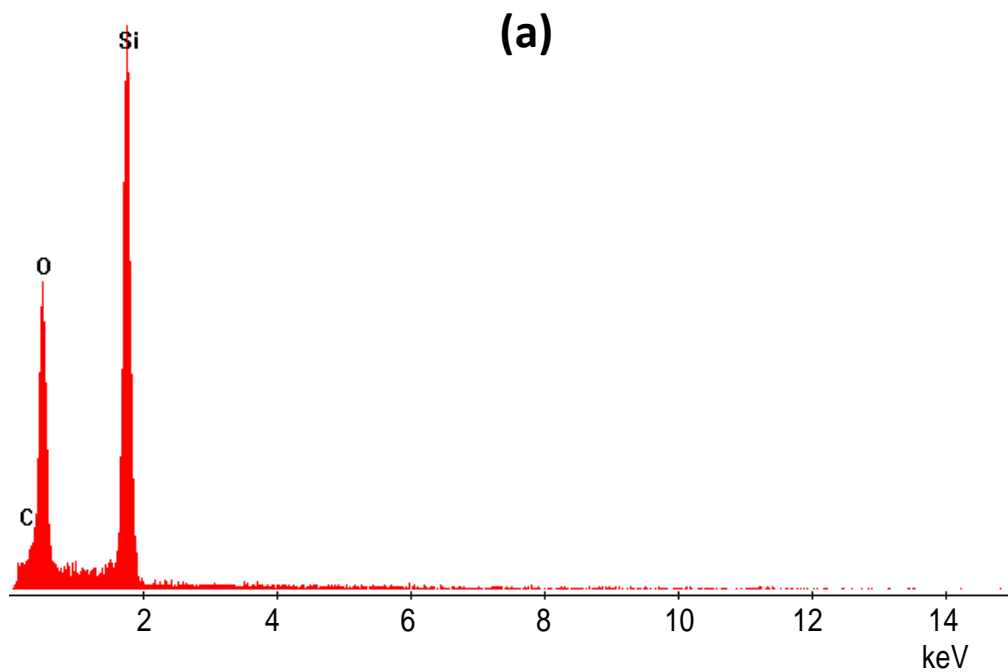


Figure 4.5 EDX results of ashes of leached (a) Bamboo leaves and (b) cogon grass [Intensity of EDX in count per second]

Table 4.3
Purity of silica and silica content in raw biomass estimated based on EDX[†]

Biomass	Silica content in ash (wt%)		Silica content in raw biomass ^{† †} (wt%)
	Unleached	Leached	
Bamboo leaf	71.5	81.3	20.3 ± 0.95
Cogon grass	31.4	83.4	2.9 ± 0.03
Rice husk	70.3	86.6	11.4 ± 0.70
Rice straw	58.2	86.6	8.8 ± 0.87

[†] Average based on three replicates

^{† †} Silica content of each replicate is calculated based on EDX results and its corresponding ash content which are combusted in electric furnace

the large amount of fixed carbon that present in the ashes. According to Krishnarao *et al.* (Krishnarao *et al.*, 2001), the existence of potassium in biomass under rapid heating could cause the carbon to embed in potassium thus led to the formation of fixed carbon. As indicated by EDX result shown in **Figure 4.4 (b)**, the potassium content of cogon grass is very high, i.e., approximately 18.7 wt%. Hence, high amount of potassium content could cause the presence of large amount of fixed carbon in their ashes and reduce the purity of silica obtained.

In order to further improve the purity of silica in ash, acid leaching was applied to biomass prior combustion. Using the 2² factorial designs, bamboo leaves and cogon grass were leached by hydrochloric acid with three replicates. Rice husks and rice straw were also leached to compare the silica content. The effect of acid concentration and duration of leaching are shown in **Figure 4.6**. ANOVA results based on 95% level of confidence are tabulated in **Table 4.4**, where in all case; the effectiveness of potassium removal is increased as concentration of hydrochloric acid increased. There is no significant influence of the leaching duration in removing potassium from all the four

biomasses. This suggests that leaching can be done in a shorter period to reduce energy consumption.

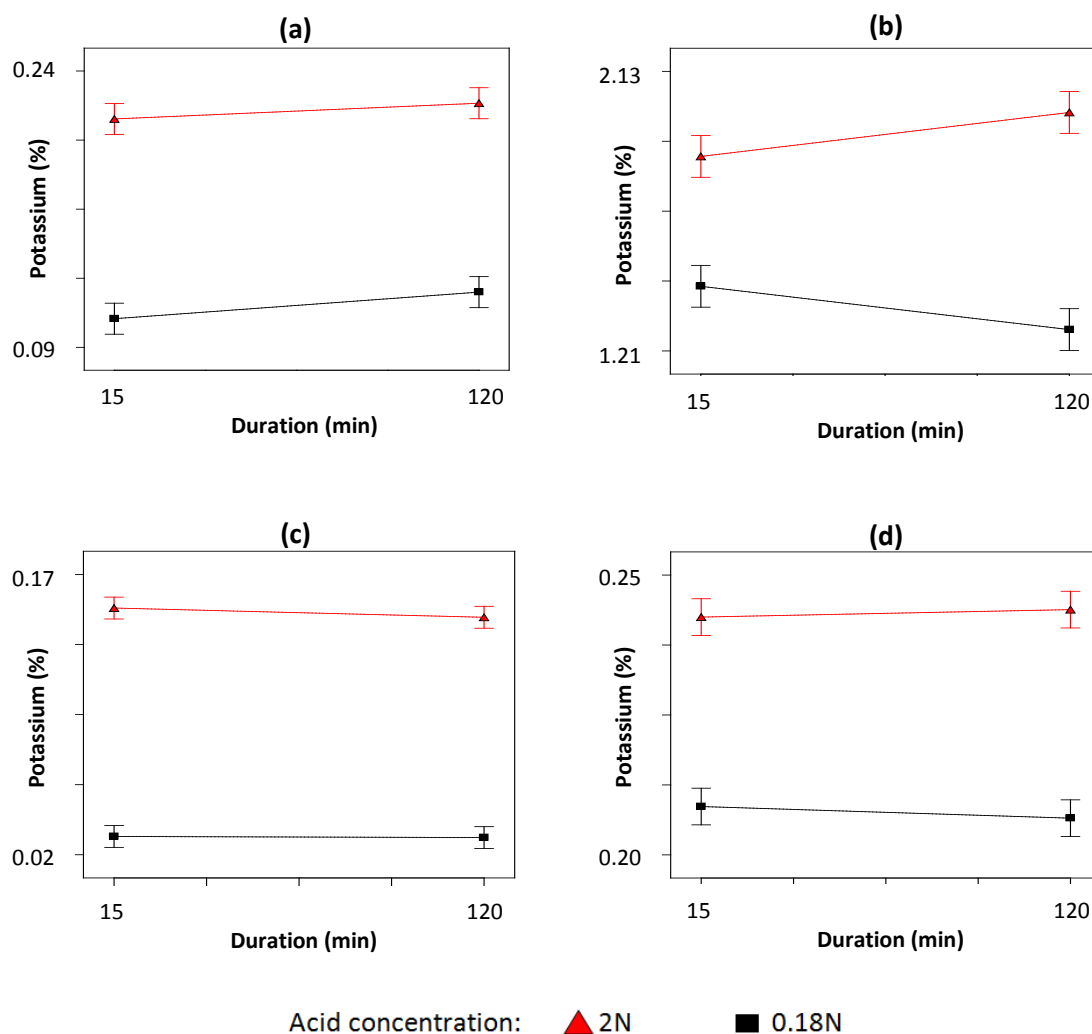


Figure 4.6 Weight fraction (%) of potassium leached from biomass (a) bamboo leaves, (b) cogon grass, (c) rice husks and (d) rice straw

Among the biomass, cogon grass exhibits anomalies from two aspects. Firstly, it contains high amount of potassium (Figure 4.6(b), approximately 2 wt%), i.e. about 10 times higher as compared to others. Second, the interaction of leaching duration and acid concentration is significant (Table 4.4). The effectiveness of potassium removal increased with acid concentration. Leaching duration does not influence potassium removal at low acid concentrations. This result shows that the interaction of the two factors is significant and has positive slope, suggesting that high acid concentration

Table 4.4
Summary of ANOVA on potassium leaching based on coded parameters

Statistical measure	Biomass	Bamboo leaves	Cogon grass	Rice husks	Rice straw
	Leaching duration	0.06	0.98	0.48	0.87
<i>p-value</i> †	Acid concentration	< 0.0001	< 0.0001	< 0.0001	< 0.0001
	Interaction	0.60	0.01	0.58	0.44
Adjusted R^2 of model		0.97	0.93	0.99	0.96

† *p-value obtained from ANOVA of three replicates. p -value > 0.05 indicates the corresponding parameter has no significant effect on the leaching*

coupled with long leaching periods facilitates potassium removal. This conclusion is reasonable because cogon grass contains large quantities of potassium, and low acid concentration is a limiting reactant. Longer leaching periods at low acid concentrations does not increase the amount of potassium removed because the concentration of acid used is insufficient to remove all of the potassium in cogon grass. With high acid concentration, the leaching reaction can proceed and remove all of the potassium.

4.1.3 CHNS - carbon content and organic matters

The elemental contents of organic compounds within biomass were determined by CHNS analysis and the results are tabulated in [Table 4.5](#). Cogon grass shows the highest carbon content, which is why it contains the highest amount of organic compounds among the biomass. The different proportion of all C, H and N in cogon grass explained why its reaction kinetics is different from other biomass. Rice husks and rice straw show different proportion of carbon and hydrogen even they are

Table 4.5
Elemental analysis of CHNS[†]

Biomass	C (wt%)	H (wt%)	N (wt%)	S (wt%)	Residue (wt%)	Empirical formula of organic compound^{† †} (wt%)
Bamboo leaf	32.3	4.2	0.54	0.22	62.7	C _{1.00} H _{1.56} O
Cogon grass	41.5	5.3	0.92	0.36	51.9	C _{1.10} H _{1.67} O
Rice husks	38.7	4.8	0.43	0.33	55.7	C _{1.14} H _{1.68} O
Rice straw	38.3	4.9	0.88	0.32	55.6	C _{1.04} H _{1.60} O

[†] Average based on three replicates

^{† †} Empirical formulae are estimated assuming that residues contain oxygen and silica only. Oxygen in organic compound was then estimated by subtracting silica content in [Table 4.3](#) from the residue.

parts of the same plant (paddy). The high fraction of residue in bamboo leaf is related to its high silica content. Empirical formulae of organic compounds in biomass are calculated based on CHNS analysis. By comparing this with the empirical formula of cellulose (C_{1.2}H₂O), it suggests that organic compound in rice husks and cogon grass have very similar structure with cellulose. This is generally agreed with what had been reported by other researchers (Mansaray and Ghaly, 1998) where organic portions of rice husks are mainly made up of cellulose and lignin. Empirical formula of bamboo leaf and rice straw deviates appreciably indicates different organic compounds.

4.1.4 XRD and amorphicity

[Figure 4.7](#) shows the diffractogram of ashes from unleached biomass that combusted at 650 °C. Diffractograms of bamboo leaf, rice husk and rice straw exhibit featureless pattern and diffuse peak at 23°. As mentioned earlier by other researchers (Hamdan et al., 1997), these peaks are corresponding to amorphous silica with some

short range primitive structures. This confirmed that silica extracted from these three biomass are amorphous.

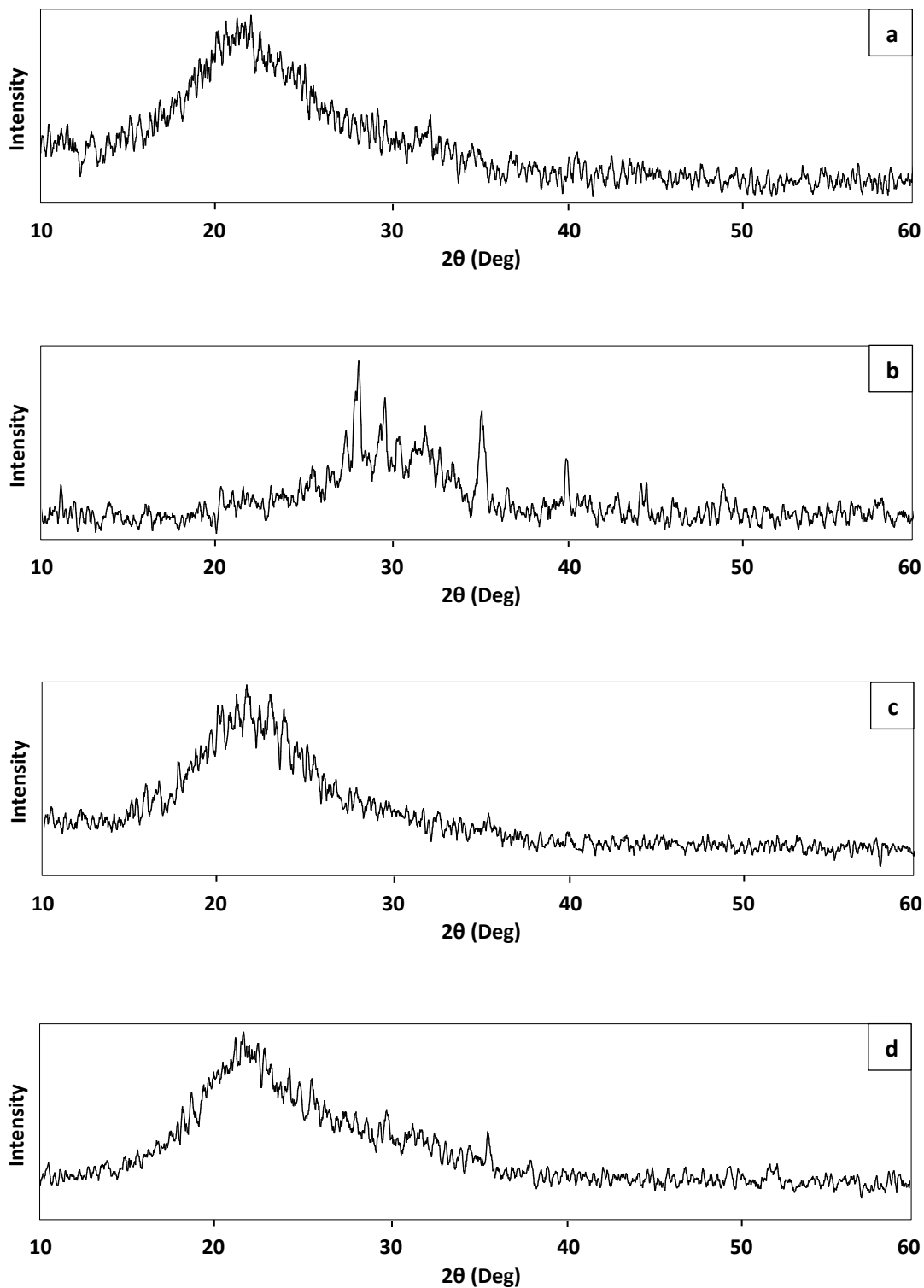


Figure 4.7 XRD results of unleached (a) bamboo leaves, (b) cogon grass, (c) rice husk and (d) rice straw combusted in air at 650°C [Intensity in count/second]

For cogon grass, sharp peaks are observed at 28° , 29° and 35° (**Figure 4.7(b)**). These peaks were initially suspected to be crystalline silica in the form tridymite. However, it is very unlikely that tridymite crystallized at 650°C since tridymite forms at least at 750°C (Zhang et al., 2010). In order to examine this, cogon grass were combusted at lower temperatures, i.e. 500°C , 550°C and 600°C . The ashes formed were analyzed with XRD and the result are shown in **Figure 4.8**. Those sharp peaks are still present at lower combustion temperatures and thus they are not tridymite.

Refined analysis on the diffractogram reveals that these sharp peaks are actually related to the presence of potassium and calcium compounds that present in cogon grass. Those sharp peaks are corresponding to the crystals of sylvite (KCl) and calcium carbonate (CaCO_3).

In order to verify the effect of potassium and calcium traces on XRD analyses, further studies were carried out on the acid leached biomass and the result is shown in **Figure 4.9**. It is very clear that all sharp peaks that were previously present in the unleached cogon grass are now disappeared in acid leached samples. This, together with the evidence of the complete removal of potassium traces in leached biomass (*refer to Figure 4.5(b)*), verified that sharp peaks in **Figure 4.7(b)** and **Figure 4.8** are attributed to the presence of crystals related to potassium and calcium compounds.

In addition, diffractogram of other leached biomass exhibit smoother spectrum, at both the diffuse peaks and also in all other regions, as compared to those unleached samples that shown in **Figure 4.7**. Small peaks that were previously observed at 2θ of 32° and 35° in **Figure 4.7** were also eliminated in leached samples. Therefore, the amorphicity of all combusted biomass increased as the result of acid leaching. This again shows that acid leaching plays an essential role in obtaining pure and amorphous silica from these biomasses, which is especially important in the case of cogon grass.

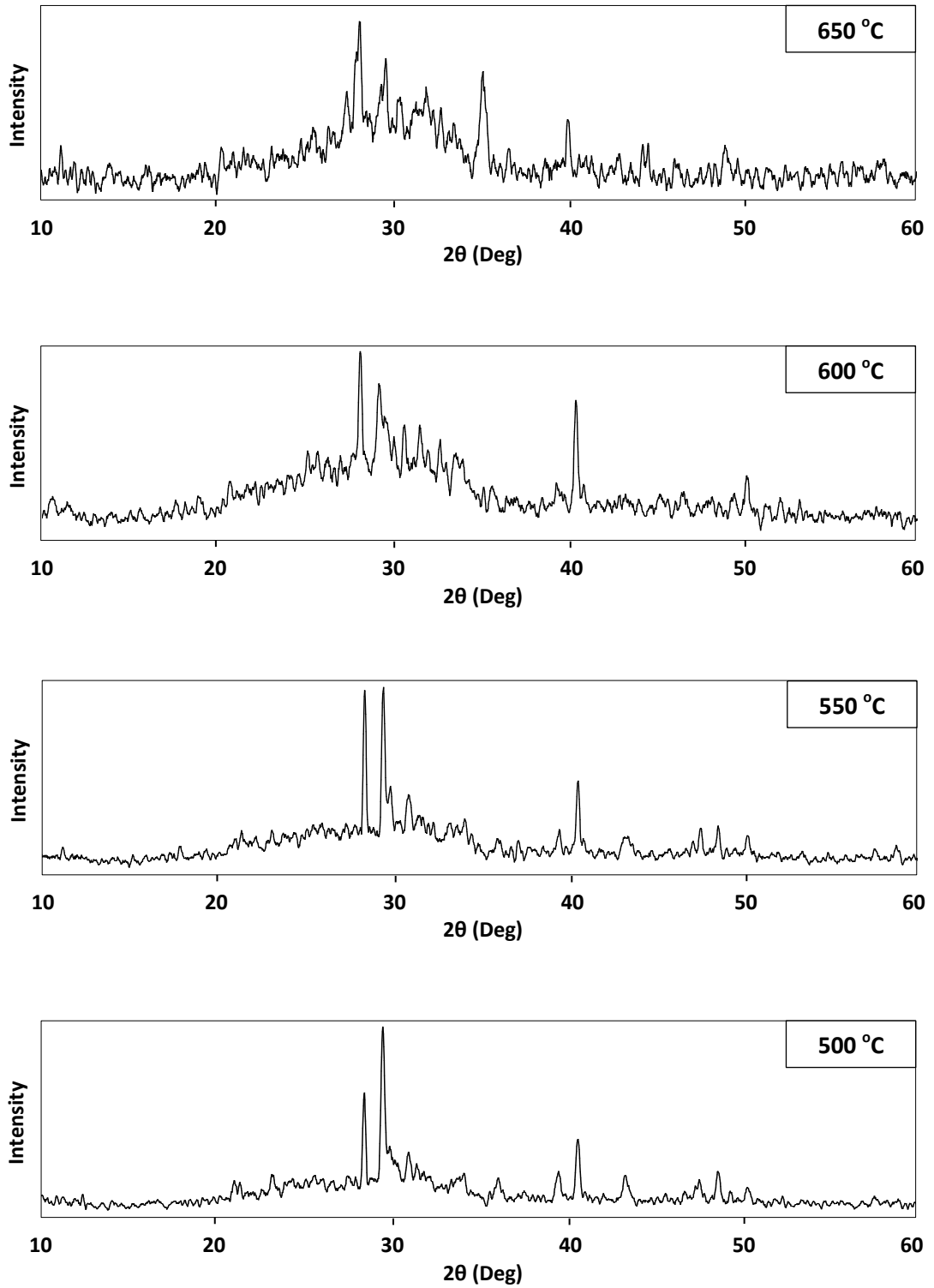


Figure 4.8 XRD results of cogon grass combusted at various temperatures [Intensity in count/second]

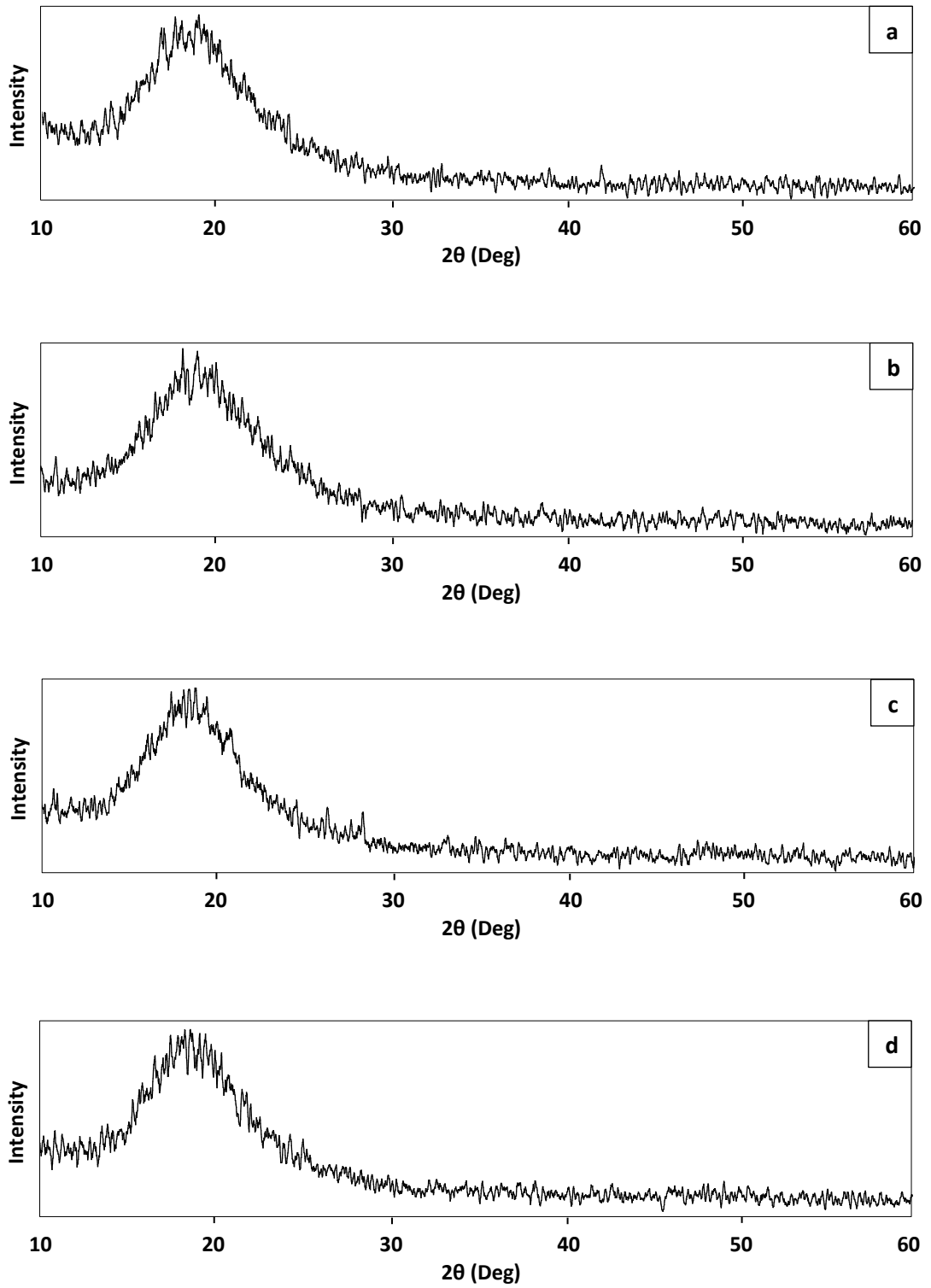


Figure 4.9 XRD results of acid leached (a) bamboo leaf, (b) cogon grass, (c) rice husk and (d) rice straw combusted in air at 650°C [Intensity in count/second]

4.1.5 Determination of kinetic parameters

Figure 4.10 shows the DTG of bamboo leaf and cogon grass obtained under three heating rates. The decomposition of bamboo leaf and cogon grass began at

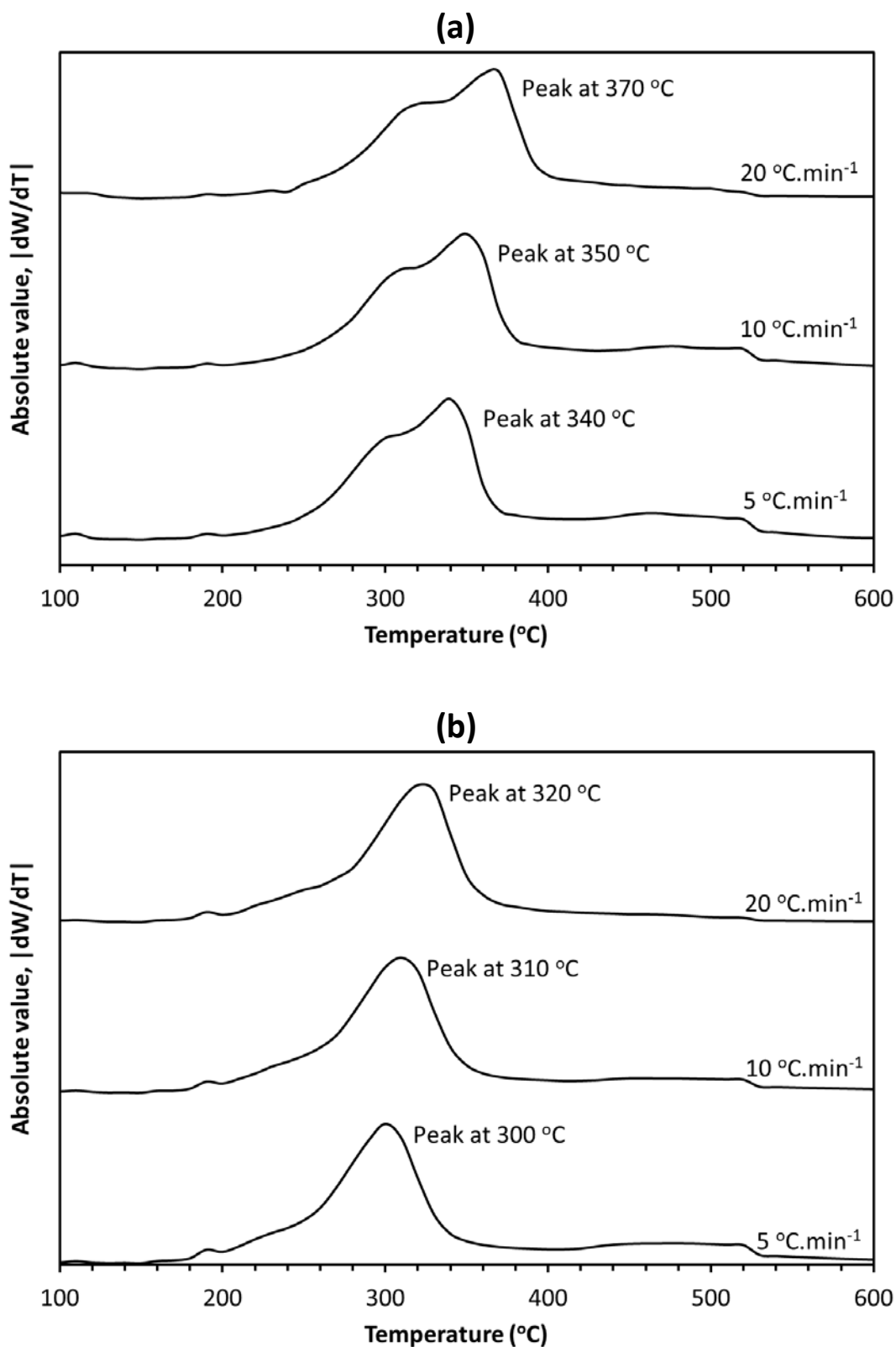


Figure 4.10 Differential thermogravimetry (DTG) of (a) bamboo leaf , (b) cogon grass

approximately 200 °C and 180 °C, respectively. For bamboo leaf, the DTG increased rapidly to 300 °C and displayed a short plateau before reaching peaks around 340 – 370 °C. As comparison, DTG peaks of cogon grass are relatively smooth and sharp. As the heating rates increased, peaks of decomposition of major constituents in bamboo leaf and cogon grass are shifted to higher temperature. Peak shifts actually indicate the decomposition is a series of reactions, rather than single step decomposition. As heating rates increased and the temperature rapidly increased, the formation of intermediate components was delayed. Subsequent decomposition of major constituents were then suppressed and caused the peaks to shift to higher temperature. This is supported by the sharp bends observed in isothermal heating at 650 °C (Figure 4.11). As the result of the delay in reaction under high heating rates, considerable amount of samples continued to decompose even the temperature had reached 650 °C.

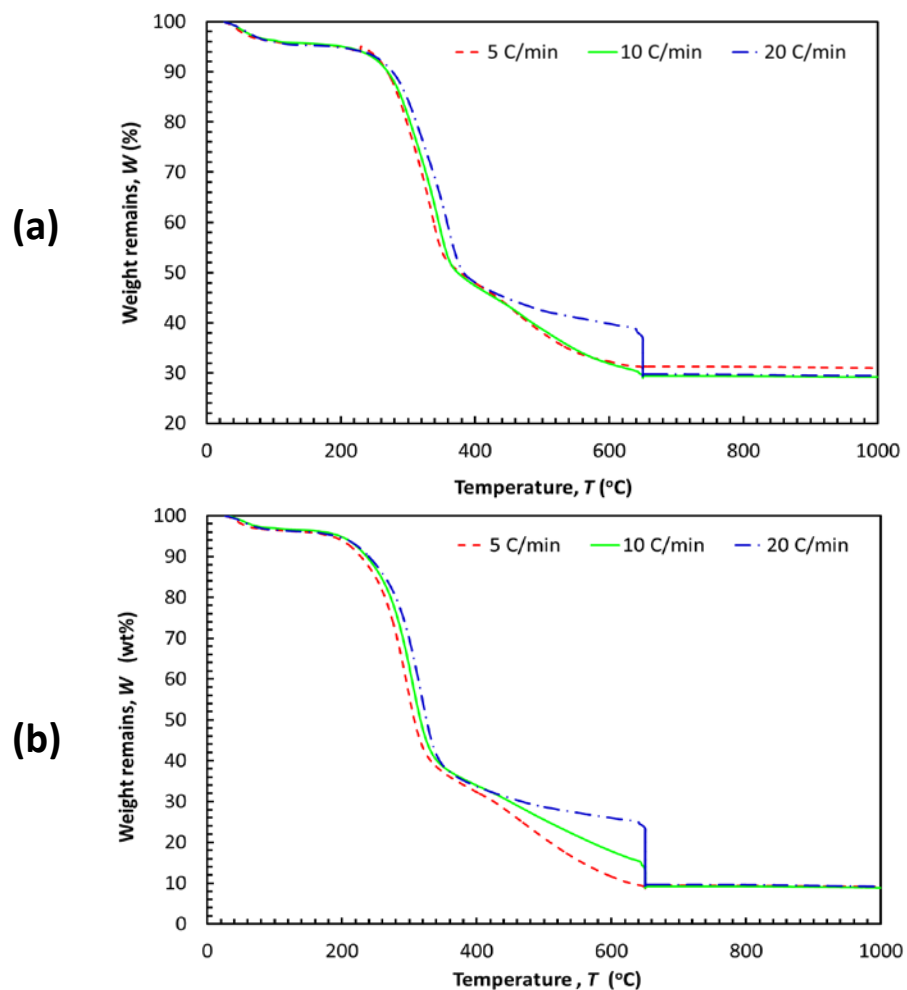


Figure 4.11 Thermograms of (a) bamboo leaf and (b) cogon grass

To determine the activation energy and frequency factor of the first decomposition, non-isothermal iso-conversional TGA data at three different rates were fitted with the Flynn-Wall-Ozawa model. As shown in Figure 4.12, the TGA data fitted well into the model.

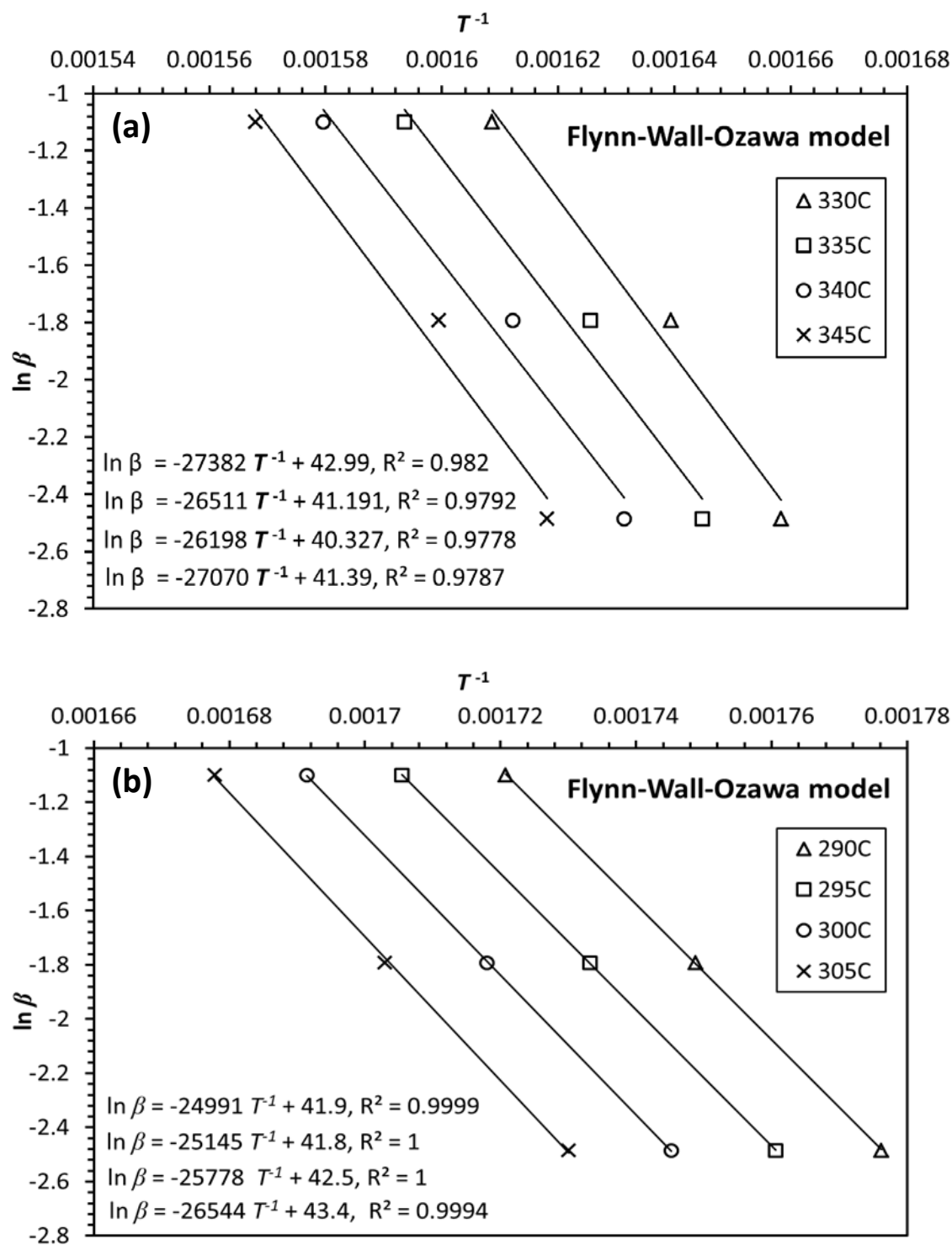


Figure 4.12 TGA iso-conversional data of (a) bamboo leaf and (b) cogon grass at three heating rates ($\beta = 5, 10$ and 20 °C.min⁻¹) fitted using the *Flynn-Wall-Ozawa* model.

The slopes (equivalent to $\frac{E_a}{R}$) obtained varied from 26198 to 27382 for bamboo leaf and 24991 to 26554 for cogon grass. Thus, the average activation energies calculated for bamboo leaf and cogon grass are $211.7 \pm 3.8 \text{ kJ mol}^{-1}$ and $202.5 \pm 5.1 \text{ kJ mol}^{-1}$, respectively. The corresponding average frequency factor (\bar{A}) calculated are $(4.5 \pm 4.6) \times 10^{15} \text{ s}^{-1}$ and $(7.9 \pm 6.7) \times 10^{15} \text{ s}^{-1}$.

Figure 4.13 shows the DSC result of bamboo leaf and cogon grass. A small endotherm was observed between 30 °C and 120 °C, which is attributed to the vaporisation of moisture. Similar to the TGA results, the DSC results also show two stages of decomposition for both biomass. For cogon grass, the corresponding peaks of the two stages of decomposition were observed at 313 °C and 439 °C, similar to the temperatures observed in the TGA results as shown in Figure 4.10 (b). The endotherm was followed by a large exotherm from 150 °C to 415 °C that was caused by the decomposition of organic substances. The heat of combustion at this initial stage of decomposition was 7.885 kJ g^{-1} . In the second stage of decomposition from 415 °C to 500 °C, the exotherm released 2.763 kJ.g^{-1} . Therefore, the lower heating value (LHV) of cogon grass was determined as the total heat of combustion of the two stages, i.e., 10.648 kJ g^{-1} . For bamboo leaf, the heat of combustion from 150 °C up to the end of plateau at 376.8°C is 4.229 kJ g^{-1} . This added with the heat released in between 376.8°C to 500 °C (4.481 kJ g^{-1}) gives LHV of 8.709 kJ g^{-1} . The LHV of both the bamboo leaf and cogon grass obtained is comparable to the common wood fuels and bagasse (Lower and Higher Heating Values of Gas, Liquid and Solid Fuels 2011, Typical calorific values of fuels, Wood as a Fuel - List and values of wood fuel). Hence, they can be used as a fuel in industrial applications in which the remaining ash can be converted to bio-silica. Alternatively, the heat released by cogon grass can be used to sustain its combustion to produce silica without using additional energy.

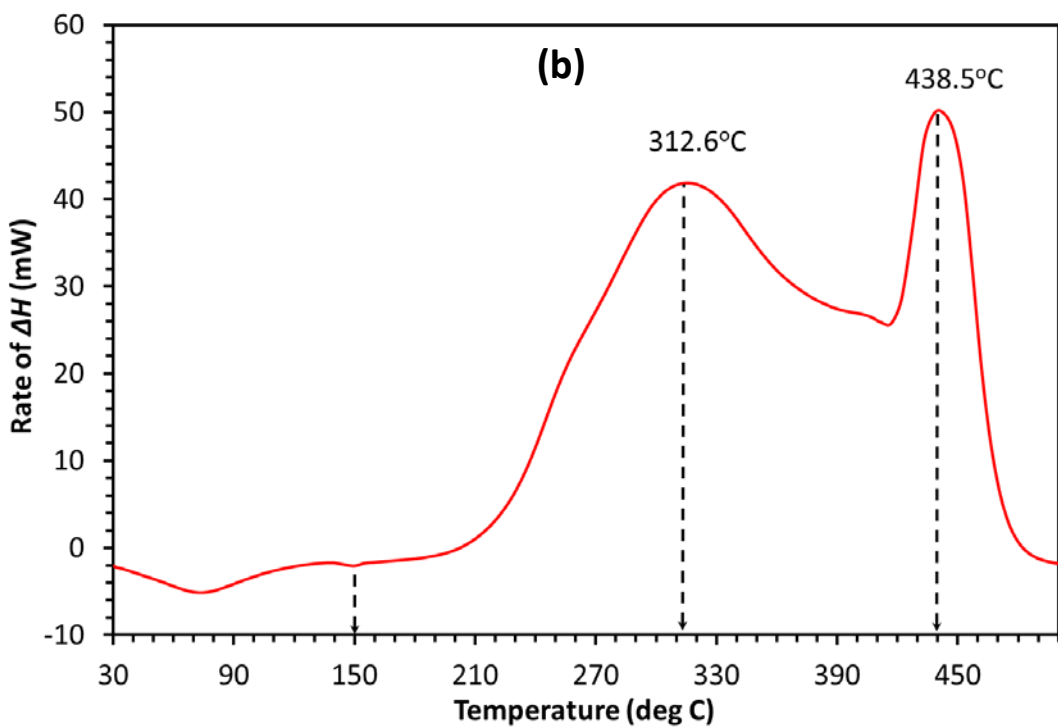
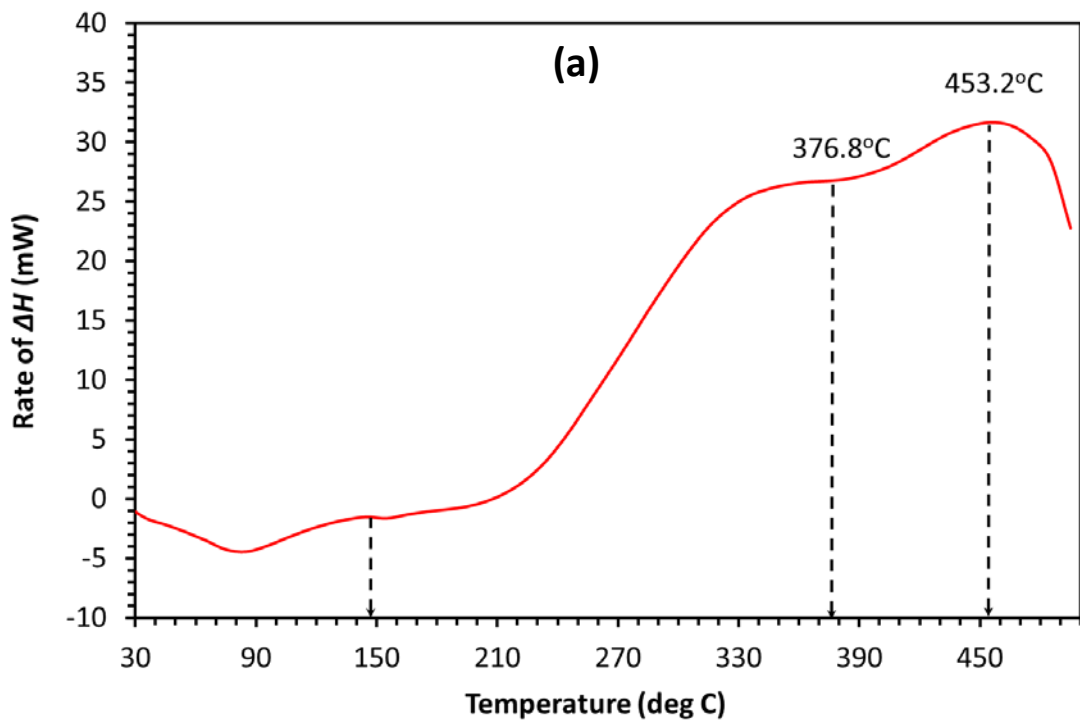


Figure 4.13 DSC result of (a) bamboo leaf and (b) cogon grass combusted in air

4.1.6 Summary

From the results in [section 4.1](#), it revealed that bamboo leaves has great potential to produce high purity amorphous silica. The silica content in bamboo leaves (20.3 wt% \pm 0.95) is even higher than rice husks. Interestingly, unlike speculated previously in other literatures (Shilling, 1993, Dozier, 1998), cogon grass has very low silica content (2.9 wt% \pm 0.03). This confusion may be the result of assuming the ash of cogon grass contains mainly silica. By subtracting the high amount of fixed carbon that cannot be removed by combustion, the remained silica content is much lower than what was expected from its ash. Despite its low silica content, silica extraction of cogon grass is still an alternative to reduce its undesired abundance. Based on the 10 metric tons of cogon grass can be cut down per hectare of land (Kohli et al., 2008), a conserve estimate on 500 million hectares of infested land can provide 145 million metric tons of amorphous silica reserve. In addition, based on the calculated kinetic parameters and LHV, the heat released (10648 kJ g⁻¹) during decomposition may also be reused to sustain the combustion of cogon grass, or be channeled to other applications as a zero-cost fuel. However, the removal of potassium from cogon grass is essential in ensuring the purity and quality of amorphous silica to be extracted. Based on the calculated kinetic parameters and LHV, the heat released during decomposition may also be reused to sustain the combustion of bamboo leaf and cogon grass, or be channeled to other applications as a zero-cost fuel.

Based on the result, only silica from bamboo leaves was further produced in large amount and used to synthesize water glass as precursor for silica aerogel. The characteristics of water glass produced are reported in [section 4.2](#).

4.2 Preparation of water glass as precursor

The bamboo leaf silica obtained in [section 4.1](#) was dissolved to prepare water glass. Effect of processing parameters including temperature, time, agitation speed, concentration of NaOH, ratio of silica mass to NaOH volume to the silica yield (ξ) in water glass was investigated and optimized.

4.2.1 Optimization of silica yield (ξ) in water glass

The effect of five selected processing parameters on the silica yield in water glass was studied, and the results are shown in [Figure 4.14](#). Among these parameters, the time, the temperature and the agitation speed generally have stronger influence on the silica yield than the NaOH concentration and the mass-to-volume ratio. The silica yield increased as the time ([Figure 4.14\(a-d\)](#)), the temperature ([Figure 4.14\(a, e-g\)](#)) or the agitation speed ([Figure 4.14\(d, g, i-j\)](#)) increased. This relationship is expected because these three factors contribute to the increase in diffusion and reaction rate of BLS in the NaOH solution. The temperature generated the largest response on the silica yield when it was increased, followed by the agitation speed and the time. Hence, a silica yield that approaches unity can be achieved in a shorter time at elevated temperatures. Similarly, the silica yield can be increased when higher agitation speed or longer reaction time is applied, but the effect is less significant for high temperature. By comparison, the NaOH concentration and the mass-to volume ratio have no significant effect on ξ . However, they exhibit some interaction as can be seen in [Figure 4.14\(h\)](#). The corresponding ANOVA regression model is summarized in [Table 4.6](#).

With the adjusted R^2 value of 0.97, the model is sufficiently explained using the five proposed processing parameters. [equation \(4.1\)](#) shows the model with the involved regressed coefficients of processing parameters.

$$\xi = \frac{1}{10000} (90.7t + 268.7 T - 43.7 C - 48.9 R + 47.9 A - 5186) \quad (4.1)$$

Because the parameters t , T and A contribute positively to ξ , all corresponding regressed coefficients are > 0 . Although ξ responds negatively to the increase of C and R , their individual effects are relatively small as compared to the other parameters. As shown in [Table 3.1](#) where $2 \leq C \leq 6$ and $12 \leq R \leq 60$ in this study, their products with the regressed coefficients are on average one to two orders of magnitude smaller than the

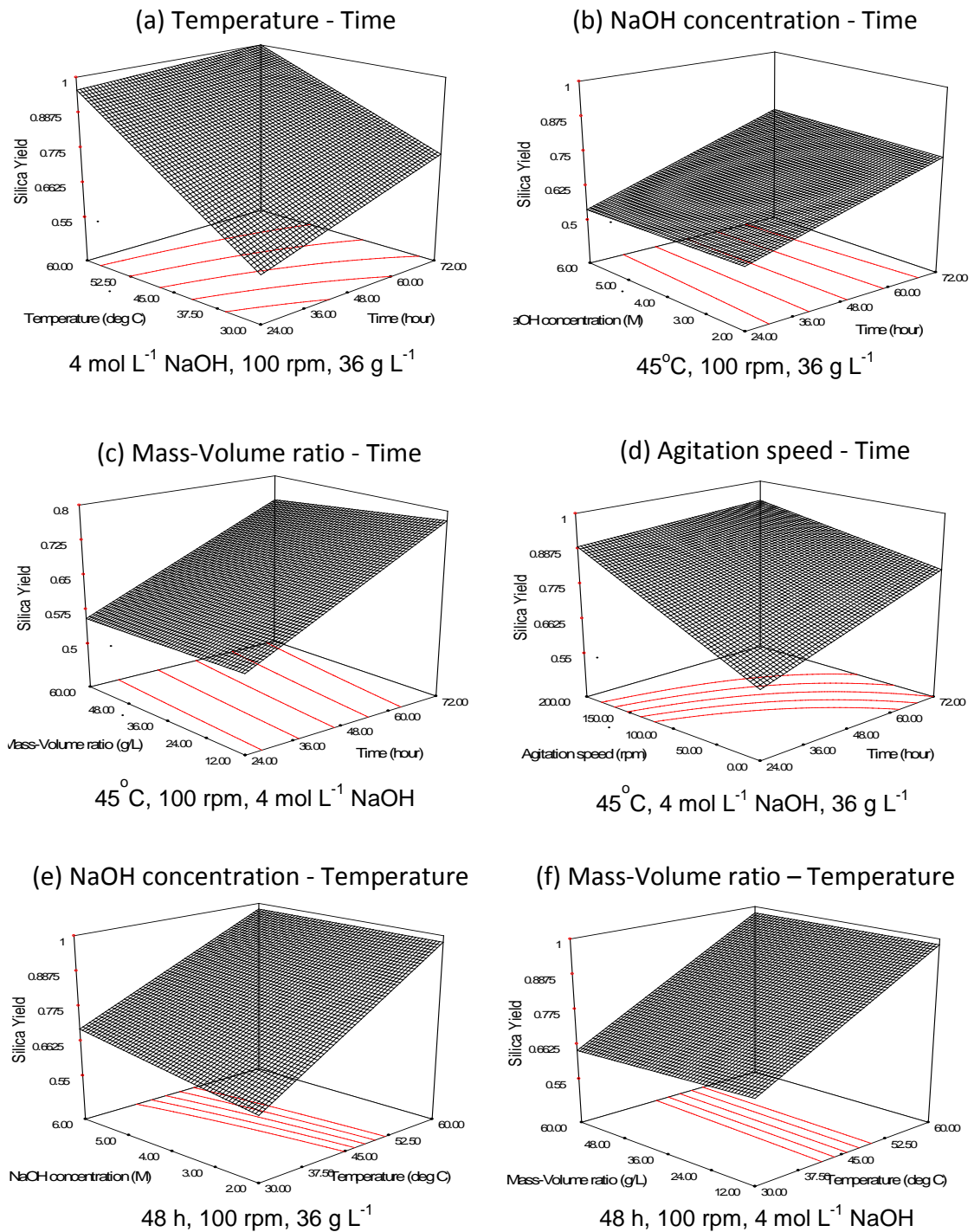
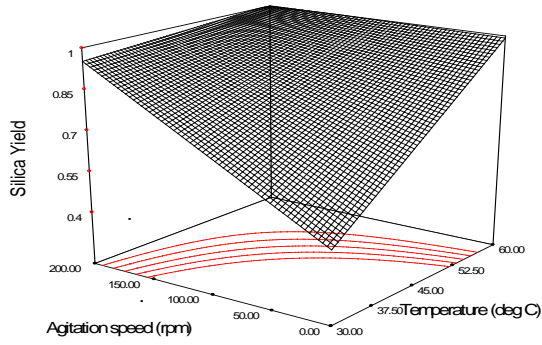
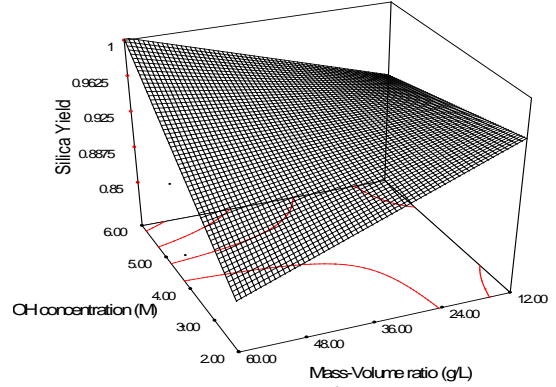


Figure 4.14. Effects of the processing parameters on the silica yield in water glass

(g) Agitation speed – Temperature

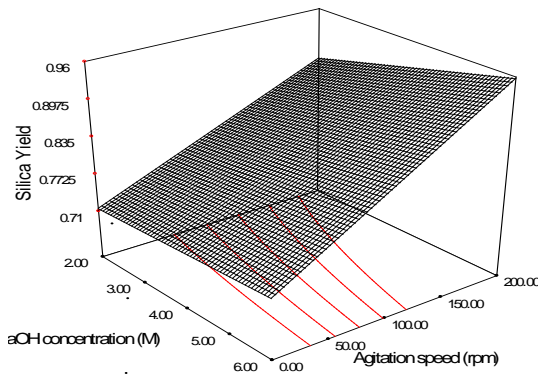
48 h, 4 mol L⁻¹ NaOH, 36 g L⁻¹

(h) Mass-Volume ratio – NaOH concentration

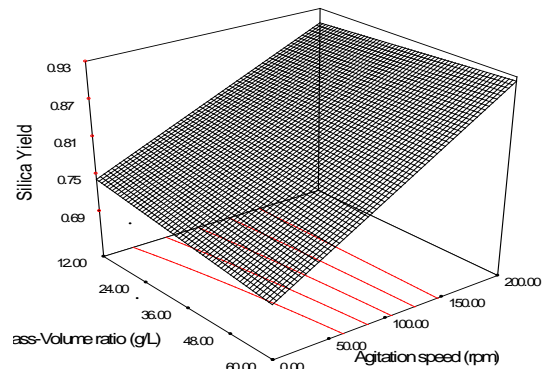


48 h, 45 °C, 100 rpm

(i) NaOH concentration – Agitation speed

48 h, 45 °C, 36 g L⁻¹

(j) Mass-Volume ratio – Agitation speed

48 h, 45 °C, 4 mol L⁻¹ NaOH**Figure 4.14 cont.** Effects of the processing parameters on the silica yield in water glass

other effects. Hence, the negative effect of these two parameters only become significant when t , T and A are low. Moreover, the interaction between C and R and its effect on ξ will be discussed in later section.

Table 4.6

Effect of processing parameters on the silica yield in water glass †

Processing parameters		
<i>p</i> -value of	<i>Time</i>	0.027
	<i>Temperature</i>	0.004
	<i>Concentration of NaOH</i>	0.139
	<i>Mass (BLS) / Volume (NaOH) ratio</i>	0.573
	<i>Agitation speed</i>	0.011
	Adjusted R² of model	0.97

† ANOVA at 95% level of confidence

To minimize both energy and time consumption in the process, this study aimed to minimize the required time, temperature and agitation speed to achieve silica yield of $\xi = 1$. All the three parameters cannot be minimized simultaneously because the mass transfer in the reaction can become extremely slow. Thus, only two of the three parameters are minimized, and the mass transfer is achieved by the remaining parameter in one of the following methods:

- i. Forced convection created by only agitation (A); or
- ii. Natural convection due to the temperature gradient and increase of diffusivity at higher temperature (T); or
- iii. Diffusion that occurs with time (t)

The optimized results are shown in [Figure 4.15](#). To obtain water glass with the highest silica concentration, all optimizations were aimed to achieve the maximum mass-to-volume ratio of 60 g L^{-1} . As $\xi \rightarrow 1$, the silica concentration of water glass, $C_{\text{SiO}_2} \rightarrow R/M_{\text{SiO}_2} \approx 1 \text{ M}$ when $R = 60 \text{ g L}^{-1}$ under the optimized conditions. In every case, the lowest possible temperature was set to 30°C because the room temperature does not require any heating or cooling in the process. The result shows that the processing time can be reduced to 2 hours if agitation or/and high temperature is applied. The reflux of the reactant mixture at higher temperature may further reduce the required time and agitation. However, such process must not be performed using glass container because the silica in glass can leach out due to the concentrated NaOH at high temperature.

As observed in [Figure 4.14\(h\)](#), the mass-to-volume ratio (R) and the NaOH concentration (C) are related. This relationship can be explained by the stoichiometry of the reaction between NaOH and bamboo leaf silica, which produces sodium metasilicate;

under high pH, this compound will further convert to a more ionic species called sodium orthosilicate, as shown in Figure 4.16.

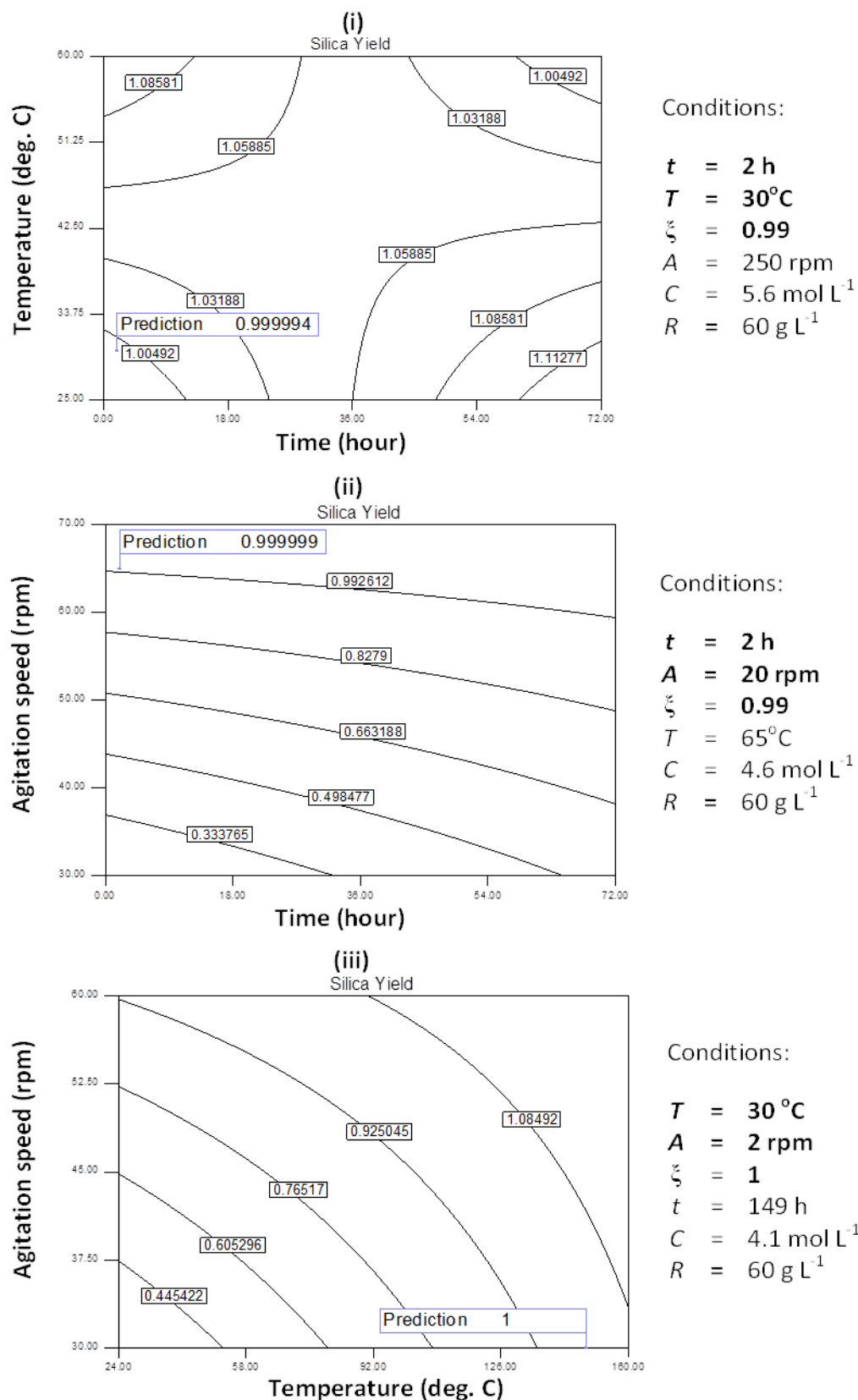


Figure 4.15. Optimization of the processing conditions with minimum (i) t - T , (ii) t - A and (iii) T - A

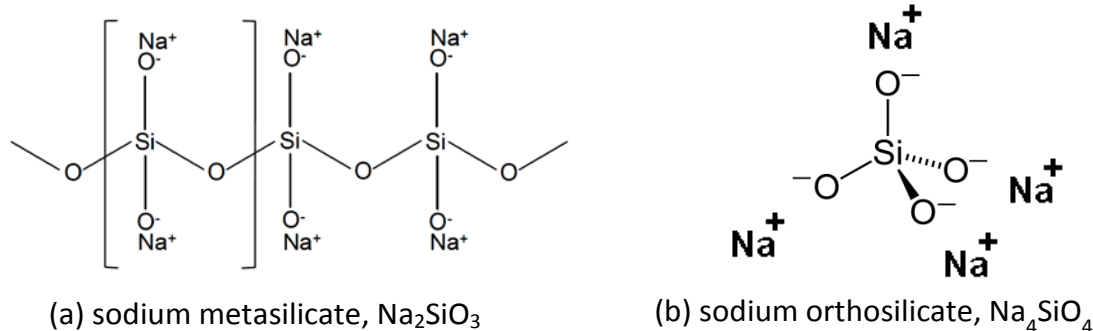
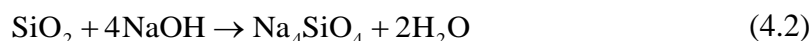


Figure 4.16. Forms of silicates may present in water glass

Since the NaOH concentration was at least 2 mol L^{-1} , it is reasonable to assume that the BLS dissolved into NaOH to form sodium orthosilicate according to the following stoichiometry:



Based on the stoichiometry, the molar ratio of SiO_2 : NaOH must be at least 1:4, i.e., $n_{\text{SiO}_2}/n_{\text{NaOH}} < 1/4$. This requirement implies that for a complete dissolution of bamboo leaf silica in NaOH, the ratio R/C must be < 15 . In this work, the maximum mass-to-volume ratio and the minimum NaOH concentration are 60 g L^{-1} and 2 mol L^{-1} , respectively. Hence, $R/C > 15$ and NaOH became the limiting reactants in these experiments. This result implies that ξ is always less than unity under such conditions, as shown in Figure 4.14h. For example, ξ at 12 g L^{-1} , 2 mol L^{-1} ($R/C = 6$) is 0.95 and decreased to 0.85 when R increased to 60 g L^{-1} ($R/C = 30$). Because the NaOH concentration also increased to 6 mol L^{-1} , $R/C = 10$ and ξ approached unity.

High silica yield was expected for notably low R/C . However, the result is the opposite, where the lowest ξ is produced when the ratio R/C is small. This result implies that some unknown mechanism had suppressed the dissolution of silica when either a high NaOH concentration or low bamboo leaf silica mass is used. It might be

caused by the high concentration of OH^- ions, which led to formation of electric double layers. These double layers prevented the OH^- ions from further reaching the remaining unreacted bamboo leaf silica. Thus, a complete conversion of bamboo leaf silica to water glass does not occur at both notably low and high R/C ratios. In this study, $\xi \rightarrow 1$ in the range of $10 < R/C < 15$. Because of this relationship between the NaOH concentration and the mass-to-volume ratio, their effect can be coupled to provide:

$$\xi = \frac{1}{10000} (90.7 t + 268.7 T + 9.7 RC + 47.9 A - 5186) \quad (4.3)$$

where $10 < R/C < 15$.

4.2.2 Characterizations of water glass

Water glass was synthesized under the optimized condition in [Figure 4.15\(i\)](#), which can be performed at room temperature. Complete conversion of bamboo leaf silica under such condition was confirmed where $\xi = 1$, which produced water glass with a silica concentration of 1 mol L^{-1} (3.5 wt%, 1.12 g cm^{-3}) and $\text{pH} > 14$. To determine the purity of the water glass, the water glass was dried and analyzed using EDX, and the result is shown in [Figure 4.17](#). It was verified that the water glass was pure and contained only sodium silicate. Water glass is usually graded by the molar ratio of $\text{SiO}_2 : \text{Na}_2\text{O}$, which is known as the modulus R . The modulus R of this water glass, which was calculated based on the elemental composition as shown in [Figure 4.17](#) is 0.85, which is lower than the range of 2.1-3.75 of the industrial grade. However, it is not uncommon that water glass that is synthesized from ashes has a low modulus R (Shi et al., 2010). Because a high mass (m_{BS}) to volume (V_{NaOH}) ratio is required to produce water glass with a high modulus R . Thus, the reactant mixture form viscous slurry, and it is difficult to dissolve the silica.

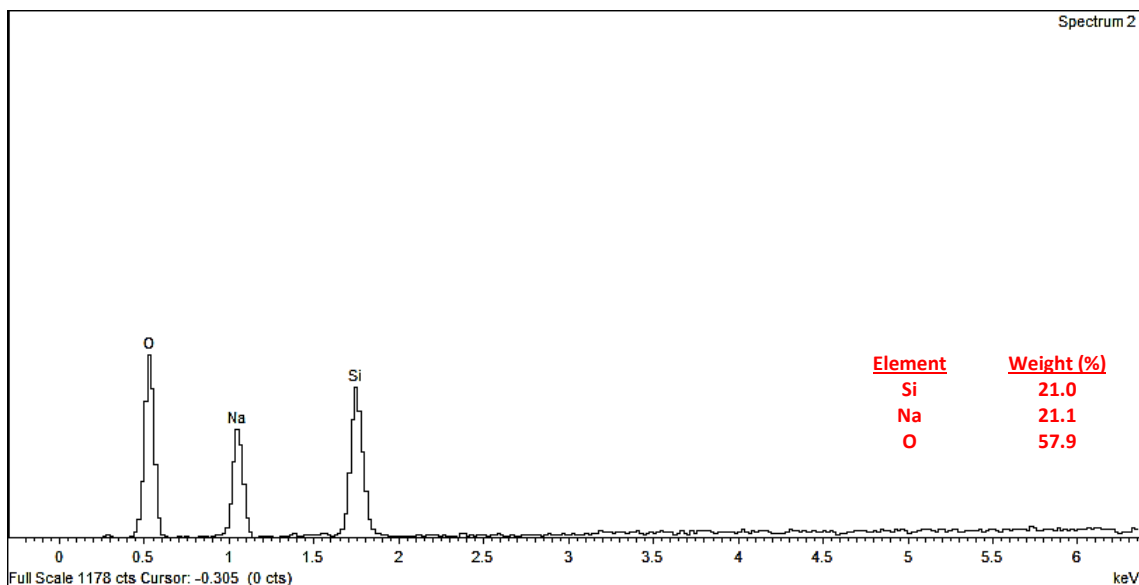


Figure 4.17. EDX spectrum of water glass that synthesized from the bamboo leaf silica

4.2.3 Summary

It is confirmed that water glass with a silica concentration of 1 mol L^{-1} (3.5 wt%, 1.12 g cm^{-3}) and a modulus R of 0.85 can be synthesized from bamboo leaf. In the synthesis process, different parameters including the temperature, the time and the agitation speed had proved to have positive response to increase the silica yield in water glass. It was also discovered that the silica yield depends on the ratio of R/C ; to achieve a high silica yield, this ratio is in the range of $10 < R/C < 15$. The statistical correlation obtained from the result may be used to estimate the silica yield and the silica concentration in water glass and to optimize the necessary condition in the process. The water glass produced based on the optimized conditions in [Figure 4.15 \(i\)](#) was used to synthesize pure silica aerogel in [section 4.3](#).

4.3 Synthesis of silica aerogel

Bamboo leaf water glass was gelled at different pH to synthesize aerogel with ultralow silica concentration. The properties including time of gelation, particle size, density, porosity, shrinkage, fractal dimension, specific surface area, total pore volume, pores size distribution, thermal conductivity and thermal stability of bamboo leaf aerogels were studied. Finally, the most suitable mode of gelation is determined to synthesize aerogel for opacification.

4.3.1 Hydrogels

4.3.1.1 Opacity of hydrogels

Figure 4.18 shows the degree of transparency of hydrogel formed. The corresponding time of gelation is shown in Table 4.7. It is observed that hydrogel TEOS 15 is transparent while BLG 3.5B is almost opaque white. Others are translucent where TEOS 3.5 is purplish and both BLG 3.5N and BLG 3.5E are slightly yellowish.

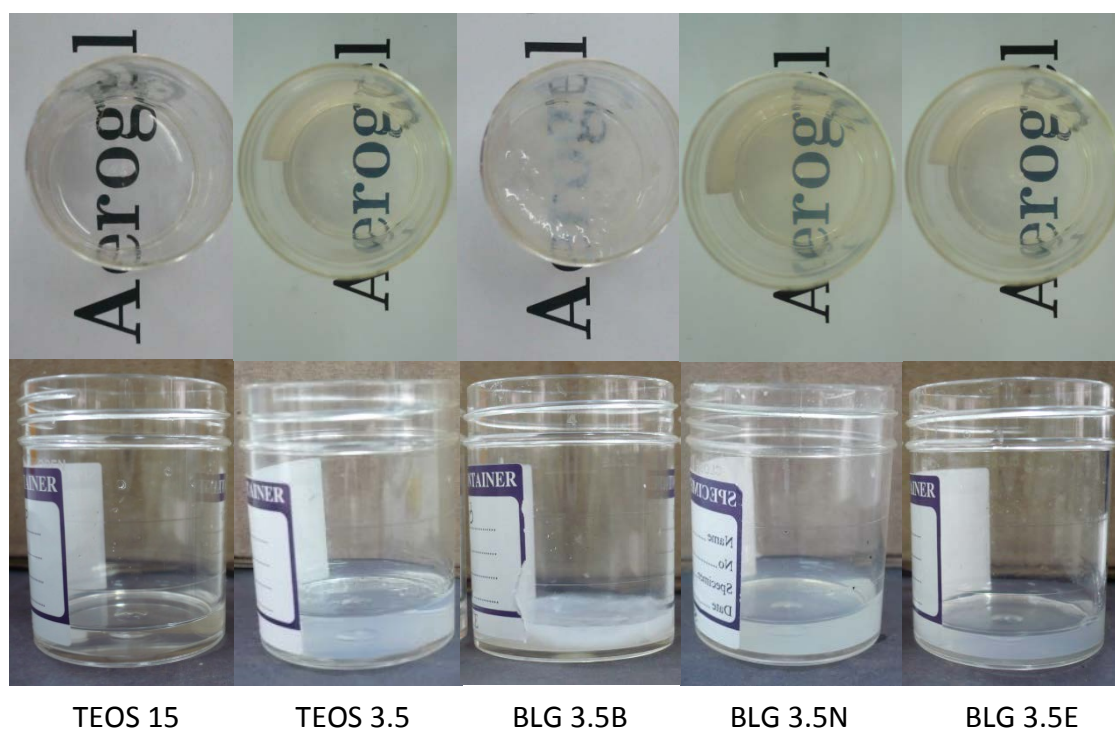


Figure 4.18. Colour of hydrogel formed. Top view (*up*) and side view (*down*)

Opacity of samples are increasing following the order of TEOS 15 < BLG 3.5E < TEOS 3.5 < BLG 3.5N < BLG 2.5B. All hydrogel, except BLG 3.5B, has exhibits “spongy elastic feel” when they were pressed by finger. In addition, when containers of these hydrogels were knocked on one side, vibration in the container can be felt. Conversely, BLG 3.5B is soft and exhibits permanent deformation when it was pressed. No vibration is felt when its container was knocked on one side. Based on [Table 4.7](#), gelation occurred fast when pH is adjusted to >7, which can be seen in samples TEOS 15, TEOS 3.5, BLG 3.5N and BLG 3.5B. Under acidic pH, as in the case of BLG 3.5E, it took approximately 18 hours to form hydrogel.

Table 4.7
Time of gelation

Sample	TEOS 15	TEOS 3.5	BLG 3.5B	BLG 3.5N	BLG 3.5E
Gelation time	< 10 s	4.5 min	< 10 s	2.5 min	~18 h

Hydrogels had shown different degrees of opacity to visible light. These differences can be attributed to the various sizes and orientation of scatterer in hydrogels. It is known that the domain of light scattering is depending on the dimensionless size parameter ($\hat{\alpha}$):

$$\hat{\alpha} = \frac{\pi d_p}{\lambda} \quad (4.4)$$

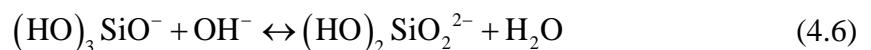
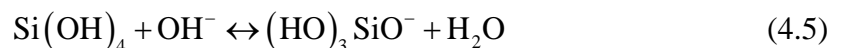
where d_p is the particle diameter and λ is the wavelength of incident light. Using average particle sizes, $\hat{\alpha}$ values were calculated and shown in [Table 4.8](#). All samples has approximately $1 < \hat{\alpha} < 10$. Thus, these scattering is close to Mie scattering, with their scattering intensity is proportional to the square of particle diameter (van de Hulst, 1957) . Since α parameter of BLG 3.5B is large, its scattered intensity becomes at least an order of magnitude larger than other samples. This can be one of the causes of its opaque white appearance. Whereas, the purplish appearance of TEOS 3.5 can be the

Table 4.8 $\hat{\alpha}$ -parameter of samples

Sample	TEOS 15	TEOS 3.5	BLG 3.5B	BLG 3.5N	BLG 3.5E
$\hat{\alpha}$ at average λ	7.7	4.8	10.6	5.5	5.0

result of Rayleigh scattering. As TEOS 3.5 contains 38% of particles with $0.6 \leq d_p \leq 0.8$ nm, which corresponds to $0.0034 \leq \hat{\alpha} \leq 0.0046$, these particles are sufficiently small to cause Rayleigh scattering. The purplish appearance of TEOS 3.5 is a consequence of the well-known $1/\lambda^4$ intensity dependence of Rayleigh scattering, where it scattered more short λ light in violet region. Since other samples do not have large percentage of small particles as in the case of TEOS 3.5, Rayleigh scattering in these samples is not obvious.

The opacity of hydrogels also reflects the orientation of particles. If particles' orientation in hydrogel is highly anisotropic and inhomogeneous, refractive index of particles can be greatly varied over short distance. The fluctuations of refractive index can lead to diffuse refraction that gives hydrogels translucent appearance. This suggests that particles orientation in opaque sample (i.e. BLG 3.5B) is less isotropic than translucent samples (i.e. TEOS 3.5, BLG 3.5N and BLG 3.5E). Whereas, the particles' orientation in translucent samples is also less isotropic than the transparent sample (i.e. TEOS 15). This anisotropy can be caused by the difference in mechanisms of gelation occurred in different pH. It is known that in basic condition, monomers $\text{Si}(\text{OH})_4$ are partially ionized and in equilibrium with themselves in silica sol (Iler, 1979):



In addition, other polymeric ionic species including HSiO_3^- and $\text{Si}(\text{OH})_5^-$ also can present in the sol solution (Iler, 1979). When pH of sol decreased (pH ~ 9), some of these ionic species condensed to form siloxane bond. However, due to ionic repulsion, only part of these ionic sites can turn into siloxane bond. As a result, the local number of bridging oxygen between silicon atoms (Q^n , $0 \leq n \leq 4$) can varied greatly across the gel. This agreed with NMR study reported (Li et al., 2013), where the percentage of Q^n in gel formed in base (pH 9.9) shown the order of $Q^3 > Q^4 > Q^2$ (51:31:18 %). The NMR results also shown that gel formed at pH 3 has $Q^4 > Q^3 > Q^2$ (57:37:6 %), i.e. Q^2 and Q^3 present in gels formed at pH 9.9 has greatly outnumber those formed at pH 3. The distribution of $Q^2 - Q^4$ becomes less narrow in gel formed in basic condition. This causes significant fluctuations in density and refractive index in the gel, inducing severe diffuse refraction which makes gel opaque.

Conversely, under acidic condition, $\text{Si}(\text{OH})_4$ monomers condensed slowly in quasi-equilibrium manner. Siloxane bonds formed are more isotropic (higher fraction of Q^4). Therefore, refraction index is relatively constant across the hydrogel, which making them transparent or translucent. BLG 3.5E gelled very slowly (Table 4.7) in acidic pH, the non-uniformity in the gel is low and therefore more transparent than others. TEOS 3.5 and BLG 3.5N that gelled at pH 7 are less transparent than BLG 3.5E because gelation occurred fast in neutral pH, and induced certain degree of non-uniformity in the density of gel. However, this is different when the concentration of silica is high in TEOS 15. As silica concentration increased, monomers of silicic acid are sufficiently close to each other and tend to condense all the four silanol groups at high rate. Hence, most silicon has Q^4 and refractive index is constant. This makes TEOS 15 transparent.

The distribution of Q^n in various samples is also supported by the elastic behavior of hydrogel. For instance, BLG 3.5B has less Q^4 bonding and this increased probability of forming cyclic silica species. Particles of these cyclic species are more likely to agglomerate and not bonded together. When stresses applied, agglomerates slipped and deformed permanently. For other samples that contain more Q^4 bonding, particles are more likely bonded with each other. This bond gives rise to the elastic behavior of hydrogels formed. Furthermore, the vibration felt in hydrogels can be interpreted as transfer of wave through these continuous bonds within the gel. BLG 3.5B without such continual linkage hence does not exhibit vibration.

4.3.1.2 Particle sizes of hydrosols

Figure 4.19 shows the average particle sizes of hydrosols in various pH. The smallest particle size is observed at pH 4.5. Generally, particle sizes increased as pH increased from 4.5 to 9.5. The particle sizes of bamboo leaf water glass are larger than TEOS, except at pH 4.5. Comparing TEOS 15 with TEOS 3.5 that gelled at pH 7, TEOS 15 with higher silica concentration has larger particle size.

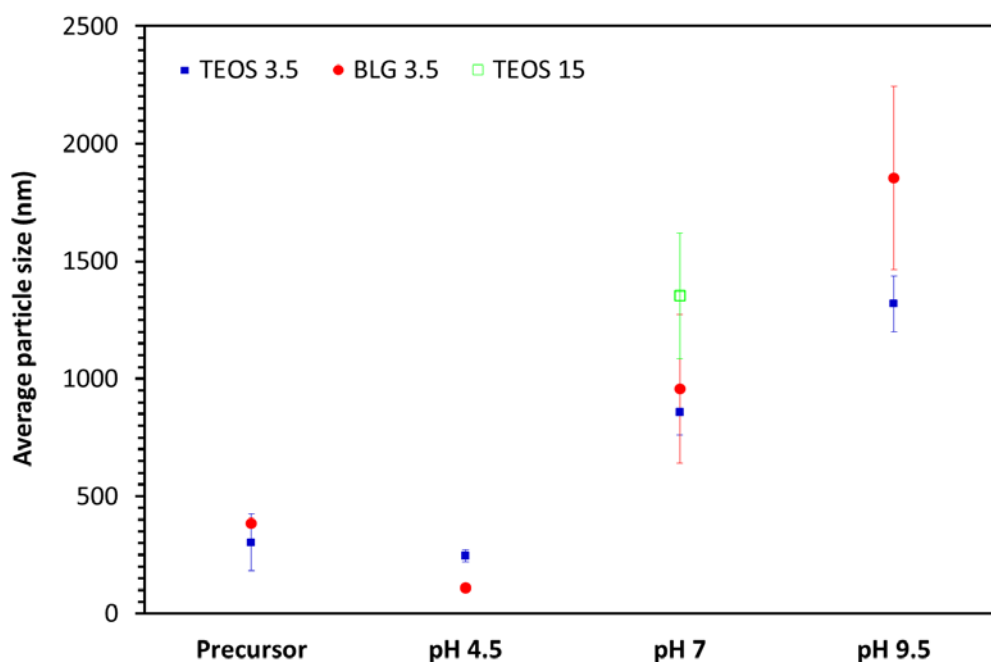


Figure 4.19. Average particle sizes of hydrosols

Similarly, gelation mechanisms had also affected the particle size of hydrosol. In basic condition, due to ionic repulsion, silicon atoms are mainly condensed through Q^2 and Q^3 (Li et al., 2013). As a result, these condensed species are not in compact dense state. Dimers, linear trimers and branched tetramers are dominant species (Brinker and Scherer, 1990) in the context.

According to Brinker and Scherer (Brinker and Scherer, 1990), though dimerization rate is low, once dimers formed they quickly condensed with less compact species to form larger clusters. In addition, the *Diffusion-Limited-Clusters-Aggregation* (DLCA) model (Witten and Sander, 1981) suggests that monomers condensed preferentially with larger clusters. Hence, these clusters grow rapidly to form large but less compact particles. This explained the large particle size and low elastic behavior of BLG 3.5B which gelled at pH 9.5. It is therefore expected that density of BLG 3.5B aerogel is lower than other samples as the result of this less compact cluster condensation. Conversely, in acidic condition, monomers experienced less ionic repulsion and more silicon atoms can condense through Q^4 . As a result, the condensed species are more compact and has smaller particles size. Thus, based on particle sizes in [Figure 4.19](#), the bulk density of aerogels are expected to increase following the order of $BLG\ 3.5N < TEOS\ 3.5 < BLG\ 3.5E$.

4.3.1.3 Removal of salts from hydrogels

Hydrogels formed were soaked in deionized water to remove salts. [Figure 4.20](#) shows the salts remained in gel against the soaking period. Hydrogel that formed by acidifying water glass with nitric acid contains less salts as compared to hydrochloric acid. However, the salts content in HCl gel is lower than HNO_3 after the soaking period had exceeded 48 hours. Hence, HCl was used throughout this work to synthesize

aerogel. Hydrogels formed were soaked in deionized water for 48 hours before subjected to further processing.

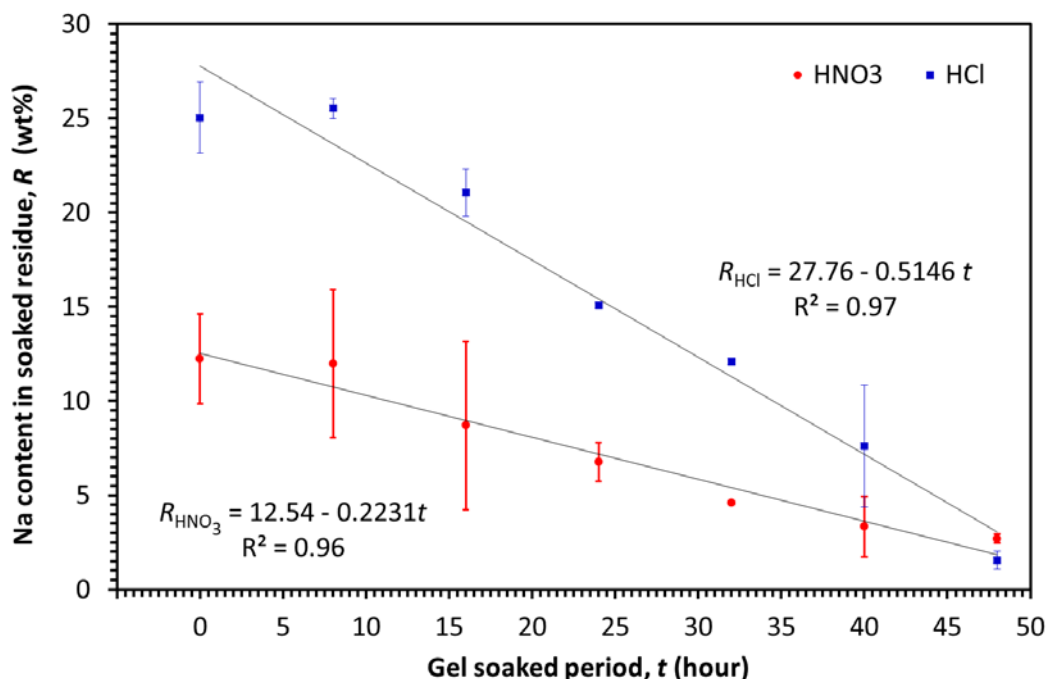


Figure 4.20. Degree of salts removal in hydrogels as a function of soaking period

4.3.2 Aerogels

4.3.2.1 Visual observation

Figure 4.21 shows appearance of silica aerogel synthesized from bio-silica before and after supercritical drying. Aerogels obtained are white in colour with little bluish ray scattered off the surface. This is due to Rayleigh scattering where short wavelength visible light are scattered by nano size particles within aerogel. It seems that aerogels obtained are not transparent. However, it is then discovered that when intense light are directed on aerogels, part of the light transmitted through the aerogel giving off yellowish light on surrounding objects. This is evidenced from **Figure 4.21(c & d)**, where photographs were taken on aerogels with and without camera flash. As light in blue region was scattered more by silica aerogel, light with longer wavelength (next to infrared region) transmitted through the aerogel which produced yellowish image.

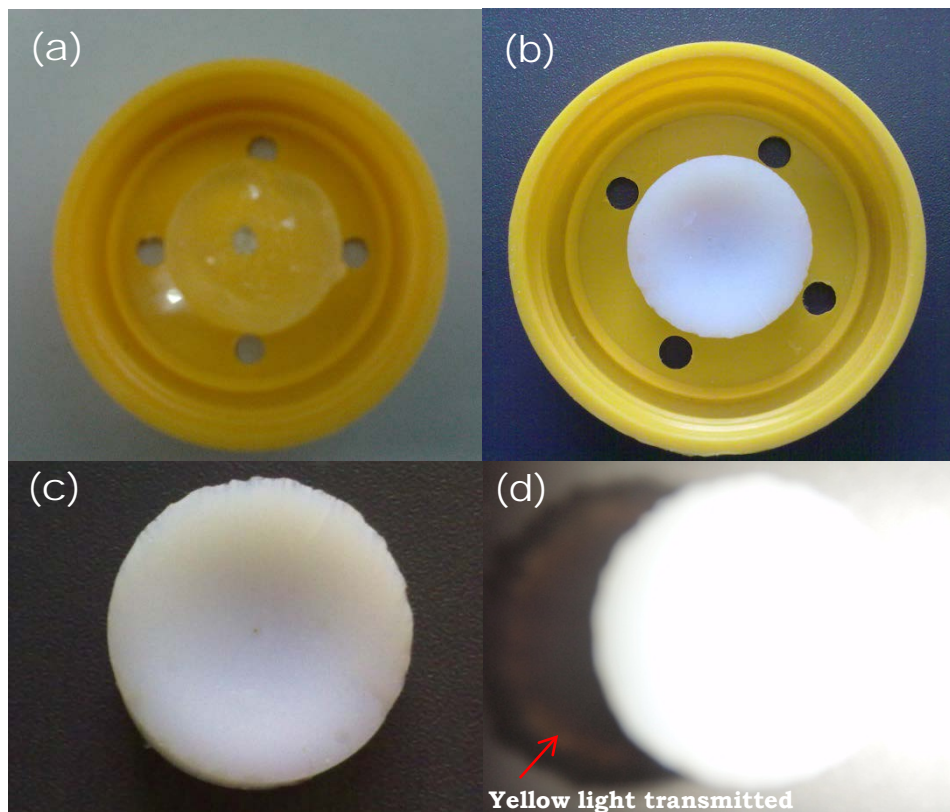


Figure 4.21. Photographs of (a) Hydrogel (before drying), (b) aerogel (after drying), (c) aerogel taken without camera flash and (d) aerogel taken with camera flash

4.3.2.2 Density, porosity, shrinkage and amorphicity

Aerogels obtained were extremely light weight and brittle. [Figure 4.22](#) shows the comparison of bulk density, true density, porosity and shrinkage of aerogels. From [Figure 4.22](#), density, porosity and shrinkage obtained from bamboo leaves and rice husks are all agreed with the aerogel synthesized via conventional route (*refer* [Table 2.2](#)). In order to ensure aerogels are completely dried and no further shrinkage occur after SCF drying, aerogels were all heated to 200 °C for 24 hours. Measurement was repeated to detect any changes in their mass and volume. From these repeated measurements, no changes in those quantities are observed, hence confirming pore liquid were completely removed in SCF process.

The true density of TEOS 15 is 2.01 g.cm⁻³, which agreed with density of amorphous silica reported elsewhere (Pierre and Rigacci, 2011). This is because TEOS

15 was synthesized without silylation. True density for other silylated samples is higher than amorphous silica, i.e. between 2.37 and 3.13 g.cm⁻³. TEOS 15 has the highest bulk density, which is 3.4 to 4.2 times higher than other samples. Excluding TEOS 15, bulk density of other samples is much closer to each other (0.069 g.cm⁻³ ± 9%), with the lowest value of 0.064 g.cm⁻³ (BLG 3.5B). Porosity of these samples is also very close (97.4 ± 0.5%), except for TEOS 15. BLG 3.5B has the highest porosity (98%) while TEOS 15 has the lowest (86.5%). Similarly, BLG 3.5B shows the highest shrinkage (37.3±0.09%) while TEOS 15 shows the lowest (17.1 ± 1.7%).

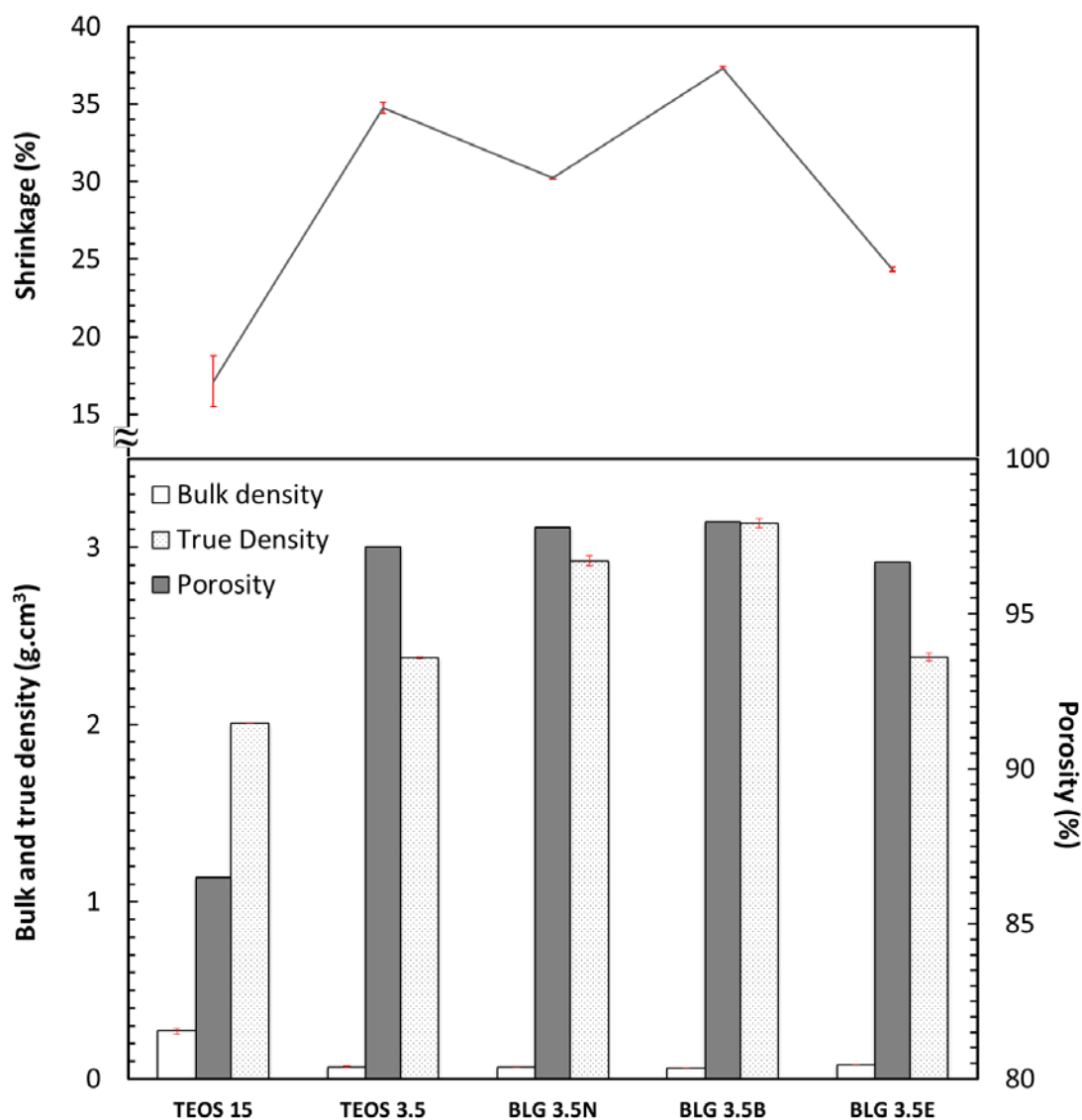


Figure 4.22. Comparison of density, porosity and shrinkage of aerogels

Due to different gelation mechanisms, the bulk density increased in the order of BLG 3.5N < TEOS 3.5 < BLG 3.5E, which agreed with the results of particle sizes. The high density of TEOS 15 is caused by its high silica concentration. Since TEOS 15 has high silica concentration and not silylated, particles condensed are highly compact, which in turn reduced its porosity. However, it experienced least shrinkage because it mainly consists of Q⁴ that can resist large capillary stresses during drying. Conversely, BLG 3.5B experienced the largest shrinkage because its particles are condensed in less compact manner. With majority of Q² and Q³ bonding, pores in BLG 3.5B collapsed easily during drying and thus shrunk severely. Though BLG 3.5B experienced the largest shrinkage, its bulk density is still the lowest among the samples. This is due to hydrogel of various samples have different volumes. For 6 ml of water glass, the volume of BLG 3.5B and BLG 3.5N hydrogels formed is 9 ml and 8.025 ml, respectively. Despite BLG 3.5B experienced higher shrinkage, its final volume is still larger than BLG 3.5N after drying, i.e. 5.64 ml and 5.59 ml, respectively. Since both samples used same amount of water glass, the density of BLG 3.5B is therefore lower than BLG 3.5N. Among samples with low silica content (3.5wt%), BLG 3.5E has the lowest shrinkage and largest bulk density. This is due to BLG 3.5E gelled slowly and more Q⁴ bonds are formed to resist drying stresses.

XRD results of aerogels are shown in [Figure 4.23](#). It is observed that all samples exhibit diffuse peak in between $15^\circ \leq 2\theta \leq 30^\circ$ that centered c.a. 23° , which is the unique characteristics of amorphous silica (Hamdan et al., 1997). Except for TEOS 15, a small peak is also observed c.a. $2\theta = 28.5^\circ$ for all other samples. The small peak may be attributed to the existence of silylated methyl groups on the surface of these samples. This is reasonable since the only difference between these samples and TEOS 15 is no silylation was applied for the latter. This is supported by XRD results reported elsewhere, where no such peak is observed on both non-silylated silica gel (Pijarn et al.,

2010, Pouretedal and Kazemi, 2012, Gao et al., 2009, Hsieh et al., 2009) and precipitated silica (Shui et al., 2010, Balamurugan and Saravanan, 2012, Ma et al., 2012). Though Kalapathy, Protor and Shultz (Kalapathy et al., 2002) reported peak observed in the similar synthesis can cause by sodium chloride, but the peak is at $2\theta > 30^\circ$ and thus not the one observed in Figure 4.23. In addition, TEOS 15 was also synthesized by acidification of HCl. If the peak at $2\theta \approx 28.5^\circ$ is caused by salts then the same peak should also be observed in TEOS 15. Hence, it is concluded that the small peak is not caused by NaCl.

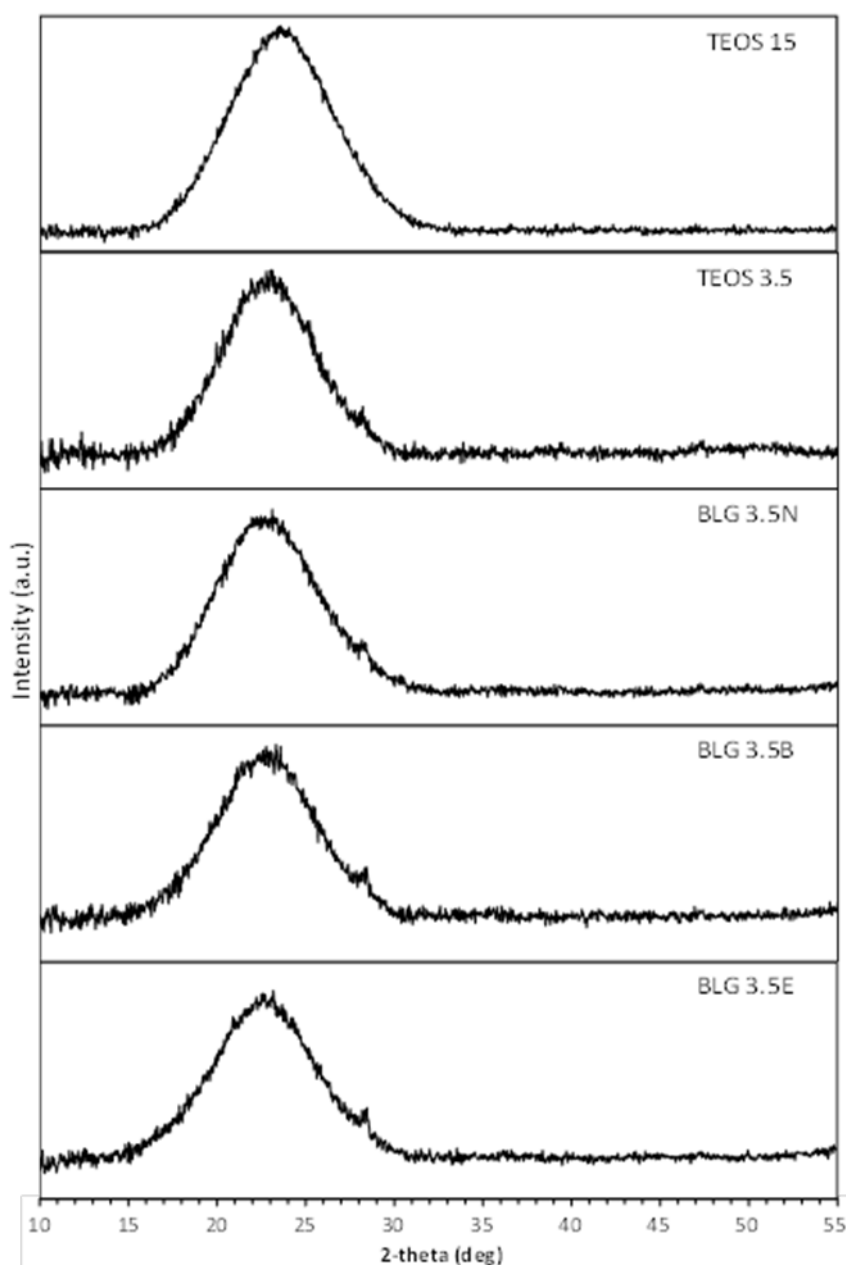


Figure 4.23. XRD diffractograms of aerogels

4.3.2.3 Microstructure and fractal dimensions

SAXS results of aerogels are shown in Figure 4.24. The scattering plot is divided into three regimes. In each of these regimes, the scattering intensity is expected

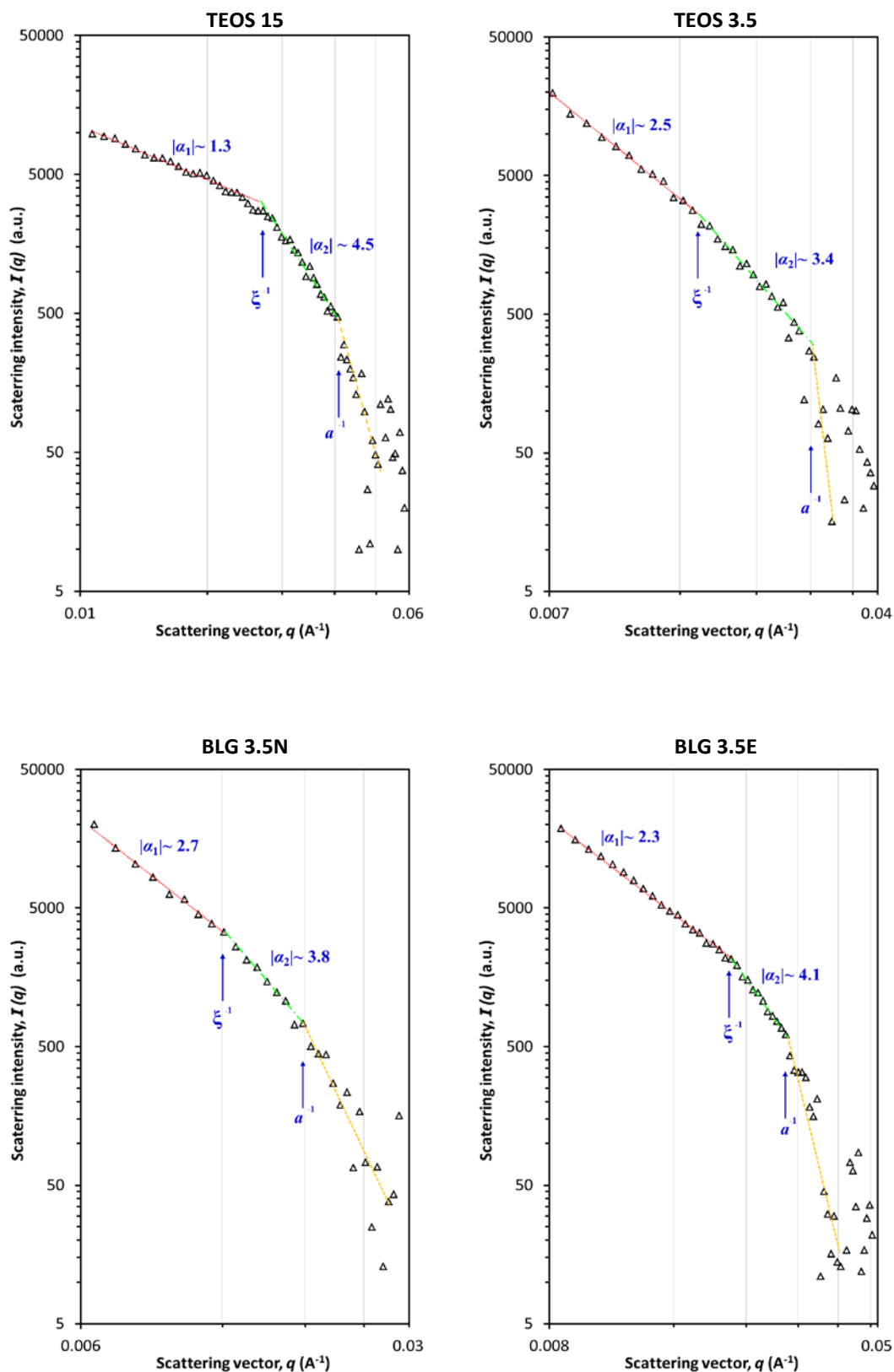


Figure 4.24. SAXS scattering plot of aerogels

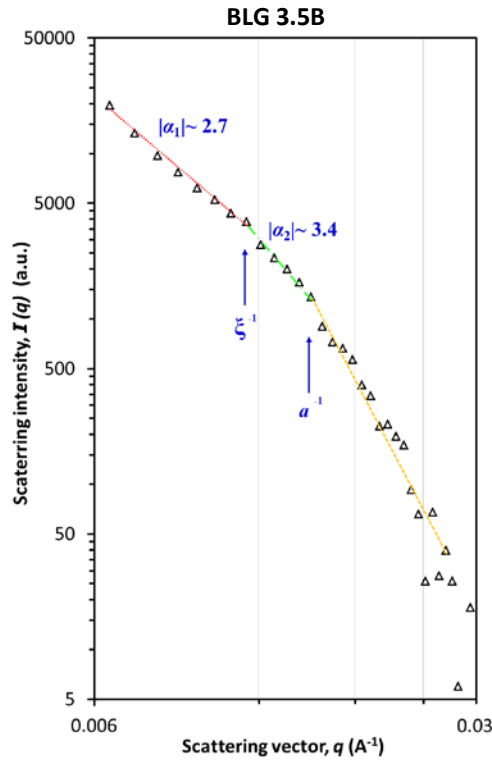


Figure 4.24. (continue) SAXS scattering plot of aerogels

to obey the power law in the form of $I(q) \sim q^{-\alpha}$. The corresponding apparent mass fractal dimension ($D_f = |\alpha_1|$), surface fractal dimension ($D_s = 6 - |\alpha_2|$), characteristic length of fractal (ζ), primary particle size (a) and fractality range (ζ/a) was determined based on method reported (Donatti et al., 2001a, Vollet et al., 2006, Borne et al., 1995, Donatti et al., 2001b) and tabulated in [Table 4.9](#). All samples have $2.3 \leq D_f \leq 2.7$ except TEOS 15. TEOS 15 has the lowest value of both D_f and D_s , i.e. 1.3 and 1.5, respectively. TEOS 15 also has both the smallest of a and ζ . The primary particle size and characteristic length of samples ranged from 2.46 to 6.69 nm and 3.91 to 8.79nm, respectively. Among the samples with low concentration of silica, BLG 3.5E has the smallest primary particle size.

The SAXS results show that BLG 3.5B has the largest primary particle size, as suggested previously by its gelation mechanism. The fractal structure of BLG 3.5B only began when its primary particle grown to 6.69 nm, and diminished quickly as it reached

Table 4.9

Fractals structural parameters determined by SAXS

Sample	D_f	D_s	a (nm)	ζ (nm)	ζ/a	S/V (nm ⁻¹)
TEOS 15	1.3	1.5	2.46	3.91	1.59	1.63
TEOS 3.5	2.5	2.6	3.61	6.67	1.85	0.63
BLG 3.5N	2.7	2.2	5.62	8.26	1.47	1.38
BLG 3.5B	2.7	2.6	6.69	8.79	1.31	1.36
BLG 3.5E	2.3	1.9	3.35	4.68	1.40	0.68

8.79 nm. This gives it the smallest fractality range ($\zeta/a=1.31$) among the samples. This may due to its microstructure collapsed severely in drying which is evidenced from its large shrinkage. For BLG 3.5E with $D_s \approx 2$, this indicates its surface is very close to smooth surface. Sample contains high concentration of silica and should produce densely pack structure. Thus, TEOS 15 was expected to have the closest fractal dimension to ordinary solid objects ($D_f = 3$ and $D_s = 2$). However, microstructure of TEOS 15 is highly fractal in mass and also on surface, which deviates most from ordinary solid objects. Albeit its density is high, it still presents high degree of fractality in the range of 2.46 to 3.91 nm. Hence, it shows that dense materials with low porosity does not necessary indicate low degree of fractality in their microstructure.

4.3.2.4 Adsorption properties

Figure 4.25 shows the BET specific surface area of aerogels. TEOS 15 has the largest specific surface area, i.e., $641.7 \pm 1 \text{ m}^2 \text{ g}^{-1}$ and BLG 3.5B has the smallest, i.e., $247.7 \pm 0.5 \text{ m}^2 \text{ g}^{-1}$. This may be the consequence of pore collapse and shrinkage occurred during drying in BLG 3.5B. For samples with low silica concentration, their specific surface area increased in the order of BLG 3.5B < TEOS 3.5 < BLG 3.5N < BLG 3.5E. There is a reflection trend observed in the BET surface area and its nanoparticle size, i.e. higher the BET surface area smaller the nanoparticle size in aerogels. TEOS 15 has the smallest particle size, which is agreed with the SAXS result.

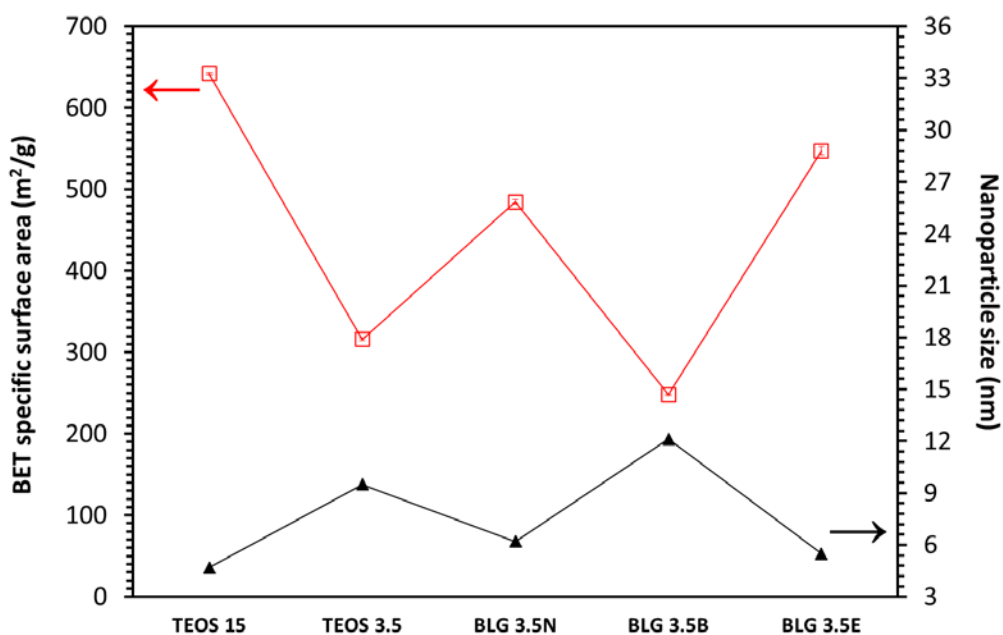


Figure 4.25. BET specific surface area and nanoparticle size of aerogels

The corresponding total pore volume and pore size is shown in [Figure 4.26](#). The total pore volume of aerogels ranged from 0.28 to 2.72 m³ g⁻¹. This is relatively low as compared to result reported elsewhere (Tang and Wang, 2005, Bangi et al., 2010, Bangi et al., 2009, Rao et al., 2007a, Rao et al., 2001). Whereas, the average pore size is closed to other reported values (Sarawade et al., 2012, Sarawade et al., 2011, Li and Wang, 2008, Nayak and Bera, 2009b). BLG 3.5B has both the smallest total pore volume and average pore size, i.e. 0.29 ± 0.08 m³ g⁻¹ and 11.4 ± 1.4 nm, respectively.

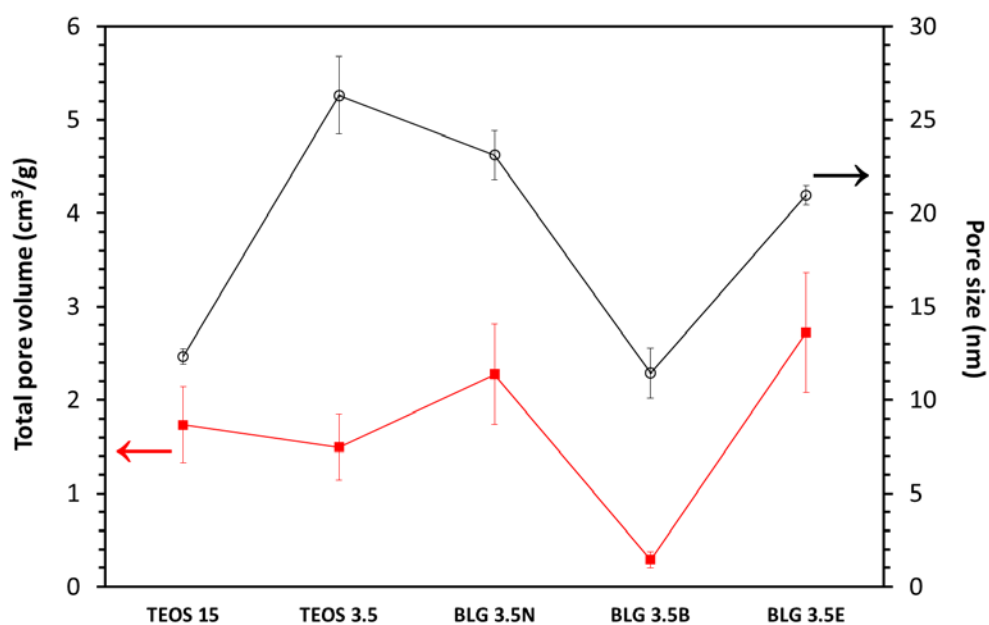


Figure 4.26. Pore volume and average pores size of aerogels

The adsorption-desorption behavior of aerogels is shown in Figure 4.27. All aerogel samples exhibit type IV isotherm. Hysteresis observed in isotherms indicates

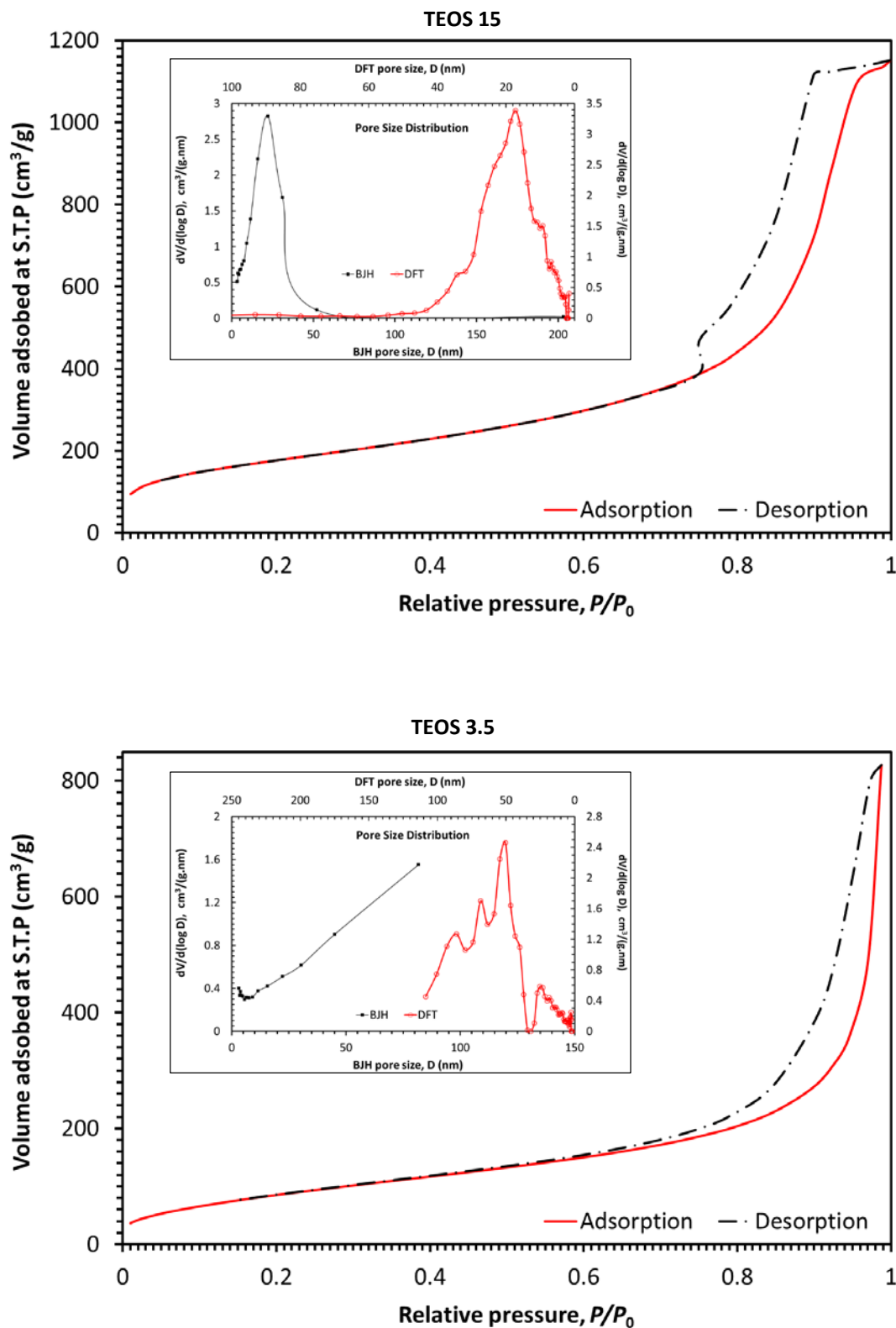


Figure 4.27. Adsorption-Desorption isotherm of aerogels. Insets show the pore size distribution calculated based on BJH (adsorption) and DFT method

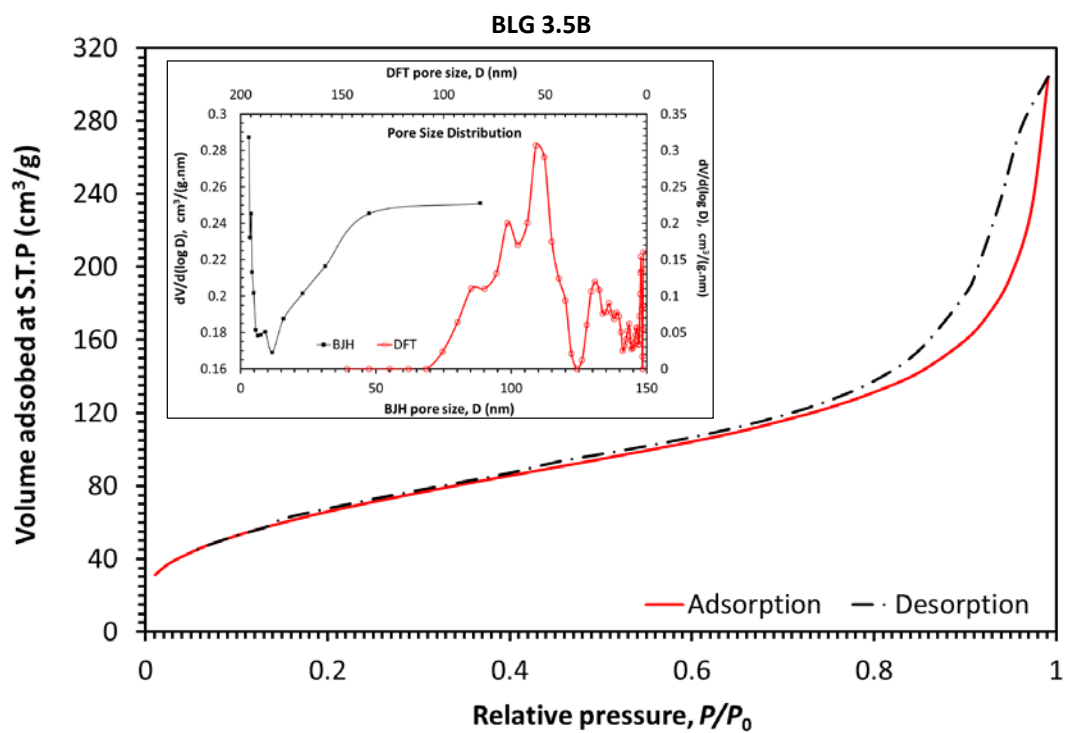
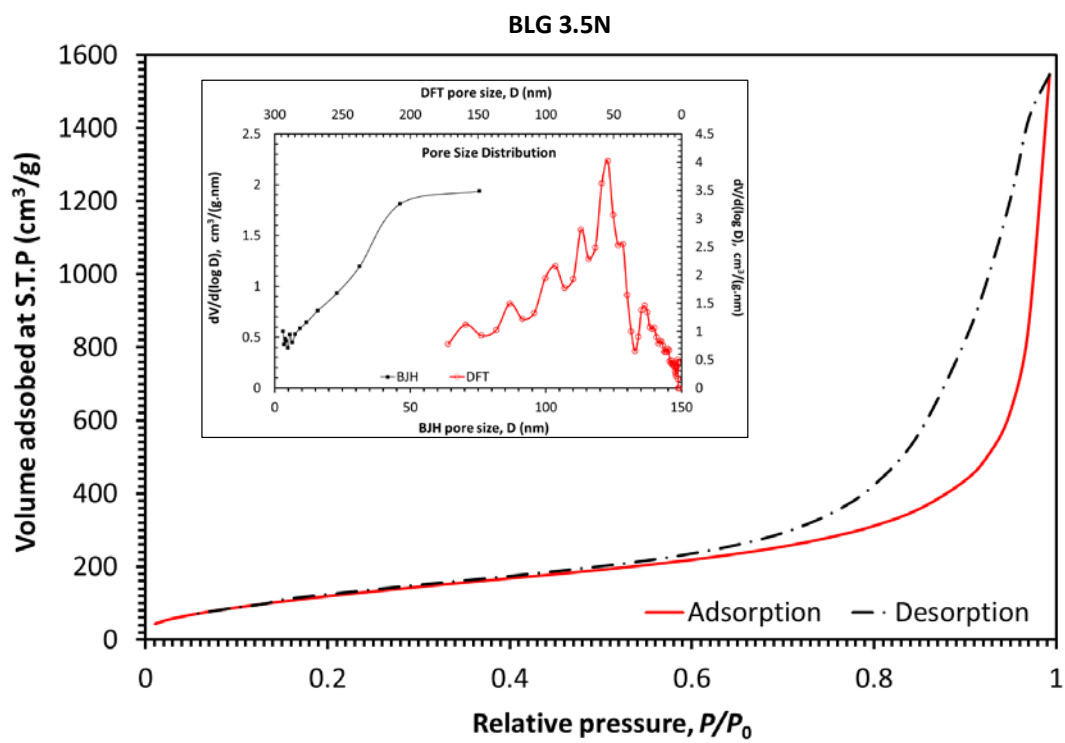


Figure 4.27. (continue) Adsorption-Desorption isotherm of aerogels. Insets show the pore size distribution calculated based on BJH (adsorption) and DFT method

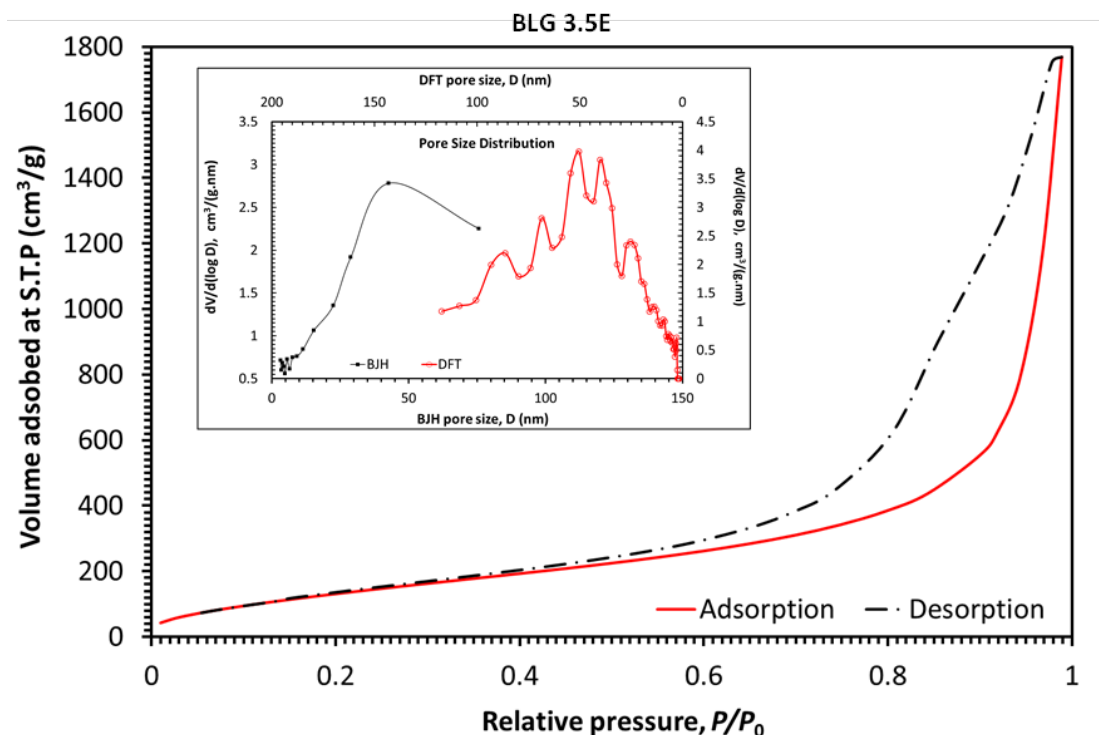


Figure 4.27. (continue) Adsorption-Desorption isotherm of aerogels. Insets show the pore size distribution calculated based on BJH (adsorption) and DFT method

capillary condensation in macropores (> 50 nm) and mesopores (2-50 nm). TEOS 15 again shows very different adsorption-desorption behavior than other samples. Spinodal evaporation is observed at $p/p_0 \approx 0.9$ and hysteresis closure occurred at $p/p_0 \approx 0.75$ in TEOS 15. For other samples, no spinodal evaporation was observed and all exhibit hysteresis closure at $0.4 \leq p/p_0 \leq 0.5$. Except for TEOS 15, isotherm of other samples rises rapidly as $p/p_0 \rightarrow 1$, which indicates the samples contain macropores (Sing et al., 1985). Because the total pore volume does not include macropores, BLG 3.5B has low density even total pore volume is small. It can be deduced that BLG 3.5B contains larger amount of macropores than others. This indirectly supports the idea that BLG 3.5B contains many cyclic species and forming agglomerates. Agglomerates that loosely stacked on each other caused the formation of many macropores. Furthermore, TEOS 15 has similar pore size distribution calculated by both DFT and BJH (adsorption) method. The pore size distribution of TEOS 15 is monodisperse, which mainly consists

of mesopores that centered c.a. 20 nm. For other samples, the pore size distributions calculated by DFT are very different from those calculated via BJH (adsorption) method. The BJH pore size distribution of these samples mainly consists of macropores (> 50 nm). The BJH pore size distribution of BLG 3.5B is also different from others, where it contains large proportion of small pores (< 5nm). Unlike result calculated via BJH method, DFT pore size distribution of samples with low silica concentration show high degree of polydispersity. These samples have the largest proportion of pores in size of \approx 50 nm. They also contain relatively high proportion of pores in size of approximately 25, 80 and 100 nm. Among all samples, only TEOS 15 and BLG 3.5B contains micropores (< 2 nm), i.e. 1.9% and 9.3% respectively. The existence of micropores in TEOS 15 and BLG 3.5B causes their average pore size was only about half of other samples.

The adsorption-desorption isotherms with hysteresis closure at $p/p_0 \approx 0.4$ can be interpreted as the existence of considerable amount of medium and small mesopores in the samples. This explains the very different pore size distribution obtained via BJH and DFT method. As BJH can underestimate size of small to medium mesopores, it failed to detect micropores (Lowell et al., 2004). The difference also indicates the assumption of cylindrical pores in BJH method is inappropriate in this context, except in TEOS 15. The pore size distribution of TEOS 15 estimated by both BJH and DFT methods are similar. This suggests that TEOS 15 has different pore geometry than other samples, i.e. TEOS 15 mainly consists of cylindrical pores. The development of micropores in TEOS 15 and BLG 3.5B may be correlated to their rapid gelation (*refer to Table 4.7*). Hence, it is proposed if particles condensed quickly to induce “instant” rigidity on gel, it can prevent sequential growth on particles and eventually preserve micropores formed in early stage of condensation. On the other hand, if sol particles took longer time to gel (TEOS 3.5, BLG 3.5N and BLG 3.5E), particles are allowed to grow slowly in the proximity of micropores. This may eliminate proportion of

micropores and promote development of larger pores. These micropores may also be converted into close pores.

One would expect the increase in porosity and decrease in bulk density will creates more pores and can cause the specific surface area to also increase. This concept had motivated correlations such as (Wei et al., 2011):

$$S_{\text{correlated}} = \left(\frac{324.3}{\rho_{\text{ae}}} + 5.03 \right) \times 10^5 \quad (4.7)$$

where $S_{\text{correlated}}$ = correlated specific surface area ($\text{m}^2 \cdot \text{g}^{-1}$), and

ρ_{ae} = bulk density ($\text{kg} \cdot \text{m}^{-3}$) of aerogel.

It turned out that TEOS 15 with the lowest porosity and largest bulk density, has the largest specific surface area. In order to illustrate this, specific surface area was calculated based on equations (3.15) and (4.7) and shown in Table 4.10.

Table 4.10
Comparison of specific surface area obtained via various methods

Samples	ρ_{ae} ($\text{g} \cdot \text{cm}^{-3}$)	S_{BET} ($\text{m}^2 \cdot \text{g}^{-1}$)	S_{SAXS} ($\text{m}^2 \cdot \text{g}^{-1}$)	$S_{\text{correlated}}$ ($\text{m}^2 \cdot \text{g}^{-1}$)
TEOS 15	0.271	641.7	810.8	622.7
TEOS 3.5	0.189	315.9	264.8	675.1
BLG 3.5N	0.065	484.7	470.7	1005.8
BLG 3.5B	0.064	247.7	81.3	1011.3
BLG 3.5E	0.079	547.2	571.4	911.9

The comparison shown that $S_{\text{correlated}}$ is quite accurate in describing TEOS 15, i.e. aerogel with high silica content. However, it is not suitable to be used in aerogel with low silica content. This revealed that at low silica concentration, aerogel with high porosity and low density not necessarily gives high specific surface area. The S_{SAXS} value calculated is very close to value measured except for BLG 3.5B. This may due to the S/V ratio of BLG 3.5B is very low. Therefore, it is important to note that the specific surface area is not only varied inversely with ρ_{ae} of aerogel, but also depending on its S/V ratio.

4.3.2.5 Chemical groups on surface

The *FT-IR* spectra of aerogels are shown in Figure 4.28. All spectra show a large peak at 799 and 1059 cm^{-1} , which is corresponding to bending and stretching modes of Si — O — Si groups in silica (Alba et al., 1996, Lenza and Vasconcelos, 2001). The presence of silylated HMDZ on the aerogel's surface can be verified by the peaks at 840 cm^{-1} and 1260 cm^{-1} , which correspond to Si — C bonds. The absorption at 1450 cm^{-1} is related to the C — H bonds that present in the silylated methyl (CH_3 —) groups. As comparison, these silylation-related groups are not observed in the spectrum of TEOS 15. TEOS 15 also shows larger absorption by silanol groups (Si — OH) at 937 cm^{-1} . This is reasonable because the silanol groups on the surface of silylated samples had been substituted by silylated agent and therefore giving smaller absorption peak.

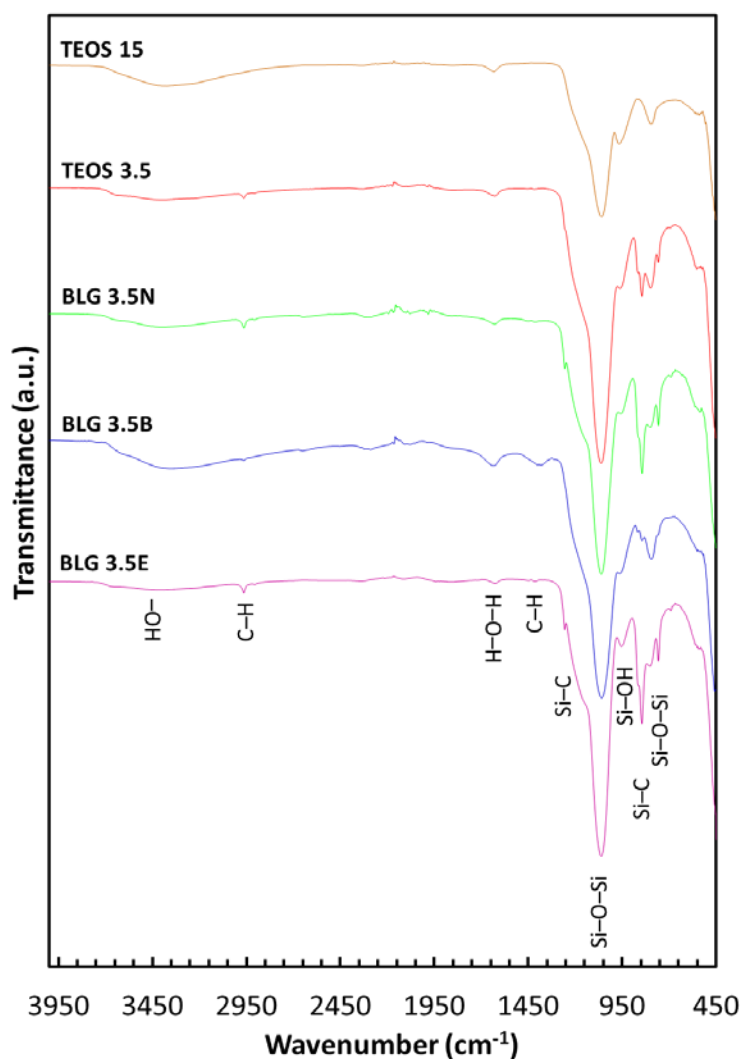


Figure 4.28. *FT-IR* spectra of aerogels

Both TEOS 15 and BLG 3.5B had shown broad peak around 3431 cm^{-1} , which is caused by — OH bond in water molecules and silanol groups. This is common for TEOS 15 as it is not being silylated and thus its surface is covered by silanol groups. The non-silylated TEOS 15 is hygroscopic in nature and tends to absorb water vapor. However, it is uncommon for BLG 3.5B to have such absorption since it is silylated. BLG 3.5B also shows relative large absorption at 1639 cm^{-1} , which is related to bending modes of the water molecules adsorbed. In addition, absorption by Si — C bonds of BLG 3.5B is less intense than other silylated samples, which indicates lower degree of silylation. However, BLG 3.5B is proven hydrophobic as it repelled water. This paradox can be resolved if the outer surface of its agglomerates is covered by silylation agent but the inner surface is not. As the outer surface is silylated, it resists liquid water penetration due to high surface tension of water. On the other hand, the inner surface of agglomerate is not silylated, water vapor with lower surface tension can penetrate into inner surface and adsorbed on it. This is again consistent with the idea that BLG 3.5B is made up of cyclic species which gelled rapidly. The cyclic species causes its inner surface difficult to be silylated by large HMDZ molecules due to steric hindrance. As a result, the degree of silylation on BLG 3.5B is lower than other samples. In contrast, molecules of water vapor are smaller and have low surface tension, which allowed them to penetrate and adsorb onto its inner surface easily.

4.3.2.6 Thermal conductivity

The thermal conductivity of aerogels measured at ambient condition is shown in [Figure 4.29](#). The thermal conductivity measured is generally agreed with range reported elsewhere (Rao et al., 2007a, In-Sub et al., 2008, Zeng et al., 1995a, Zhao et al., 2012). TEOS 15 has the highest conductivity while BLG 3.5E has the lowest. Among samples with low silica concentration, BLG 3.5B has the highest thermal conductivity. For the

three samples that gelled with similar mechanism (TEOS 3.5, BLG 3.5N and BLG 3.5E), their thermal conductivity (indicated by red hollow dots) can be correlated with apparent mass fractal dimension in Figure 4.29. This indirectly indicates that thermal conductivity is related to fractality, in which highly fractal structure can reduce thermal conductivity of aerogels.

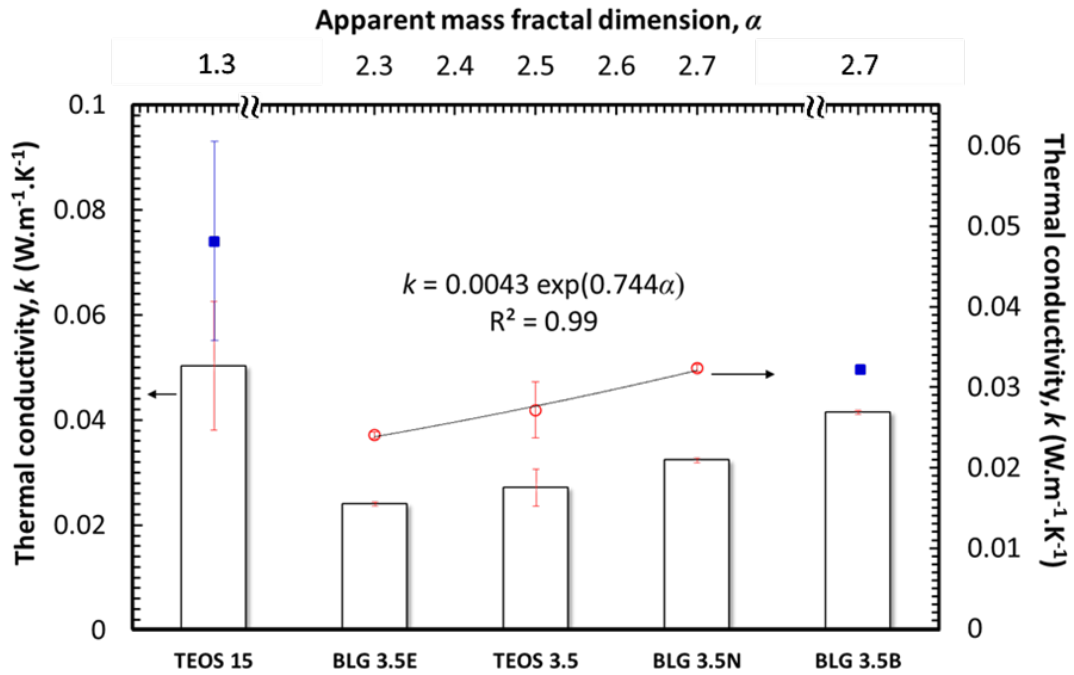


Figure 4.29. Thermal conductivity of aerogels and the correlation with fractal dimension (left axis refers to k value for bar chart, whereas right axis refers to k value for correlation with fractal dimension)

Thermal conductivity obtained in Figure 4.29 was compared with theoretical model. The total thermal conductivity (λ_T) is given as:

$$\lambda_T = \lambda_g + \lambda_r + \lambda_s \quad (4.8)$$

where λ_g , λ_r and λ_s are gaseous, radiative and solid conductivity, respectively.

According to Zeng's model (Zeng et al., 1995b), λ_g can be determined as:

$$\lambda_g = \frac{60.22 \times 10^5 \Pi p T^{-0.5}}{0.25 S_{\text{BET}} \rho_{\text{ac}} \Pi^{-1} + 4.01 \times 10^9 p T^{-1}} \quad (4.9)$$

where p = pressure in bar,

T = temperature in K,

- S_{BET} = BET specific surface area in $\text{m}^2.\text{kg}^{-1}$,
 ρ_{ae} = bulk density of aerogel in $\text{kg}.\text{m}^{-3}$, and
 Π = porosity

Whereas the radiative conductivity can be estimated as (Lu et al., 1995):

$$\lambda_r = \frac{16}{3} \left(\frac{\sigma n^2 T^3}{\rho_{\text{ae}} e} \right) \quad (2.5)$$

- where σ = *Stefan-Boltzmann* constant ($5.67 \times 10^{-8} \text{ W}.\text{m}^{-2}$),
 n = refractive index of aerogel given by Henning and Svensson's correlation (Henning and Svensson, 1981):

$$n = 1 + 0.21 \rho_{\text{ae}} \quad (4.10)$$

- with ρ_{ae} = bulk density of aerogel in $\text{g}.\text{cm}^{-3}$
 e = specific *Rosseland* mean extinction coefficients.

For silica aerogel at ambient condition, it is approximately $37.5 \text{ m}^2.\text{kg}^{-1}$ (Wei et al., 2013). The solid conductivity of skeletal silica in aerogel is determined using density scaling law proposed by Lu *et. al* (Lu et al., 1992):

$$\lambda_s = \tilde{C} \rho_{\text{ae}}^\varphi \quad (2.7)$$

- where φ = scaling exponent (1.5 ± 0.1 for monolithic silica aerogel) and
 \tilde{C} = pre-factor that depends on the interconnectivity of particles in aerogels (Lu et al., 1995). Here, it is first assumed that $\tilde{C} = 1$.

The calculated conductivities are tabulated in [Table 4.11](#).

Table 4.11

Thermal conductivities calculated based on [equations \(4.8 – 4.12\)](#) compared with total conductivity measured in [Figure 4.29](#).

Sample	λ_g	λ_r	λ_s	λ_T	$\lambda_{\text{measured}}$	$\hat{\lambda}_s$
TEOS 15	0.0047	0.0009	0.141	0.1467	0.0503	0.0447
TEOS 3.5	0.0179	0.0034	0.018	0.0389	0.0272	0.0059
BLG 3.5N	0.0159	0.0036	0.016	0.0358	0.0324	0.0129
BLG 3.5B	0.0196	0.0036	0.016	0.0393	0.0415	0.0183
BLG 3.5E	0.0136	0.0029	0.022	0.0388	0.0240	0.0075

All thermal conductivities are in unit $\text{W}.\text{m}^{-1}.\text{K}^{-1}$

It can be seen that the calculated values tend to overestimate the total thermal conductivity. This is due to the pre-factor value $\tilde{C} = 1$ assumed in [equation \(4.11\)](#) may not be realistic. In order to elaborate this, the true solid conductivity $\hat{\lambda}_s$ is calculated by subtracting λ_g and λ_r from $\lambda_{\text{measured}}$:

$$\hat{\lambda}_s = \lambda_{\text{measured}} - \lambda_g - \lambda_r \quad (4.11)$$

Except BLG 3.5B, the $\hat{\lambda}_s$ values obtained ([Table 4.11](#)) are found to correlate well with [equation \(4.11\)](#), where the regressed parameters are $\varphi = 1.46$ and $\tilde{C} = 0.3$. Reversed calculation of [equation \(4.11\)](#) on sample BLG 3.5B gives very different value $\tilde{C} = 1.14$. This indicates interconnectivity of particles in BLG 3.5B is very different from others. This again suggests that gelation mechanism of BLG 3.5B in basic condition has affected the structure and properties of the aerogel formed. The extremely low thermal conductivity of aerogel is commonly attributed to its particles that connected with “torturous” path which ended with many “dead ends”. As mentioned earlier, monomers of BLG 3.5B that gelled in basic pH exhibits ionic repulsion on their surface. The formation of individual, rather spherical particles is probable. These particles are not “torturous linked” as in common aerogel. Without the compact links (Q^4) between particles, these large spherical particles in BLG 3.5B can collapsed easily during drying. As those large particles touched each other, it provides large amount of contact points for heat transfer. This is reflected by its high interconnectivity inferred from its high value of $\tilde{C} = 1.14$. This is also supported by the very low degree of fractality ([Table 4.9](#)) observed in BLG 3.5B.

4.3.2.7 Thermal stability

The thermal stability of aerogels up to 600 °C is shown in Figure 4.30. No peak was observed for TEOS 15 because it is not silylated and contains silica only. Peaks are observed around 495°C in other silylated samples. This is generally agreed with results reported elsewhere (Shewale et al., 2008, Hegde and Rao, 2007, Gurav et al., 2009a) which the peak is attributed to the decomposition of silylated methyl (—CH_3) groups on those samples. No significant change in weight is observed beyond 600 °C.

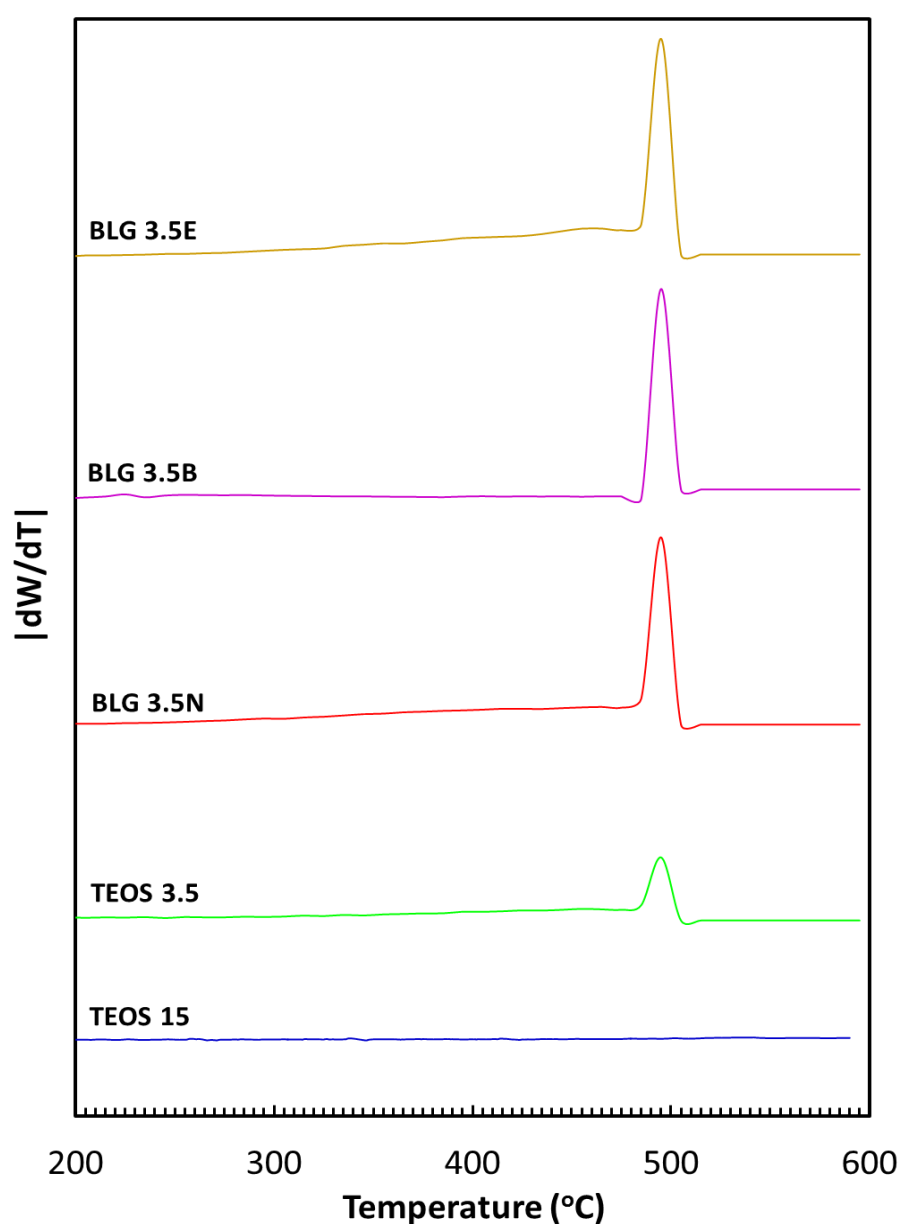


Figure 4.30. Thermal stability of aerogels determined by TGA

4.3.2.8 Summary

Silica aerogel was successfully synthesized using bamboo leaf as silica source. The properties of aerogel obtained are comparable to the aerogel synthesized with TEOS. The pH of gelation is proven to have significant effect on the properties of aerogel formed. Aerogel synthesized in acidic condition exhibits more attractive properties, including low shrinkage (24.3%), large specific surface area ($547.2 \text{ m}^2 \text{ g}^{-1}$), large pore volume ($2.72 \text{ cm}^3 \text{ g}^{-1}$) and low thermal conductivity ($0.024 \text{ W m}^{-1} \text{ K}^{-1}$). Whereas, aerogel synthesized in basic condition has very different properties. It has small pore volume ($0.287 \text{ cm}^3 \text{ g}^{-1}$) and pore size (11.44 nm), large primary particles (6.69 nm), small specific surface area ($247.7 \text{ m}^2 \text{ g}^{-1}$), low degree of fractality (6.69), strong absorption of water, and high thermal conductivity ($0.0415 \text{ W m}^{-1} \text{ K}^{-1}$). The properties of aerogel synthesized at neutral pH are very similar with those gelled in acidic condition. However, its gelation period (2.5 min) is much shorter than gel formed at acidic pH (18 h). Due to this reason, water glass was gelled at neutral pH in [section 5.2](#) for the opacification purpose.

RESULTS AND DISCUSSION

CHAPTER 5 OPACIFICATION OF BAMBOO LEAF AEROGEL

Results related to extraction of silica and synthesis of bamboo leaf aerogel obtained in [Chapter 4](#) is carried to this chapter for opacification purpose. In this section, the characteristics of opacified aerogel and the corresponding optimizations will be discussed.

5.1 Synthesis and characterizations of activated carbon

Activated carbon was produced from bamboo leaves. Effects of carbonization time and temperature on the amount of bio-char produced were studied and an empirical model was developed for these parameters. The activation temperature and activation time were optimized to minimize the burnt off and density of activated carbon synthesized. Properties of activated carbon synthesized at optimized conditions were investigated to confirm its suitability be used as opacifier in bamboo leaf aerogel.

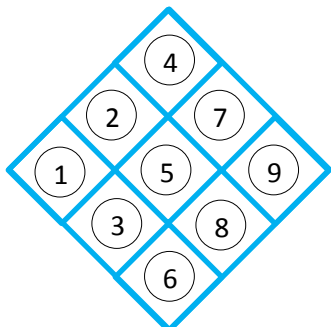
5.1.1 Carbonization

Bamboo leaves were carbonized at various temperatures and time to retain the maximum amount of bio-char. Based on the empirical formula of the organic matter in bamboo leaf estimated in [Table 4.5](#), the organic matter contain 40.6 wt% of carbon. Because the bamboo leaf contains 20.3 wt% of silica (*refer* to [Table 4.3](#)) and the remaining 79.7 wt% are organic matters. It means 40.6 wt% in the 79.7 wt% is carbon, i.e. raw bamboo leaf contains 32.4 wt% of carbon. This value agreed with the carbon percentage obtained in EDX, i.e. 33.9 ± 0.9 wt%. Hence, carbonization should be carried out where at weight loss of bamboo leaf is at least $100 - (20.3 + 32.4) = 47.3$ wt%. This is to ensure that the bio-char produced contains silica and carbon only. From the TGA result ([Figure 4.2a](#)), the time needed to achieve such weight loss at a heating rate of $10 \text{ }^\circ\text{C min}^{-1}$ is approximately 35 minutes. Thus, the range of 25 min – 45 min of

carbonization time is chosen to minimize the carbon loss. For activation temperature, range of 300°C – 450°C is selected because the decomposition of bamboo leaf occurred around 350°C, as shown in Figure 4.10 (a). By using a central composite design (CCD), Figure 5.1 shows bamboo leaves carbonized in various temperatures and times. It is observed that samples obtained above the center point temperature (375 °C) and time (35 min) yield grey samples, indicating high carbon loss. The grey colour of sample is caused by ash residue that mainly contained white silica.



Sample's position and condition:



Sample	1	2	3	4	5	6	7	8	9
Time (min)	21	25	25	35	35	35	45	45	49
Temperature (°C)	375	450	300	481	375	267	450	300	375

Figure 5.1 Photographs of bamboo leaves carbonized at various temperatures and time

This is more obvious in Figure 5.2, where bio-char remained in pieces when carbonized at 300 °C but became powder when carbonized at 450 °C. Based on CCD, the bio-char produced is correlated with carbonization time and temperature as second order empirical model below:

$$\text{Bio-char produced (\%)} = \beta_0 + \beta_1 T^2 + \beta_2 t^2 + \beta_3 Tt + \beta_4 T + \beta_5 t \quad (5.1)$$

where

T = carbonization temperature (°C)

t = carbonization time (minute)

β_n = coefficients of correlation

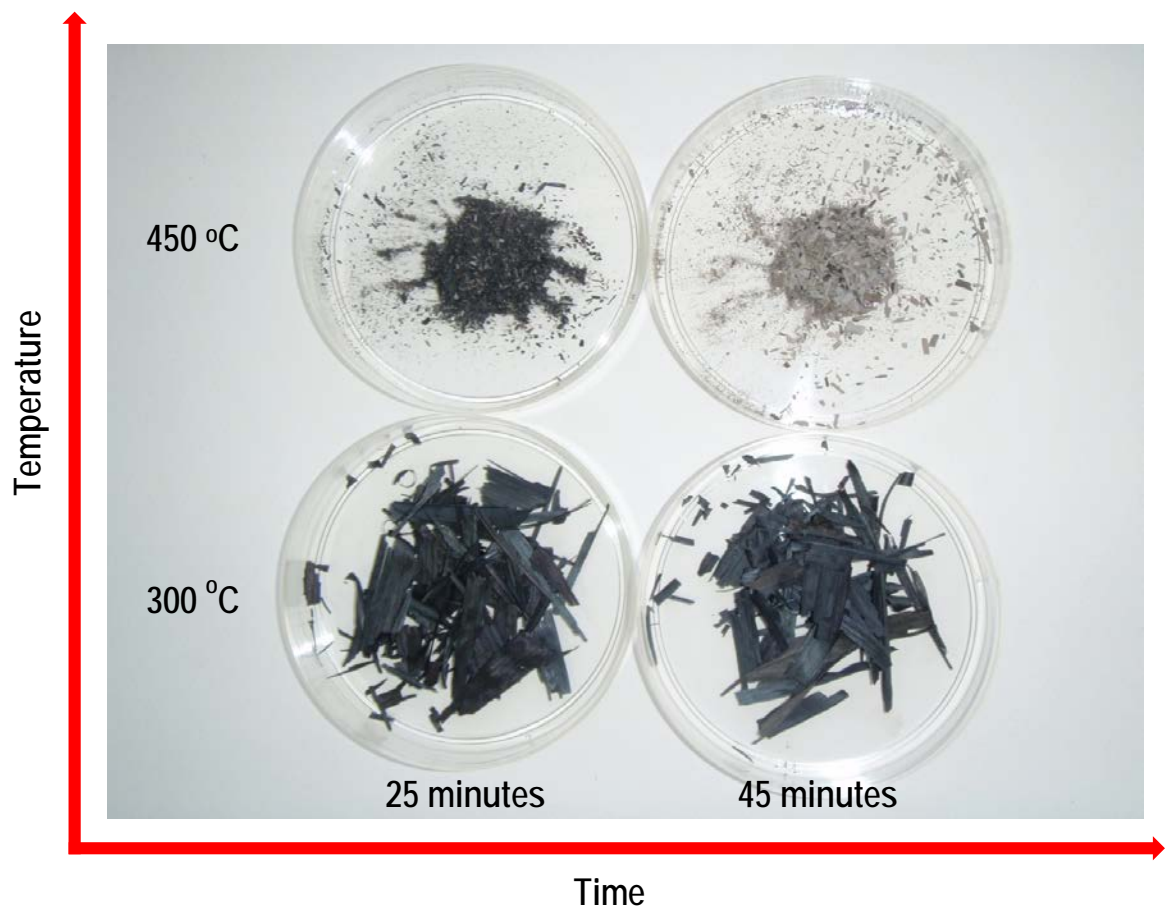


Figure 5.2 Photograph (*close up view*) of bamboo leaves carbonized at axial points of CCD

Table 5.1 shows the ANOVA (95% level of confidence) results of model in equation (5.1). It shows that the interaction term in this case is not significant. A response surface is plotted based on the model in Figure 5.3. It can be observed that bio-char produced decreased at high temperature and long carbonization time. This is reasonable because high temperature can increase the rate of reaction and more carbon can escape into gas phase in prolong heating. The response surface is quite linear with the larger response to the carbonization temperature than the carbonization time. As the most intense decomposition of bamboo leaf occurred after 350 °C, the temperature was chosen to maximize the bio-char produced. Simultaneously, the carbonization time is minimized to 25 min as to reduce the energy input in the process. Combination of these optimum conditions gave a maximum bio-char of 41.8 wt%. The value obtained is 11 wt% less than the sum of carbon and silica in bamboo leaf. This is common since not all the carbon can be retained in the bio-char. Some of the carbon had formed gaseous compounds such as carbon dioxide and carbon monoxide during the decomposition.

Table 5.1
Summary of ANOVA on carbonization of bamboo leaf based on coded parameters

Terms	Parameter	<i>p</i> -value	Coefficients (Coded)	Coefficients (Actual)
Second order	T ²	<0.0001	2.93	5.21 × 10 ⁻⁴
Second order	t ²	<0.0001	3.31	3.31 × 10 ⁻²
Interaction	T t	0.46	0.37	4.87 × 10 ⁻⁴
First order	T	<0.0001	- 14.38	- 0.59
First order	t	<0.0001	- 3.38	- 2.84
Mean	β ₀	<0.0001	29.84	233.8
Adjusted R² of model				0.98

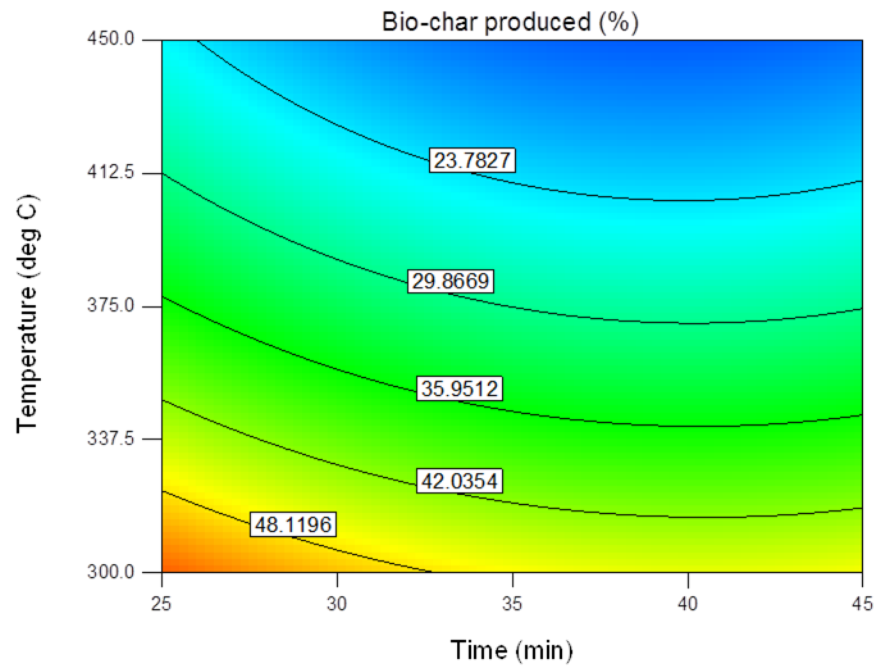
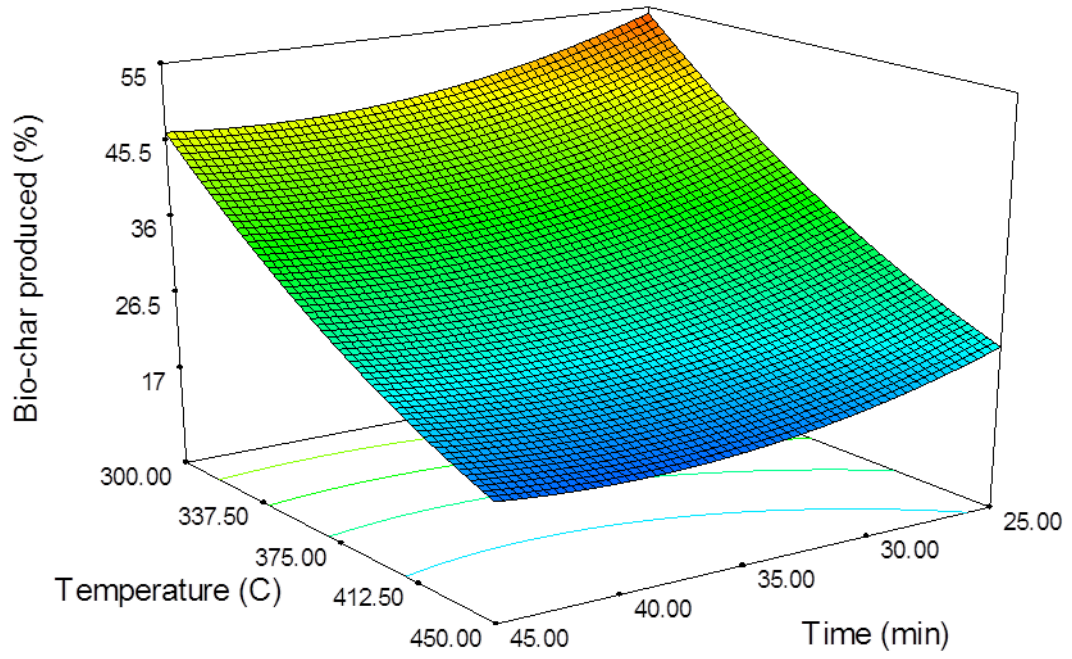


Figure 5.3 Response surface of experimental region and the corresponding contour plot for the carbonization of bamboo leaf

Similar approach was applied to the activation process, where the activation temperature and time were optimized to minimize the carbon burnt off and density of activated carbon produced. Regressions on the carbon burnt off and density are

tabulated in Table 5.2 and Table 5.3, respectively. The corresponding response surfaces are illustrated in Figure 5.4 and Figure 5.5.

Table 5.2
Effect of activation temperature and time to the carbon burnt-off

Terms	Parameter	<i>p</i> -value	Coefficients (Coded)	Coefficients (Actual)
Second order	T ²	0.08	0.84	3.37×10^{-4}
Second order	t ²	0.48	-0.32	-3.51×10^{-4}
Interaction	T t	0.45	0.29	1.93×10^{-4}
First order	T	0.0062	0.87	-0.33
First order	t	<0.0001	1.61	-9.11×10^{-4}
Mean	β_0	<0.0003	82.31	159.2
Adjusted R² of model				0.83

Table 5.3
Effect of activation temperature and time to the density of activated carbon

Terms	Parameter	<i>p</i> -value	Coefficients (Coded)	Coefficients (Actual)
Second order	T ²	<0.0039	0.024	9.61×10^{-6}
Second order	t ²	<0.041	0.015	1.72×10^{-5}
Interaction	T t	0.06	0.012	7.96×10^{-6}
First order	T	<0.0001	-0.031	-0.011
First order	t	0.0019	-0.016	-6.57×10^{-3}
Mean	β_0	<0.0001	0.53	3.57
Adjusted R² of model				0.88

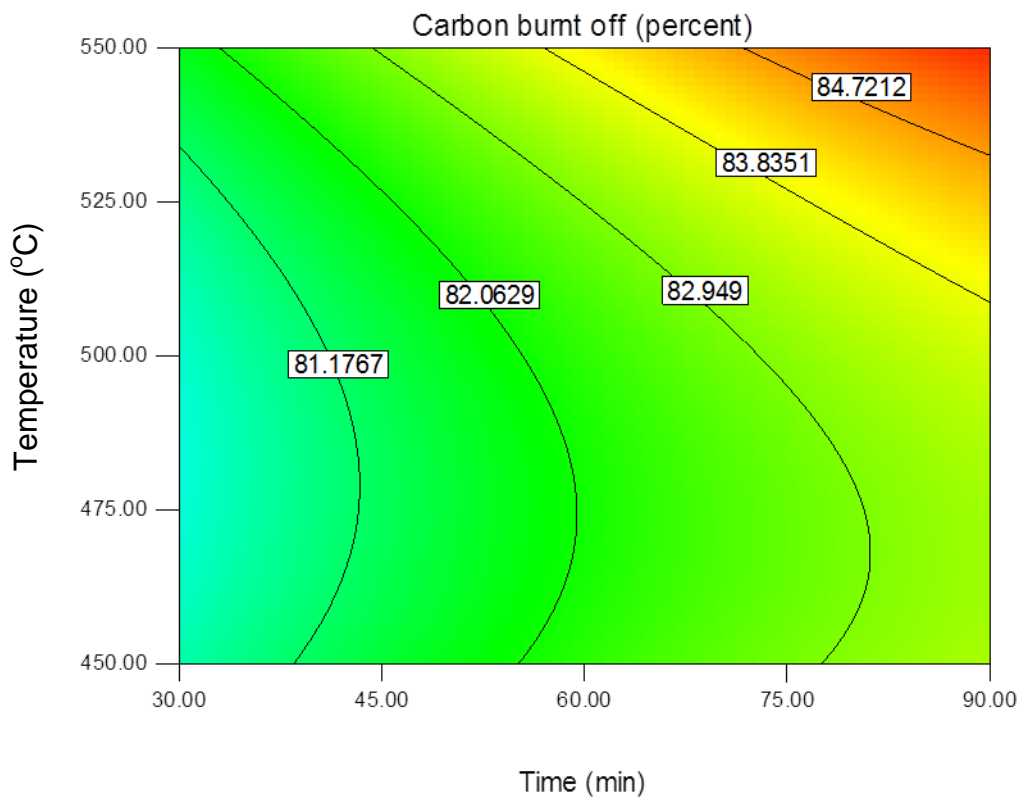
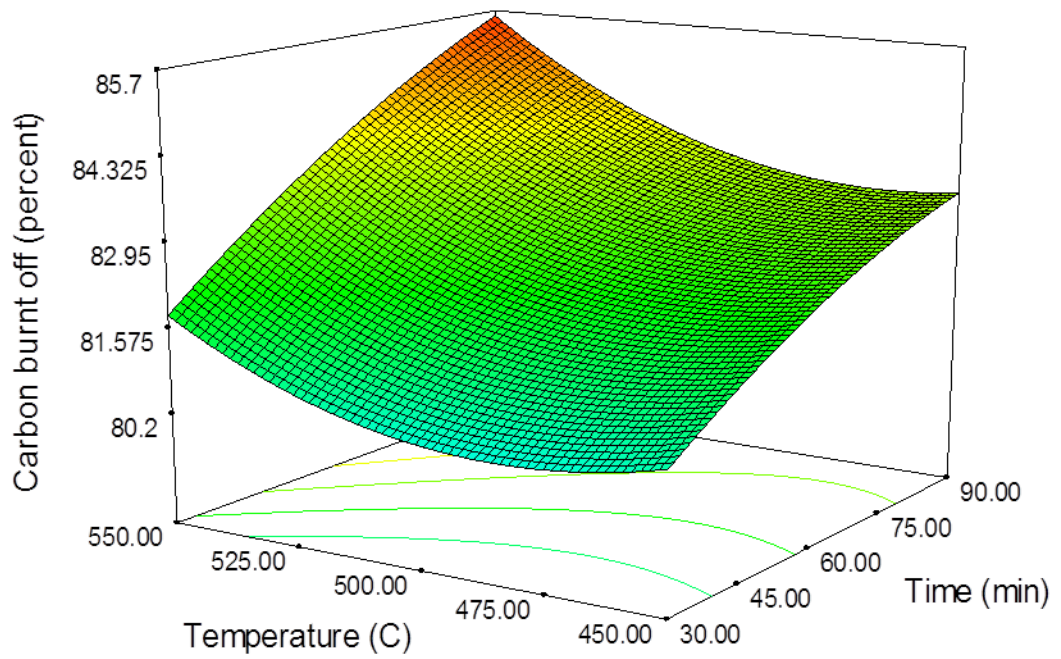


Figure 5.4 Response surface of carbon burnt off and the corresponding contour plot for the activation of bio-char

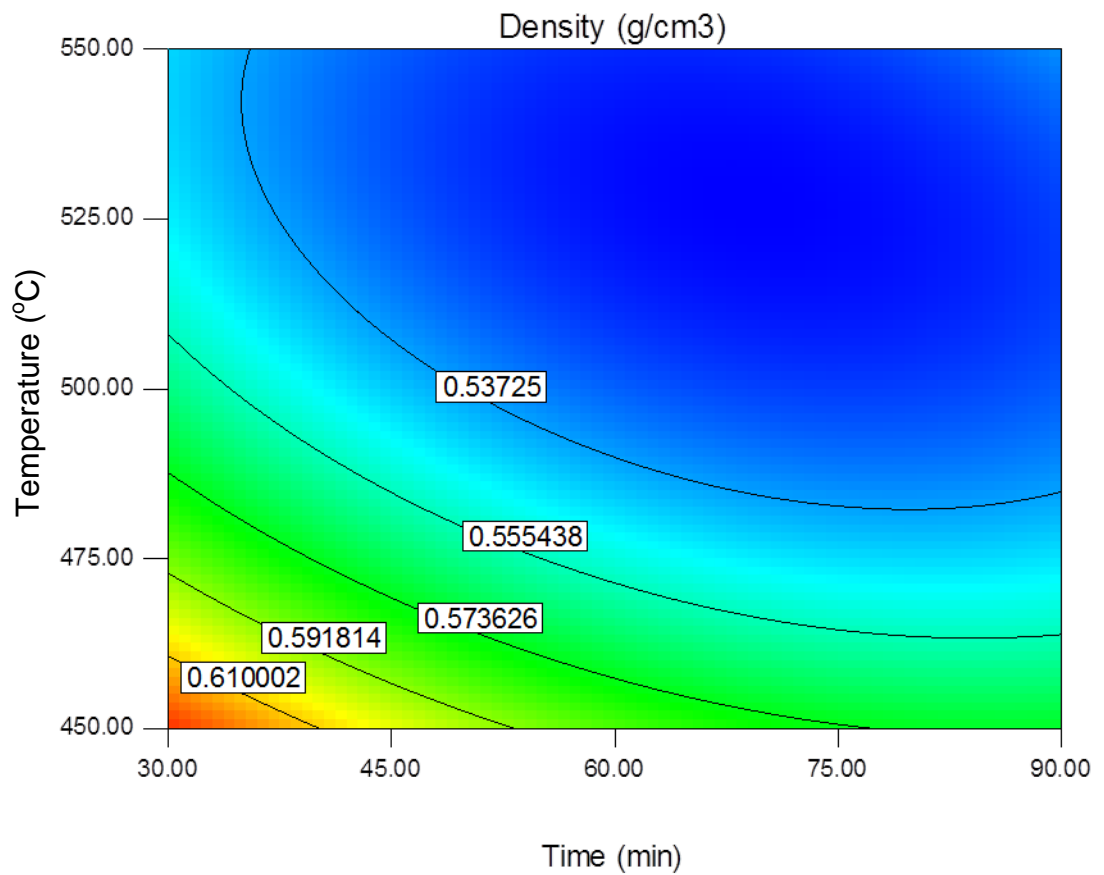
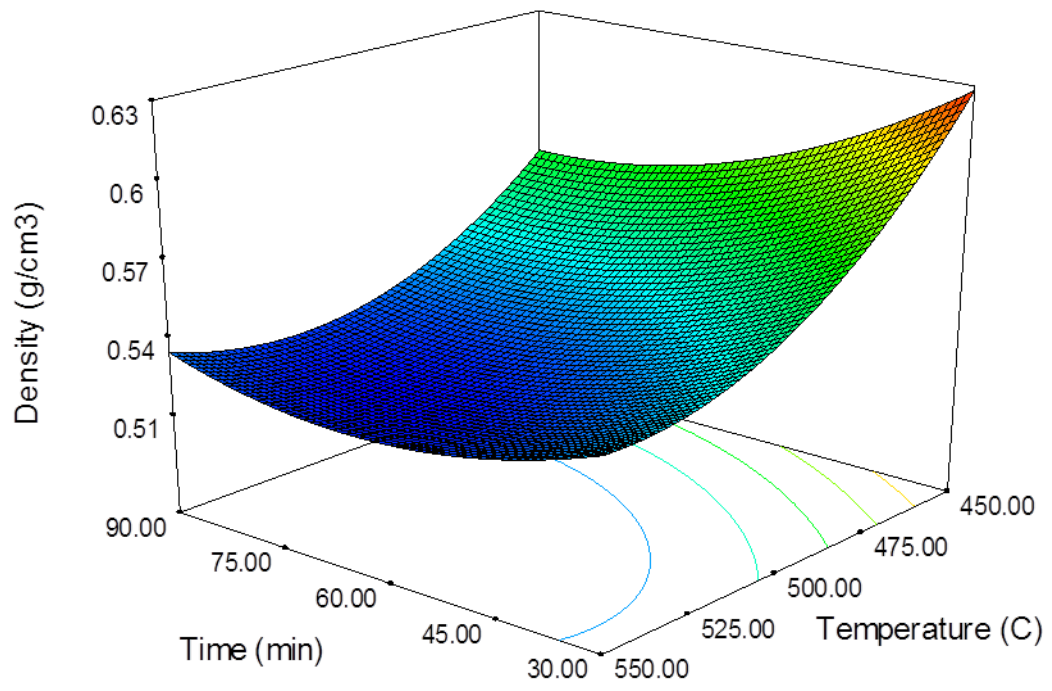


Figure 5.5 Response surface of density and the corresponding contour plot for the activation of bio-char

Figure 5.4 shows that the response of carbon burnt off is rather linear to both of the activation temperature and time. However, its response to activation time is larger than the temperature. This is why the second order term including T^2 and t^2 has no significant effect (both have p -value > 0.05) on the burnt off. In addition, the carbon burnt off does not increase appreciably with temperature in low temperature range ($450^\circ\text{C} - 500^\circ\text{C}$). Hence, low activation temperature and short activation time should be used to minimize the burnt off.

For the response of density in Figure 5.5, it decreased substantially with increasing activation time at low temperature. However, the effect of activation time to the density diminished at high temperature. This suggests high activation temperature should be applied to obtain activated carbon with low density. This is against the condition to minimize carbon burnt off where low temperature is preferred. Therefore, an optimum temperature is needed to minimize both the burnt off and density. It is also aimed to minimize the activation time. The condition of such optimization is found at 515°C and 20 min, which gave 79.8 % carbon burnt off and activated carbon with the density of 0.57 g cm^{-3} .

5.1.2 Properties of activated carbon

In order to confirm the activated carbon obtained is suitable to be used as opacifier in bamboo leaf aerogel, its properties including purity, specific surface area, infrared absorption, amorphicity and fractal dimension were determined.

The purity of activated carbon produced was studied by EDX and the result is shown in the Figure 5.6. The activated carbon contained 93 ± 1.2 wt% of carbon, 6.6 ± 1.6 wt% of oxygen and the remaining are traces of silica, potassium and calcium.

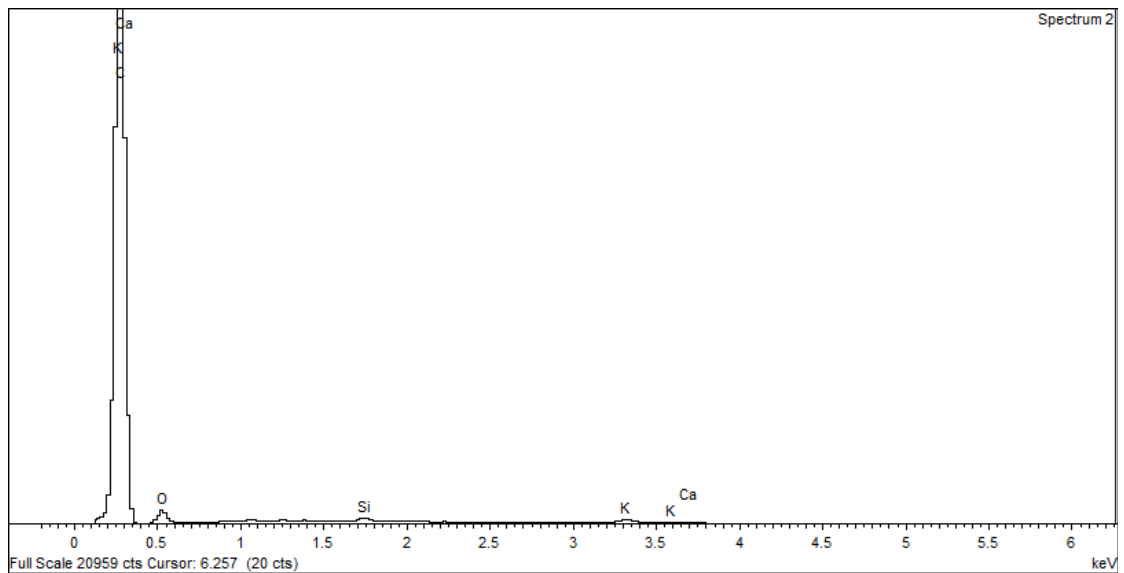


Figure 5.6 EDX spectrum of activated carbon

The amorphicity of activated carbon is confirmed with XRD in [Figure 5.7](#) and it is compared with the carbon black. The result agreed with the diffractogram of porous carbon reported elsewhere previously (Charreteur et al., 2009, Charreteur et al., 2008). Both the diffractograms exhibit similar behavior where diffuse peak was observed at 2θ between 20-30 degrees. These diffuse peaks that centered c.a. $2\theta = 25$ degrees indicate the amorphous nature of activated carbon and carbon black used.

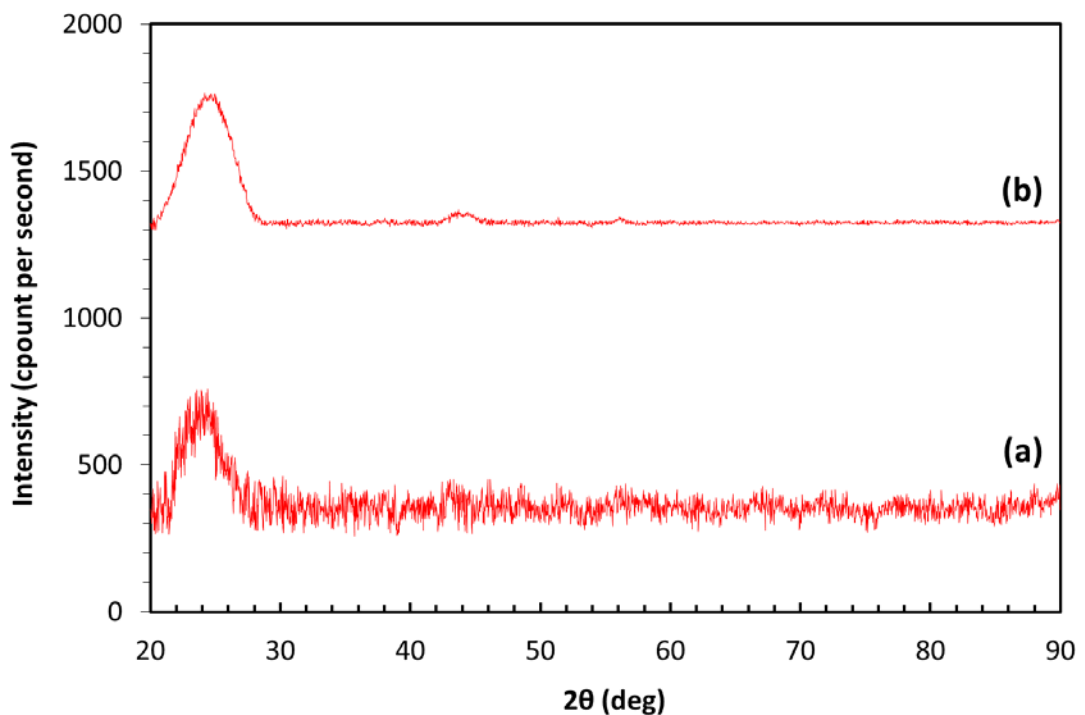


Figure 5.7 EDX spectra of (a) activated carbon (b) carbon black N330

As shown in Table 5.4, The BET specific surface activated carbon is higher than the carbon black. This is expected because activated carbon is more porous than carbon black.

Table 5.4
Adsorption characteristics of activated carbon

Sample	BET specific surface area ($\text{m}^2 \text{g}^{-1}$)	DFT total pore volume ($\text{cm}^3 \text{g}^{-1}$)	Average BJH adsorption pore size (nm)
Activated carbon	696.7 ± 5.6	0.16	15.4
Carbon black N330	175.7 ± 0.4	0.82	24.3

Figure 5.8 show that activated carbon obtained has average of 63% of infrared transmission. The infrared transmission is rather constant over the entire range from 2.5 μm – 22 μm . As compared with activated carbon, the carbon black has lower average infrared transmission of 20%. It can then indirectly infer that carbon is more effective in reducing radiative loss than activated carbon. Nonetheless, the activated carbon is still

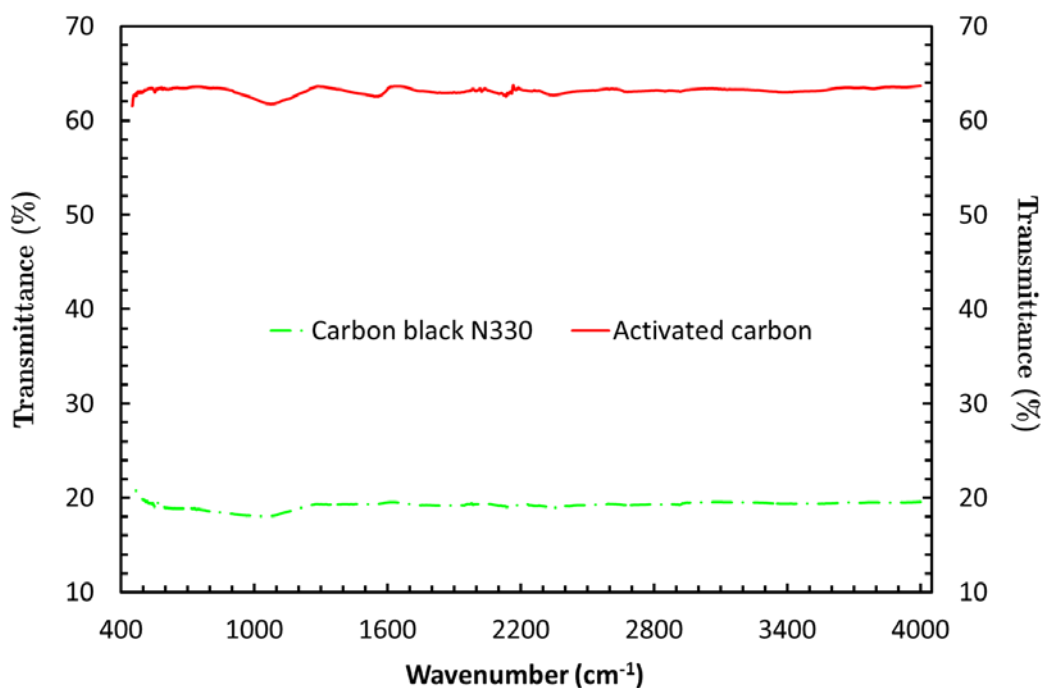


Figure 5.8 Infrared absorption of activated carbon and carbon black N330

able to mask out the mid-infrared (3 μm – 8 μm) transmission that might leak out in pure silica aerogel.

Fractal characteristics of activated carbon are shown in [Table 5.5](#). The mass fractal dimension of activated carbon is closed to 3, which indicates its internal structure is slightly fractal. The activated carbon also exhibits large surface fractal structure with $D_s = 2.91$. This large surface fractal dimension implies activated carbon has very high surface roughness. As comparison, the carbon black has lower mass fractal dimension, i.e., 1.89. However, the value of D fitted has extremely large confidence interval that spanned across 14 orders of magnitude. Thus, it is concluded that the microstructure of carbon black cannot be fitted in to the model. However, the SAXS data ($\log I$ against $\log q$) of carbon black exhibits fairly wide range of linear behavior. Thus, it can be fitted well into linear model to give very large surface fractal dimension.

Table 5.5
Fractal characteristics of activated carbon fitted at 95% level of confidence

	<u>Activated carbon</u>	<u>Carbon black</u>
<u>Mass fractal characteristics using equation (3.11)</u>		
Mass fractal dimension, D	3.14 ± 0.27	1.89 ± 2.15
Characteristics length, ζ (nm)	45.6 ± 8.2	$9873 \pm 1.7E7$
Adjusted R^2 of model fitted	0.99	0.98
<u>Surface fractal characteristics using equation (3.10)</u>		
Surface fractal dimension, D_s	2.91 ± 0.15	3.95 ± 0.15
Adjusted R^2 of model fitted	0.99	0.99

5.1.3 Summary

Activated carbon was successfully synthesized from bamboo leaf. The condition of carbonization and activation was optimized to reduce carbon burnt off and density. The activated carbon synthesized exhibits desired properties for opacification of silica aerogel such as high purity, low transmission of mid-infrared ray and highly fractal microstructure.

5.2 Opacification of silica aerogel with activated carbon

Silica aerogel were opacified with activated carbon produced to optimize its thermal conductivity. Factors including carbon loading, silica concentration on water glass and temperature were studied. Effects of these parameters were combined to develop an empirical model. The regressed model was used to derive an optimal carbon loading – silica concentration tie line that minimized the thermal conductivity at various temperatures. The thermal conductivity of aerogels opacified with activated carbon was also compared with those opacified with carbon black.

5.2.1 Effect of temperature

It is known that the total thermal conductivity of aerogel is the sum of three mode of heat transfer as stated in [equation \(4.8\)](#):

$$\lambda_T = \lambda_g + \lambda_r + \lambda_s \quad (4.8)$$

where the radiative transfer (λ_r) is expressed in [equation \(2.5\)](#) as:

$$\lambda_T = \frac{16}{3} \left(\frac{\sigma n^2 T^3}{\rho_{ae} e} \right) + (\lambda_g + \lambda_s) \quad (5.2)$$

Hence, total thermal conductivity increased with temperature as shown in [Figure 5.9](#).

Assuming that λ_g , λ_s and e are fairly weak functions of temperature, the total thermal

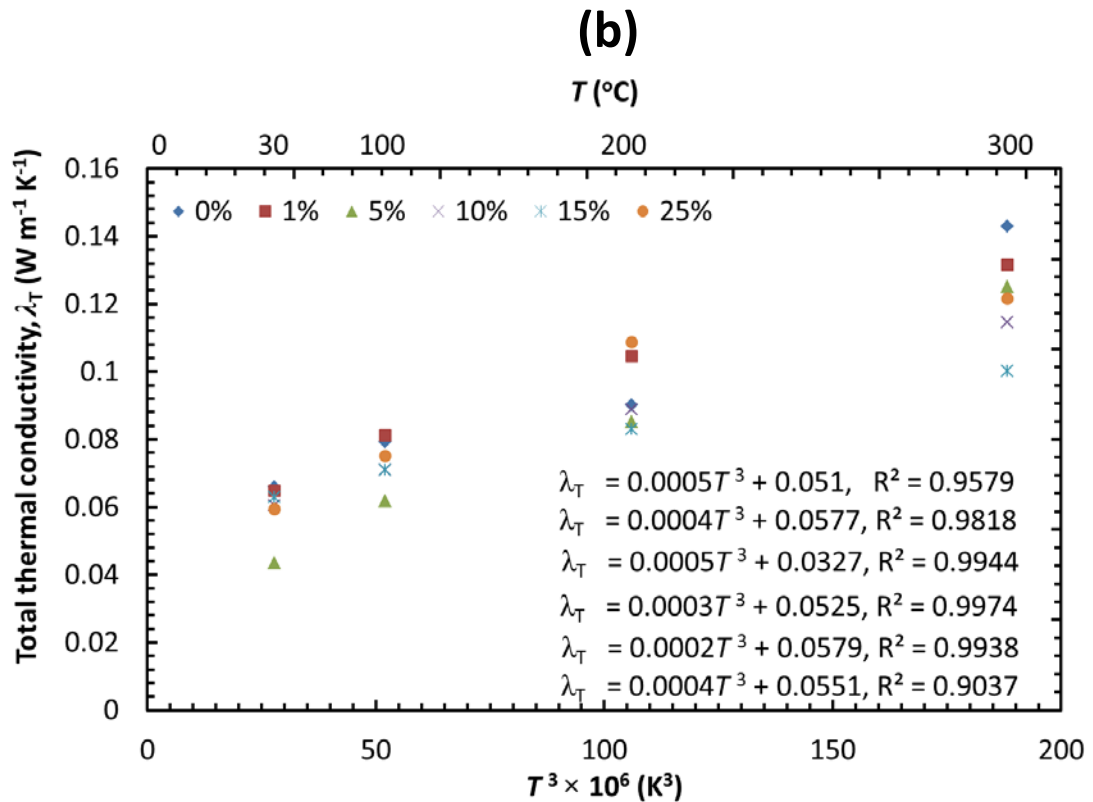
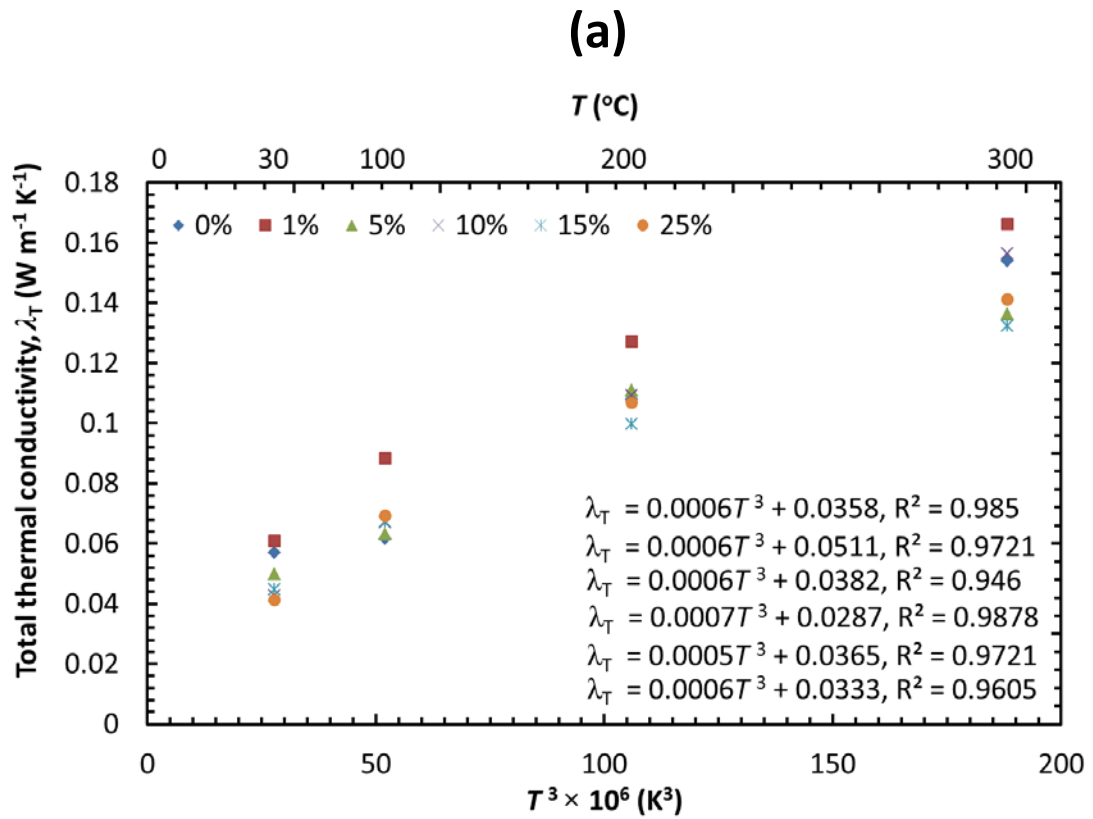


Figure 5.9 Linear dependence of total thermal conductivity to T^3 at various carbon loading (0-25 wt%). (a) 3.22 wt%, (b) 4.25 wt% and (c) 10 wt% of silica concentration in water glass. Regressed equations are shown following the sequence of increasing carbon loading from top to bottom.

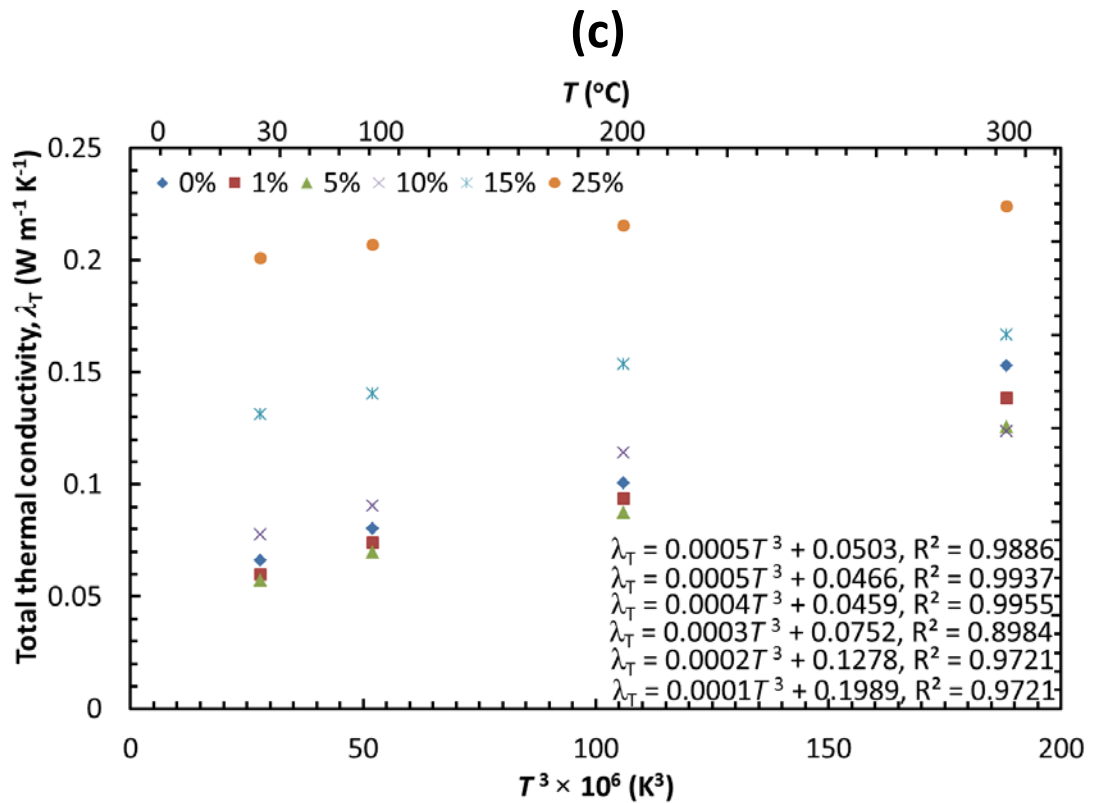


Figure 5.9 (continue) Linear dependence of total thermal conductivity to T^3 at various carbon loading (0-25 wt%). (a) 3.22 wt%, (b) 4.25 wt% and (c) 10 wt% of silica concentration in water glass. Regressed equations are shown following the sequence of increasing carbon loading from top to bottom.

conductivity is thus expected to show linear dependence on T^3 . Figure 5.9 has proved such linear dependence.

In every case, the y-intercept of plot is representing the sum of solid conductivity (λ_s) and gas conductivity (λ_g). General trend were observed in the values of y-intercept where it is initially decreased but later increased as carbon loading increased. This implies neither high nor low carbon loading can minimize the thermal conductivity, i.e., an optimal carbon loading exists at different temperature and silica concentration. On one hand, the increasing carbon loading will increase the density of aerogel and thus its solid conductivity as in equation (2.7). On the other hand, the increasing density also may lower the gas conductivity based on equation (4.9). Physically, these two effects might be seen as the tussle between the increasing skeletal conduction due to increase in its solid connectivity, with the decrease in gas conduction

due to pore size reduction; while the density of aerogel increased. Hence, an optimal carbon loading exists as the balance of these two effects.

Similarly, the increase of silica concentration from 3.22 – 10 wt% caused the aerogel density to increase. It is observed that the y-intercepts of plots generally increased when silica concentration of water glass increased. This can be interpreted as effect of the increase in solid conduction is greater than the decrease in gas conduction, as the density of aerogel increased. Slope of plots had shown the opposite trend where it decreased with increasing silica concentration. Since the slope contributes positively to radiative transfer, it indicates reduction of λ_r at higher silica concentration. Such observation can be attributed to the inverse relation of λ_r with aerogel density (ρ_{ae}) shown in [equation \(2.5\)](#). As a result, the increase in solid conduction (λ_s) is offset by the reduction in gas conduction (λ_g) and radiative transfer (λ_r). Hence, optimal silica concentration shall also exist to minimize the total thermal conductivity. This effect is better illustrated by combining the three modes of heat transfer in term of aerogel density as follow:

$$\lambda_T = \underbrace{\tilde{C} \rho_{ae}^\varphi}_{\text{Solid conduction}} + \underbrace{\frac{16}{3} \left(\frac{\sigma n^2 T^3}{\rho_{ae} e} \right)}_{\text{Radiation}} + \underbrace{\frac{60.22 \times 10^5 \Pi p T^{-0.5}}{0.25 S_{\text{BET}} \rho_{ae} \Pi^{-1} + 4.01 \times 10^9 p T^{-1}}}_{\text{Gas conduction}} \quad (5.3)$$

5.2.2 Effect of carbon loading

It is known that carbon doped into aerogel can reduce the radiative conductivity but also increased the solid conductivity. This is confirmed in [Figure 5.10](#) where all plot show a local minimum as carbon loading increased. However, the addition of small

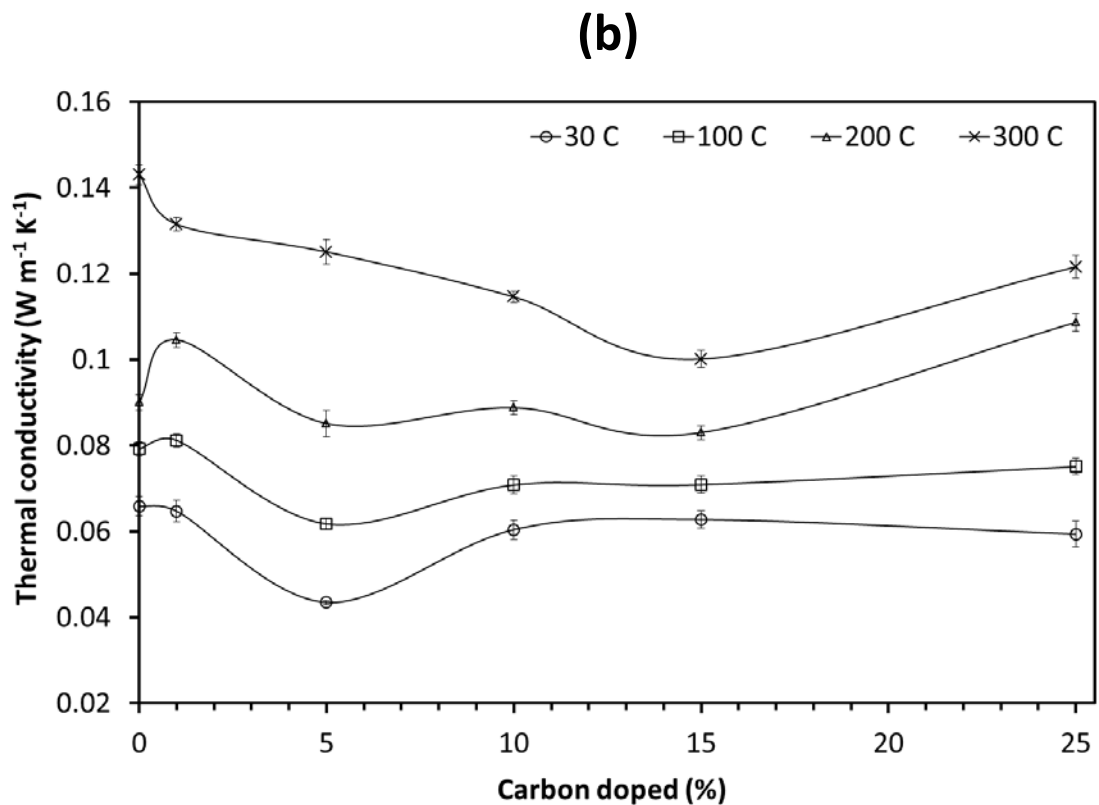
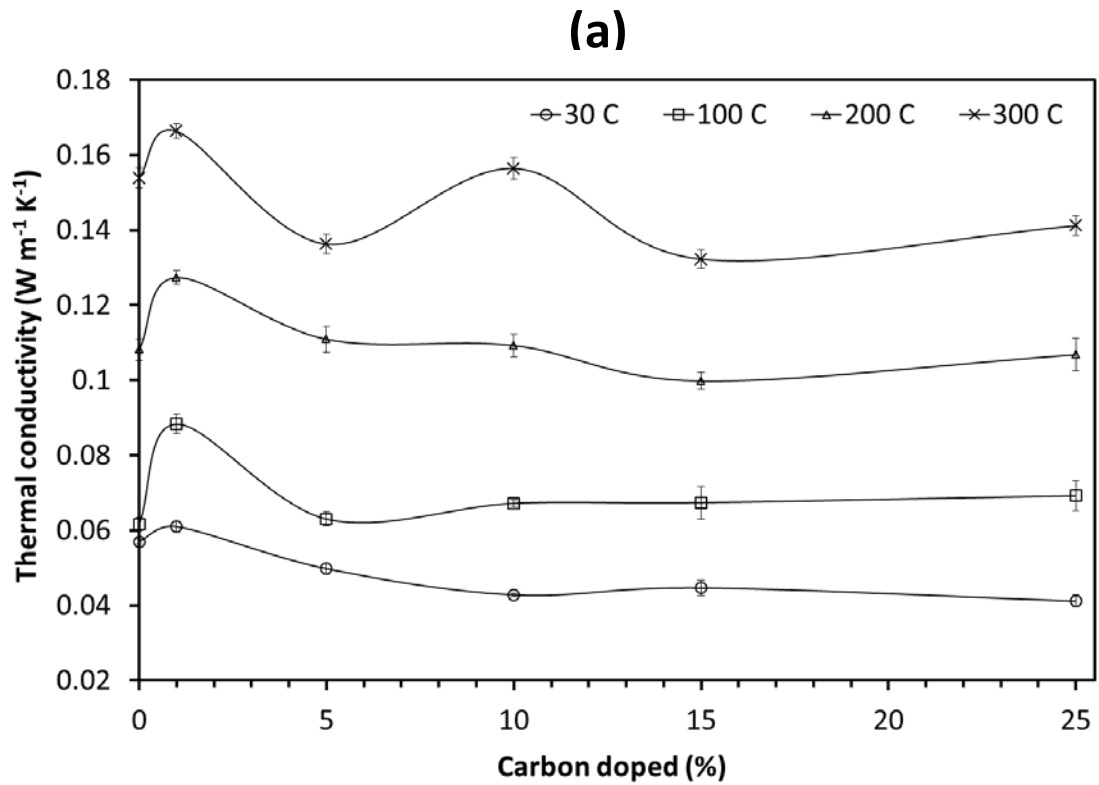


Figure 5.10 Effect of carbon loading to total thermal conductivity at various temperatures (30 – 300 °C). (a) 3.22 wt%, (b) 4.25 wt% and (c) 10 wt% of silica concentration in water glass.

(c)

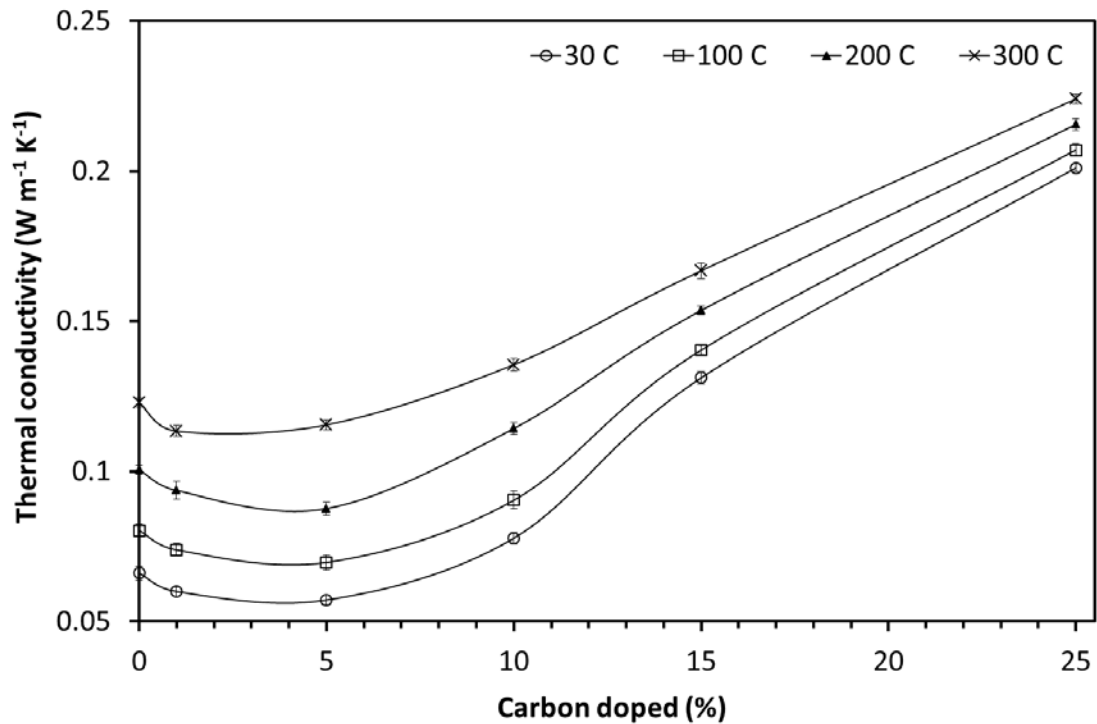


Figure 5.10 (continue) Effect of carbon loading to total thermal conductivity at various temperatures (30-300 °C). (a) 3.22 wt%, (b) 4.25 wt% and (c) 10 wt% of silica concentration in water glass.

amount of carbon (1% carbon) not necessary reduce the thermal conductivity. Under low silica concentration ([Figure 5.11\(a\)](#) and [Figure 5.11\(b\)](#)), the thermal conductivity of aerogel doped with 1% of carbon are generally higher than the non-opacified silica aerogel. This may due to the addition of only 1% of carbon is not sufficient to mask out all the cross section of aerogel to reduce its radiative conductivity effectively. In contrast, the carbon doped increased the solid conductivity of opacified aerogel and overall had increased its thermal conductivity. The effect of opacification start to be obvious when higher amount of carbon is added. In general, the thermal conductivity decreased to a minimum and then increased again. The thermal conductivity increased again because very high carbon loading increased the solid conductivity rapidly.

In [Figure 5.10\(c\)](#), the situation is different at high silica concentration. The addition with even 1% of carbon had reduced the thermal conductivity lower than the

non-opacified aerogel. This is because mass 1% carbon added in low silica concentration is different from the high silica concentration. Since the mass of 1% carbon added to high silica concentration is much larger, it can spread out throughout the cross section of aerogel sample. As a result, it can reduce the radiative heat loss effectively even the carbon loading was only 1%.

5.2.3 Effect of silica concentration in water glass

Effect of silica concentration to total thermal conductivity is shown in Figure 5.11. As comparison, total thermal conductivity was estimated based on equation (5.3) for the density range corresponding to the range silica concentration used. The plot obtained in Figure 5.12(a) is resembled to Figure 5.11, hence indicating results in Figure 5.11 agreed with the theoretical prediction. Figure 5.11 shows that total thermal conductivity generally increased as silica concentration increased. As mentioned earlier in section 5.2.1, this is caused by increase in solid conductivity (λ_s) in which the

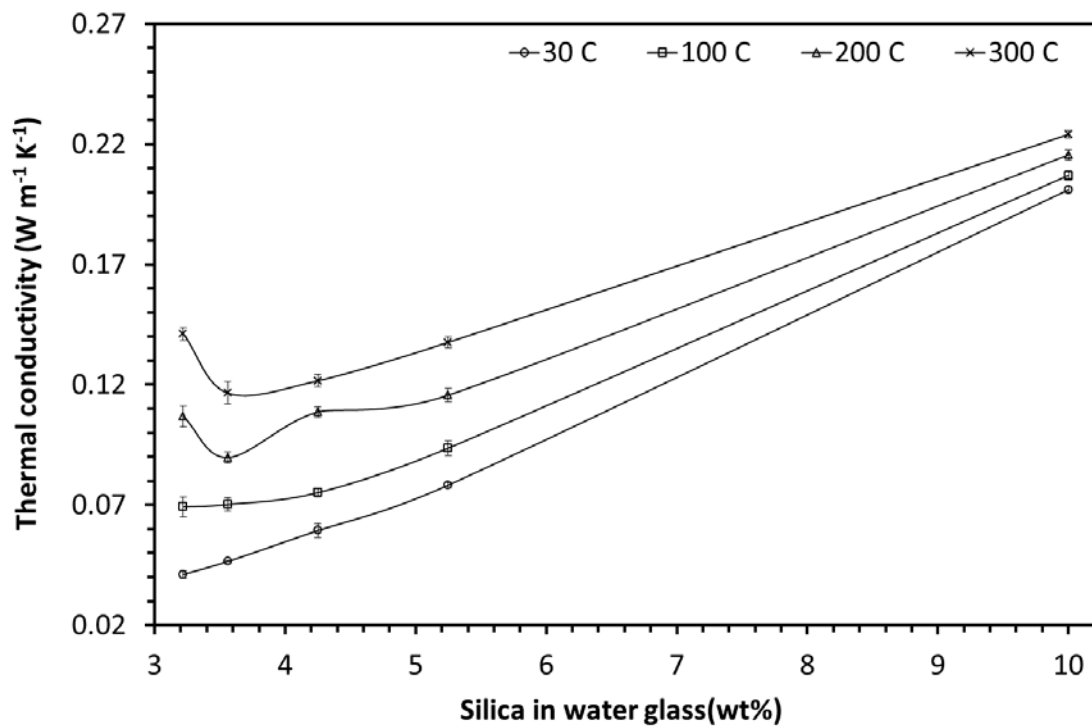


Figure 5.11 Effect of silica concentration in water glass to total thermal conductivity of opacified aerogel (25 wt% carbon) at various temperatures (30 – 300 °C).

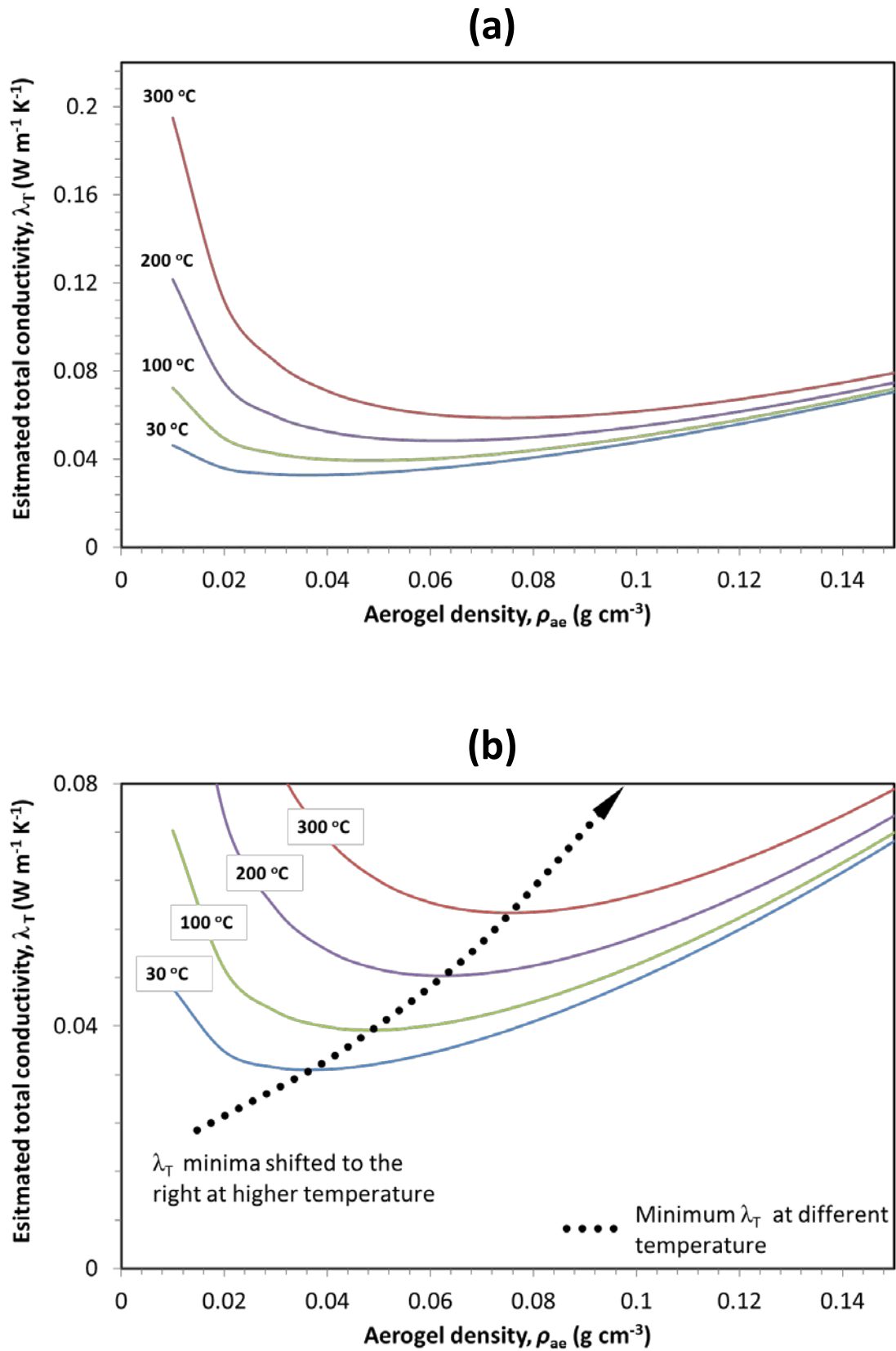


Figure 5.12 (a) Estimated effect of aerogel density to the total thermal conductivity and (b) Minima of λ_T at various temperatures. Total thermal conductivity was estimated using [equation \(5.3\)](#) with $C=1$, $\varphi=1.5$, average $e = 40 \text{ m}^2 \text{ kg}^{-1}$, $\rho_s = 2.2 \text{ g cm}^{-3}$, $n=1$, average $S_{\text{BET}} = 400 \text{ m}^2 \text{ g}^{-1}$ and $p=1 \text{ bar}$.

increase in silica concentration contributes to higher degree of solid connectivity. Though the gas conductivity (λ_g) is also reduced with increasing silica concentration, its contribution to the overall thermal conductivity at ambient temperature is relatively insignificant. At higher temperature, the increase in silica concentration has more profound effect on both the gas conductivity (λ_g) and radiative conductivity (λ_r). If high temperature is applied to aerogel, it can increase the gas conduction and radiation simultaneously, as shown in [equation \(5.3\)](#). In order to reduce λ_g and λ_r at high temperature, density of aerogel should also be increased. However, the advantage of higher density is counter balance by the increase in solid conductivity. Consequently, an optimal silica concentration that minimized total thermal conductivity is observed at 200 °C and 300 °C. The existence of such optimal silica concentration can be proven by finding the minimum λ_T at each temperature as follow:

$$\lambda_T = \tilde{C} \rho_{ae}^\varphi + \frac{16}{3} \left(\frac{\sigma n^2 T^3}{\rho_{ae} e} \right) + \frac{60.22 \times 10^5 \Pi p T^{-0.5}}{0.25 S_{BET} \rho_{ae} \Pi^{-1} + 4.01 \times 10^9 p T^{-1}} \quad (5.3)$$

Minimum λ_T exist when,

$$\therefore \frac{\partial}{\partial \rho_{ae}} (\lambda_T) \Big|_{T,p,n,e,\tilde{C},\varphi} = 0 \quad (5.4)$$

$$\therefore \frac{\partial}{\partial \rho_{ae}} (\lambda_s) \Big|_{\tilde{C},\varphi} + \frac{\partial}{\partial \rho_{ae}} (\lambda_r) \Big|_{T,n,e} + \frac{\partial}{\partial \rho_{ae}} (\lambda_g) \Big|_{T,p} = 0 \quad (5.5)$$

For solid conductivity λ_s ,

$$\frac{\partial}{\partial \rho_{ae}} (\lambda_s) \Big|_{\tilde{C},\varphi} = \frac{\partial}{\partial \rho_{ae}} (\tilde{C} \rho_{ae}^\varphi) \Big|_{\tilde{C},\varphi} = \varphi \tilde{C} \rho_{ae}^{\varphi-1} \quad (5.6)$$

For radiative conductivity λ_r ,

$$\left. \frac{\partial}{\partial \rho_{ac}} (\lambda_r) \right|_{T,n,e} = \left. \frac{\partial}{\partial \rho_{ac}} \left\{ \frac{16}{3} \left(\frac{\sigma n^2 T^3}{\rho_{ac} e} \right) \right\} \right|_{T,n,e} = -\frac{16}{3} \left(\frac{\sigma n^2 T^3}{\rho_{ac}^2 e} \right) \quad (5.7)$$

For gas conductivity λ_g ,

$$\left. \frac{\partial}{\partial \rho_{ac}} (\lambda_g) \right|_{T,p} = \left. \frac{\partial}{\partial \rho_{ac}} \left\{ \frac{60.22 \times 10^5 \Pi p T^{-0.5}}{0.25 S_{BET} \rho_{ac} \Pi^{-1} + 4.01 \times 10^9 p T^{-1}} \right\} \right|_{T,p} \quad (5.8)$$

Since the porosity (Π) is also a function of ρ_{ac} , the partial derivative of λ_g is easier to be evaluated in term of Π . $\partial/\partial \Pi$ was first applied to λ_g ,

$$\left. \frac{\partial}{\partial \rho_{ac}} (\lambda_g) \right|_{T,p} = \frac{\partial \Pi}{\partial \rho_{ac}} \left. \frac{\partial}{\partial \Pi} (\lambda_g) \right|_{T,p} \quad (5.9)$$

where

$$\begin{aligned} \left. \frac{\partial}{\partial \Pi} (\lambda_g) \right|_{T,p} &= \left. \frac{\partial}{\partial \Pi} \left\{ \frac{60.22 \times 10^5 \Pi p T^{-0.5}}{0.25 S_{BET} \rho_{ac} \Pi^{-1} + 4.01 \times 10^9 p T^{-1}} \right\} \right|_{T,p} \quad (5.10) \\ &= \frac{(0.25 S_{BET} \rho_{ac} \Pi^{-1} + 4.01 \times 10^9 p T^{-1}) \left\{ \frac{\partial}{\partial \Pi} (60.22 \times 10^5 \Pi p T^{-0.5}) \right\}}{(0.25 S_{BET} \rho_{ac} \Pi^{-1} + 4.01 \times 10^9 p T^{-1})^2} - \\ &\quad \frac{(60.22 \times 10^5 \Pi p T^{-0.5}) \left\{ \frac{\partial}{\partial \Pi} (0.25 S_{BET} \rho_{ac} \Pi^{-1} + 4.01 \times 10^9 p T^{-1}) \right\}}{(0.25 S_{BET} \rho_{ac} \Pi^{-1} + 4.01 \times 10^9 p T^{-1})^2} \end{aligned}$$

$$\begin{aligned} \therefore \left. \frac{\partial}{\partial \Pi} (\lambda_g) \right|_{T,p} &= \frac{(0.25 S_{BET} \rho_{ac} \Pi^{-1} + 4.01 \times 10^9 p T^{-1}) (60.22 \times 10^5 p T^{-0.5})}{(0.25 S_{BET} \rho_{ac} \Pi^{-1} + 4.01 \times 10^9 p T^{-1})^2} - \\ &\quad \frac{(60.22 \times 10^5 \Pi p T^{-0.5}) \left[-0.25 S_{BET} \left(\frac{\Pi \rho_s + \rho_{ac}}{\Pi^2} \right) \right]}{(0.25 S_{BET} \rho_{ac} \Pi^{-1} + 4.01 \times 10^9 p T^{-1})^2} \quad (5.11) \end{aligned}$$

Combining equations (3.8), (5.9) and (5.10) yield,

$$\left. \frac{\partial}{\partial \rho_{\text{ae}}} (\lambda_{\text{g}}) \right|_{T,p} = \frac{\partial \Pi}{\partial \rho_{\text{ae}}} \frac{\partial}{\partial \Pi} (\lambda_{\text{g}}) \Big|_{T,p} = -\frac{1}{\rho_{\text{s}}} \frac{\partial}{\partial \Pi} (\lambda_{\text{g}}) \Big|_{T,p} \quad (5.12)$$

$$\begin{aligned} \therefore \left. \frac{\partial}{\partial \rho_{\text{ae}}} (\lambda_{\text{g}}) \right|_{T,p} = & -\frac{1}{\rho_{\text{s}}} \left\{ \frac{(0.25 S_{\text{BET}} \rho_{\text{ae}} \Pi^{-1} + 4.01 \times 10^9 pT^{-1})(60.22 \times 10^5 pT^{-0.5})}{(0.25 S_{\text{BET}} \rho_{\text{ae}} \Pi^{-1} + 4.01 \times 10^9 pT^{-1})^2} \right. \\ & \left. + \frac{(60.22 \times 10^5 \Pi pT^{-0.5}) \left[0.25 S_{\text{BET}} \left(\frac{\Pi \rho_{\text{s}} + \rho_{\text{ae}}}{\Pi^2} \right) \right]}{(0.25 S_{\text{BET}} \rho_{\text{ae}} \Pi^{-1} + 4.01 \times 10^9 pT^{-1})^2} \right\} \end{aligned} \quad (5.13)$$

Hence, based on equation (5.4), minimum λ_{T} at a temperature can be calculated when,

$$\begin{aligned} \varphi \tilde{C} \rho_{\text{ae}}^{\varphi-1} - \frac{16}{3} \left(\frac{\sigma n^2 T^3}{\rho_{\text{ae}}^2 e} \right) - \frac{1}{\rho_{\text{s}}} \left\{ \frac{(0.25 S_{\text{BET}} \rho_{\text{ae}} \Pi^{-1} + 4.01 \times 10^9 pT^{-1})(60.22 \times 10^5 pT^{-0.5})}{(0.25 S_{\text{BET}} \rho_{\text{ae}} \Pi^{-1} + 4.01 \times 10^9 pT^{-1})^2} \right. \\ \left. + \frac{(60.22 \times 10^5 \Pi pT^{-0.5}) \left[0.25 S_{\text{BET}} \left(\frac{\Pi \rho_{\text{s}} + \rho_{\text{ae}}}{\Pi^2} \right) \right]}{(0.25 S_{\text{BET}} \rho_{\text{ae}} \Pi^{-1} + 4.01 \times 10^9 pT^{-1})^2} \right\} = 0 \end{aligned} \quad (5.14)$$

Equation (5.14) was solved numerically to obtain ρ_{ae} at various temperatures and the result ($\lambda_{\text{T, min}}$) is shown in Figure 5.12(b). Selection of the aerogel density that minimized total thermal conductivity at a given temperature can be estimated using equation (5.14). Plot in Figure 5.12(a) suggests that the minima of plot are shifted to the right as temperature increased. This implies the optimal silica concentration will increase as temperature increased. Comparison of Figure 5.11 with Figure 5.12(b) also

suggests that minimum λ_T for 30 °C and 100 °C should exist outside the experimental range, i.e., silica concentration less than 3.22 wt%. This explained why minimum value of λ_T is not observed for 30 °C and 100 °C in [Figure 5.11](#).

5.2.4 Modeling and optimization

Experimental data obtained was first fitted into a second order model shown in [equation \(5.15\)](#). The result of statistical analysis of the model is summarized in [Table 5.6](#). All the parameters are significant in the model except T^2 . The corresponding response surface at different temperatures was shown in [Figure 5.13](#). The response surfaces account well for the behavior of opacified aerogel at low Θ_{Si} and Θ_C . They show optimal values that minimized the total thermal conductivity as explained previously in [section 5.2.2](#) and [5.2.3](#). However, the model failed to account the behavior of opacified aerogel at high Θ_{Si} and Θ_C . For instance, with $\Theta_{Si} = 10$ wt%, the opacification at any temperature not only will not help to reduce the total thermal conductivity but increase λ_T instead. The error is due to the model does not gives minimum point in such regions. Similarly, at high Θ_C , no optimal Θ_{Si} that can minimize λ_T exist in the model.

$$\lambda_T = \tau_0 + \tau_1 \Theta_{Si}^2 + \tau_2 \Theta_C^2 + \tau_3 T^2 + \tau_4 \Theta_{Si} \Theta_C + \tau_5 \Theta_{Si} T + \tau_6 \Theta_C T + \tau_7 \Theta_{Si} + \tau_8 \Theta_C + \tau_9 T \quad (5.15)$$

where

Θ_{Si}	=	silica concentration in water glass, in wt%
Θ_C	=	carbon loading in aerogel, in wt%
T	=	temperature of λ_T measurement
τ_i	=	regressed coefficients of parameters

At low temperatures, even this may be explained as the minimum points exist outside the experimental region as suggested in [section 5.2.4](#), but the minimum points are still not observed as temperature increase. Hence, the model is not appropriate to account for the behavior of opacified aerogel in the region of high Θ_{Si} and Θ_C .

It also can be observed in [Figure 5.13](#) that there exist regions which minimized the total thermal conductivity at different temperatures. Such region implies that it is always possible to minimize the total thermal conductivity at a given temperature by using various combinations of Θ_{Si} and Θ_C . These combinations of Θ_{Si} and Θ_C form

Table 5.6
Total thermal conductivity data fitted into second order model [[Equation \(5.15\)](#)]

Terms	Parameter	<i>p</i> -value	Coefficients (Coded)	Coefficients, τ_i (Actual)
Second order	Θ_{Si}^2	<0.0001	0.021	1.83×10^{-3}
Second order	Θ_C^2	<0.0001	0.018	1.13×10^{-4}
Second order	T^2	0.798	7.28×10^{-4}	3.99×10^{-8}
Interaction	$\Theta_{Si} \Theta_C$	<0.0001	0.036	8.48×10^{-4}
Interaction	$\Theta_{Si} T$	<0.0001	-8.95×10^{-3}	-1.96×10^{-5}
Interaction	$\Theta_C T$	0.0002	-8.87×10^{-3}	-5.26×10^{-6}
First order	Θ_{Si}	<0.0001	0.023	-0.0248
First order	Θ_C	<0.0001	0.024	-5.63×10^{-3}
First order	T	<0.0001	0.032	4.17×10^{-4}
Mean	τ_0	<0.0001	0.085	0.114
Adjusted R^2 of model				0.893

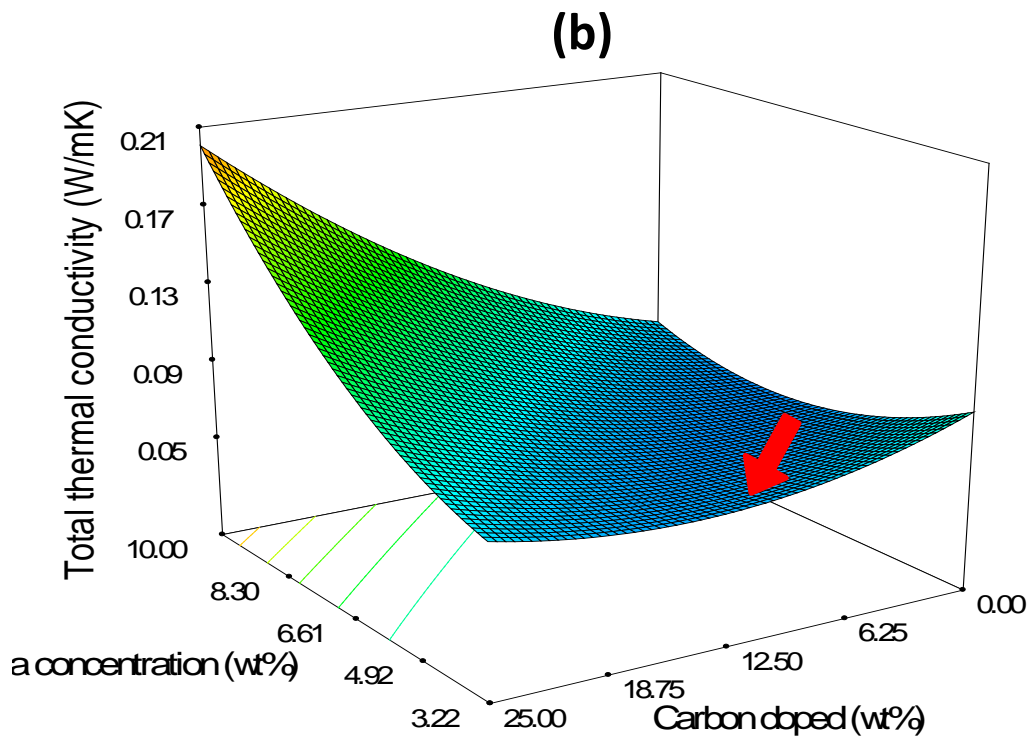
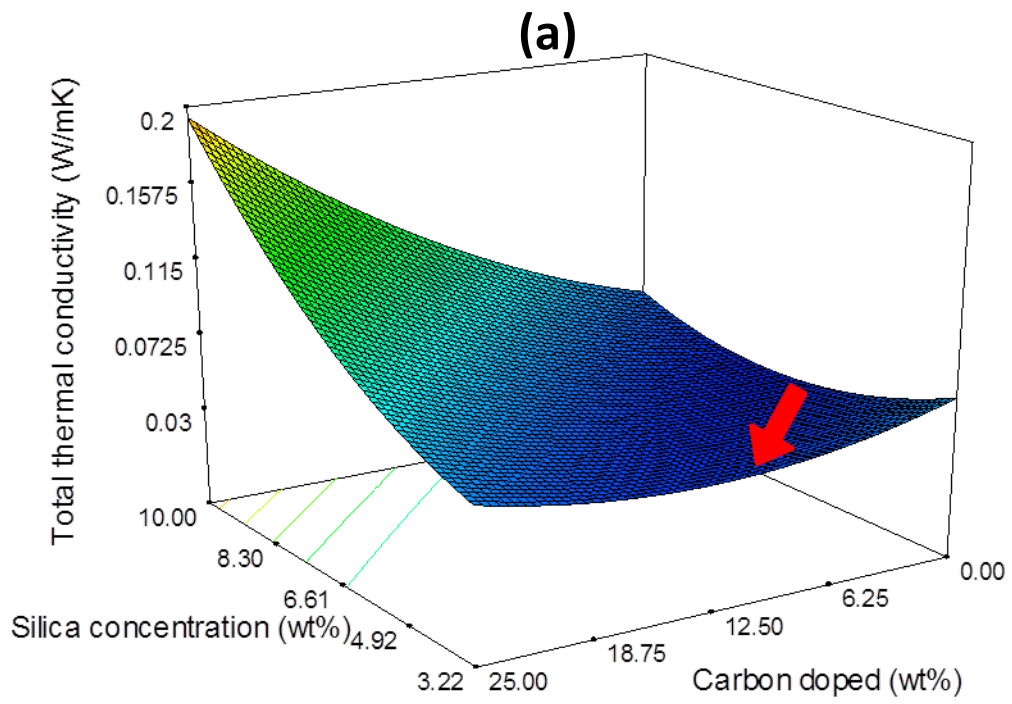


Figure 5.13 Response surface of total thermal conductivity fitted with second order model at (a) 30 °C, (b) 100 °C, (c) 200 °C and (d) 300 °C.

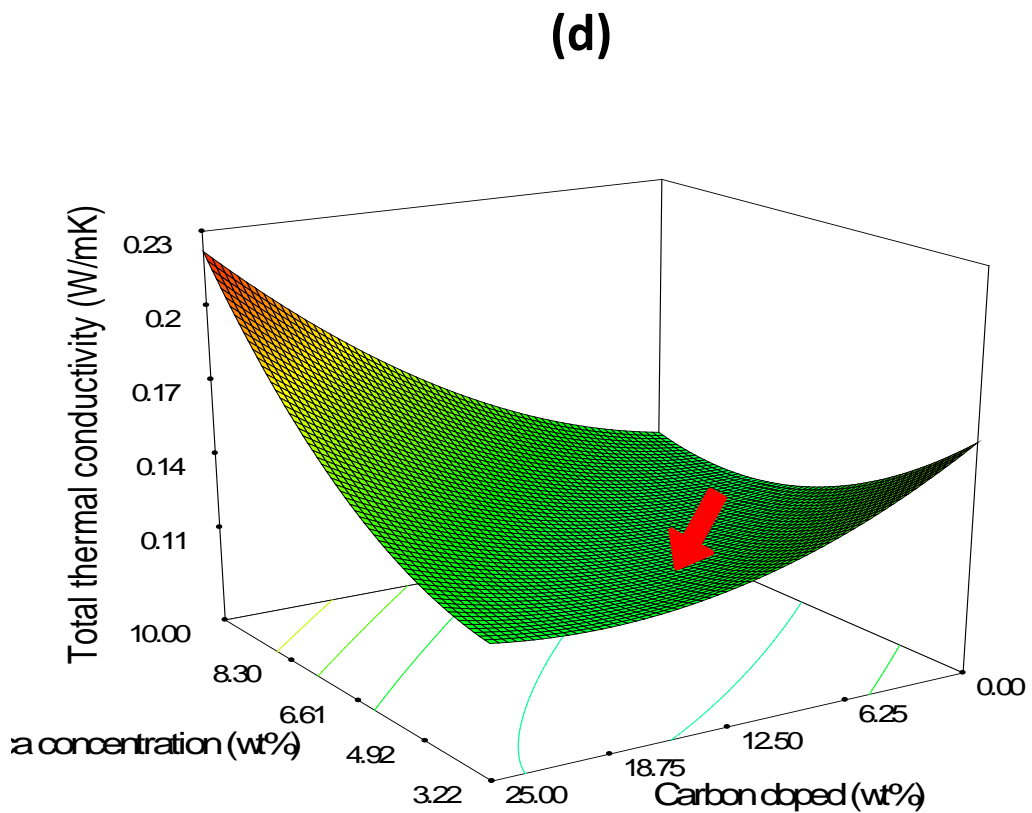
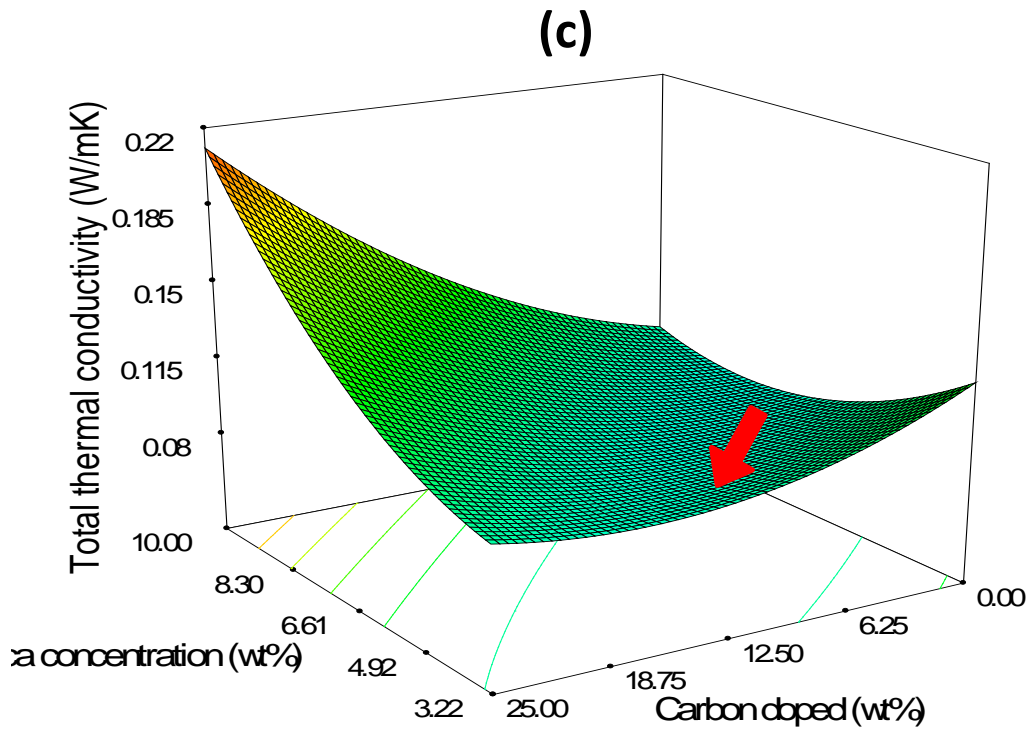


Figure 5.13 (continue) Response surface of total thermal conductivity fitted with second order model at (a) 30 °C, (b) 100 °C, (c) 200 °C and (d) 300 °C.

tie lines that can be derived from the regressed model as follows:

$$\begin{aligned}
 \lambda_T = & \tau_0 + \\
 & \tau_1 \Theta_{Si}^2 + \tau_2 \Theta_C^2 + \\
 & \tau_4 \Theta_{Si} \Theta_C + \tau_5 \Theta_{Si} T + \tau_6 \Theta_C T + \\
 & \tau_7 \Theta_{Si} + \tau_8 \Theta_C + \tau_9 T
 \end{aligned} \tag{5.16}$$

The tie line can be derived by using its partial derivative at constant temperature,

$$\left. \frac{\partial \lambda_T}{\partial \Theta_C} \right|_{\Theta_{Si}, T} = 2\tau_2 \Theta_C + \tau_4 \Theta_{Si} + \tau_6 T + \tau_8 \tag{5.17}$$

To minimize λ_T ,

$$\begin{aligned}
 \left. \frac{\partial \lambda_T}{\partial \Theta_C} \right|_{\Theta_{Si}, T} &= 0 \\
 2\tau_2 \Theta_C + \tau_4 \Theta_{Si} + \tau_6 T + \tau_8 &= 0 \\
 \therefore \Theta_{C, \min \lambda_T} &= -\frac{(\tau_4 \Theta_{Si} + \tau_6 T + \tau_8)}{2\tau_2}
 \end{aligned} \tag{5.18}$$

At a given temperature, the value of $\Theta_{C, \min \lambda_T}$ shows linear relation with Θ_{Si} as shown in [Figure 5.14](#). Since the slope of plot is $-(\tau_4/2\tau_2)$ and both τ_2 and τ_4 are positive, the optimal tie line suggests that lower carbon loading should be used to opacify aerogel with higher silica concentration. Once again, the tie line can only be used as an approximation at low Θ_{Si} and Θ_C , and deviates appreciably from reality as Θ_{Si} and Θ_C increase. Rearrange [equation \(5.18\)](#), yields,

$$\Theta_{C, \min \lambda_T} = -\left(\frac{\tau_6}{2\tau_2}\right)T - \left(\frac{\tau_4 \Theta_{Si} + \tau_8}{2\tau_2}\right) = -\left(\frac{\tau_6}{2\tau_2}\right)T + \text{constant} \tag{5.19}$$

Hence, it can be deduced that for an aerogel with given silica concentration, $\Theta_{C, \min \lambda_T}$ increased linearly with temperature as in [Figure 5.15](#). The plot has positive slope

because $\tau_6 < 0$. This is in agreement with the theoretical model developed by Zeng (Zeng et al., 1995) where the optimal carbon loading increased linearly with temperature.

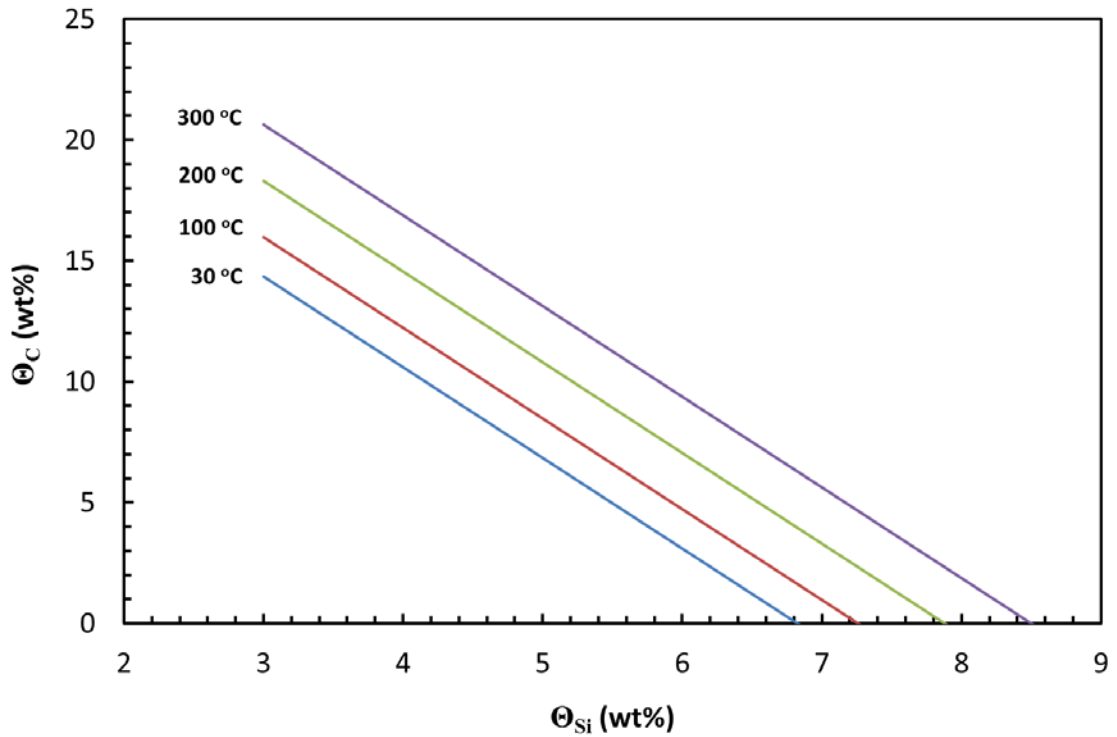


Figure 5.14 Optimal tie lines to minimize total thermal conductivity of opacified aerogel at various temperatures based on [equation \(5.18\)](#)

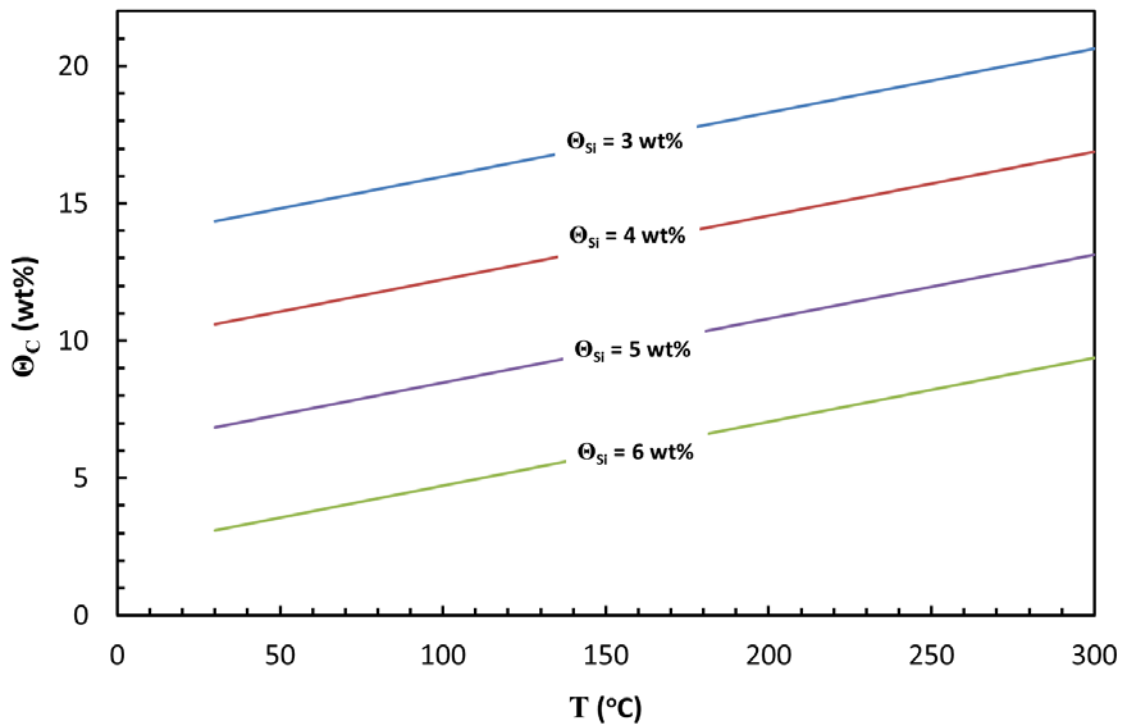


Figure 5.15 Optimal tie lines to minimize total thermal conductivity of opacified aerogel with various silica concentrations based on [equation \(5.18\)](#)

Figure 5.13 also shows that the $\Theta_{Si} - \Theta_C$ tie line shifted to the left (indicated by red arrows) as the temperature increased. This indicates that higher silica concentration and carbon loading is required to minimize the total thermal conductivity of opacified aerogel.

As the second order model is inadequate to describe the behavior of opacified aerogel at high Θ_{Si} and Θ_C , the data are fitted to third order model in equation (5.20).

$$\begin{aligned} \lambda \gamma = & \gamma_0 + \\ & \gamma_1 \Theta_{Si}^3 + \gamma_2 \Theta_C^3 + \gamma_3 T^3 + \\ & \gamma_4 \Theta_{Si} \Theta_C T + \gamma_5 \Theta_{Si}^2 \Theta_C + \gamma_6 \Theta_{Si}^2 T + \gamma_7 \Theta_{Si} \Theta_C^2 + \gamma_8 \Theta_{Si} T^2 + \gamma_9 \Theta_C^2 T + \gamma_{10} \Theta_C T^2 \\ & \gamma_{11} \Theta_{Si}^2 + \gamma_{12} \Theta_C^2 + \gamma_{13} T^2 + \\ & \gamma_{14} \Theta_{Si} \Theta_C + \gamma_{15} \Theta_{Si} T + \gamma_{16} \Theta_C T + \\ & \gamma_{17} \Theta_{Si} + \gamma_{18} \Theta_C + \gamma_{19} T \end{aligned} \quad (5.20)$$

From the statistical analysis shown in Table 5.7, the model has larger value of adjusted- R^2 than the second order model. Hence, the third order model is more appropriate in describing the behavior of opacified aerogel at high Θ_{Si} and Θ_C . This is evidenced in the response surfaces as shown in Figure 5.16. Unlike second order model shown in Figure 5.13, optimal Θ_{Si} and Θ_C values are observed in Figure 5.16 even at high Θ_{Si} and Θ_C . The model can be simplified by eliminating insignificant parameters based on Table 5.7 as:

$$\begin{aligned} \lambda \gamma = & \gamma_0 + \gamma_2 \Theta_C^3 + \gamma_6 \Theta_{Si}^2 \gamma + \gamma_7 \Theta_{Si} \Theta_C^2 + \gamma_9 T \Theta_C^2 + \gamma_{11} \Theta_{Si}^2 \\ & \gamma_{12} \Theta_C^2 + \gamma_{14} \Theta_{Si} \Theta_C \gamma_{15} \Theta_{Si} \gamma_{16} \Theta_C \gamma_{18} \Theta_C \gamma_{19} T \end{aligned} \quad (5.21)$$

Table 5.7
Total thermal conductivity data fitted into third order model [Equation (5.20)]

Terms	Parameter	<i>p</i> -value	Coefficients (Coded)	Coefficients, γ_i (Actual)
Third order	Θ_{Si}^3	0.831	-3.87×10^{-3}	-9.94×10^{-5}
Third order	Θ_C^3	0.002	-0.02	-1.03×10^{-5}
Third order	T^3	0.646	-2.34×10^{-3}	-9.53×10^{-10}
Second order interaction	$\Theta_{Si} \Theta_C T$	0.154	-3.89×10^{-3}	-6.8×10^{-7}
Second order interaction	$\Theta_{Si}^2 \Theta_C$	0.991	5.66×10^{-5}	3.94×10^{-7}
Second order interaction	$\Theta_{Si}^2 T$	0.0003	0.016	1.05×10^{-5}
Second order interaction	$\Theta_{Si} \Theta_C^2$	0.0012	0.011	2.15×10^{-5}
Second order interaction	$\Theta_{Si} T^2$	0.154	4.78×10^{-3}	7.73×10^{-8}
Second order interaction	$\Theta_C^2 T$	0.0024	0.01	4.88×10^{-7}
Second order interaction	$\Theta_C T^2$	0.261	-3.94×10^{-3}	-1.73×10^{-8}
Second order	Θ_{Si}^2	0.018	0.02	2×10^{-3}
Second order	Θ_C^2	<0.0001	0.022	3.04×10^{-4}
Second order	T^2	0.574	1.64×10^{-3}	2.66×10^{-7}
First order interaction	$\Theta_{Si} \Theta_C$	<0.0001	0.036	4.28×10^{-4}
First order interaction	$\Theta_{Si} T$	<0.0001	-0.012	-1.81×10^{-4}
First order interaction	$\Theta_C T$	<0.0001	-9.79×10^{-3}	-7.79×10^{-6}
First order	Θ_{Si}	0.317	0.018	-0.017
First order	Θ_C	<0.0001	0.045	-5.11×10^{-3}
First order	T	0.009	0.016	8.27×10^{-4}
Mean	γ_0	<0.0001	0.085	0.063
Adjusted R^2 of model				0.922

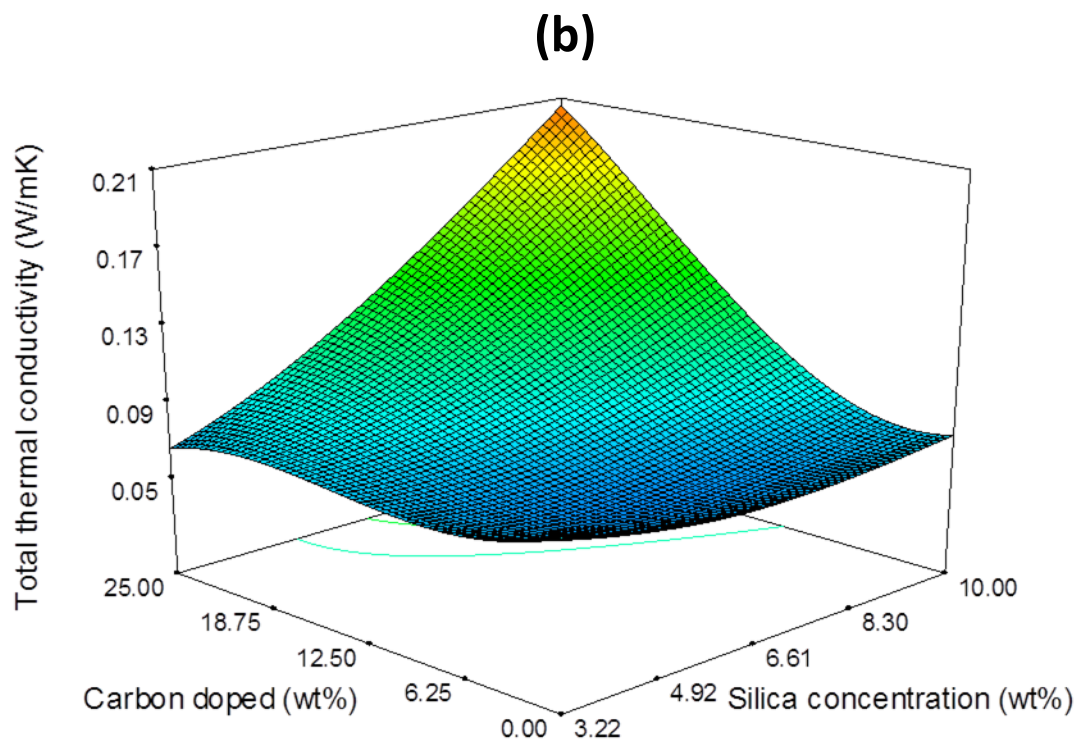
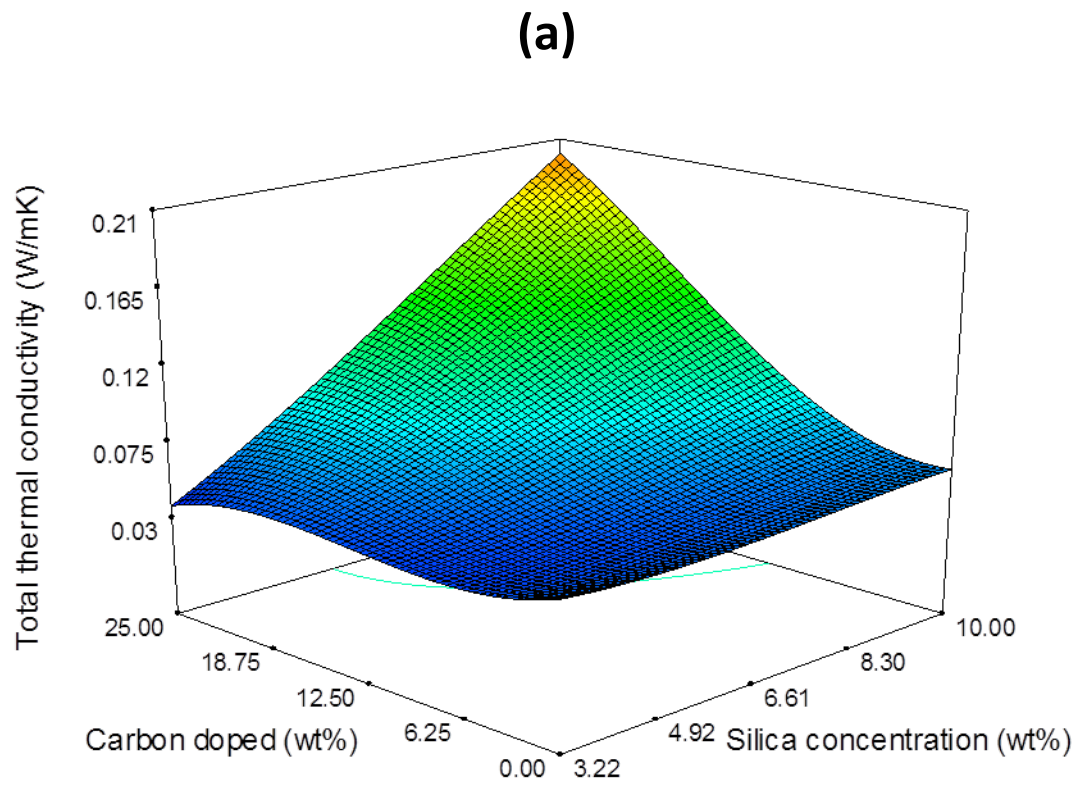


Figure 5.16 Response surface of total thermal conductivity fitted with third order model at (a) 30 °C, (b) 100 °C, (c) 200 °C and (d) 300 °C.

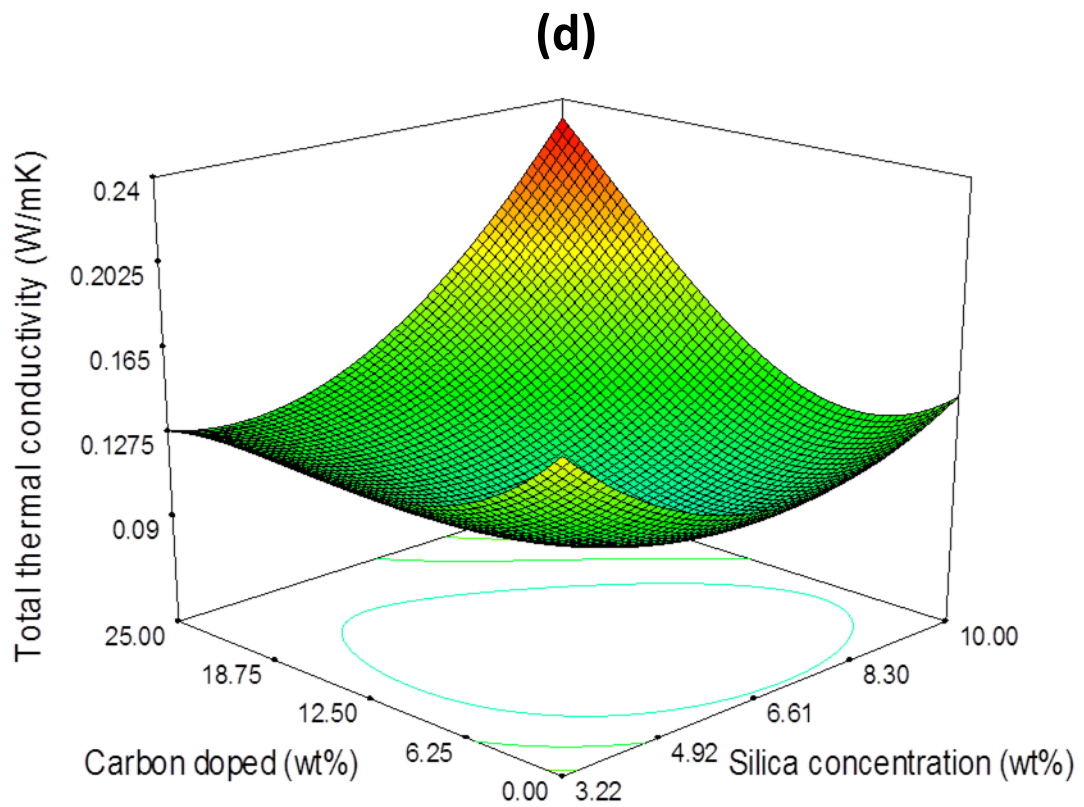
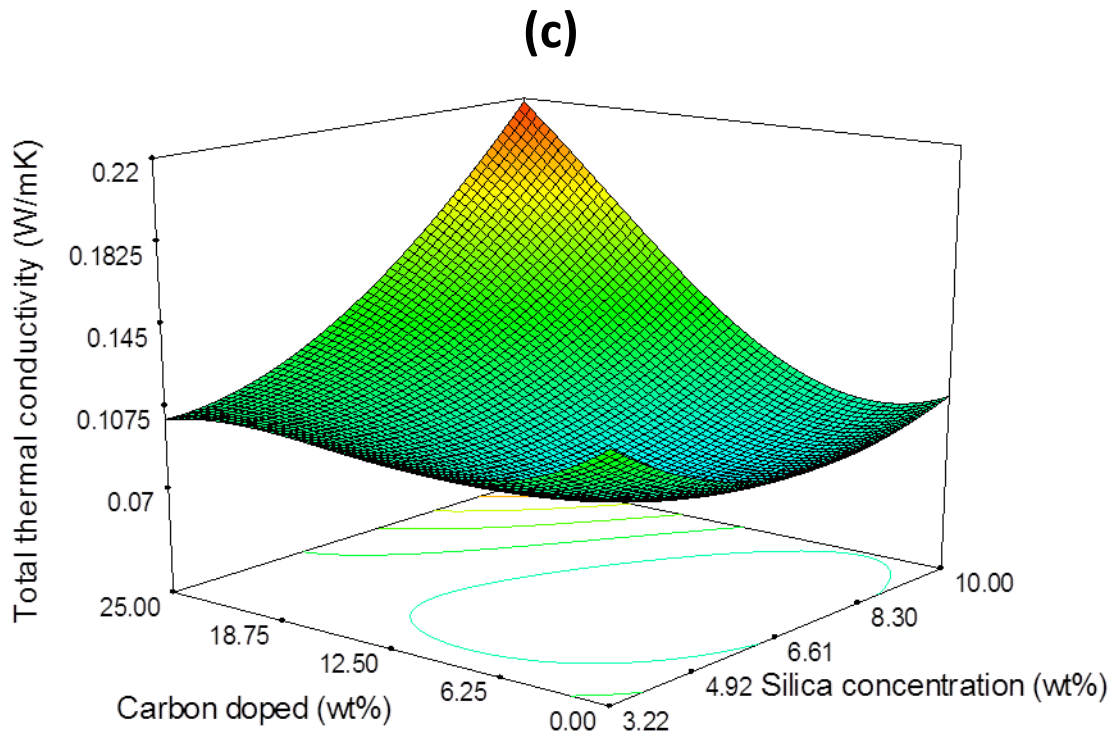


Figure 5.16 (continue) Response surface of total thermal conductivity fitted with third model at (a) 30 °C, (b) 100 °C, (c) 200 °C and (d) 300 °C.

Similarly, the tie line that minimized total thermal conductivity can be derived by equating the partial derivative in [equation \(5.22\)](#) to zero,

$$\left. \frac{\partial \lambda_T}{\partial \Theta_C} \right|_{\Theta_{Si}, T} = 3\gamma_2 \Theta_C^2 + 2\gamma_7 \Theta_{Si} \Theta_C + 2\gamma_9 T \Theta_C + 2\gamma_{12} \Theta_C + \gamma_{14} \Theta_{Si} + \gamma_{16} T + \gamma_{18} \quad (5.22)$$

$$\therefore 3\gamma_2 \Theta_C^2 + 2\gamma_7 \Theta_{Si} \Theta_C + 2\gamma_9 T \Theta_C + 2\gamma_{12} \Theta_C + \gamma_{14} \Theta_{Si} + \gamma_{16} T + \gamma_{18} = 0$$

Solve for Θ_C yield,

$$\Theta_{C, \min \lambda_T} = \frac{-2(\gamma_7 \Theta_{Si} + \gamma_9 T + \gamma_{12}) \pm \left\{ (\gamma_7 \Theta_{Si} + \gamma_9 T + \gamma_{12})^2 - \gamma_2 (\gamma_{14} \Theta_{Si} + \gamma_{16} T + \gamma_{18}) \right\}^{\frac{1}{2}}}{6\gamma_2} \quad (5.23)$$

Thus, $\Theta_{Si} - \Theta_C$ optimal lines at a given temperature can be plotted as in [Figure 5.17](#). The tie lines show the same trend as the second order model in [Figure 5.14](#) where

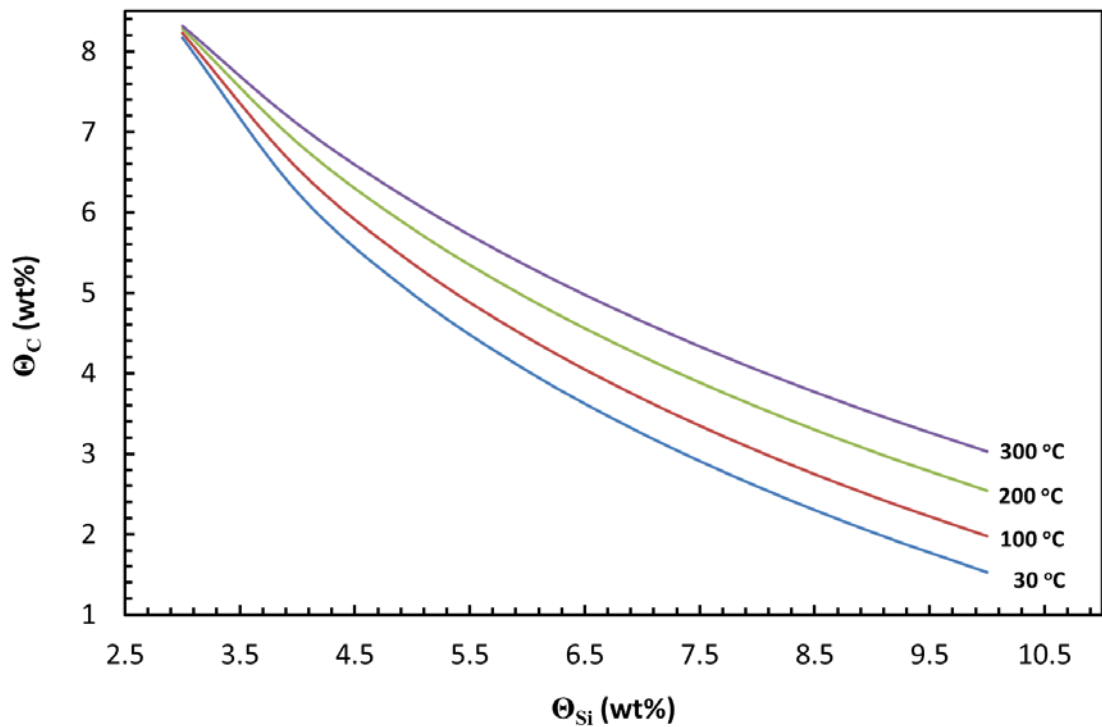


Figure 5.17 Optimal tie lines to minimize total thermal conductivity of opacified aerogel at various temperatures based on [equation \(5.23\)](#)

the increase in silica concentration is always accompany by decrease in carbon loading in order to minimize λ_T . However, due to the constant negative slope, the second order model suggests infinite decrease in Θ_{Si} as Θ_C increased. The third order model gives a better correction in this context because its negative slope decreased as Θ_C increased. Unlike what suggested by second order model where no carbon is needed to minimize λ_T , the decrease slope in third order model means a minimum amount of Θ_C is still needed to minimize the λ_T at high Θ_{Si} .

The optimal carbon loading for third order model at various temperatures is plotted in Figure 5.18. Though the plot is quadratic in nature, it is relative linear in the range of experiment and closed to the linear dependence exhibited by second order model in Figure 5.15. Hence, the linear relationship between optimal Θ_C and temperature in second order model may be just an approximation of the real behaviour of opacified aerogel.

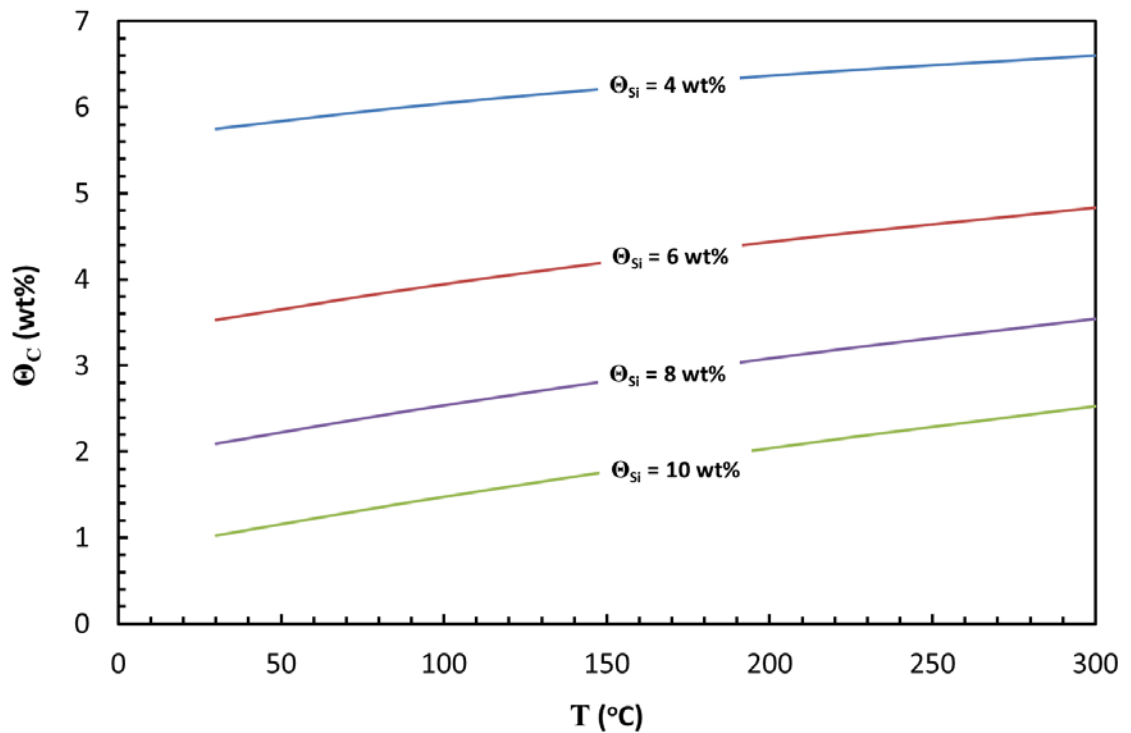


Figure 5.18 Optimal tie lines to minimize total thermal conductivity of opacified aerogel with various silica concentrations based on equation (5.23)

Another difference between the response surfaces of second order (Figure 5.13) and third order (Figure 5.16) model is that second order model has relatively flat minimum line (indicated by red arrow in Figure 5.13). Whereas, a local minimum point in third order model becomes more obvious as temperature increased. This implies at a given temperature, the minimum total thermal conductivity is confined in a rather small region in third order model. In second order model, the minimum λ_T at a given temperature is more robust to different combinations of $\Theta_{Si} - \Theta_C$. In contrast, the minimum λ_T at a given temperature in third order model requires only a specific combination of $\Theta_{Si} - \Theta_C$. Deviation of this specific combination of $\Theta_{Si} - \Theta_C$ will cause the λ_T to increase significantly, despite the partial minimum λ_T in respect to either Θ_{Si} or Θ_C can still be obtained by utilizing the tie lines in Figure 5.17. In order to find the exact minimum λ_T of at a given temperature using third order model, the partial derivative of equation (5.21) in respect Θ_{Si} to is given as,

$$\left. \frac{\partial \lambda_T}{\partial \Theta_{Si}} \right|_{\Theta_C, T} = 2\gamma_6 \Theta_{Si} + \gamma_7 \Theta_C^2 + 2\gamma_{11} \Theta_{Si} + \gamma_{14} \Theta_C + \gamma_{15} T \quad (5.24)$$

The partial minimum of λ_T in respect to Θ_{Si} is obtained by equating equation (5.24) to zero, which yield,

$$\therefore \Theta_{Si, \min \lambda_T} = -\frac{(\gamma_7 \Theta_C^2 + \gamma_{14} \Theta_C + \gamma_{15} T)}{2(\gamma_6 + \gamma_{11})\gamma_2} \quad (5.25)$$

Hence, the specific combination of $\Theta_{Si} - \Theta_C$ that gives exact minimum of λ_T at a given temperature can be determined by solving equations (5.23) and (5.25). The result is summarized two tie lines ($T - \Theta_{Si}$ and $\Theta_{Si} - \Theta_C$) in Figure 5.19. The figure can be used to determine the best combination of $\Theta_{Si} - \Theta_C$ that minimize λ_T at a given

temperature. For instance, at 200 °C, the optimal Θ_{Si} is read from the $T-\Theta_{Si}$ tie line as ~ 8 wt%. The corresponding optimal value of Θ_C can be further determined using the tie line $\Theta_{Si}-\Theta_C$ (~ 2.8 wt%) as shown in Figure 5.19. Hence, such tie lines can be used to determine formula (recipe) of $\Theta_{Si}-\Theta_C$ to minimize thermal conductivity of aerogel at the desired operating temperature.

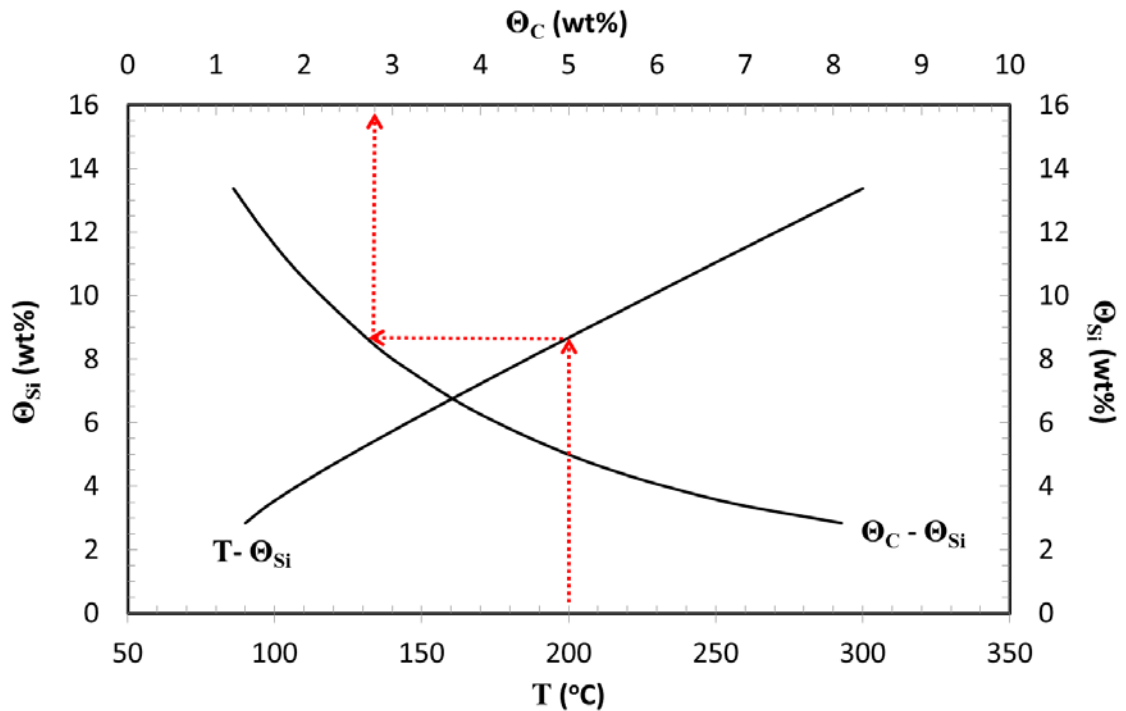
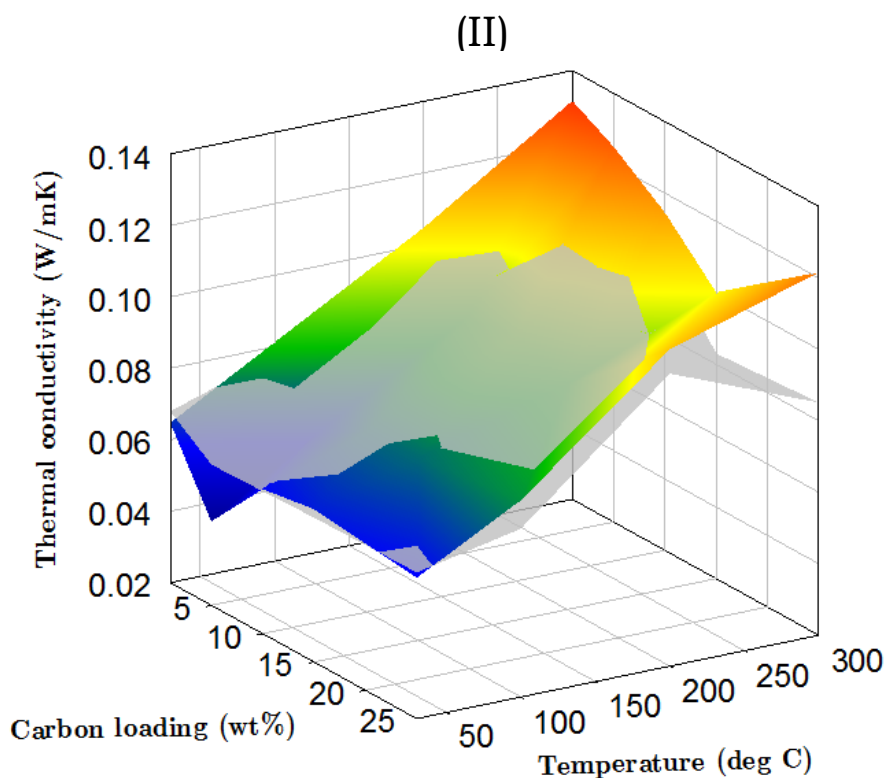
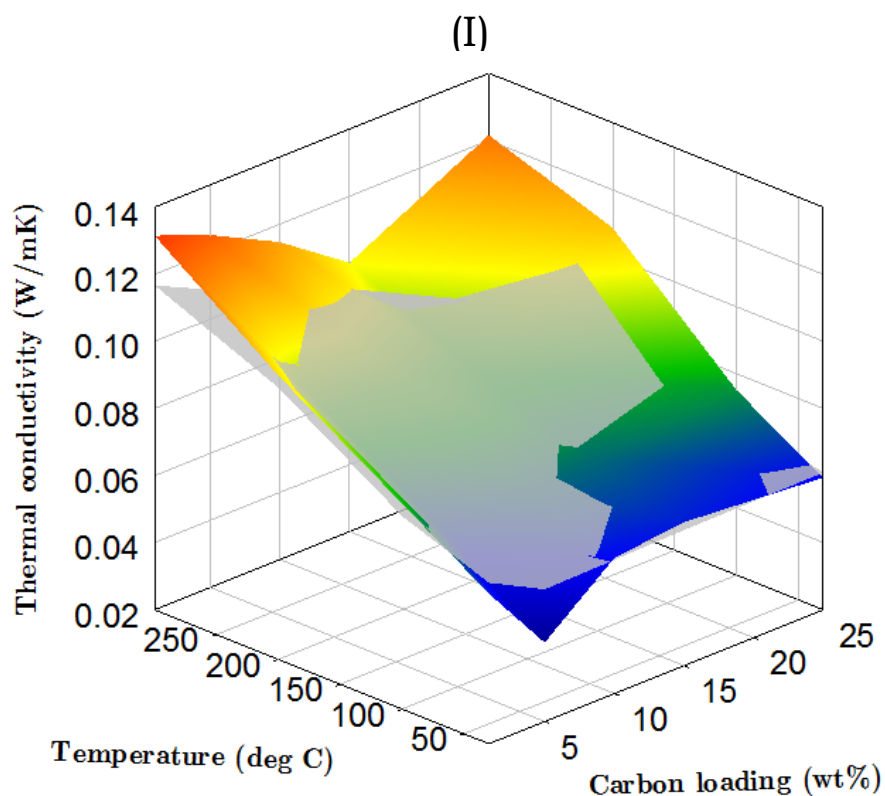



Figure 5.19 Optimal tie lines to minimize total thermal conductivity of opacified aerogel at a given temperature obtained from solutions of equations (5.23) and (5.25)

5.2.5 Comparisons with other aerogels

Aerogels opacified with activated carbon were compared with those opacified with carbon black and the result is shown in Figure 5.20. Generally, the thermal conductivity of aerogels opacified with activated carbon is lower than carbon black at low temperature range ($\sim 30 - 150$ °C). As temperature increase ($\sim 200 - 300$ °C), thermal conductivity of aerogel opacified with activated carbon increase faster than those opacified with carbon black. Thus, carbon black opacification is more effective than activated carbon in blocking heat under high temperature. Both the plots show a



 Opacified with activated carbon


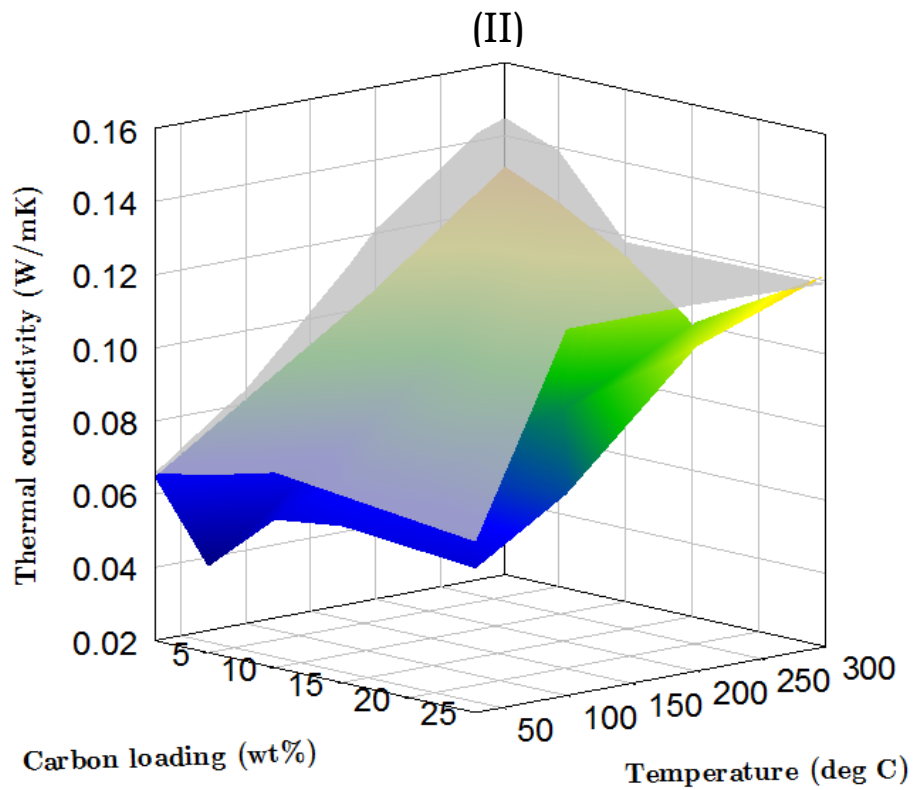
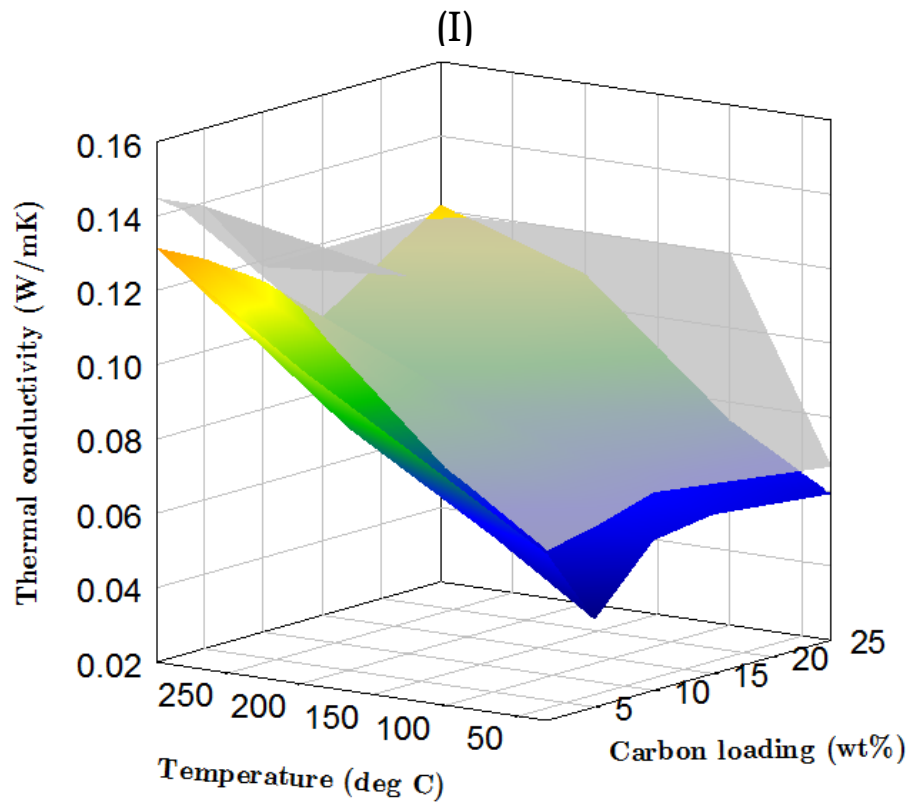
 Opacified with carbon black

Figure 5.20 Comparison of thermal conductivity of bamboo leaf aerogels opacified activated carbon and carbon black. Both types of aerogel are synthesized with 4.25 wt% of silica concentration and 1 – 25 wt% of carbon loading. (I) and (II) are rotated views to illustrate the comparison clearly.

kink at each level of temperature. This again verified that an optimal carbon loading exists to minimize the thermal conductivity. The kink at 30 °C occurs at approximately 5 wt% of carbon and shifted to approximately 15 wt% at 300 °C. This optimal carbon loading shifted because more carbon is needed to absorb the larger amount of radiation at high temperature.

These results verified that the use of porous activated carbon had reduced the solid conductivity of opacified aerogel. The thermal conductivity of carbon black opacification is larger than activated carbon (at ~30 – 150 °C) because of its high density that contributes directly to the increase in solid conductivity of aerogel. At higher temperature range (~ 200 – 300 °C), however, the advantage of low density is override by high radiative conductivity as indicated by the T^3 dependence in [equation \(2.5\)](#). This is reasonable since activated carbon had shown higher infrared transmission than carbon black ([Figure 5.8](#)). Based on Wien's displacement law, as temperature increase to the range of 200 -300 °C, the wavenumber corresponding to the maximum intensity of radiation is shifted to 1630 – 1980 cm^{-1} . As the infrared transmission of activated carbon is higher than carbon in this range ([Figure 5.8](#)), the aerogel opacified with carbon black is more effective in masking the radiation thus giving lower total conductivity. The higher infrared transmittance of activated carbon may cause by its porous nature where radiation may passes through the porous structure without absorbed much by the activated carbon.

The bamboo leaf aerogel was also compared with TEOS aerogel. [Figure 5.21](#) shows both the plots exhibit the similar trends in response to temperature and carbon loading. It is obvious that the thermal conductivity of bamboo leaf aerogels is lower than TEOS aerogels, which is in average 16.13% lower than TEOS aerogels. Such differences again verified that thermal conductivity of aerogel can be different even they were synthesized with same silica concentration and opacified with same amount of



Bamboo leaf aerogels



TEOS aerogels

Figure 5.21 Comparison of thermal conductivity of aerogels bamboo leaf aerogels with TEOS aerogels. Both types of aerogel are synthesized with 4.25 wt% of silica concentration and opacified with 0 – 25 wt% of activated carbon. (I) and (II) are rotated views to illustrate the comparison clearly.

activated carbon. The differences may be attributed to the high density of TEOS aerogels since higher density causes higher solid conductivity. This is supported by the higher density of TEOS aerogels shown in Figure 5.22. The bulk density of bamboo leaf aerogels are generally agreed with other reported values mentioned in Table 2.2. Recall that TEOS condensed through higher amount of Q^4 siloxane bond than water glass, it caused the density of TEOS aerogels be higher than bamboo leaf aerogels. Hence, controlling the distributions of Q^4 , Q^3 and Q^2 siloxane bonds will be the key to control the thermal conductivity and other properties of silica aerogels.

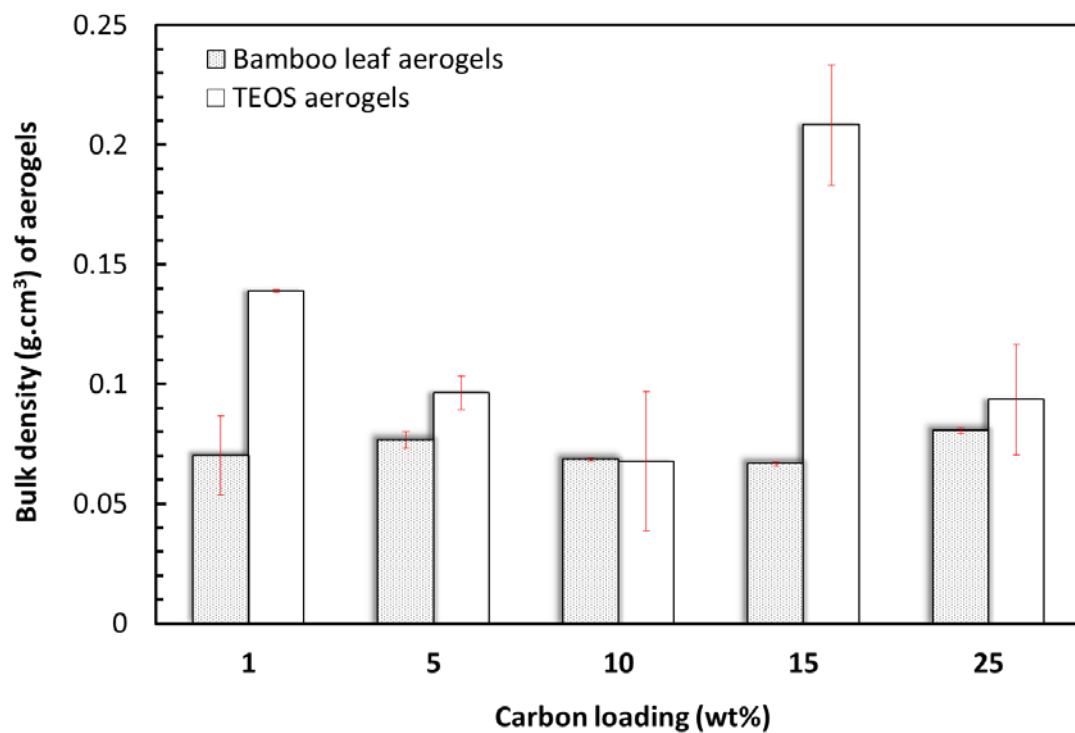


Figure 5.22 Bulk density of bamboo leaf aerogels compared with TEOS aerogels. All aerogels were synthesized with 4.25 wt% silica concentration and opacified with 1 – 25 wt% of activated carbon.

5.2.6 Summary

Activated carbon had been successfully synthesized from bamboo leaf and used to opacified bamboo leaf aerogel. The results show that carbon loading and silica concentration have great influence on the thermal conductivity of opacified aerogel. The combined effects of these parameters are both related implicitly to the density of aerogel. The dependence of minimum thermal conductivity to aerogel density was derived and illustrated in this chapter. Statistical regression developed was used to derive tie lines that minimize thermal conductivity of aerogel with proper combination of carbon loading and silica concentration. Comparison with TEOS aerogels proven that thermal conductivity of bamboo leaf aerogels is generally lower than TEOS aerogels. In term of opacifiers, activated carbon is more effective than carbon black in opacifying aerogel under low temperature ($\sim 30 - 150$ °C). However, the thermal conductivity of activated carbon aerogels is higher than carbon black aerogels in the temperature ranged from $\sim 200 - 300$ °C.

CHAPTER 6

CONCLUSIONS AND RECOMMENDATIONS

6.1 Conclusions

Bio-silica was successfully extracted from bamboo leaves and cogon grass to study their suitability to replace alkoxides as precursor in the synthesis of silica aerogel. Based on the study, cogon grass contains relatively low concentration of silica (2.9 ± 0.1 wt%). Nevertheless, this grass is still a potential source of silica due to the natural abundance of the grass. Bamboo leaves is found to contains 20.3 ± 2.8 wt% of amorphous silica, i.e., about double of rice husks which had been long recognized as biomass with very high silica content. The characterizations performed also confirm that the overall quality of amorphous silica obtained from bamboo leaves and cogon grass is rivals those extracted from others sources. However, the purity of silica obtained is highly dependent on how well the minerals in biomass can be removed. The result of acid leaching shows that effective removal of minerals can be achieved via long leaching periods and high acid concentration.

The bio-silica was used to prepare water glass as precursor in the synthesis of silica aerogel. Water glass with a silica concentration of 1 mol L^{-1} (3.5 wt%, 1.12 g cm^{-3}) and a modulus R of 0.85 was successfully prepared from bamboo leaf. It is found that processing parameters including dissolution temperature, dissolution time and agitation speed play essential role in maximizing the silica yield in water glass. It was also discovered that the silica yield depends on the ratio of R/C ; to achieve a high silica yield, this ratio must be in the range of $10 < R/C < 15$. The statistical correlation obtained from the result was used to optimize the condition in the process to maximize silica yield in water glass.

The properties of aerogel synthesized by bamboo leaf water glass are comparable to the aerogel synthesized with TEOS. It is discovered that bamboo leaf

aerogel synthesized in acidic condition exhibits more attractive properties. However, the bamboo aerogel was later prepared under neutral pH because the aerogel synthesized has very similar with those gelled in acidic condition but only require very short gelation period (less than 2.5 minutes).

The difference of properties caused by different gelation mechanisms is suspected to be related to the number of siloxane bond (Q^n) condensed during gelation. With larger number of siloxane bonds formed between silicon atoms, particles in aerogel aggregated in a more compact manner thus more attractive properties. It is also discovered that many correlations obtained from aerogel with high silica concentration do not agree with the measured properties of aerogel with low silica concentration. The thermal conductivity is also found to be correlated with fractal dimension of aerogel. This indirectly indicates that thermal conductivity is related to fractality, in which highly fractal structure can reduce thermal conductivity of aerogels.

Activated carbon used to opacify aerogel was also synthesized from bamboo leaves. The processing conditions in carbonizing and activating the carbon were optimized to reduce the carbon burnt off. The results indicate that the thermal conductivity of aerogel is reduced after being opacified with activated carbon. The thermal conductivity of the aerogel opacified with activated carbon is close to that of the aerogel opacified with carbon black. Thus, bamboo leaves can be a single source of both silica and carbon to synthesize opacified aerogel. Comparison with TEOS aerogels proven that thermal conductivity of bamboo leaf aerogels is generally lower than TEOS aerogels. Hence, it is proved that the replacement of alkoxides with bamboo leaves as precursor to synthesize and opacify silica aerogel is feasible. The result also shows that the opacified aerogels are stable up to 495 °C. Hence, bamboo leaves can be a potential inexpensive source of material to produce opacified aerogel that is suitable to be used as a thermal insulating material at high temperatures (200-500 °C).

Various models have been developed to optimize the processing conditions to achieve minimum thermal conductivity. Based on the models, various condition tie-lines were developed to estimate the total thermal conductivity. Such tie-lines may be useful in deciding the optimal combinations of carbon loading and silica concentration to synthesize opacified aerogel with minimum thermal conductivity at a given temperature.

It is suspected that the characteristics of the carbon dispersed in the aerogel precursors (TEOS alkoxides or water glass) prior to gelation may alter the gelation mechanism and affect the particle growth. As a result, the synthesized aerogels possess different microstructures and physical properties. Further investigation should be performed to study how the nature of the carbon added will affect the microstructure of the aerogel.

6.2 Novelty and contributions

The novelty of this work lies on the fact that silica aerogel can be synthesized and opacified by using bamboo leaf as a source of both the silica and activated carbon.

The results of this work may contribute in the following ways:

(I) Offers a cheap alternative source to synthesize aerogel

Bamboo leaf is confirmed containing high silica content that able to replace toxic alkoxide precursors to synthesize aerogel. The production cost of silica aerogel may be reduced as bamboo leaf has no commercial value presently.

(II) Aerogels opacified with activated carbon is comparable to carbon black

Beside carbon black, activated carbon is also proven can be used to opacify silica aerogel. The reduction of thermal conductivity by activated carbon at high temperature may have potential applications in hot gas piping, furnace lining and fire protection equipment. The reuse of bamboo leaf to synthesize activated carbon reduces the waste produced in the process. Carbon in biomass can be captured in the form of activated carbon rather than release it as carbon dioxide/ monoxide to the environment. Less carbon emission is achieved for the process.

(III) Development of optimal processing tie-lines for opacified aerogel

Tie-lines developed can be used to determine combinations of silica concentration and carbon loading that can be used to minimize thermal conductivity of aerogel at a given temperature. Thus, proper formula of silica concentration and carbon loading can be designed based on the temperature of interests to minimize the thermal conductivity of aerogel.

6.3 Recommendations for future work

All measurements of thermal conductivity were carried out under ambient pressure in this work due to equipment constraint. As the gas conduction of evacuated samples would be greatly reduced, it is recommended to study the thermal conductivity of bamboo leaf aerogel under near-vacuum pressure.

Further study should be carried out to investigate the relations between fractal structures on the thermal conductivity of aerogels. The correlation observed between these two in this work suggests that fractal structures may be the key parameter that affects the thermal conductivity rather than density and porosity of aerogel. This work also revealed that fractal structure may in turn be controlled by microstructural evolution governed by gelation mechanism. Hence, further study can be carried out on the gelation mechanism by altering the endpoint pH and pH swing.

The silica concentration of water glass used to synthesize aerogel is limited by the viscous slurry formed when more than 10 wt% of bio-silica is loaded to sodium hydroxide. Hence, method to produce water glass with larger amount of bio-silica may be attempted. This may increase the strength of aerogel produced and thus making ambient drying of the bamboo leaf aerogel plausible in the future.

Activated carbon used to opacify aerogel in this work is selected based on the optimum combination of carbon burnt-off and density. Since activated carbon with smaller particle size may cover the cross section of aerogel more effectively, less amount of activated carbon will be require in opacification. This may in turn reduce the solid conductivity contributed by activated carbon in the aerogel. Thus, effects such as particle size and porosity of activated carbon to the thermal conductivity can be further investigated in the future.

REFERENCES

- Lower and Higher Heating Values of Gas, Liquid and Solid Fuels. Biomass Energy Data Book, 2011, Available from:
http://cta.ornl.gov/bedb/appendix_a/Lower_and_Higher_Heating_Values_of_Gas_Liquid_and_Solid_Fuels.pdf. [17/7/2013].
- Typical calorific values of fuels, Available from:
http://www.biomassenergycentre.org.uk/portal/page?_pageid=75,20041&_dad=portal&_schema=PORTAL. [17/7/2013].
- Wood as a Fuel - List and values of wood fuel., Available from:
<http://www.woodenergy.ie/woodasafuel/listandvaluesofwoodfuelparameters-part1/>. [17/7/2013].
- ALAOUI, A. H., WOIGNIER, T., PHALIPPOU, J. & SCHERER, G. W. (1998) Room temperature densification of aerogel by isostatic compression. *Journal of Sol-Gel Science and Technology*, 13, 365-369.
- ALBA, M. D., LUAN, Z. H. & KLINOWSKI, J. (1996) Titanosilicate mesoporous molecular sieve MCM-41: Synthesis and characterization. *Journal of Physical Chemistry*, 100, 2178-2182.
- ANDERSON, A. M., CARROLL, M. K., GREEN, E. C., MELVILLE, J. T. & BONO, M. S. (2010) Hydrophobic silica aerogels prepared via rapid supercritical extraction. *Journal of Sol-Gel Science and Technology*, 53, 199-207.
- ARAVIND, P. R. & SORARU, G. D. (2011) High surface area methyltriethoxysilane-derived aerogels by ambient pressure drying. *Journal of Porous Materials*, 18, 159-165.
- BALAMURUGAN, M. & SARAVANAN, S. (2012) Producing nanosilica from *Sorghum vulgare* seed heads. *Powder Technology* 224, 345–350.
- BANGI, U. K. H., DHERE, S. L. & RAO, A. V. (2010) Influence of various processing parameters on water-glass-based atmospheric pressure dried aerogels for liquid marble purpose. *Journal of Materials Science*, 45, 2944-2951.
- BANGI, U. K. H., RAO, A. P., HIRASHIMA, H. & RAO, A. V. (2009) Physico-chemical properties of ambiently dried sodium silicate based aerogels catalyzed with various acids. *Journal of Sol-Gel Science and Technology*, 50, 87–97.
- BANGI, U. K. H., RAO, A. V. & RAO, A. P. (2008a) A new route for preparation of sodium-silicate-based hydrophobic silica aerogels via ambient-pressure drying. *Science and Technology of Advanced Materials*, 9.
- BANGI, U. K. H., RAO, A. V. & RAO, A. P. (2008b) A new route for preparation of sodium-silicate-based hydrophobic silica aerogels via ambient-pressure drying. *Science and Technology of Advanced Materials*, 9, 35006.
- BHAGAT, S. D., KIM, Y.-H., AHN, Y.-S. & YEO, J.-G. (2006) Textural properties of ambient pressure dried water-glass based silica aerogel beads: One day synthesis. *Microporous and Mesoporous Materials*, 96, 237-244.
- BHAGAT, S. D., KIM, Y.-H., AHN, Y.-S. & YEO, J.-G. (2007a) Rapid synthesis of water-glass based aerogels by in situ surface modification of the hydrogels. *Applied Surface Science*, 253, 3231–3236.
- BHAGAT, S. D., KIM, Y.-H., MOON, M.-J., AHN, Y.-S. & YEO, J.-G. (2007b) A cost-effective and fast synthesis of nanoporous SiO₂ aerogel powders using water-glass via ambient pressure drying route. *Solid State Sciences*, 9, 628-635.
- BHAGAT, S. D., OH, C.-S., KIM, Y.-H., AHN, Y.-S. & YEO, J.-G. (2007c) Methyltrimethoxysilane based monolithic silica aerogels via ambient pressure drying. *Microporous and Mesoporous Materials*, 100, 350-355.

- BHAGAT, S. D., PARK, K.-T., KIM, Y.-H., KIM, J.-S. & HAN, J.-H. (2008) A continuous production process for silica aerogel powders based on sodium silicate by fluidized bed drying of wet-gel slurry. *Solid State Sciences*, 10, 1113-1116.
- BORNE, A., CHEVALIER, B., CHEVALIER, J. L., QUENARD, D., ELALOUI, E. & LAMBARD, J. (1995) Characterization of silica aerogel with the atomic-force microscope and SAXS. *Journal of Non-Crystalline Solids*, 188, 235-242.
- BRAJNIK, D., KORPAR, S., MEDIN, G., STARIC, M. & STANOVNIK, A. (1994) Measurement of Sr-90 activity with Cherenkov radiation in a silica aerogel. *Nuclear Instruments & Methods in Physics Research Section a-Accelerators Spectrometers Detectors and Associated Equipment*, 353, 217-221.
- BRAJNIK, D., MEDIN, G., STANOVNIK, A. & STARIC, M. (1995) Determination of high energy beta-emitters with a Ge spectrometer or Cherenkov radiation in an aerogel. *Science of the Total Environment*, 173, 225-230.
- BRINKER, C. J. & SCHERER, G. W. (1990) *Sol-Gel Science : The Physics and Chemistry of Sol-Gel Processing* Boston, Academic Press.
- CARLSON, G., LEWIS, D., MCKINLEY, K., RICHARDSON, J. & TILLOTSON, T. (1995) Aerogel commercialization - technology, markets and costs. *Journal of Non-Crystalline Solids*, 186, 372-379.
- CHANDRADASS, J., KANG, S. & BAE, D. S. (2008) Synthesis of silica aerogel blanket by ambient drying method using water glass based precursor and glass wool modified by alumina sol. *Journal of Non-Crystalline Solids*, 354, 4115-4119.
- CHAO, X., JUN, S. & BIN, Z. (2009) Ultralow density silica aerogels prepared with PEDS. *Journal of Non-Crystalline Solids*, 355, 492-495.
- CHARRETEUR, F., JAOUEN, F. & DODELET, J.-P. (2009) Iron porphyrin-based cathode catalysts for PEM fuel cells: Influence of pyrolysis gas on activity and stability. *Electrochimica Acta*, 54, 6622-6630.
- CHARRETEUR, F., JAOUEN, F., RUGGERI, S. & DODELET, J.-P. (2008) Fe/N/C non-precious catalysts for PEM fuel cells: Influence of the structural parameters of pristine commercial carbon blacks on their activity for oxygen reduction. *Electrochimica Acta* 53, 2925-2938.
- CUI, S., LIU, Y., FAN, M. H., COOPER, A. T., LIN, B. L., LIU, X. Y., HAN, G. F. & SHEN, X. D. (2011) Temperature dependent microstructure of MTES modified hydrophobic silica aerogels. *Materials Letters*, 65, 606-609.
- CUTRUFELLO, M. G., ROMBI, E., FERINO, I., LOCHE, D., CORRIAS, A. & CASULA, M. F. (2011) Ni-based xero- and aerogels as catalysts for nitroxidation processes. *Journal of Sol-Gel Science and Technology*, 60, 324-332.
- DAI, S., JU, Y. H., GAO, H. J., LIN, J. S., PENNYCOOK, S. J. & BARNES, C. E. (2000) Preparation of silica aerogel using ionic liquids as solvents. *Chemical Communications*, 243-244.
- DELLA, V. P., KUHN, I. & HOTZA, D. (2002) Rice husk ash as an alternate source for active silica production. *Materials Letters* 57, 818-821.
- DENG, Z. S., WEI, J. D., WU, A. M., BAO, Y. P., WANG, J., SHEN, J., ZHOU, B. & CHEN, L. Y. (2000) Hydrophobic SiO₂ aerogels prepared with polyethoxydisiloxanes. *Journal of Inorganic Materials*, 15, 381-384.
- DIAS, A. S., PILLINGER, M. & VALENTE, A. A. (2006) Mesoporous silica-supported 12-tungstophosphoric acid catalysts for the liquid phase dehydration of D-xylose. *Microporous and Mesoporous Materials*, 94, 214-225.

- DIAS, J. M., ALVIM-FERRAZ, M. C. M., ALMEIDA, M. F., RIVERA-UTRILLA, J. & SANCHEZ-POLO, M. (2007) Waste materials for activated carbon preparation and its use in aqueous-phase treatment: A review. *Journal of Environmental Management*, 85, 833-846.
- DOMINGUEZ, M., TABOADA, E., IDRIS, H., MOLINS, E. & LLORCA, J. (2010) Fast and efficient hydrogen generation catalyzed by cobalt talc nanolayers dispersed in silica aerogel. *Journal of Materials Chemistry*, 20, 4875-4883.
- DOMINGUEZ, M., TABOADA, E., MOLINS, E. & LLORCA, J. (2008) Co-SiO₂ aerogel-coated catalytic walls for the generation of hydrogen. *Catalysis Today*, 138, 193-197.
- DONATTI, D. A., RUIZ, A. I. & VOLLET, D. R. (2001a) From sol to aerogel: a study of the nanostructural characteristics of TEOS derived sonogels. *Journal of Non-Crystalline Solids*, 292, 44-49.
- DONATTI, D. A., RUIZ, A. I. & VOLLET, D. R. (2001b) From sol to aerogel: a study of the nanostructural characteristics of TEOS derived sonogels. *Journal of Non-Crystalline Solids* 292 44-49.
- DORCHEH, A. S. & ABBASI, M. H. (2008a) Silica aerogel; synthesis, properties and characterization. *Journal of Materials Processing Technology*, 199, 10-26.
- DORCHEH, A. S. & ABBASI, M. H. (2008b) Silica aerogel; synthesis, properties and characterization. *Journal of Materials Processing Technology*, 199, 10-26.
- DOZIER, H., GAFFNEY, J.F., MCDONALD, S.K., JOHNSON, E.R.R.L., SHILLING, D.G. (1998) Cogongrass in the United States: History, ecology, impacts, and management. *Weed Technology*, 12, 737-743.
- DU, X., WANG, C., LI, T. & CHEN, M. (2009) Studies on the performances of silica aerogel electrodes for the application of supercapacitor. *Ionics*, 15, 561-565.
- DWIVEDI, V. N., SINGH, N. P., DAS, S. S. & SINGH, N. B. (2006) A new pozzolanic material for cement industry: Bamboo leaf ash. *International Journal of Physical Sciences*, 1, 106-111.
- EHRBURGERDOLLE, F., DALLAMANO, J., ELALOUI, E. & PAJONK, G. M. (1995) Relations between the texture of silica aerogels and their preparation. *Journal of Non-Crystalline Solids*, 186, 9-17.
- EINARSRUD, M. A. & NILSEN, E. (1998a) Strengthening of water glass and colloidal sol based silica gels by aging in TEOS. *Journal of Non-Crystalline Solids*, 226, 122-128.
- EINARSRUD, M. A. & NILSEN, E. (1998b) Thermal and temporal aging of silica gels in monomer solutions. *Journal of Sol-Gel Science and Technology*, 13, 317-322.
- FISHER, T., HAJALIGOL, M., WAYMACK, B. & KELLOGG, D. (2002) Pyrolysis behavior and kinetics of biomass derived materials. *Journal of Analytical and Applied Pyrolysis*, 62, 331-49.
- FOLETTI, E. L., GRATIERI, E., OLIVEIRA, L. H. D. & JAHN, S. R. L. (2006) Conversion of rice hull ash into soluble sodium silicate. *Materials Research*, 9, 335-338.
- FRELTOFT, T., KJEMS, J. K. & SINHA, S. K. (1986) Power-law correlations and finite-size effects in silica particle aggregates studied by small-angle neutron-scattering. *Physical Review B*, 33, 269-275.
- FRICKE, J. (1988) Aerogels - highly tenuous solids with fascinating properties. *Journal of Non-Crystalline Solids*, 100, 169-173.
- FRICKE, J., CAPS, R., BUTTNER, D., HEINEMANN, U. & HUMMER, E. (1987) Silica aerogel - a light-transmitting thermal superinsulator. *Journal of Non-Crystalline Solids*, 95-6, 1167-1174.
- FRICKE, J. & EMMERLING, A. (1992a) Aerogels. *Journal of the American Ceramic Society*, 75, 2027-2036.

- FRICKE, J. & EMMERLING, A. (1992b) Aerogels - preparation, properties, applications. *Structure and Bonding*, 77, 37-87.
- FRICKE, J. & EMMERLING, A. (1998) Aerogels - Recent progress in production techniques and novel applications. *Journal of Sol-Gel Science and Technology*, 13, 299-303.
- GAO, G. M., ZOU, H. F., GAN, S. C., LIU, Z. J., AN, B. C., XU, J. J. & LI, G. H. (2009) Preparation and properties of silica nanoparticles from oil shale ash. *Powder Technology*, 191, 47-51.
- GAUTHIER, B. M., BAKRANIA, S. D., ANDERSON, A. M. & CARROLL, M. K. (2004) A fast supercritical extraction technique for aerogel fabrication. *Journal of Non-Crystalline Solids*, 350, 238-243.
- GROSS, J., CORONADO, P. R. & HRUBESH, L. W. (1998) Elastic properties of silica aerogels from a new rapid supercritical extraction process. *Journal of Non-Crystalline Solids*, 225, 282-286.
- GURAV, J. L., NADARGI, D. Y. & RAO, A. V. (2008) Effect of mixed Catalysts system on TEOS-based silica aerogels dried at ambient pressure. *Applied Surface Science*, 255, 3019-3027.
- GURAV, J. L., RAO, A. V. & NADARGI, D. Y. (2009a) Study of thermal conductivity and effect of humidity on HMDZ modified TEOS based aerogel dried at ambient pressure. *Journal of Sol-Gel Science and Technology*, 50, 275-280.
- GURAV, J. L., RAO, A. V., RAO, A. P., NADARGI, D. Y. & BHAGAT, S. D. (2009b) Physical properties of sodium silicate based silica aerogels prepared by single step sol-gel process dried at ambient pressure. *Journal of Alloys and Compounds*, 476, 397-402.
- HAEREID, S., ANDERSON, J., EINARSRUD, M. A., HUA, D. W. & SMITH, D. M. (1995a) Thermal and temporal aging of TMOS-based aerogel precursors in water. *Journal of Non-Crystalline Solids*, 185, 221-226.
- HAEREID, S., DAHLE, M., LIMA, S. & EINARSRUD, M. A. (1995b) Preparation and properties of monolithic silica xerogels from TEOS-based alcogels aged in silane solutions. *Journal of Non-Crystalline Solids*, 186, 96-103.
- HAEREID, S., NILSEN, E. & EINARSRUD, M. A. (1996) Properties of silica gels aged in TEOS. *Journal of Non-Crystalline Solids*, 204, 228-234.
- HAMDAN, H., MUHID, M. N. M., ENDUD, S., LISTIORINI, E. & RAMLI, Z. (1997) Si-29 MAS NMR, XRD and FESEM studies of rice husk silica for the synthesis of zeolites. *Journal of Non-Crystalline Solids*, 211, 126-131.
- HAYASE, G., KANAMORI, K., KAZUKI, K., HANADA, T. & IOP (2011) Synthesis of New Flexible Aerogels from MTMS/DMDMS via Ambient Pressure Drying. *3rd International Congress on Ceramics*.
- HDACH, H., WOIGNIER, T., PHALIPPOU, J. & SCHERER, G. W. (1990) Effect of aging and pH on the modulus of aerogels. *Journal of Non-Crystalline Solids*, 121, 202-205.
- HE, F., ZHAO, H. L., QU, X. H., ZHANG, C. J. & QIU, W. H. (2009) Modified aging process for silica aerogel. *Journal of Materials Processing Technology*, 209, 1621-1626.
- HEGDE, N. D., HIRASHIMA, H. & RAO, A. V. (2007) Two step sol-gel processing of TEOS based hydrophobic silica aerogels using trimethylethoxysilane as a co-precursor. *Journal of Porous Materials*, 14, 165-171.
- HEGDE, N. D. & RAO, A. V. (2007) Physical properties of methyltrimethoxysilane based elastic silica aerogels prepared by the two-stage sol-gel process. *Journal of Materials Science*, 42, 6965-6971.
- HENNING, S. & SVENSSON, L. (1981) Production of silica aerogel. *Physica Scripta*, 23, 697-702.

- HERRMANN, G., IDEN, R., MIELKE, M., TEICH, F. & ZIEGLER, B. (1995) On the way to commercial production of silica aerogel. *Journal of Non-Crystalline Solids*, 186, 380-387.
- HOLZMUELLER, E. J. & JOSE, S. (2011) Invasion success of cogongrass, an alien C-4 perennial grass, in the southeastern United States: exploration of the ecological basis. *Biological Invasions*, 13, 435-442.
- HOSSEINI, M. M., SHAO, Y. X. & WHALEN, J. K. (2011) Biocement production from silicon-rich plant residues: Perspectives and future potential in Canada. *Biosystems Engineering*, 110, 351-362.
- HOU, G. H. (2003) Preparation of SiO₂ aerogel by rice husk. *Journal of Inorganic Materials*, 18, 407-412.
- HRUBESH, L. W., CORONADO, P. R. & SATCHER, J. H. (2001) Solvent removal from water with hydrophobic aerogels. *Journal of Non-Crystalline Solids*, 285, 328-332.
- HRUBESH, L. W. & PEKALA, R. W. (1994) Thermal-properties of organic and inorganic aerogels. *Journal of Materials Research*, 9, 731-738.
- HSIEH, Y., DU, Y. X., JIN, F. M., ZHOU, Z. Y. & ENOMOTO, H. (2009) Alkaline pre-treatment of rice hulls for hydrothermal production of acetic acid. *Chemical Engineering Research and Design*, 87, 13-18.
- HUMMER, E., LU, X., RETTELBACH, T. & FRICKE, J. (1992) Heat-transfer in opacified aerogel powders. *Journal of Non-Crystalline Solids*, 145, 211-216.
- HUMMER, E., RETTELBACH, T., LU, X. & FRICKE, J. (1993) Opacified silica aerogel powder insulation. *Thermochimica Acta*, 218, 269-276.
- HÜSING, N. & SCHUBERT, U. (2000) Aerogels. *Ullmann's Encyclopedia of Industrial Chemistry*. Wiley-VCH Verlag GmbH & Co. KGaA.
- HWANG, H. J., KIM, C. E. & CHA, Y. C. (2007) Strengthening of water glass based aerogel by TEOS. IN KIM, H., HOJO, J. & LEE, S. W. (Eds.) *Eco-Materials Processing and Design VIII*. Stafa-Zurich, Trans Tech Publications Ltd.
- HWANG, S.-W., KIM, T.-Y. & HYUN, S.-H. (2008) Optimization of instantaneous solvent exchange/surface modification process for ambient synthesis of monolithic silica aerogels. *Journal of Colloid and Interface Science*, 322, 224-230.
- ILER, R. K. (1979) *The Chemistry of Silica : Solubility, polymerization, colloid and surface properties, and biochemistry* New York, John Wiley.
- IN-SUB, H., JONG-CHUL, P., SE-YOUNG, K. & KI-SEOG, H. (2008) Fabrication of the monolithic silica aerogels using sodium silicate and its network strengthening. IN PAN, W. & GONG, J. H. (Eds.) *High-Performance Ceramics V, Pts 1 and 2*. Stafa-Zurich, Trans Tech Publications Ltd.
- IOANNIDOU, O. & ZABANIOTOU, A. (2007) Agricultural residues as precursors for activated carbon production - A review. *Renewable & Sustainable Energy Reviews*, 11, 1966-2005.
- JANKOVIC, B. (2008) Kinetic analysis of the nonisothermal decomposition of potassium metabisulfite using the model-fitting and isoconversional (model-free) methods. *Chemical Engineering Journal*, 139, 128-35.
- JENSEN, K. I., SCHULTZ, J. M. & KRISTIANSEN, F. H. (2004) Development of windows based on highly insulating aerogel glazings. *Journal of Non-Crystalline Solids*, 350, 351-357.
- JONES, J. C. (1998) Indirect evidence of relatively high thermal conductivities in powdered activated carbons. *Fuel*, 77, 1679-1681.
- KALAPATHY, U., PROCTOR, A. & SHULTZ, J. (2000) A simple method for production of pure silica from rice hull ash. *Bioresource Technology*, 73, 257-262.

- KALAPATHY, U., PROCTOR, A. & SHULTZ, J. (2002) An improved method for production of silica from rice hull ash. *Bioresource Technology*, 85, 285-289.
- KAMIYA, K., OKA, A., NASU, H. & HASHIMOTO, T. (2000) Comparative study of structure of silica gels from different sources. *Journal of Sol-Gel Science and Technology*, 19, 495-499.
- KANAMORI, K. (2011) Organic inorganic hybrid aerogels with high mechanical properties via organotrialkoxysilane-derived sol-gel process. *Journal of the Ceramic Society of Japan*, 119, 16-22.
- KIM, C. E., YOON, J. S. & HWANG, H. J. (2009) Synthesis of nanoporous silica aerogel by ambient pressure drying. *Journal of Sol-Gel Science and Technology*, 49, 47-52.
- KISTLER, S. S. (1931) Coherent expanded aerogels and jellies. *Nature*, 127, 741.
- KISTLER, S. S. (1932) Coherent Expanded-Aerogels. *Journal of Physical Chemistry*, 36, 52.
- KOHLI, R. K., JOSE, S., SINGH, H. P. & BATISH, D. R. (2008) *Invasive Plants and Forest Ecosystems*, Florida, CRC Press.
- KRISHNARAO, R. V., SUBRAHMANYAM, J. & KUMAR, T. J. (2001) Studies on the formation of black particles in rice husk silica ash. *Journal of the European Ceramic Society*, 21, 99-104.
- KUHN, J., GLEISSNER, T., ARDUINISCHUSTER, M. C., KORDER, S. & FRICKE, J. (1995) Integration of mineral powders into SiO₂ aerogels. *Journal of Non-Crystalline Solids*, 186, 291-295.
- KUWAGAKI, H., MEGURO, T., TATAMI, J., KOMEYA, K. & TAMURA, K. (2003) An improvement of thermal conduction of activated carbon by adding graphite. *Journal of Materials Science*, 38, 3279-3284.
- LAZAR, G., ZELLAMA, K., VASCAN, I., STAMATE, M., LAZAR, I. & RUSU, I. (2005) Infrared absorption properties of amorphous carbon films. *Journal of Optoelectronics and Advanced Materials*, 7, 647-652.
- LEE, D., STEVENS, P. C., ZENG, S. Q. & HUNT, A. J. (1995) Thermal characterization of carbon-opacified silica aerogels. *Journal of Non-Crystalline Solids*, 186, 285-290.
- LEE, O. J., LEE, K. H., YIM, T. J., KIM, S. Y. & YOO, K. P. (2002) Determination of mesopore size of aerogels from thermal conductivity measurements. *Journal of Non-Crystalline Solids*, 298, 287-292.
- LENZA, R. F. S. & VASCONCELOS, W. L. (2001) Preparation of silica by sol-gel method using formamide. *Materials Research*, 4, 189-194.
- LI, J., HAYAKAWA, S., SHIROSAKI, Y. & OSAKA, A. (2013) Revisiting structure of silica gels from water glass: an ¹H and ²⁹Si MAS and CP-MAS NMR study. *J Sol-Gel Sci Technol*, 65, 135-142.
- LI, T. & WANG, T. (2008) Preparation of silica aerogel from rice hull ash by drying at atmospheric pressure. *Materials Chemistry and Physics*, 112, 398-401.
- LI, X., LI, Y., ZHANG, S. & YANG, L. (2007) Study on the SiO₂ aerogels doped with TiO₂ powder prepared by rice hull ash. *Rare Metal Materials and Engineering*, 36, 43-45.
- LIN, B. L., CUI, S., LIU, X. Y., SHEN, X. D., LIU, Y. & HAN, G. F. (2011) Preparation and Characterization of HMDS Modified Hydrophobic Silica Aerogel. *Current Nanoscience*, 7, 1042-1045.
- LIOU, T. H. & WU, S. J. (2010) Kinetics Study and Characteristics of Silica Nanoparticles Produced from Biomass-Based Material. *Ind. Eng. Chem. Res.*, 49, 8379-8387.

- LIU, H., SHA, W., COOPER, A. T. & FAN, M. (2009) Preparation and characterization of a novel silica aerogel as adsorbent for toxic organic compounds. *Colloids and Surfaces a-Physicochemical and Engineering Aspects*, 347, 38-44.
- LIU, M.-L., YANG, D.-A. & QU, Y.-F. (2008) Preparation of super hydrophobic silica aerogel and study on its fractal structure. *Journal of Non-Crystalline Solids*, 354, 4927-4931.
- LOWE S, B. M., BOUDJELA, S, DE POORTER M (2004) *100 of the world's worst invasive alien species a selection from the global invasive species database*, Published by Invasive Species Specialist Group (ISSG) a specialist group of the Species survival Commission (SSC) of the World Conservation Union (IUCN).
- LOWELL, S., SHIELDS, J. E., THOMAS, M. A. & THOMMES, M. (2004) *Characterization of Porous Materials and Powders: Surface Area, Pore Size and Density*, Springer.
- LU, X., ARDUINI-SCHUSTER, M. C., KUHN, J., NILSSON, O., FRICKE, J. & PEKALA, R. W. (1992) 255, 971.
- LU, X., CAPS, R., FRICKE, J., ALVISO, C. T. & PEKALA, R. W. (1995) Correlation between structure and thermal-conductivity of organic aerogels. *Journal of Non-Crystalline Solids*, 188, 226-234.
- LUX, A., LUXOVA, M., ABE, J., MORITA, S. & INANAGA, S. (2003) Silicification of bamboo (*Phyllostachys heterocycla* Mitf.) root and leaf. *Plant and Soil*, 255, 85-91.
- MA, X., ZHOU, B., GAO, W., QU, Y., WANG, L., WANG, Z. & ZHU, Y. (2012) A recyclable method for production of pure silica from rice hull ash. *Powder Technology*, 217, 497-501.
- MACDONALD, G. E. (2007) Cogongrass: the plant's biology, distribution, and impacts in the Southeastern US. IN LOEWENSTEIN NJ, M. J. (Ed.) *The regional cogongrass conference: a cogongrass management guide*. Auburn University.
- MAHADIK, D. B., RAO, A. V., KUMAR, R., INGALE, S. V., WAGH, P. B. & GUPTA, S. C. (2012) Reduction of processing time by mechanical shaking of the ambient pressure dried TEOS based silica aerogel granules. *Journal of Porous Materials*, 19, 87-94.
- MANSARAY, K. G. & GHALY, A. E. (1998) Thermal degradation of rice husks in nitrogen atmosphere. *Bioresource Technology*, 65, 13-20.
- MARTIN, J. E. (1986) Scattering exponents for polydisperse surface and mass fractals. *Journal of Applied Crystallography*, 19, 25-27.
- MEZZA, P., PHALIPPOU, J. & SEMPERE, R. (1999) Sol-gel derived porous silica films. *Journal of Non-Crystalline Solids*, 243, 75-79.
- MOHANAN, J. L. & BROCK, S. L. (2004) A new addition to the aerogel community: unsupported US aerogels with tunable optical properties. *Journal of Non-Crystalline Solids*, 350, 1-8.
- MOHAPATRA, S., SAKTHIVEL, R., ROY, G. S., VARMA, S., SINGH, S. K. & MISHRA, D. K. (2011) Synthesis of beta-SiC Powder from Bamboo Leaf in a DC Extended Thermal Plasma Reactor. *Materials and Manufacturing Processes*, 26, 1362-1368.
- MOHMOD, A. L. (1999) R&D needs related to bamboo and rattan small enterprises. *INBAR-Workshop of Member Countries*. Beijing, China.
- MONER-GIRONA, M., MARTINEZ, E., ESTEVE, J., ROIG, A., SOLANAS, R. & MOLINS, E. (2002) Micromechanical properties of carbon-silica aerogel composites. *Applied Physics a-Materials Science & Processing*, 74, 119-122.
- MONER-GIRONA, M., ROIG, A., BENITO, M. & MOLINS, E. (2003a) Aerogel thin film synthesis by a supercritical fluid-assisted sol-gel route in a single processing unit. *Journal of Materials Chemistry*, 13, 2066-2068.

- MONER-GIRONA, M., ROIG, A., MOLINS, E. & LLIBRE, J. (2003b) Sol-gel route to direct formation of silica aerogel microparticles using supercritical solvents. *Journal of Sol-Gel Science and Technology*, 26, 645-649.
- MOTOMURA, H., FUJII, T. & SUZUKI, M. (2006) Silica deposition in abaxial epidermis before the opening of leaf blades of *Pleioblastus chino* (Poaceae, Bambusoideae). *Annals of Botany* 97, 513-519.
- MOTOMURA, H., MITA, N. & SUZUKI, M. (2002) Silica accumulation in long-lived leaves of *Sasa veitchii* (Carriere) Rehder (Poaceae-Bambusoideae). *Annals of Botany*, 90, 149-152.
- NADARGI, D. Y., LATTHE, S. S. & RAO, A. V. (2009) Effect of post-treatment (gel aging) on the properties of methyltrimethoxysilane based silica aerogels prepared by two-step sol-gel process. *Journal of Sol-Gel Science and Technology*, 49, 53-59.
- NADARGI, D. Y. & RAO, A. V. (2009) Methyltriethoxysilane: New precursor for synthesizing silica aerogels. *Journal of Alloys and Compounds*, 467, 397-404.
- NATARAJAN, E., NORDIN, A. & RAO, A. N. (1998) Overview of combustion and gasification of rice husk in fluidized bed reactors. *Biomass & Bioenergy*, 14, 533-546.
- NAYAK, J. P. & BERA, J. (2009a) Preparation of Silica Aerogel by Ambient Pressure Drying Process using Rice Husk Ash as Raw Material. *Transactions of the Indian Ceramic Society*, 68, 91-94.
- NAYAK, J. P. & BERA, J. (2009b) Preparation of Silica Aerogel by Ambient Pressure Drying Process using Rice Husk Ash as Raw Material. *Trans. Indian Ceram. Soc.*, 68, 91-94.
- NAZRIATI, SETYAWAN, H. & WINARDI, S. (2011) Synthesis of Silica Aerogel from Bagasse Ash by Ambient Pressure Drying. IN ISKANDAR, F., KHAIRURRIJAL & ABDULLAH, M. (Eds.) *4th Nanoscience and Nanotechnology Symposium*. Melville, Amer Inst Physics.
- NOVAK, Z. & KNEZ, Z. (1997) Diffusion of methanol-liquid CO₂ and methanol-supercritical CO₂ in silica aerogels. *Journal of Non-Crystalline Solids*, 221, 163-169.
- PAJONK, G. M. (1991) Aerogel catalysts. *Applied Catalysis*, 72, 217-266.
- PARK, B. D., WI, S. G., LEE, K. H., SINGH, A. P., YOON, T. H. & KIM, Y. S. (2003) Characterization of anatomical features and silica distribution in rice husk using microscopic and micro-analytical techniques. *Biomass Bioenerg.*, 25, 319-327.
- PHALIPPOU, J., SCHERER, G. W., WOIGNIER, T., BOURRET, D. & SEMPERE, R. (1995) Ultraporous materials with low permeability. *Journal of Non-Crystalline Solids*, 186, 64-72.
- PIERRE, A. C. & RIGACCI, A. (2011) SiO₂ Aerogels. IN AEGERTER, M. A. (Ed.) *Aerogels Handbook, Advances in Sol-Gel Derived Materials and Technologies*. Springer Science.
- PIJARN, N., JAROENWORALUCK, A., SUNSANEEYAMETHA, W. & STEVENS, R. (2010) Synthesis and characterization of nanosized-silica gels formed under controlled conditions. *Powder Technology*, 203, 462-468.
- PLANTARD, G., GOETZ, V. & PY, X. (2010) A direct method for porous particle density characterization applied to activated carbons. *Advanced Powder Technology*, 21, 592-598.
- POURETEDAL, H. & KAZEMI, M. (2012) Characterization of modified silica aerogel using sodium silicate precursor and its application as adsorbent of Cu²⁺, Cd²⁺, and Pb²⁺ ions. *International Journal of Industrial Chemistry* 3:20.
- RANGARAJAN, B. & LIRA, C. T. (1991) The effect of aging on acid-catalyzed aerogels. *Journal of Non-Crystalline Solids*, 136, 111-118.

- RAO, A. P., PAJONK, G. M. & RAO, A. V. (2005a) Effect of preparation conditions on the physical and hydrophobic properties of two step processed ambient pressure dried silica aerogels. *Journal of Materials Science*, 40, 3481-3489.
- RAO, A. P. & RAO, A. V. (2009) Improvement in optical transmission of the ambient pressure dried hydrophobic nanostructured silica aerogels with mixed silylating agents. *Journal of Non-Crystalline Solids*, 355, 2260-2271.
- RAO, A. P. & RAO, A. V. (2010) Modifying the surface energy and hydrophobicity of the low-density silica aerogels through the use of combinations of surface-modification agents. *Journal of Materials Science*, 45, 51-63.
- RAO, A. P., RAO, A. V. & PAJONK, G. M. (2005b) Hydrophobic and physical properties of the two step processed ambient pressure dried silica aerogels with various exchanging solvents. *Journal of Sol-Gel Science and Technology*, 36, 285-292.
- RAO, A. P., RAO, A. V., PAJONK, G. M. & SHEWALE, P. M. (2007a) Effect of solvent exchanging process on the preparation of the hydrophobic silica aerogels by ambient pressure drying method using sodium silicate precursor. *Journal of Materials Science*, 42, 8418-8425.
- RAO, A. V., GANBAVLE, V. V., BANGI, U. K. H. & DHERE, S. L. (2011) Influence of preparation conditions on nanoporous structure and optical transmission of sodium silicate based ambient pressure dried aerogels employing shaking. 18, 751-759.
- RAO, A. V. & HARANATH, D. (1999) Effect of methyltrimethoxysilane as a synthesis component on the hydrophobicity and some physical properties of silica aerogels. *Microporous and Mesoporous Materials*, 30, 267-273.
- RAO, A. V., HEGDE, N. D. & HIRASHIMA, H. (2007b) Absorption and desorption of organic liquids in elastic superhydrophobic silica aerogels. *Journal of Colloid and Interface Science*, 305, 124-132.
- RAO, A. V., KALESH, R. R., AMALNERKAR, D. P. & SETH, T. (2003a) Synthesis and characterization of hydrophobic TMES/TEOS based silica aerogels. *Journal of Porous Materials*, 10, 23-29.
- RAO, A. V., KULKARNI, M. M., AMALNERKAR, D. P. & SETH, T. (2003b) Superhydrophobic silica aerogels based on methyltrimethoxysilane precursor. *Journal of Non-Crystalline Solids*, 330, 187-195.
- RAO, A. V., NILSEN, E. & EINARSRUD, M. A. (2001) Effect of precursors, methylation agents and solvents on the physicochemical properties of silica aerogels prepared by atmospheric pressure drying method. *Journal of Non-Crystalline Solids*, 296, 165-171.
- RAO, A. V., RAO, A. P. & KULKARNI, M. M. (2004) Influence of gel aging and $\text{Na}_2\text{SiO}_3/\text{H}_2\text{O}$ molar ratio on monolithicity and physical properties of water-glass-based aerogels dried at atmospheric pressure. *Journal of Non-Crystalline Solids*, 350, 224-229.
- REICHENAUER, G. (2004) Thermal aging of silica gels in water. *Journal of Non-Crystalline Solids*, 350, 189-195.
- REIM, M., BECK, A., KORNER, W., PETRICEVIC, R., GLORA, M., WETH, M., SCHLIERMANN, T., FRICKE, J., SCHMIDT, C. & POTTER, F. J. (2002) Highly insulating aerogel glazing for solar energy usage. *Solar Energy*, 72, 21-29.
- REIM, M., KORNER, W., MANARA, J., KORDER, S., ARDUINI-SCHUSTER, M., EBERT, H. P. & FRICKE, J. (2005) Silica aerogel granulate material for thermal insulation and daylighting. *Solar Energy*, 79, 131-139.

- RIGACCI, A., ACHARD, P., EHRBURGER-DOLLE, F. & PIRARD, R. (1998) Structural investigation in monolithic silica aerogels and thermal properties. *Journal of Non-Crystalline Solids*, 225, 260-265.
- ROGACKI, G. & WAWRZYNIAK, P. (1995) Diffusion of ethanol-liquid CO₂ in silica aerogel. *Journal of Non-Crystalline Solids*, 186, 73-77.
- SARAWADE, P., KIM, J., HILONGA, A., QUANG, D., JEON, S. & KIM, H. (2011) Synthesis of sodium silicate-based hydrophilic silica aerogel beads with superior properties: Effect of heat-treatment *Journal of Non-Crystalline Solids* 357, 2156-2162.
- SARAWADE, P. B., KIM, J.-K., HILONGA, A. & KIM, H. T. (2010) Production of low-density sodium silicate-based hydrophobic silica aerogel beads by a novel fast gelation process and ambient pressure drying process. *Solid State Sciences*, 12, 911-918.
- SARAWADE, P. B., QUANG, D. V., HILONGA, A., JEON, S. J. & KIM, H. T. (2012) Synthesis and characterization of micrometer-sized silica aerogel nanoporous beads. *Materials Letters*, 81, 37-40.
- SCHERER, G. W., GROSS, J., HRUBESH, L. W. & CORONADO, P. R. (2002) Optimization of the rapid supercritical extraction process for aerogels. *Journal of Non-Crystalline Solids*, 311, 259-272.
- SCHERER, G. W., HAEREID, S., NILSEN, E. & EINARSRUD, M. A. (1996) Shrinkage of silica gels aged in TEOS. *Journal of Non-Crystalline Solids*, 202, 42-52.
- SCHERER, G. W. & SMITH, D. M. (1995) Cavitation during drying of a gel. *Journal of Non-Crystalline Solids*, 189, 197-211.
- SCHULTZ, J. M., JENSEN, K. I. & KRISTIANSEN, F. H. (2005) Super insulating aerogel glazing. *Solar Energy Materials and Solar Cells*, 89, 275-285.
- SHEWALE, P. M., RAO, A. V. & RAO, A. P. (2008) Effect of different trimethyl silylating agents on the hydrophobic and physical properties of silica aerogels. *Applied Surface Science*, 254, 6902-6907.
- SHI, F., LIU, J.-X., SONG, K. & WANG, Z.-Y. (2010) Cost-effective synthesis of silica aerogels from fly ash via ambient pressure drying. *Journal of Non-Crystalline Solids*, 356, 2241-2246.
- SHILLING, N. C. C. A. D. G. (1993) Cogongrass, *Imperata cylindrica* (L.) Beauv.: A Good Grass Gone Bad! IN FLORIDA DEPARTMENT OF AGRICULTURE & CONSUMER SERVICES, D. O. P. I. (Ed.).
- SHLYAKHTINA, A. & OH, Y.-J. (2008) Transparent SiO₂ aerogels prepared by ambient pressure drying with ternary azeotropes as components of pore fluid. *Journal of Non-Crystalline Solids*, 354, 1633-1642.
- SHUI, M., SONG, Y., REN, Y. & WANG, X. (2010) Structural analysis of amorphous silica prepared by water glass-based precursors and its thermal, spectral characterization. *Physica B*, 405, 1316-1320.
- SING, K. S. W., EVERETT, D. H., HAUL, R. A. W., MOSCOU, L., PIEROTTI, R. A., ROUQUEROL, J. & SIEMIENIEWSKA, T. (1985) Reporting physisorption data for gas solid systems with special reference to the determination of surface-area and porosity (recommendations 1984). *Pure and Applied Chemistry*, 57, 603-619.
- SMITH, D. M., MASKARA, A. & BOES, U. (1998) Aerogel-based thermal insulation. *Journal of Non-Crystalline Solids*, 225, 254-259.
- SMITHA, S., SHAJESH, P., ARAVIND, P. R., KUMAR, S. R., PILLAI, P. K. & WARRIER, K. G. K. (2006) Effect of aging time and concentration of aging solution on the porosity characteristics of subcritically dried silica aerogels. *Microporous and Mesoporous Materials*, 91, 286-292.

- STANDEKER, S., NOVAK, Z. & KNEZ, Z. (2007) Adsorption of toxic organic compounds from water with hydrophobic silica aerogels. *Journal of Colloid and Interface Science*, 310, 362-368.
- STANDEKER, S., NOVAK, Z. & KNEZ, Z. (2009) Removal of BTEX vapours from waste gas streams using silica aerogels of different hydrophobicity. *Journal of Hazardous Materials*, 165, 1114-1118.
- STANGL, R., PLATZER, W. & WITTEW, V. (1995) IR emission-spectroscopy of silica aerogel. *Journal of Non-Crystalline Solids*, 186, 256-263.
- STROM, R. A., MASMOUDI, Y., RIGACCI, A., PETERMANN, G., GULLBERG, L., CHEVALIER, B. & EINARSRUD, M. A. (2007) Strengthening and aging of wet silica gels for up-scaling of aerogel preparation. *Journal of Sol-Gel Science and Technology*, 41, 291-298.
- SUI, R. H., RIZKALLA, A. S. & CHARPENTIER, P. A. (2004) Synthesis and formation of silica aerogel particles by a novel sol-gel route in supercritical carbon dioxide. *Journal of Physical Chemistry B*, 108, 11886-11892.
- TAI, Y., YAMAGUCHI, W., TAJIRI, K. & KAGEYAMA, H. (2009) Structures and CO oxidation activities of size-selected Au nanoparticles in mesoporous titania-coated silica aerogels. *Applied Catalysis a-General*, 364, 143-149.
- TAJIRI, K., IGARASHI, K. & NISHIO, T. (1995) Effects of supercritical drying media on structure and properties of silica aerogel. *Journal of Non-Crystalline Solids*, 186, 83-87.
- TAMON, H., KITAMURA, T. & OKAZAKI, M. (1998) Preparation of silica aerogel from TEOS. *Journal of Colloid and Interface Science*, 197, 353-359.
- TANG, Q. & WANG, T. (2005) Preparation of silica aerogel from rice hull ash by supercritical carbon dioxide drying. *Journal of Supercritical Fluids*, 35, 91-94.
- TEIXEIRA, J. (1988) Small-angle scattering by fractal systems. *Journal of Applied Crystallography*, 21, 781.
- TEWARI, P. H., HUNT, A. J. & LOFFTUS, K. D. (1985) Ambient-temperature supercritical drying of transparent silica aerogels. *Materials Letters*, 3, 363-367.
- THY, P., JENKINS, B. M., GRUNDTVIG, S., SHIRAKI, R. & LESHER, C. E. (2006) High temperature elemental losses and mineralogical changes in common biomass ashes. *Fuel*, 85, 783-795.
- TSAI, W. T., LEE, M. K. & CHANG, Y. M. (2007) Fast pyrolysis of rice husk: Product yields and compositions. *Bioresour. Technol.*, 98, 22-28.
- VACHER, R., WOIGNIER, T., PELOUS, J. & COURTENS, E. (1988) Structure and self-similarity of silica aerogels. *Physical Review B*, 37, 6500-6503.
- VAN DE HULST, H. C. (1957) *Light Scattering by Small Particles*, New York, Dover Publications.
- VANBOMMEL, M. J. & DEHAAN, A. B. (1995) Drying of silica aerogel with supercritical carbon-dioxide. *Journal of Non-Crystalline Solids*, 186, 78-82.
- VATSALA (2003) *Bamboos in India*, New Delhi, National Institute of Science Communication and Information Resources.
- VILLAR-COCINA, E., MORALES, E. V., SANTOS, S. F., SAVASTANO, H. & FRIAS, M. (2011) Pozzolan behavior of bamboo leaf ash: Characterization and determination of the kinetic parameters. *Cement and Concrete Composites*, 33, 68-73.
- VOLLET, D. R., DONATTI, D. A., RUIZ, A. I. & GATTO, F. R. (2006) Mass fractal characteristics of wet sonogels as determined by small-angle x-ray scattering and differential scanning calorimetry. *Physical Review B*, 74.
- WAGH, P. B., BEGAG, R., PAJONK, G. M., RAO, A. V. & HARANATH, D. (1999) Comparison of some physical properties of silica aerogel monoliths synthesized by different precursors. *Materials Chemistry and Physics*, 57, 214-218.

- WANG, J., KUHN, J. & LU, X. (1995) Monolithic silica aerogel insulation doped with TiO₂ powder and ceramic fibers. *Journal of Non-Crystalline Solids*, 186, 296-300.
- WANG, J., SHEN, J., NI, X., WANG, B., WANG, X. & LI, J. (2010) Acoustic Properties of Nanoporous Silica Aerogel. *Rare Metal Materials and Engineering*, 39, 14-17.
- WANG, L. J., ZHAO, S. Y. & YANG, M. (2009) Structural characteristics and thermal conductivity of ambient pressure dried silica aerogels with one-step solvent exchange/surface modification. *Materials Chemistry and Physics*, 113, 485-490.
- WEI, G., LIU, Y., ZHANG, X. & DU, X. (2013) Radiative heat transfer study on silica aerogel and its composite insulation materials. *Journal of Non-Crystalline Solids*, 362, 231-236.
- WEI, G., LIU, Y., ZHANG, X., YU, F. & DU, X. (2011) Thermal conductivities study on silica aerogel and its composite insulation materials. *International Journal of Heat and Mass Transfer*, 54, 2355-2366.
- WEI, T.-Y., LU, S.-Y. & CHANG, Y.-C. (2009a) A New Class of Opacified Monolithic Aerogels of Ultralow High-Temperature Thermal Conductivities. *Journal of Physical Chemistry C*, 113, 7424-7428.
- WEI, T. Y., CHANG, T. F., LU, S. Y. & CHANG, Y. C. (2007) Preparation of monolithic silica aerogel of low thermal conductivity by ambient pressure drying. *Journal of the American Ceramic Society*, 90, 2003-2007.
- WEI, T. Y., LU, S. Y. & CHANG, Y. C. (2009b) A New Class of Opacified Monolithic Aerogels of Ultralow High-Temperature Thermal Conductivities. *Journal of Physical Chemistry C*, 113, 7424-7428.
- WITTEN, T. A., JR. & SANDER, L. M. (1981) Diffusion-Limited Aggregation, a Kinetic Critical Phenomenon. *Physical Review Letters*, 47, 1400-1403.
- WU, G. M., WANG, J., SHEN, J., YANG, T. H., ZHANG, Q. Y., ZHOU, B., DENG, Z. S., BIN, F., ZHOU, D. P. & ZHANG, F. S. (2000) Properties of sol-gel derived scratch-resistant nano-porous silica films by a mixed atmosphere treatment. *Journal of Non-Crystalline Solids*, 275, 169-174.
- WU, G. Y., YU, Y. X., CHENG, X. & ZHANG, Y. (2011) Preparation and surface modification mechanism of silica aerogels via ambient pressure drying. *Materials Chemistry and Physics*, 129, 308-314.
- YALCIN, N. & SEVINC, V. (2001) Studies on silica obtained from rice husk. *Ceramics International*, 27, 219-224.
- ZENG, S. Q., HUNT, A. & GREIF, R. (1995a) Theoretical modeling of carbon content to minimize heat-transfer in silica aerogel. *Journal of Non-Crystalline Solids*, 186, 271-277.
- ZENG, S. Q., HUNT, A. & GREIF, R. (1995b) Transport-properties of gas in silica aerogel. *Journal of Non-Crystalline Solids*, 186, 264-270.
- ZENG, S. Q., HUNT, A. & GREIF, R. (1995) Theoretical modeling of carbon content to minimize heat-transfer in silica aerogel. *Journal of Non-Crystalline Solids*, 186, 271-277.
- ZHANG, H. X., ZHAO, X., DING, X. F., LEI, H., CHEN, X., AN, D. M., LI, Y. L. & WANG, Z. C. (2010) A study on the consecutive preparation of D-xylose and pure superfine silica from rice husk. *Bioresource Technology* 101, 1263-1267.
- ZHAO, J. J., DUAN, Y. Y., WANG, X. D. & WANG, B. X. (2012) A 3-D numerical heat transfer model for silica aerogels based on the porous secondary nanoparticle aggregate structure. *Journal of Non-Crystalline Solids*, 358, 1287-1297.

LIST OF PUBLICATIONS

1. K.W. Kow, Rozita Yusoff, A.R. Aziz, E.C. Abdullah (2014). Thermal insulative performance of bamboo leaf aerogel opacified using activated carbon compared with carbon black. *Advanced Materials Research*. (941) 2482.
2. K.W. Kow, Rozita Yusoff, A.R. Aziz, E.C. Abdullah 2014, “Silica aerogel synthesized via bamboo leaves”. Paper presented at the *4th International Congress on Green Process Engineering (GPE 2014)*, Sevilla Spain.
3. K.W. Kow, Rozita Yusoff, A.R. Aziz, E.C. Abdullah (2014). Physicochemical properties of bamboo leaf aerogels synthesized via different modes of gelation. *Applied Surface Science*. (301) 161-172.
4. K.W. Kow, Rozita Yusoff, A.R. Aziz, E.C. Abdullah (2014). Characterisation of bio-silica synthesised from cogon grass (*Imperata cylindrica*). *Powder Technology*. (254) 206-13.
5. K.W. Kow, Rozita Yusoff, A.R. Aziz, E.C. Abdullah (2014). From bamboo leaf to aerogel: Preparation of water glass as a precursor. *Journal of Non-Crystalline Solids*. (386) 76-84.
6. K.W. Kow, Rozita Yusoff, A.R. Aziz, E.C. Abdullah 2013, “Synthesis of carbon-opacified-silica-aerogel using bamboo leaf”. Paper presented at the *International Conference on the Science and Engineering of Materials 2013 (ICoSEM2013)*, Kuala Lumpur Malaysia.
7. K.W. Kow, Rozita Yusoff, A.R. Aziz. (2011). Amorphous silica from bamboo leaves. In: *Proc. of 3rd International Congress on Green Process Engineering (GPE 2011)*, December 6-8, Kuala Lumpur, Malaysia. pp 262.

Appendix A

Originality report

7/20/2014

Turnitin Originality Report



Turnitin Originality Report

PhD Thesis by KOW KIEN WOH
From Postgraduate - Assignment
(POSTGRADUATE)

Similarity Index

6%

Similarity by Source

Internet Sources	2%
Publications	5%
Student Papers	0%

Processed on 20-Jul-2014 20:12 MYT
ID: 440230761

Word Count: 35570

SOURCES:

- 1 < 1% match (publications)
[Aambre, B. "Surface characterization of acidic ceria/zirconia prepared by direct sulfation". *Applied Surface Science*. 20100501.](#)

- 2 < 1% match (Internet from 23-Jun-2014)
http://www.docstoc.com/docs/113530728/Progress_in_Biomass_and_Bioenergy-Production

- 3 < 1% match (publications)
[Hasan Erdem Camurlu. "Sol-gel thin films with anti-reflective and self-cleaning properties". *Chemical Papers*. 02/15/2012](#)

- 4 < 1% match (publications)
[Nicola Hüsing. "Aerogels—Airy Materials: Chemistry, Structure, and Properties". *Angewandte Chemie International Edition*. 02/02/1998](#)

- 5 < 1% match (publications)
[Mille, Christian, and Robert W. Corkery. "A structural and thermal conductivity study of highly porous, hierarchical polyhedral nanofoam shells made by condensing silica in microemulsion films on the surface of emulsified oil drops". *Journal of Materials Chemistry A*. 2013.](#)

- 6 < 1% match (publications)
[Herrmann, G. "On the way to commercial production of silica aerogel". *Journal of Non-Crystalline Solids*. 19950602](#)

- 7 < 1% match (publications)
[Liu, Y. "Decomposition of ilmenite by concentrated KOH solution under atmospheric pressure". *International Journal of Mineral Processing*. 200611](#)

- 8 < 1% match (publications)
[Zeng, S.O. "Theoretical modeling of carbon content to minimize heat transfer in silica aerogel". *Journal of Non-Crystalline Solids*. 19950802](#)

- 9 < 1% match (Internet from 04-Jul-2010)
<http://www.dstuns.iltm.ac.in/teaching-and-presentations/teaching/undergraduate%20courses/vy305-molecular-architecture-and-evolution-of-functions/presentations/presentations-2007/seminar-2/P4.pdf>

- 10 < 1% match (publications)
[Hans-Peter Ebert. "Thermal Properties of Aerogels". *Aerogels Handbook*. 2011](#)

- 11 < 1% match (publications)
[A. Parvathy Rao. "Effect of solvent exchanging process on the preparation of the hydrophobic silica aerogels by ambient pressure drying method using sodium silicate precursor". *Journal of Materials Science*. 08/08/2007](#)

- 12 < 1% match (publications)
[Bi, C., and G.H. Tang. "Effective thermal conductivity of the solid backbone of aerogel". *International Journal of Heat and Mass Transfer*. 2013.](#)

- 13 < 1% match (publications)
[Tjong, S.C. "Nanocrystalline materials and coatings". *Materials Science & Engineering B*. 20040930](#)

- 14 < 1% match (Internet from 28-Nov-2012)
<http://144.206.159.178/#/611/598626/14147214.pdf>

- 15 < 1% match (Internet from 01-Jul-2014)
<http://dns2.asia.edu.tw/~vsho/YSHO-English/Database/P-R.docx>

- 16 < 1% match (publications)

https://turnitin.com/newreport_printview.asp?eq=0&eb=1&esm=0&oid=440230761&sid=0&n=0&m=0&svr=1&r=36.049573961645365&lang=en_us

1/55